Nonlinear Terahertz Spectroscopy in One and Two Dimensions

DISSERTATION

zur Erlangung des akademischen Grades

Dr. rerum naturalium
(Dr. rer. nat.)
im Fach Physik

eingereicht an der
Mathematisch-Naturwissenschaftlichen Fakultät I
Humboldt-Universität zu Berlin

von
Dipl.-Phys. Wilhelm Kühn
20. Oktober 1980 in Hattingen

Präsident der Humboldt-Universität zu Berlin:
Prof. Dr. Jan-Hendrik Olbertz

Dekan der Mathematisch-Naturwissenschaftlichen Fakultät I:
Prof. Dr. Andreas Herrmann

Gutachter:
1. Prof. Dr. Elsässer
2. Prof. Dr. Hamm
3. Prof. Dr. Masselink

eingereicht am: 09. Dezember 2010
Tag der mündlichen Prüfung: 10. Februar 2011

Abstract

The presented thesis concerns fundamentals and applications of nonlinear terahertz (THz) spectroscopy. Two widely used sources for THz radiation, the quantum cascade laser (QCL) and a laser-induced plasma, are investigated by means of THz spectroscopy. This thesis demonstrates for the first time a gain recovery time of several hundred femtoseconds within a QCL. Furthermore, we explored the exact generation process of THz pulses within a laser-induced two-color plasma. A comparison with theoretical predictions identifies unambiguously the ionisation current as origin of the emitted THz radiation. Besides, the influence of propagation effects within the plasma is experimentally examined and theoretically explained.

Novel methods of THz spectroscopy in one and in two dimensions are developed and applied to different semiconductor heterostructures. These methods employ in particular the phase information of the electric field, which is easy to access at THz frequencies. We use the electric field of THz pulses for high-field transport experiments on ultrafast time scales. Within this quantum-kinetic regime, the electron velocity decouples from phonon modes of the crystal lattice and quasi-ballistic transport becomes feasible during the first hundreds of femtoseconds even at room temperature. Mathematically this effect is rooted in the polaron equations of motion. We develope a dynamic polaron model, which reproduces the experimental results on short time scales as well as the published values on long time scales. At low temperatures of 80 K, we find additional THz-induced interband tunneling in GaAs. The temperature dependent tunneling rate depends essentially on the decoherence time of the induced process.

Furthermore, a novel method of collinear 2D THz spectroscopy is developed and applied to quantum well structures. An elaborated noncollinear beam geometry, applied in conventional 2D experiments at infrared frequencies, is not necessarily required. Frequency vectors are introduced to explain the underlying process of N-wave mixing not in space, but in time. This allows for a collinear beam geometry to measure all nonlinear signals simultaneously and to avoid tedious phasing procedures. We used this new method to decompose Rabi oscillations on intersubband transitions into nonlinear signals of different order. For large pulse areas the perturbation theory and thus the concept of N-wave mixing breaks down. The first 2D correlation spectra in the THz frequency range demonstrate energetic couplings between polaronic states within an asymmetric double quantum well structure. Another experiment displays for the first time the 2D correlation spectrum of a 2π Rabi flop on the intersubband transition of a multiple quantum well structure.

Zusammenfassung

Die vorliegende Dissertation behandelt Grundlagen und Anwendungen der nichtlinearen Terahertzspektrospie (THz). Zwei verbreitete Quellen für THz-Strahlung, der Quantenkaskadenlaser sowie ein Laser-induziertes Plasma, werden mittels der THz-Spektroskopie untersucht. Diese Arbeit zeigt erstmalig, dass sich die Inversion des Quantenkaskadenlasers nach einer Störung schon innerhalb von hundert Femtosekunden wieder erholt. Außerdem wurde der exakte Generationsprozess von THz Impulsen in einem Laser-induzierten zwei-Farben Plasma untersucht. Unsere experimentellen Ergebnisse im Vergleich mit theoretischen Simulationen identifizieren eindeutig den Ionisationsstrom im Plasma als Ursache der Emission von THz Strahlung. Auch der Einfluss von Ausbreitungseffekten im Plasma wird experimentell gemessen und theoretisch erklärt.

Neue Spektroskopiemethoden in ein und zwei Zeitdimensionen werden entwickelt und auf verschiedene Halbleiterstrukturen angewendet. Diese Methoden nutzen insbesondere die, im THz-Bereich leicht zugängliche, Phaseninformationen des elektrischen Feldes aus. Wir nutzen das elektrische Feld des THz-Impulses um Hochfeld-Transportexperimente auf ultrakurzen Zeitskalen durchzuführen. In diesem quanten-kinetischen Regime entkoppelt sich die Bewegung des Elektrons von den Phononmoden des Kristalls, und quasiballistischer Transport in den ersten hundert Femtosekunden wird selbst bei Raumtemperatur möglich. Mathematisch liegt dieser Effekt in den Bewegungsgleichungen des Polarons begründet. Wir entwickeln ein dynamisches Polaronmodell, welches sowohl die experimentellen Ergebnisse auf kurzen Zeitskalen als auch Literaturwerte auf langen Zeitskalen zuverlässig reproduziert. Bei niedrigen Temperaturen von 80 K tritt zusätzlich THz-induziertes Interbandtunneln in GaAs auf. Die temperaturabhängige Tunnelrate hängt dabei wesentlich von der Dekohärenzrate des induzierten Prozesses ab.

Desweiteren wird eine kollineare 2D THz Spektroskopiemethode entwickelt und erstmals an Quantentrogstrukturen angewendet. Eine komplizierte, nichtkollineare Strahlgeometrie, wie sie bei 2D Experimenten im infraroten Frequenzbereich häufig angewendet wird, ist prinzipiell nicht notwendig. Die eingeführten Frequenzvektoren erklären das zugrundeliegende N-Wellen Mischen analog zum Raum auch in der Zeit. So können mit einer kollinearen Strahlgeometrie alle nichtlinearen Signale simultan gemessen werden und aufwendige Phasenkorrekturen umgangen werden. Mit diesem Konzept wurden Rabi-Oszillationen an Intersubbandübergängen in Signale verschiedener nichtlinearer Ordnung zerlegt und die Grenzen der angewandten Störungstheorie aufgezeigt. Die ersten 2D Korrelationsspektren im THz-Bereich demonstrieren die energetischen Kopplungen zwischen verschiedenen polaronischen Zuständen in einer asymmetrischen Doppel-Quantentrogstruktur. Weitere Messungen an einer Sequenz von Einzel-Quantentrögen weisen eine 2π Rabi-Oszillation am Intersubbandübergang nach.

Contents

1 Introduction 1

2 Nonlinear Terahertz Spectroscopy 5
- 2.1 Terahertz Pulse Generation . . . 5
  - 2.1.1 Ti:Sapphire Laser System . . . 5
  - 2.1.2 Frequency Mixing in Nonlinear Crystals . . . 7
  - 2.1.3 THz Pulse Generation in Laser-Induced Plasmas . . . 10
- 2.2 Phase-Resolved Detection using Electrooptic Sampling . . . 16
- 2.3 Spectroscopic Concepts at THz Frequencies . . . 19
  - 2.3.1 The Phase-resolved Detection Suggests a 2D Approach . . . 19
  - 2.3.2 Field-Induced Effects Studied by Nonlinear THz Spectroscopy . . . 20

3 Coherent Ballistic High-Field Transport in GaAs 27
- 3.1 Basic Concepts . . . 27
- 3.2 Experimental Results . . . 31
- 3.3 The Influence of Scattering Processes on High-Field Transport in GaAs . . . 37
- 3.4 Dynamic Quantum-Kinetic Polaron Model . . . 40
- 3.5 A Quantum-Kinetic View on Previous Experiments . . . 46

4 Terahertz-Induced Interband Tunneling of Electrons in GaAs 49
- 4.1 Tunneling and the Role of Decoherence . . . 49
- 4.2 Experimental Results . . . 51
- 4.3 Discussion . . . 51
- 4.4 Dependence of the Tunneling Rate upon the Decoherence Rate . . . 55
- 4.5 Model Calculations . . . 58

5 Phase-Resolved Pump-Probe Experiments on a Quantum Cascade Laser 63
- 5.1 Quantum Cascade Lasers . . . 63
- 5.2 Experimental Results . . . 66
- 5.3 Discussion . . . 70

6 Collinear Two-Dimensional Terahertz Spectroscopy 75
- 6.1 2D Spectroscopy at Infrared Frequencies . . . 75
- 6.2 N-Wave Mixing in Space and in Time . . . 79
- 6.3 Collinear Two-Dimensional THz Spectroscopy . . . 84
- 6.4 Decomposition of Rabi Flops into Nonlinear Signals of Different Orders . . . 87
- 6.5 From the Photon Echo to the 2D Correlation Spectrum . . . 95
- 6.6 Phasing Procedures . . . 101
- 6.7 2D THz Correlation Spectroscopy on Multiple Quantum Wells . . . 106
- 6.8 Energetic Couplings between Asymmetric Double Quantum Wells . . . 110

6.9 Remarks on Collinear 2D Spectroscopy 117
6.10 General Relation between k and ω 119

7 Conclusions 125

Semiclassical Boltzmann Transport Equation 129

Multiple Quantum Well Samples 133

Publications 137

1 Introduction

Spectroscopy employs light to learn about the properties of matter. Depending on the frequency and the applied method, different information is extracted from a sample. Raman spectroscopy in the infrared reveals phonon modes, nuclear magnetic resonance experiments at radio frequencies explore chemical environments and X-rays image the inner structure of a crystal. And terahertz (THz) light? Which THz-specific features may lead to new scientific insight and applications?—This thesis explores scientific issues in the field of nonlinear THz spectroscopy. Strong few-cycle THz pulses are used to induce nonlinear processes and a field-resolved detection monitors them on a femtosecond (fs) timescale.

The THz region was utilized relatively late for spectroscopic purposes. Efficient generation and detection schemes were missing and the range between microwaves and infrared light was often considered the THz gap. THz frequencies were too high for electronic methods, i.e., carriers in motion, and too low for optical methods, i.e., the emission of photons (Fig. 1.1).

It was in 1975, when D. H. Auston developed a novel experimental scheme to generate and detect short THz pulses [1]. Although it was designed for optoelectronic purposes, the "Auston switch" paved in particular the way for modern THz spectroscopy [2–4]. So far most scientific experiments [5] and technical applications [6–9] employ only weak THz radiation to probe properties of the sample. The fascinating potential of strong THz pulses to actively manipulate sample systems is only rudimentarily explored. For example, a THz pulse appears on a femtosecond timescale as a very strong electric field pointing into one direction. Thus, high-field effects can be induced in a variety of samples, just by transmitting a THz pulse. During the short pulse duration nearly no heat is dissipated, so that several hundred kilovolts per centimeter (kV/cm) can be reversibly applied to a sample. This facilitated the field-ionization of Rydberg atoms in the first nonlinear THz experiment [2]. Meanwhile amplified pump pulses [10], phasematching [11–13], and pulse shaping [14] allow for the generation of much higher THz fields in the order of MV/cm [15, 16]. In combination with a field-resolved detection in free space [17, 18], our group implemented over the last years a powerful spectroscopic tool to study nonlinear THz-induced effects [15].

The new experimental possibilities initiated world-wide a dynamic research activity in the field of nonlinear THz spectroscopy. Different groups accelerated free carriers for impact ionization in InSb [19, 20] or to study the electron transport itself [4, 21, 22]. Intersubband transitions of individual quantum wells or within a quantum cascade laser (QCL) represent a further vital field for nonlinear THz spectroscopy [23–26]. THz pulses were also used to field-ionize impurities [27] or to investigate the mechanisms of superconductivity [28].

Many experimental results were analyzed only in the magnitude of the Fourier transform, as it is common at higher, optical frequencies. The recorded phase of the electric field, a specific feature at lower, THz frequencies, was often neglected [3, 5, 19, 20]. Thus, we searched for new innovate methods to conduct nonlinear spectroscopy in a THz-specific way.

The presented thesis employs strong electric THz fields in combination with a femtosecond time resolution to study high-field electron transport by new means. Our experiments on GaAs access for the first time the ballistic, quantum-kinetic regime, where the electron transport is

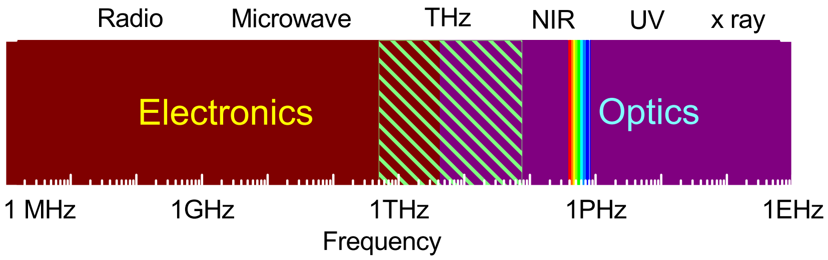

Figure 1.1: Electromagnetic fields with frequencies in the "electronic" range are usually generated by intraband motions of carriers. Photons of higher energy in the "optic" range are usually emitted by atomic transitions or interband transitions in solids. Terahertz frequencies are located between both ranges in the electromagnetic spectrum.

mainly unaffected from scattering processes. Electron transport was not only controversially discussed over the last decades [29–31], it is also of great technical relevance, since electric fields and timescales in modern electronic devices approach rapidly this quantum-kinetic regime. Furthermore, the electric THz field is employed to investigate interband tunneling in GaAs. Unlike in most static tunneling experiments, we take into account the influence of the time-dependent decoherence on the tunneling rate [32].

QCLs are used in many commercial applications as sources for THz radiation. Since these devices are still under development and various internal processes remained still unclear, we studied a QCL using a field-resolved pump-probe experiment. The recorded phase allowed us to distinguish between two different effects, the change in transmission and the change in the refractive index.

We developed this method further to a nonlinear 2D spectroscopy method at THz frequencies. The phase of the electric field is used to display energetic couplings within a two-dimensional spectrum. Since THz radiation diverges after several meters in free space, we applied a novel collinear beam geometry. The capabilities of our new method are demonstrated by several experiments on multiple quantum wells [33, 34].

The development from a one-dimensional, i.e., recording the electric field along one time axis, to a two-dimensional THz spectroscopy, i.e., recording the electric field along two time axes, can be traced throughout the entire thesis. In the first nonlinear experiments we determined the relevant electric field as the difference between one scan with the sample and another scan without the sample. The second pulse required for a collinear phase-resolved pump-probe technique introduced a delay time and thus a second time axis. Afterwards it was mainly a conceptual step to Fourier-transform the nonlinear signal in two time dimensions and interpret the obtained 2D spectra. The fascinating concept of two time dimensions is not limited to short-time spectroscopy. It will be shown, that it leads, e.g., to a simplified illustration of several relativistic effects as well.

Outline of this thesis

In the second Chapter the most relevant parts of our experimental setup, the THz generation and the THz detection, are introduced. A detailed experiment on the generation of THz pulses in laser-induced plasmas is presented. Propagation effects are considered and our experimental results are compared with the predictions of a theoretical model. Furthermore, the applied experimental concepts in the THz range are presented.

In the third and the fourth Chapter high-field transport in *n*-type bulk GaAs is investigated. The incident THz pulse at 2 THz accelerates electrons within the conduction band. The emitted electric field is measured and compared to results of a model calculation. We find ballistic transport in the first several hundred femtoseconds leading to partial Bloch oscillations. It will be shown that on short time scales and for high electron velocities a quantum-kinetic decoupling occurs, which allows for much higher electron velocities than expected from the semiclassical Boltzmann transport equation. A theoretical model based on the quasi-particle concept of polarons reproduces the observed experimental findings. At low temperatures the THz field drastically enhances the number of conduction band electrons via interband tunneling. It will be shown, that the temperature-dependent decoherence time essentially determines the tunneling rate.

In the following Chapter 5 we use resonant pulses at 25 THz to pump and probe the lasing transition of a working quantum cascade laser. The transmitted pulses comprise two kinds of information. The recorded phase shift monitors the change in the refractive index and the transmission change monitors the gain dynamics. We find an unexpected fast gain recovery on a timescale of one hundred femtoseconds, accompanied by coherent gain oscillations.

Chapter 6 presents our new method of collinear 2D THz spectroscopy and its first applications. The principles of 2D spectroscopy are explained in detail. Frequency vectors are introduced to understand the underlying *N*-wave mixing process in time. The applied collinear beam geometry allows for measuring all nonlinear signals simultaneously in the absolute phase. In the first 2D experiment Rabi oscillations on an intersubband transition are decomposed into nonlinear signals of different order. The first 2D correlation spectra in the THz range are demonstrated in experiments on a multiple quantum well structure. Furthermore, an asymmetric double quantum well structure is studied at different temperatures. Linear measurements, the pump-probe signal and the 2D correlation spectrum point to a strong coupling to LO phonons. We find for the first time cross peaks, indicating energy transfer, in the 2D correlation spectrum.

2 Nonlinear Terahertz Spectroscopy

In the following chapter we present the experimental setup and the basic spectroscopic concepts that we applied in our nonlinear THz experiments. In principle we generate strong THz pulses, excite the sample, and detect the transmitted electric field transients. The most relevant parts, the generation (Section 2.1) and the detection (Section 2.2) of THz pulses, are discussed. More technical details of the experiment are published in Refs. [35, 36]. Since the actual generation process for THz pulses was still controversial, we performed an experiment on laser-induced plasmas, which is presented in Section 2.1.3.

THz radiation covers characteristic excitations of matter and has unique optical properties. Therefore, we developed and applied two THz-specific spectroscopic concepts, which are introduced in Section 2.3.

2.1 Terahertz Pulse Generation

Nonlinear THz spectroscopy requires short, sub-picosecond THz pulses with high electric field amplitudes of several hundred kV/cm. There are lasers emitting at THz frequencies, but the achieved field amplitudes amount only to several ten kV/cm. These THz lasers operate on transitions between molecular vibrations (e.g., CO_2 laser) or intersubbands of semiconductor heterostructures (quantum cascade lasers). While the gain width of the active medium of molecular gas lasers is too narrow to generate short pulses [37], quantum cascade lasers have been shown to emit a broad spectrum [38]. But evidence of a mode-locked THz quantum cascade laser is still missing. In our experiment we convert short near-infrared pulses from a Ti:sapphire laser system with nonlinear optical methods into short THz pulses.

2.1.1 Ti:Sapphire Laser System

Our source to emit strong and short THz pulses is pumped by amplified mode-locked Ti:sapphire lasers. Thus the core equipment of our experiment is a *Femtolasers* system consisting of a *Scientific Pro* Ti:sapphire laser oscillator and a multipass amplifier *Femtopower Compact Pro*. The oscillator depicted in Fig. 2.1 is pumped by a frequency doubled continuous-wave Nd:YVO_4 laser (*Coherent Verdi 5*) with 4 W output power at a wavelength of 532 nm. Ti:sapphire as an active medium provides a broad bandwidth and has a large damage threshold. In particular it enables mode-locking within the cavity via nonlinear Kerr lensing. Therefore, the cavity is adjusted in a way, that the higher intensities of short pulses are preferred over the lower intensities of the continuous wave mode. Furthermore, the dispersion introduced by the Ti:sapphire crystal and the mirrors needs to be compensated for with two chirped mirrors. At each round trip the output coupler (OC) transmits at small fraction of the pulse, which is used for the experiment. In that way we obtain 12 fs pulses with a repetition rate of 71 MHz and an average power of 450 mW.

The main part of the output beam is used for amplification in the chirped pulse amplifier (CPA). To prevent damage of the involved optical devices, the pulses are stretched to several pi-

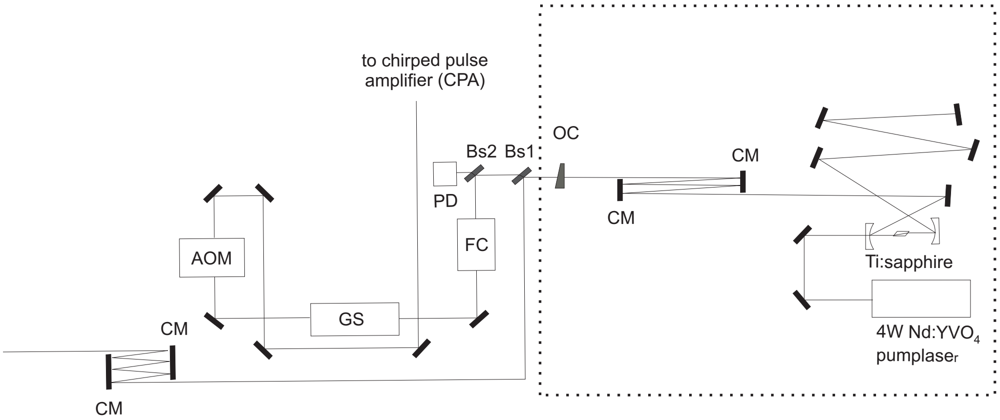

Figure 2.1: The *Femtosource Scientific Pro* oscillator consists basically of an optically pumped Ti:sapphire crystal and two chirped mirrors to compensate for the dispersion. Beamsplitters (BS) divide the beam into three parts. One part is detected with a photodiode (PD) and triggers the experiment. The second part is stretched (GS), spectrally shaped (AOM), and amplified for THz generation. The third part is precompensated by two chirped mirrors (CM) and used as a short sampling pulse for electrooptic sampling.

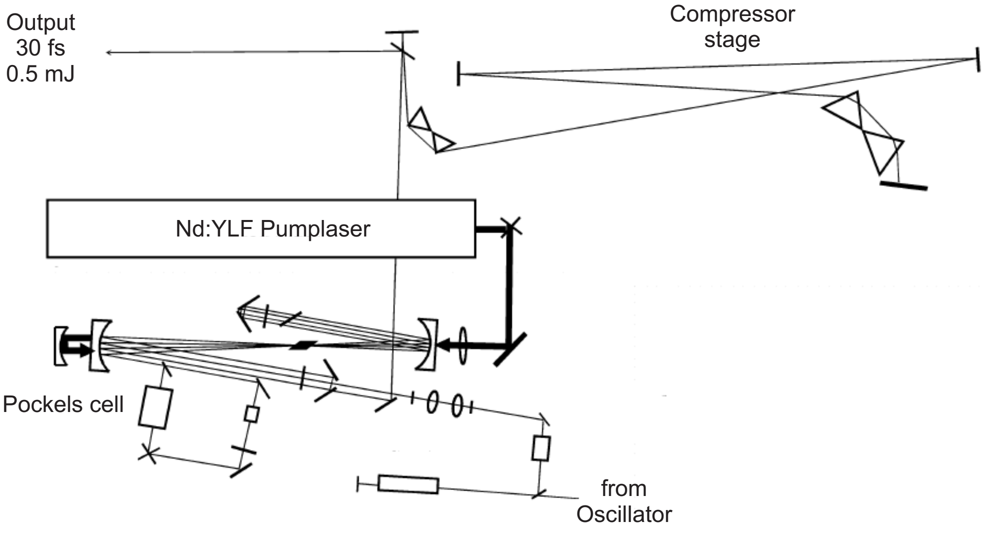

Figure 2.2: The pulse energy is amplified by five orders of magnitude during 9 passes through the Ti:sapphire crystal. The Pockels cell selects pulses at a repetition rate of 1 kHz. The compressor compensates for the dispersion of the glass stretcher and the Ti:sapphire crystal and reduces the pulse duration to approximatively 30 fs.

Table 2.1: Parameters of the oscillator and the multipass amplifier laser system

	pulse length	repetition rate	pulse energy	average output power
Oscillator	12 fs	71 MHz	6 nJ	450 mW
Amplifier	30 fs	1 kHz	500 μJ	500 mW

coseconds (ps) in a 3 cm thick glass block. A Faraday rotator (FC) protects the oscillator cavity from back reflected pulses from the amplifier. The spectral phase and the spectral intensity are shaped for optimal THz generation with an acousto-optic modulator (AOM). The multipass amplifier nearly maintains the imposed spectral features of the pulse over the entire amplification process.

The chirped pulse amplifier in Fig. 2.2 guides the pulse on 9 different passes through a second optically pumped Ti:sapphire crystal. This increases the pulse energy by five orders of magnitude. The crystal is pumped with 15 W from a frequency doubled Nd:YLF laser at repetition rate of 1 kHz. After the fourth pass also the repetition rate of the near-infrared pulses, and thus the amplified spontaneous emission (ASE), is reduced to 1 kHz using a Pockels cell. After the ninth pass the amplified pulse enters the compressor stage with carefully adjusted glass prisms for chirp compensation. As a result we obtain nearly bandwidth-limited 30 fs pulses with an energy of about 500 μJ at a repetition rate of 1 kHz. The main parameters of the laser system are listed in Table 2.1.

2.1.2 Optical Rectification and Difference-Frequency Generation in a GaSe Crystal

The conversion of optical pulses into picosecond-short photocurrents, emitting microwaves and THz frequencies, was realized the first time within a silicon structure [1]. Therefore, a first near-infrared pulse generated a photocurrent within an optoelectronic gate, which was then truncated by a short-circuit caused by a second pulse at another frequency and a larger penetration depth. These photoconductive “Auston-Switches” can be used to generate and detect microwaves and THz frequencies up to 4 THz [39, 40]. Higher electric field amplitudes of several kilovolts per centimeter were achieved several years later via difference frequency mixing in nonlinear crystals [41,42]. The peak amplitude of the generated THz field were successively increased to MV/cm [15] by the use of chirped pulse amplifiers [10], phasematching in GaSe [11–13], and acousto-optic pulse shaping of the near-infrared pulses [14].

Nonlinear optics describes the induced polarization within a material as a Taylor series of the nonlinear susceptibility $\chi^{(n)}$ [43–46]. The relevant term for THz generation is the second-order polarization described with the third-rank tensor $\chi^{(2)}$.

$$\tilde{\mathbf{P}}(\Omega) = \varepsilon_0 \chi^{(2)}(\Omega = \omega_1 - \omega_2; \omega_1, -\omega_2)\tilde{\mathbf{E}}(\omega_1)\tilde{\mathbf{E}}^*(\omega_2) \tag{2.1}$$

Susceptibilities of even nonlinear orders exist only in materials without inversion symmetry. The incident electric field induces a polarization $\tilde{\mathbf{P}}$, which emits the electric field of the converted frequency. If the electric field in Eq. (2.1) contains the frequencies ω_1 and ω_2, the nonlinear polarization will emit the frequencies $\omega_1 + \omega_2$ (sum frequency generation or, for $\omega_1 = \omega_2$, second harmonic generation) [47] and $\Omega = \omega_1 - \omega_2$ (difference-frequency generation or, for $\omega_1 = \omega_2$ optical rectification) [48].

Optical rectification emits a frequency centered at $\Omega \approx 2$ THz, not 0. This is due to the large

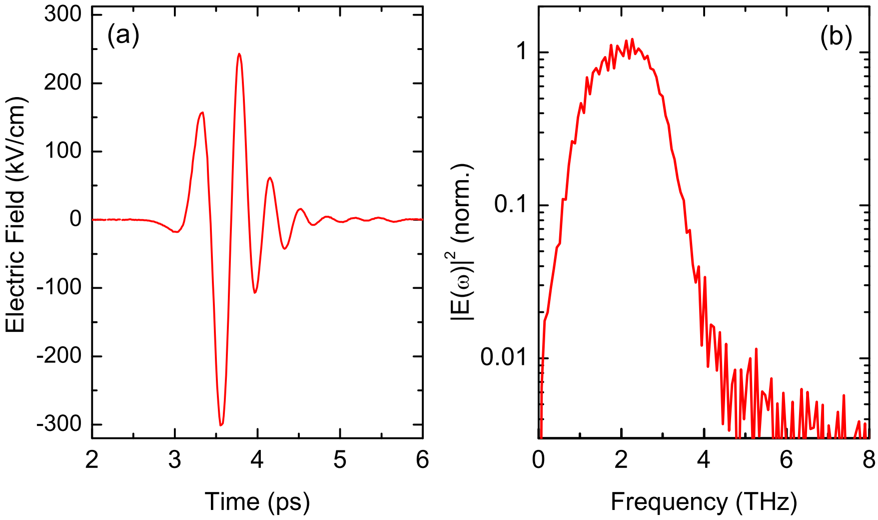

Figure 2.3: THz pulse generated via optical rectification in a GaSe crystal. Electric field amplitudes of 300 kV/cm are achieved with strong ultrashort 800 nm pulses. The pulse lasts for 500 fs and its center frequency amounts to 2 THz.

bandwidth of the incident pulses and to the undirected emission of lower frequencies. We use a single crystal of gallium selenide (GaSe) for frequency mixing because of several important advantages. It has a large relevant nonlinear susceptibility and a high damage threshold. GaSe is transparent in the near-infrared as well as in the THz range and only marginal two-photon absorption occur as a competing effect [49]. Furthermore, the generated THz field adds up throughout the entire crystal. This phasematching condition for the wave vectors $\mathbf{k}$ reads $\mathbf{K} = \mathbf{k_1} - \mathbf{k_2}$ [50,51]. For collinear incident pulses $|\mathbf{k}| = k = n\omega/c$ it is fulfilled, if the phase velocity of the THz radiation $v_p = c/n_3(\Omega)$ is equal to the group velocity of the near-infrared pump pulses $v_g = c/[n_1(\omega) + \omega dn_1/d\omega(\omega)]$ [52].

Fig. 2.3 displays a THz pulse generated in our experiment. The pulse is 500 fs long, performs only a few cycles [see Fig. 2.3 (a)] and has a center frequency of 2 THz [Fig. 2.3 (b)]. Since nonlinear effects are induced by high electric field strengths, our THz pulse is focused as tightly as possible. With a Gaussian beam profile and parabolic mirrors with a focal length of 12.7 mm, we achieve a nearly diffraction-limited spot size of 0.2 mm. The pulse energy of ≈ 25 nJ yields an electric field amplitude of 300 kV/cm. Higher THz pulse energies of 1 μJ, at the expense of an optimal beam profile, were generated with a tilted wave front technique in $LiNbO_3$ [53]. A variety of other nonlinear materials such as ZnTe [54], GaP [55] or the dielectrics $LiTaO_3$ and LiI_3 [41, 56–58] have been been used to generate THz radiation.

The spectral range between 10 THz and 50 THz is also called the “mid-infrared range”. But since the unit is THz and all experimental techniques are nearly identical, in this thesis the entire range from 1 to 50 THz will be considered THz frequencies. The main characteristic of this spectral range is the predominant detection with electrooptic sampling. To generate higher frequencies above 10 THz a similar difference frequency mixing setup is used. We employ type-I difference frequency mixing of near-infrared pulses with two spectral maxima. The spectral shape is imposed on the pulse using the acousto-optic pulse shaper. The spectral maxima are separated by the desired frequency and mixed within a GaSe crystal. The optical axis of a GaSe is always normal to the crystal surface. Electric field components pointing into this direction are

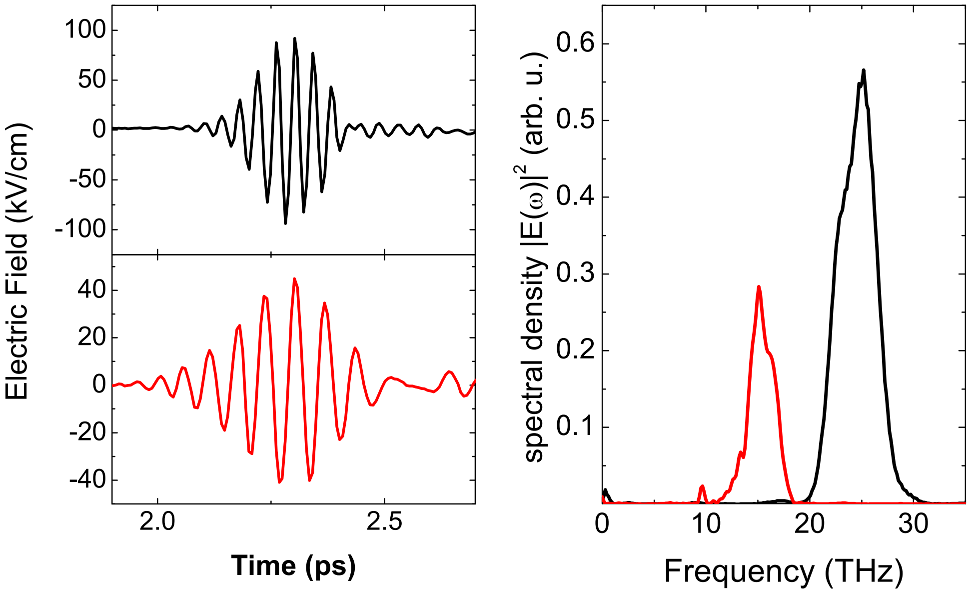

Figure 2.4: THz pulses of 15 and 25 THz generated with difference frequency mixing in GaSe. Our experimental setup generates frequencies between 10 and 30 THz with field amplitudes of up to 1 MV/cm.

considered extraordinary and experience another refractive index n_{eo} compared to the ordinary refractive index n_{o}. Tilting the angle with respect to the propagation direction changes not only the ratio of the ordinary and the extraordinary components, it changes also n_{eo} and thus the effective refractive index of the crystal [51]. This allows to select a tunable frequencies between 10 and 30 THz, which is accumulated over the crystal thickness [15].

Difference frequency mixing using a type-I phasematching geometry requires one ordinary and one extraordinary component. A diagonal incident polarization looses the factor $\sqrt{2}^{-1}$ for each component. To employ the full field strength available, we inserted a magnesium fluoride plate (MgF_2) with a high birefringence, i.e., $n_{\mathrm{o}} \neq n_{\mathrm{eo}}$. Even without birefringence both spectral maxima of the incident spectrum experience a phase difference because of the different wavelengths. A phase difference of half a wavelength is required to rotate one spectral maximum and to leave the other spectral maximum unaffected. The optical axis of the MgF_2 points normally to the surface. Therefore the difference between n_{o} and n_{eo} can be adjusted by tilting the angle of the MgF_2 plate with respect to the propagation direction. This allows for an exact adjustment of a $\lambda/2$ phase difference between the ordinary and the extraordinary polarization. In this way provide the full field strength in both axes and achieve an optimized difference frequency generation. The temporal divergence of both frequencies can be compensated for using the acousto-optic pulse shaper.

In Fig. 2.4 two examples of generated THz pulses are shown with a frequency of 15 (red) and 25 THz (black) with pulse durations of 230 and 130 fs, respectively. Depending on the frequency and the thickness of the GaSe crystal, amplitudes of 1 MV/cm (at $\approx$ 20 THz) with

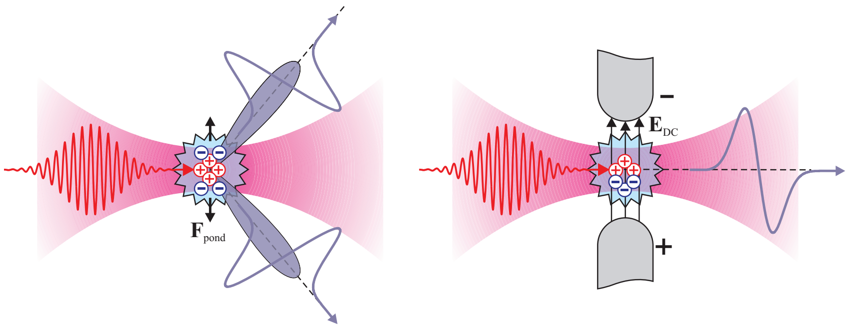

(a) Ponderomotive **(b) External DC-bias**

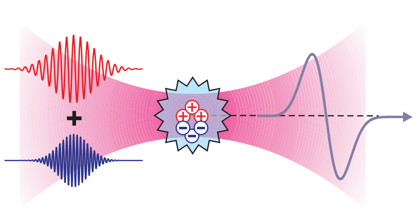

(c) ω-2ω (AC-bias) **(d) Few-cycle**

Figure 2.5: (a) A weak conical THz emission is achieved by focussing femtosecond pulses of 800 nm wavelength. An enhancement of more than one order of magnitude of the THz emission is achieved (b) through an external DC field around the plasma region or (c) the superposition of a second-harmonic field. (d) THz emission using only the fundamental is achieved, if the incident pulse is short enough, < 10 fs. The diagram is taken from Ref. [62].

energies up to 300 nJ are generated. Instead of providing both spectral components with only one pulse, also individually tunable pulses may be mixed. The idler signals of two optical parametric amplifiers yields in this way phase-locked THz pulses between 10 THz and 70 THz with field strengths of up to 100 MV/cm (at frequencies of several ten THz) [59].

2.1.3 THz Pulse Generation in Laser-Induced Plasmas

An alternative generation method uses laser-induced plasmas to generate THz pulses with a center frequency of circa 4 THz and electric field amplitudes of 400 kV/cm. Unlike frequency mixing in nonlinear crystals, this approach is not limited by the damage threshold of the material. Since ionizing atoms is a reversible process, this source has the potential to be scaled up and provide much higher THz pulse energies in the future. Moreover, the achievable bandwidth is not limited by phase-matching requirements or the transparency of the material. The approach was proposed [60] and demonstrated for the first time by Hamster *et al.* [61] in 1993. The focus of femtosecond pulses with a pulse energy of a few tens of μJ yields already sufficient intensities ($\approx 10^{14}$ Wcm^{-2}) for the ionization of gas molecules.

The first experiments generated relatively weak THz radiation, which was emitted at an angle to the propagation direction [61] [see Fig. 2.5 (a)]. Other plasma-based THz generation schemes

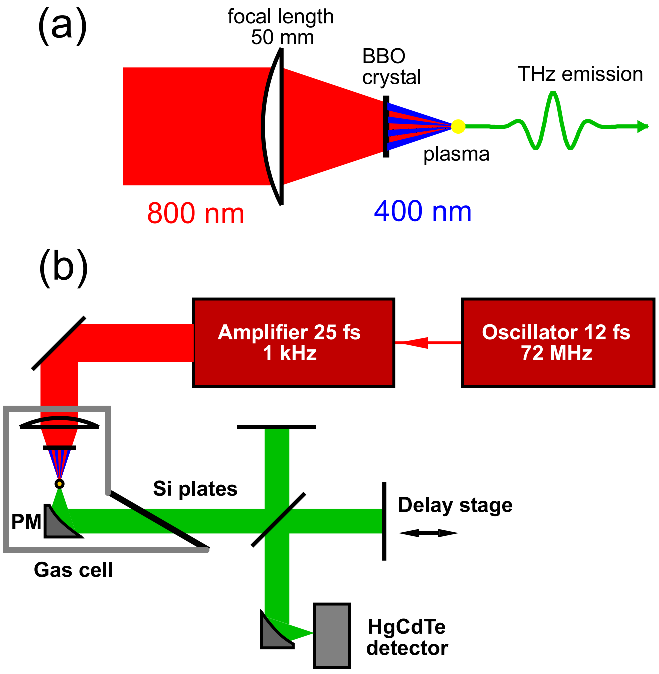

Figure 2.6: (a) Generation of a laser-induced plasma with a fundamental beam (800 nm) and its second-harmonic (400 nm). (b) The emitted radiation is collimated using a parabolic mirror (PM). A Michelson interferometer allows for measuring intensity interferograms using HgCdTe detector.

have been demonstrated to provide significantly stronger THz emission in the forward direction. Löffler *et al.* [63, 64] increased the emitted THz field strength by one order of magnitude using an externally applied DC field around the plasma region [Fig. 2.5 (b)]. At about the same time, Cook *et al.* [65] demonstrated a strongly enhanced THz emission from a plasma generated by a superposition of an 800-nm pulse with its second-harmonic field [Fig. 2.5 (c)]. The second-harmonic field, which has a constant phase-relation to the fundamental, was introduced via a thin β-barium borate (BBO) crystal placed several millimeters before the focal spot. This experimental setup found wide-spread use in THz research groups. More recently it was found [66] that a few cycle pulse with a duration of < 10 fs generates noticeable THz radiation as well [Fig. 2.5 (d)]. The spectrum of the pulse spans over an octave and thus contains the second harmonic frequency. Since the generated THz pulse depends strongly on the carrier envelope phase, this process could be used to characterize the incident pulse.

The exact generation mechanism and thus also the potential to improve the THz generation has remained unclear so far. The first phenomenological model proposed a frequency mixing processes enabled by the nonlinear electrical susceptibility of the plasma. Significant THz emission is observed only for superposition of two different frequencies within a plasma. This excludes a $\chi^{(2)}$, but suggested a $\chi^{(3)}$ four-wave rectification process. The origin of this nonlinearity has not been determined, but one could think about a Kerr effect, which also enables difference frequency mixing in nonlinear crystals. As a first step it was demonstrated that THz radiation is indeed only generated above the ionization threshold of the ambient gas. Furthermore, the generated radiation depends crucially on the relative phase between second-harmonic and fundamental pulse [67]. Kim *et al.* proposed in 2007 a model to explain the observed THz generation with a laser-induced ionization current [68]. The non-zero net current is only induced, if an additional field, like a second-harmonic or a DC field, breaks the symmetry of the fundamental field. Also a very short incident pulse itself is sufficiently asymmetric to generate noticeable THz radiation.

To unravel this question, we performed an experiment to measure systematically the spectra of the generated radiation in a two-color plasma. The results were compared with theoretical simulations carried out by the theory group of J. Herrmann and I. Babushkin. They applied for the first time the ionization current model in three spatial and one time dimension (3+1). Thus the generation process as well as propagation effects from the THz pulse through the plasma were considered. While a broad bandwidth is suggested from the ionization current model, four-wave rectification based on the Kerr effect is expected to yield a narrow spectrum of only several THz. Therefore, we measured in particular the characteristic tail of higher frequencies of the spectrum ($>$ 20 THz).

The generation scheme is shown schematically in Fig. 2.6 (a). The near-infrared pulses of 30 fs duration and 500 μJ energy from the Ti:sapphire laser system are focused with an achromatic lens with a focal length of 50 mm. A 0.1 mm thin β-barium borate (BBO) crystal cut for type-I second-harmonic generation is inserted into the convergent beam about 7 mm before the focus. The high intensities within the focal region create a plasma, which emits strong single-cycle THz pulses with amplitudes up to 400 kV/cm [16]. A parabolic mirror with a diameter of 25.4 mm at a distance of its focal length of 12.7 mm collimates the emitted radiation. An undoped window plate at Brewster angle transmits the THz pulse and blocks all frequencies in the near-infrared or visible range. The silicon window, as well as our applied electrooptic sampling setup, restricts the THz detection to the polarization component perpendicular to the incident fundamental and parallel to the second harmonic light. As displayed in Fig. 2.6 (b), the entire setup is placed in a gas cell filled with argon.

Frequencies below 20 THz are detected with electrooptic sampling setup using a ZnTe detection crystal [see Fig. 2.10 (c)]. The spectrum above 20 THz is measured using the field correlation technique [see Fig. 2.6 (b)]. A silicon window splits the beam into two different branches. Mirrors reflect both beams which are in turn recombined on the same beam splitter. By focusing with a parabolic mirror onto a nitrogen-cooled mercury cadmium telluride (HgCdTe) detector, we measure the intensity of the generated radiation. The response function of the HgCdTe detector is relatively flat over the entire frequency range from 20 THz to 170 THz. Varying the path difference between the both branches of the Michelson interferometer yields the intensity interferograms shown in Fig. 2.7 (a). The Fourier transform in Fig. 2.7 (b) shows the generated spectra above 20 THz.

We measured interferograms for different argon pressures inside the gas cell. In this way we control the plasma volume for identical field strengths. Owing to the beam geometry, we detect primarily the THz radiation generated within $\approx$ 0.3 mm around the focal spot. The almost vanishing spectrum at small argon pressure confirms that the plasma, and not the BBO crystal, acts as the source of the emitted radiation. The narrow-band emission at 25 THz below 50 mbar is caused by frequency mixing in the BBO crystal. In the region from zero to 300 mbar the generated spectral width increases strongly. The highest frequencies even beyond 50 THz are detected at pressures larger than 300 mbar. Above 500 mbar the slope of the high frequency wing remains constant. For the largest plasma spot present at 1000 mbar, the total detected THz yield decreases and the peak intensity shifts toward higher frequencies. The same phenomenon was observed in Ref. [69]. Without the BBO crystal at 1000 mbar, we found a very broad

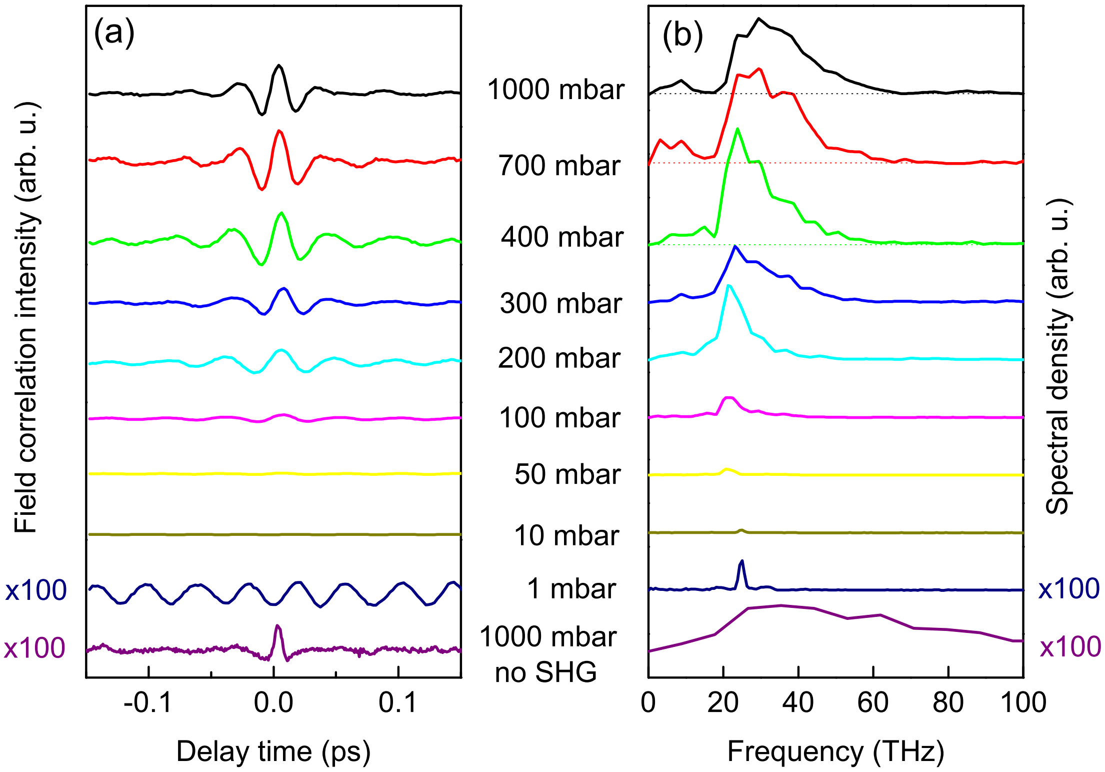

Figure 2.7: (a) Intensity interferograms of the THZ plasma source for argon pressures between 1 and 1000 mbar. (b) The Fourier transform yields the emitted spectra. Without plasma ($<$ 50 mbar) a weak BBO signal at 25 THz is observed. Vertical offsets are introduced for clarity.

spectrum with frequency components extending over 100 THz. However, this signal is about two orders of magnitude lower compared to the emission from a two-color plasma.

Our theoretical approach to model the generation process and propagation effects of THz radiation is described in detail in Ref. [70]. We assume an ionization current, which leads to THz generation. The ionization current is given by the change of the electron density $\dot{\rho}_e(t)$ at the expense of the neutral atomic density ρ_{at}. The ionization rate W_{ST} was determined in Ref. [62].

$$\dot{\rho}_e(t) = W_{\mathrm{ST}}(E)[\rho_{at} - \rho_e(t)] \tag{2.2}$$

Recent real-time experiments with sub-femtosecond time resolution found a stepwise increase of the electron density near the tunnel ionization events at the field maxima $(t_n, t_{n+1} \cdots)$ [71]. We adopt this finding and assume instantaneous ionization events $[\dot{\rho}_e(t) = \Sigma_n \rho_n \delta(t - t_n)]$ generating free electron at rest ($v_e = 0$). ρ_n and t_n describe the electron density and the time of the n^{th} ionization event. The incident electric field E accelerates the free electrons to the velocity of $v_f(t) = \frac{q}{m_e} \int_{-\infty}^{t} E(\tau) d\tau$, so that $v(t,t_n) = [v_f(t) - v_f(t_n)]$. The transverse macroscopic plasma current $\mathbf{J_e}(t)$ is described with

$$J_e(t) \sim \sum_n \rho_n \Theta(t - t_n)[v_f(t) - v_f(t_n)]. \tag{2.3}$$

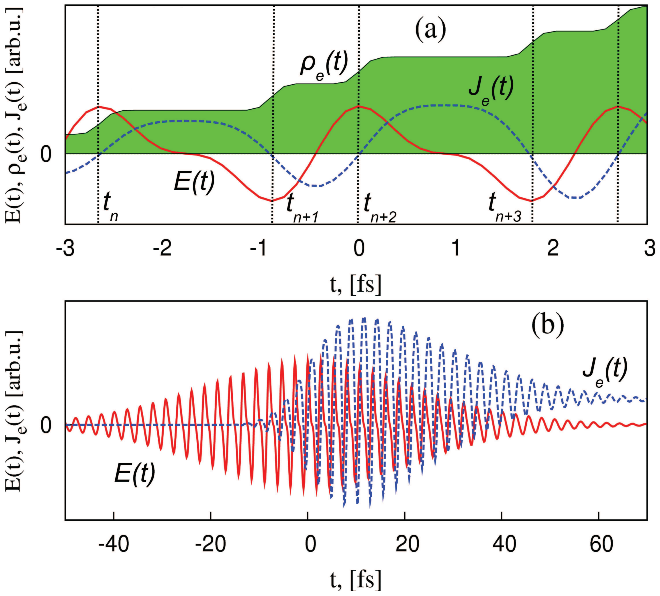

Figure 2.8: (a) The maxima of a two-color electric field $E(t)$ (red solid line) ionize neutral atoms at the time t_n. The green area depicts the electron density ρ_e. (b) The fast ionization process in combination with an asymmetric electric field leads to a slow component of the current $J_e(t)$ generating THz radiation.

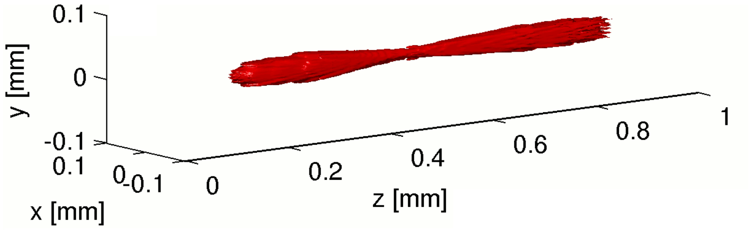

Figure 2.9: Iso-electron-density surface at $\rho_e = 5 \times 10^{17}$ cm^{-3} for 200 mbar gas pressure.

$\Theta(t)$ is the Heaviside step function to reflect the instantaneous ionization process. The generated electron density $\rho_e(t)$ (green shaded area) and the emitting plasma current $J_e(t)$ (blue dashed line) for an electric field $E(t)$ (red solid line) is shown in Fig. 2.8. The plasma current has a frequency component $\sim 1/\omega$ in the THz range, which is seen as a quasi-offset for $t > 20$ fs in Fig. 2.8 (b). The higher harmonics of the incident frequency (the THz frequency corresponds to the 0$^{\text{th}}$ order) are caused by the Fourier transform of $\Theta(t)$. The asymmetry introduced by the second-harmonic is responsible for non-zero even orders, and thus for the THz generation. The same mechanism generates multiple higher-harmonics, which are used, e.g., for the generation of attosecond pulses [72].

The consideration of all propagation effects of light allows for modeling the plasma volume, which is shown at 200 mbar gas pressure in Fig. 2.9. THz fields inside this focal region reach values on the order of GV/m and exhibit strong diffraction. In Fig. 2.10 we compare the sim-

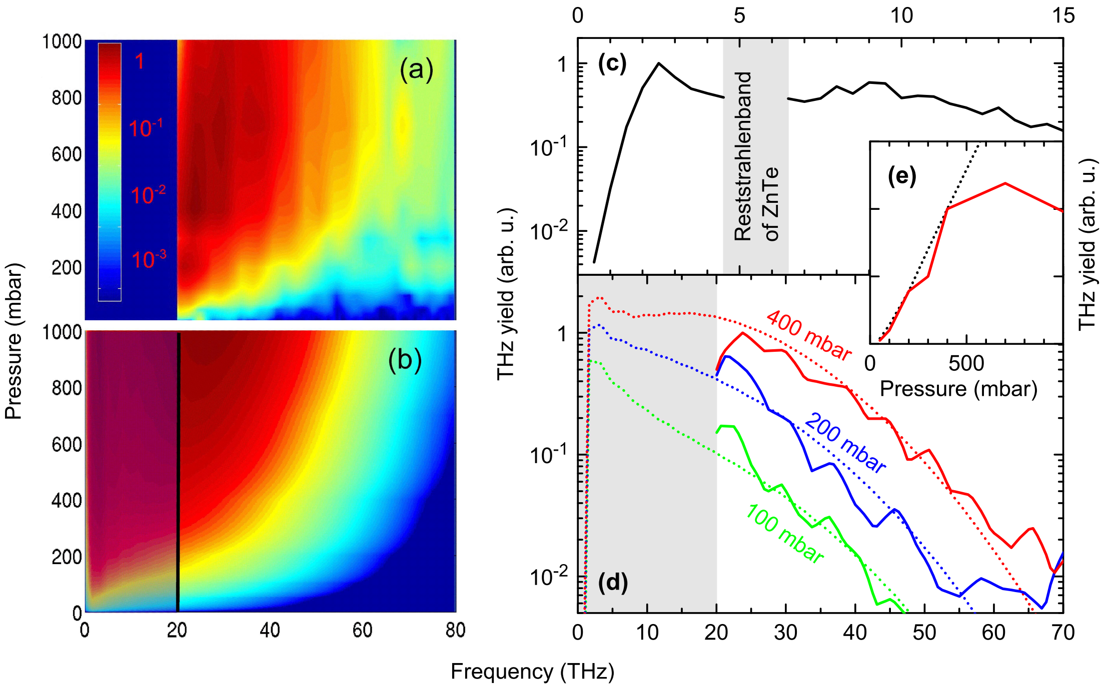

Figure 2.10: (a) Measured THz spectra and (b) simulated data for pressures between 1 and 1000 mbar. (c) The spectrum for frequencies below 1000 mbar is measured with electrooptic sampling in ZnTe. We corrected for the frequency-dependent detector response according to Ref. [73]. (d) Comparison of the experimental (solid lines) and the theoretical (dashed lines) spectra at 100 (green), 200 (blue), and 400 mbar (red). (e) The overall THz yield as a function of pressure obtained from the simulation (dashed line) and from the experiment (solid line).

ulation with the experiment. The spectrum in Fig. 2.10 (c) below 15 THz is recorded with electrooptic sampling. Generated higher frequencies above 20 THz are shown in the contour plot in Fig. 2.10 (a). The simulated spectra are obtained by an integration over the transverse coordinates (x,y). They yield a very similar contour plot shown in Fig. 2.10 (b). The spectra for 100, 200, and 400 mbar are shown as dashed lines in Fig. 2.10 (d), and the experimental spectra are shown as solid lines. We find very good agreement between experiment and simulation below 500 mbar for THz fields generated at the beginning of the plasma spot around $z = 0.2$ mm (0.3 mm before the linear focus). THz fields generated after further propagation become spectrally much broader. Hence, we conclude that the parabolic mirror in the experiment images the leading part of the plasma spot only. In agreement with experimental results up to 400 mbar, the calculated THz yield increases linearly with gas pressure [dashed line in Fig. 2.10 (e)]. The saturation of the experimental yield at higher pressures is likely due to additional THz losses upon further propagation towards the mirror, whereas the simulated yield is computed directly at the position $z = 0.2$ mm.

The observed pressure dependence of the spectral maximum and the spectral width gives insight into important features of plasma-induced THz generation. It can not be explained by the local plasma current, in which the variation of pressure only results in an amplitude scaling of the current. Instead, it originates from pressure dependent nonlinear propagation effects of

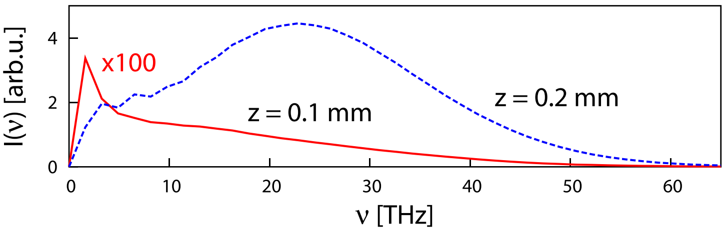

Figure 2.11: On-axis $(x = y = 0)$ spectral intensity $I(\nu)$ at $z = 0.1$ mm (solid line) and at $z = 0.2$ mm (dashed line).

the driving fields. For the intensity range and plasma interaction length of the experiment, the calculated spectral evolution of the pump pulses at 400 nm ($\frac{\omega}{2\pi} = \nu = 750$ THz) and 800 nm ($\nu = 375$ THz) shows that their spectral broadening is negligible. However, small blue-shifts $\delta\nu$ of the central frequencies are observed, which are caused by the nonlinear plasma-induced change of the refraction index [74]. These pressure-dependent shifts amount to approximatively 1 THz in the fundamental and 0.4 THz in the second harmonic at $z = 0.2$ mm for 400 mbar.

Surprisingly, these very small frequency shifts have a dramatic influence on the generated THz spectrum. This effect is most pronounced in the on-axis spectra, where the intensity is maximal. In Fig. 2.11 the calculated on-axis THz spectra for $z = 0.1$ mm (red solid line) and $z = 0.2$ mm (blue dashed line) are plotted for 400 mbar gas pressure. A dramatic change in the spectral shape and, as in the experiment, a shift of the maximal spectral density to higher frequencies is observed. Thus, the dependence of the THz spectra on pressure and propagation distance are explained by propagation effects, which modify the pump pulse frequency.

To summarize, the experimental setup for THz generation in a laser-induced plasma was presented. The spectrum of the emitted radiation was measured using a broadband field correlation. Comparison with theoretical results confirmed the ionization current within the plasma as the undoubted origin of the THz radiation. Propagation effects were studied by varying the gas pressure and thus the plasma volume. In agreement with the experimental results, the theoretical model demonstrates small blue shifts of the pump frequency within the plasma. This results in a significant broadening and a shift to higher frequencies of the generated spectrum.

2.2 Phase-Resolved Detection using Electrooptic Sampling

The detection of THz radiation was an experimental challenge for a long time. In contrast to photons in the near-infrared or visible spectral range, it is difficult to detect THz photons of only several meV. Nitrogen-cooled HgCdTe detectors are sensitive to 50 meV or 12 THz. The thermal energy of photons of even lower frequencies are detected with helium-cooled bolometers. However, these techniques yield only the intensity of the THz radiation. On the other hand, the electric field at THz frequencies oscillates relatively slow. One complete oscillation of the electric field, for instance at 2 THz, lasts about 500 fs. These time scales are accessible using femtosecond pulses from a Ti:sapphire laser system, which are used for the THz generation as well. The difference between the THz oscillation period and the duration of the oscillator pulse allows to sample the electric field of the THz pulse as a function of time. This principle was well-known already from photoconducting electronic sampling [1,39]. In 1995 Wu *et al.* applied it the first time, using the electrooptic effect of ZnTe, in free space [17,75]. This technique characterizes the THz pulse completely, i.e., one obtains from one measurement the pulse length, the spectrum, the spectral phase (the amount of chirp of second and of higher order), and the electric field amplitude (and thus the intensity).

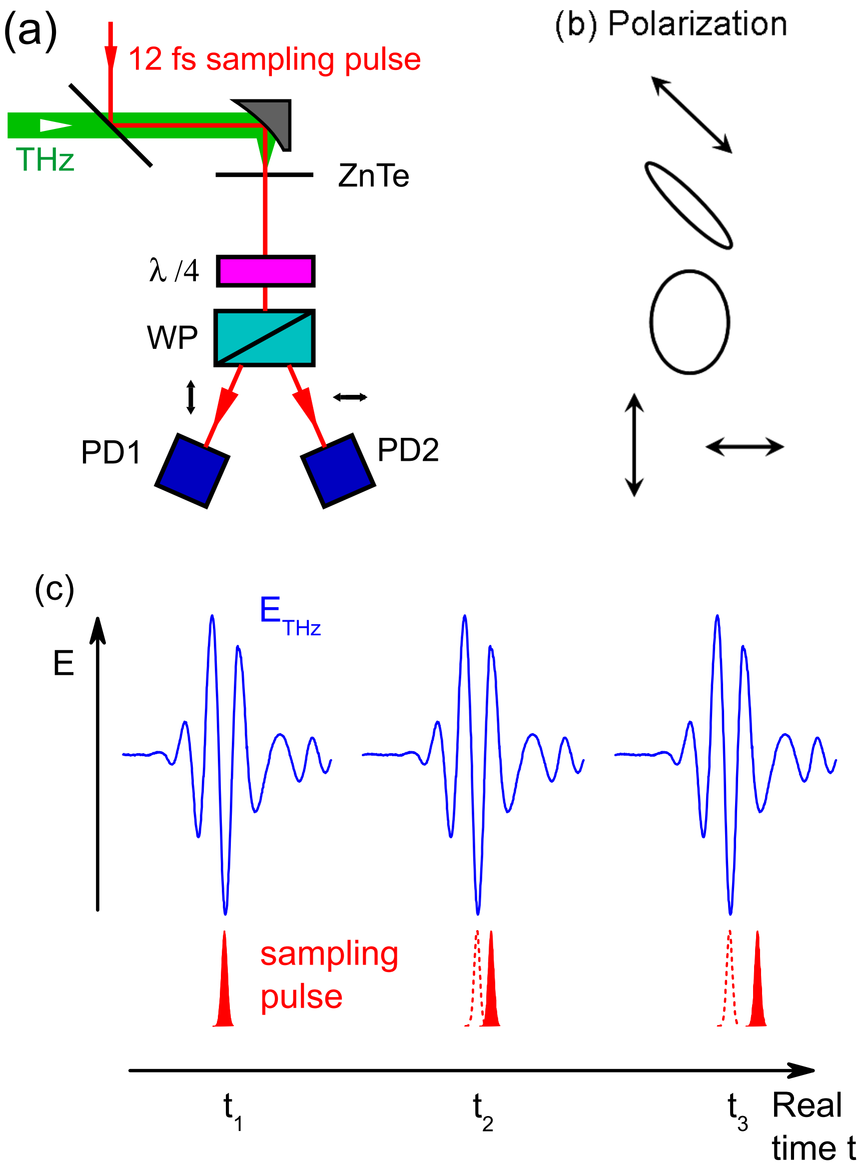

Figure 2.12: (a) Electrooptic sampling setup consisting of a ZnTe detection crystal, a $\lambda/4$ plate, a Wollaston prism (WP) and two balanced photodiodes (PD). (b) The $\lambda/4$ plate introduces a 90° phase retardation, so that electric fields of opposite sign can be distinguished. (c) By varying the pulse delay between the THz pulse (blue) and the much shorter sampling pulse (red) the THz transient as a function of time can be measured.

Electrooptic sampling uses the quasi-instantaneous refractive index change of a material in response to an applied electric field. This so-called Pockels effect [76] is a second-order nonlinearity, which occurs only in crystals without inversion symmetry. The experimental setup of electrooptic sampling is shown in Fig. 2.12 (a). The THz pulse is focused by a parabolic mirror onto an electrooptic crystal. The electric field of the THz pulse induces birefringence, which is read out by a linearly polarized 800 nm pulse of much shorter pulse duration. Both polarization components of the sampling pulse are spatially separated in a Wollaston prism and detected with two photodiodes. The difference signal of both balanced photo diodes corresponds to the change of polarization, which is linearly proportional to the electric field of the THz pulse. The complete THz transient as a function of time is measured by varying the delay between THz pulse and sampling pulse [Fig. 2.12 (c)].

An accumulation of the nonlinear signal over the entire crystal thickness is achieved, if the phase velocity of the THz frequency is equal to the group velocity of the near-infrared sampling pulse. Since this phasematching condition is fulfilled in ZnTe for a 800 nm sampling pulse and 1 THz, it has become the most popular detection crystal for electrooptic sampling [16,77,78]. Under the influence of an electric field the inverse dielectric tensor ε^{-1} changes from its zero-field value $\varepsilon^{-1}(0)$ to:

$$\varepsilon^{-1}(\mathbf{E}) = \varepsilon^{-1}(0) + r\mathbf{E} \tag{2.4}$$

Since the inverse dielectric tensor is symmetric (${\varepsilon_{i,j}}^{-1} = {\varepsilon_{j,i}}^{-1}$), $r_{ijk} = r_{jik}$. This determines the form of the third-rank tensor r. For example, ZnTe has only one independent tensor component $r_{xyz} = r_{yzx} = \cdots$, i.e., only the components which have all different indices are not equal to zero. It follows from these selection rules that the largest effect in ZnTe is obtained for (110) crystals with the THz field polarized parallel to $(1\bar{1}0)$ [79]. After propagating through a length d, this difference translates into a phase difference Γ between both polarization directions:

$$\Gamma = \frac{2\pi d}{\lambda} n^3 r_{xyz} E_{\mathrm{THz}} \tag{2.5}$$

In this equation λ is the vacuum wavelength of the sampling pulse and n is the corresponding refractive index. The probe pulse is incident on the electrooptic crystal with linear polarization directions of either (001) or $(1\bar{1}0)$. The additional phase difference of the quarter-wave plate modifies the elliptical polarization, so that both signs of the THz induced polarization change can be distinguished [see Fig. 2.12 (b)]. The resulting difference of the signals on the two photodiodes is proportional to the sine of the phase difference Γ. In most cases $\Gamma \ll 1$, so that one can approximate $\sin(\Gamma) \approx \Gamma$.

$$\frac{I_1 - I_2}{I_1 + I_2} = \sin(\Gamma) \approx \Gamma \tag{2.6}$$

Not all frequencies are detected with the same sensitivity in our electrooptic sampling setup. Because of the phonon resonances at $\omega_{\mathrm{TO}} = 5.3$ THz and $\omega_{\mathrm{LO}} = 6.2$ THz, ZnTe detects reliably only frequencies below 4 and above 8 THz. The difference between the electrooptic coefficients below and above the phonon resonance is described with the Faust-Henry coefficient [80]. For a Faust-Henry coefficient of -0.07 in ZnTe [80], the difference is negligible. The mismatch between the THz phase velocity and the group velocity of the sampling pulse determines the time resolution. Being equal for 1 THz, the mismatch increases for higher frequencies. Since Γ is integrated over the entire ZnTe thickness d, it results in a fringe pattern of the detector sensitivity. As a consequence, we use a thin ZnTe crystal (10 μm) to avoid spectral fringes and measure frequencies above 8 THz, and we use a thick ZnTe crystal (400 μm) to accumulate the signal for measurements below 4 THz. Diffraction effects limit the capability to detect lower frequencies. Using a theoretical model according to Refs. [35, 81] we calculated the focal spot of gaussian THz beams in our experiment. As a result we find that THz frequencies above 1 THz are homogeneously imaged on the ZnTe crystal and correctly measured in our setup.

In many electrooptic sampling setups a part of the amplified pulse is used as a sampling pulse. We employed the shorter 12 fs oscillator pulse to sample the THz transient instead. This allows us to detect higher frequency components up to 40 THz. Moreover, it reduces fluctuations of the electrooptic signal caused by changes in the refractive index of the optical devices. This is because we can measure both the pulse preceding the sampling pulse and the sampling pulse synchronized with the THz pulse. Taking the difference between both cancels changes of the electrooptic signal on a millisecond timescale. We achieve in this way a sensitivity of 0.1 kV/cm [82]. One disadvantage is the very different optical paths of the sampling and the amplifier pulse. The two pulses are separated immediately after the output coupler of the oscillator and are guided along different parts of the optical table. As a consequence long term temperature fluctuations influence both optical paths differently. These slow delay drifts can be compensated for by mathematical methods, which use one of the pulses as an optical ruler.

Electrooptic sampling is the ideal detection scheme for experiments in the THz spectral range. Since the highest detectable frequency is mainly determined by the duration of the sampling pulse, frequencies up to 100 THz were claimed to be measured [83]. Ongoing research efforts aim to extend the detector bandwidth or to circumvent interfering phonon modes. This is achieved by using a laser-generated plasma [84] or organic molecules embedded in polymers [85] as the electrooptic material. Also single shot electrooptic sampling [78, 86] is possible. It could substantially improve our experiment, because it reduces the measurement time and thus the temporal drifts.

2.3 Spectroscopic Concepts at THz Frequencies

Each spectral range features unique properties, which are employed in technical applications or scientific methods. A standard method for the rather young scientific field of nonlinear THz spectroscopy has not developed so far. Therefore, in this section the essential difference between electromagnetic radiation at optical frequencies (IR – UV) and in the THz spectral range is pointed out and two spectroscopic methods methods are developed to address the unique features of THz radiation.

2.3.1 The Phase-resolved Detection Suggests a 2D Approach

Electromagnetic radiation [Eq. (2.7)] is both an continuous oscillating electric field and a flux of discrete energy portions called photons. The field character, and thus the phase evolution, of light emerges in particular at lower frequencies, while the photon character, and thus the propagation direction, of light emerges towards higher frequencies. Electromagnetic spectra are obtained in two ways: by the direct measurement of the phase evolution $\omega(t)$ or via dispersion and the measurement of the propagation direction $\mathbf{k}(\omega)$.

$$\mathbf{E}(\mathbf{r},t) = \mathbf{E_0} \exp\left[i(\mathbf{kr} - \omega t)\right] + c.c. \tag{2.7}$$

Since the phase is difficult to determine at high, optical, frequencies, most spectroscopic

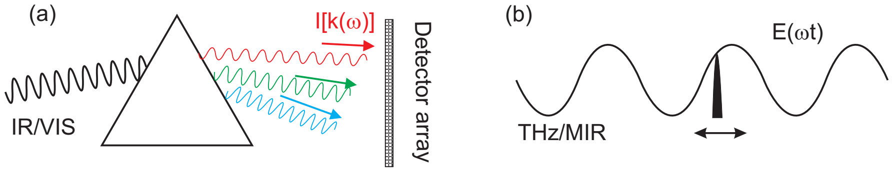

Figure 2.13: (a) The frequency of light in the IR range is determined by the spatial position of the photodiode after a dispersive element $\mathbf{E}[\mathbf{k}(\omega)]^2$. (b) The frequency in the THz range instead is measured, e.g., using electrooptic sampling, only in the time domain $E \sim e^{i\omega t}$.

experiments use the propagation direction to determine the spectrum. The photon energy in this range is comfortably detected with photodiodes. A dispersive element, like a grating or a prism, diffracts the **k** vector, depending on the frequency ω, into different propagation directions [see Fig. 2.13 (a)]. A lens maps each wavelength onto one characteristic position of an array of photodiodes. The spatial position $\mathbf{k}(\omega)\mathbf{r}$ of the photodiode in combination with the detected photon energy yields the spectrum of the electromagnetic radiation $\mid \mathbf{E}[\mathbf{k}(\omega)] \mid^2$. No phase information obtained.

This concept is not practical at THz frequencies, because the propagation direction becomes indistinct ($\mid \mathbf{k} \mid = \omega / c$) and the spatial separation of different frequency components deteriorates. Furthermore, the energy of THz photons is only difficult to detect, in particular spatially resolved using an detector array.

On the other hand, the phase evolution of the electric field $E(\omega,t) \sim e^{\omega t}$ is directly measured with electrooptic sampling. The Fourier transformation yields the spectrum of the pulse as well, but the spectral resolution is often limited due to time delayed replicas from internal reflexions of one of the involved optical elements. This constrains either the time window to Fourier transform or the replicas spectrally interfere with the actual pulse to measure. However, many recent nonlinear THz experiments neglected the incidentally obtained phase and analyzed only the recorded spectrum [5, 19, 20].

On the other hand great experimental efforts are made to measure the phase evolution at optical frequencies. Only heterodyne detection schemes, based on spectral interferometry, extract the phase evolution and enable a 2D spectroscopy. This new powerful method reveals energetic couplings, line shapes and spectral diffusion. Since the phase is comfortably measured at THz frequencies, the 2D concept addresses ideally the strength of nonlinear THz spectroscopy. 2D THz spectroscopy could display couplings of rotational modes and contribute to unravel the structure of complex molecules.

2D spectroscopy in the infrared is performed mostly using an elaborated noncollinear “box” beam geometry (see Fig. 6.4). This requires a distinct propagation direction, which is not given at THz frequencies. It will be demonstrated in this thesis, that the complete information obtained by 2D spectroscopy is contained in the temporal phase evolution. As a consequence a THz-specific collinear beam geometry can be applied.

2.3.2 Field-Induced Effects Studied by Nonlinear THz Spectroscopy

Another spectroscopic method uses the electric field of few-cycle THz pulses to induce nonlinear field effects in the sample. Electromagnetic radiation at a frequency of 2 THz has an oscillation period of 500 fs. The electric field experienced by a sample points for 250 fs into one direction. This provides sufficiently long time to initiate and to follow ultrafast processes on a femtosecond timescale. If we consider free electrons in a conduction band, they are strongly accelerated by each half-cycle of the THz pulse. Since the induced current is present only for a few hundred femtoseconds, nearly no energy is dissipated and the experiment is entirely reversible. This means we can repeat the field-induced experiment at a 1 kHz repetition rate of our laser system and improve the signal-to-noise ratio by averaging the results. In this way, one can apply electric field strengths up to 400 kV/cm [16] without any metallic contacts, just by transmitting the THz pulse through a thin sample. Even if it would be possible to apply such field strengths as a DC voltage, heat dissipation would destroy the sample within the shortest electronic switching times in the nanosecond range.

In particular THz frequencies are most suitable for ultrafast high electric field experiments. The induced momentum of a carrier is given by the product of the electric field and the effective acceleration time. The electric field of microwaves, for instance, accelerates the carriers for longer time, but the achieved field amplitudes are substantially lower. This is due to longer pulses and larger wavelengths, which can not be focused as tightly as for THz frequencies. Higher infrared frequencies on the other side, achieve even higher electric field amplitudes, but the oscillation time is of the order of only a few femtoseconds. Thus the electric field acts only for a very short time on the sample. Furthermore, competing processes, e.g., interband transitions, may be excited in this spectral range. However, initiating field effects is just the first step; in the end a microscopical picture of the induced physical processes within the sample is desired. In the following the question is considered how to obtain this information. Roughly speaking, carriers are accelerated by an external field and emit in turn an electric field. This field, containing the information of interest, needs to be detected and thoroughly analyzed.

Optical Setup and Sample Geometry

In two experiments of this thesis we investigate high-field transport on ultrafast timescales. Insight into microscopic processes occuring in the sample are obtained by measuring the reemitted field from carriers in motion. To simplify the experimental situation, we investigated a sample layer of $d = 500$ nm thickness, much thinner than one incident THz wavelength of $\lambda_{\mathrm{THz}} = 150\ \mu$m. This quasi two-dimensional geometry ensures that all carriers in the focus experience the same driving field. The carriers perform identical motions and emit coherently the electric field.

A scheme of our *n*-type GaAs sample is shown in Fig. 2.14. The sample layer (red) is 500 nm thick and doped with a moderate density of 2×10^{16} cm^{-3}. The *n*-doped GaAs is embedded between two layers (green) of 300 nm thin $Al_{0.4}Ga_{0.6}As$. On the one hand these layers prevent the GaAs sample from oxidation and surface effects and on the other hand the layers act as an etchstop. Both $Al_{0.4}Ga_{0.6}As$ layers do not contain free carriers and are optically inactive at THz frequencies. All layers are grown on a 0.5 mm semi-insulating GaAs substrate. The substrate layer provides the necessary mechanical stability while growing, but it modifies the THz transmission by unwanted dispersion and other nonlinear effects. The substrate was ground down and then it was entirely removed by selective wet chemical etching as described in Ref. [87]. Hydrogen peroxide oxidized the substrate, and the resulting GaAs oxide was continuously washed away with ammonium hydroxide. A more than ten times slower etching velocity in $Al_{0.4}Ga_{0.6}As$ basically stopped the etching process as soon as as the substrate was removed. During the etching process, the sample was fixed on an transparent, optically inactive diamond window of 300 μm thickness. Fig. 2.15 is a photograph showing the free standing

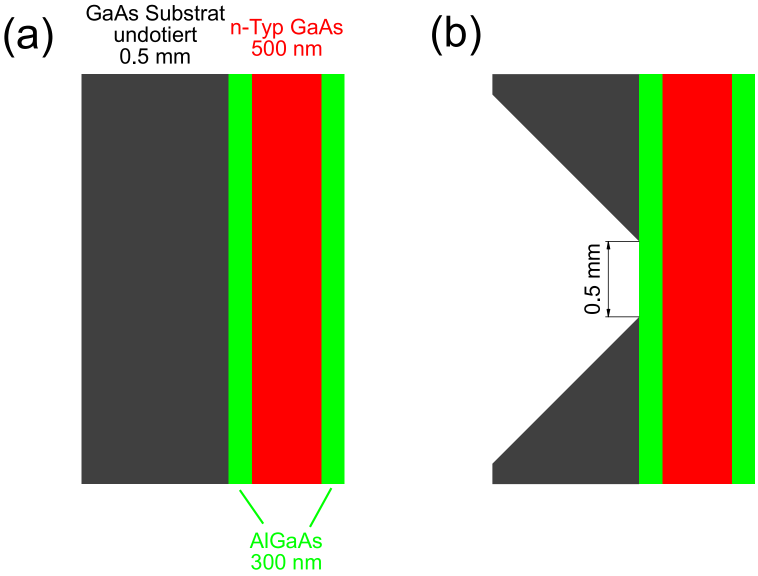

Figure 2.14: (a) A 500 nm thick n-doped layer (doping density 2×10^{16} cm^{-3}) is grown on a 0.5 mm undoped GaAs substrate and embedded between two $Al_{0.35}Ga_{0.65}As$ layers. (b) The substrate is locally removed by wet chemical etching on an area of roughly 500 μm×500 μm.

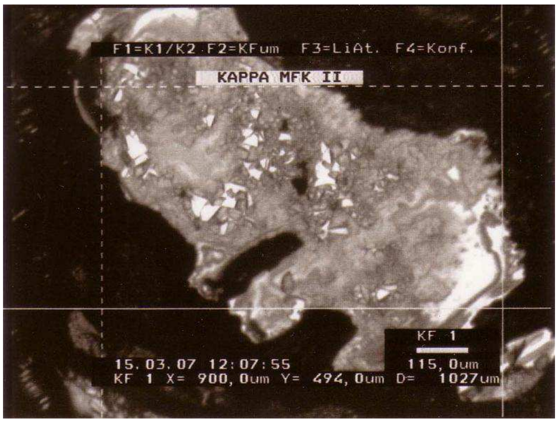

Figure 2.15: Photograph of the investigated sample under a microscope. The GaAs sustrate is locally removed by selective wet etching. The freestanding layer is seen as a bright spot.

n-type GaAs layer as a bright spot surrounded by dark GaAs substrate. The sample layer is freestanding on an area of roughly 500 μm×500 μm. That is considerable larger than our THz focal spot of 300 μm×300 μm.

The quasi-2D n-type GaAs layer is irradiated by the incident field E_{in} (blue solid line in Fig. 2.16). Free electrons are coherently accelerated, and they emit into both directions an electric field E_{em} (green solid line) and E_{re} (reflected field, green dotted line). The emitted field into transmission direction E_{em} and the incident field E_{in} add up to the field transmitted through the sample E_{trans}. Stroucken *et al.* demonstrated in Ref. [88], that this transmitted field

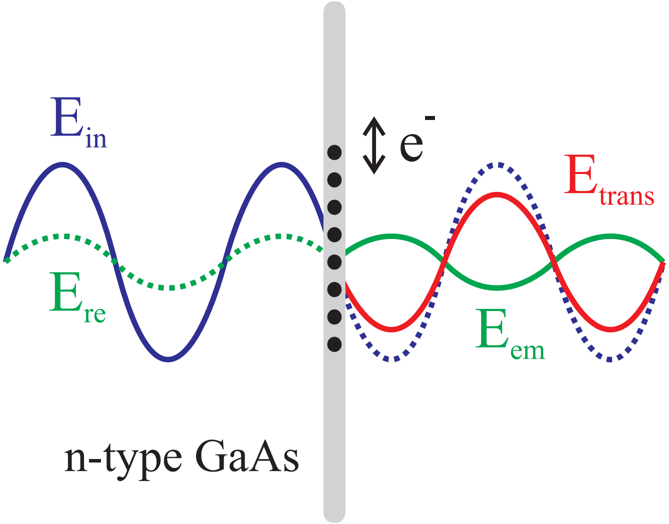

Figure 2.16: The accelerated electrons within the *n*-type GaAs layer emit the field E_{em} (solid green line) and the reflected field E_{re} (dotted green line). The superposition of the incident field E_{in} and E_{em} results in the transmitted electric field E_{trans}, shown as a red line. The latter is also the driving field acting on the electrons [88].

is identical to the local field on the sample, $E_{\mathrm{loc}} = E_{\mathrm{trans}}$. It will be shown, that our experimental setup ensures the direct imaging from the field at the sample position onto the detection crystal for electrooptic sampling (apart from a sign change). This means the transmitted electric field E_{trans} is measured with the sample in place, and the incident electric field E_{in} is measured in a second separate scan without the sample in place. After taking into account the 8 fs time shift of the sample layer, we obtain the emitted field as the difference of incident and transmitted electric fields $E_{\mathrm{em}} = E_{\mathrm{in}} - E_{\mathrm{trans}}$ [82, 88]. To summarize, the emitted field from the sample is determined by the following formulas:

$$E_{\mathrm{loc}} = E_{\mathrm{in}} + E_{\mathrm{em}}, \tag{2.8}$$

$$E_{\mathrm{loc}} = E_{\mathrm{trans}}, \tag{2.9}$$

$$E_{\mathrm{em}} = E_{\mathrm{in}} - E_{\mathrm{trans}}. \tag{2.10}$$

Correlation between Electronic Motions and the Detected Electric Field

To deduce knowledge about the electronic motions from the emitted electric field of the sample, two aspects have to be considered: the electromagnetic emission of moving electrons and the translation of the radiated field onto the ZnTe detection crystal. The latter is determined by the imaging geometry illustrated in Fig. 2.17.

The sample, and thus the moving electrons of interest, are placed in the focal spot of an off-axis parabolic mirror. The emitted radiation is collected and collimated after a short focal length of 12.7 mm to a beam with a diameter of 25 mm. After an optical path of roughly 30 cm, the parallel THz beam is refocused with a further parabolic mirror of the same focal length onto the ZnTe detection crystal. According to the theory for gaussian beams explained in Ref. [89], the local electric field on the sample E_{loc} is imaged by two focussing elements directly onto

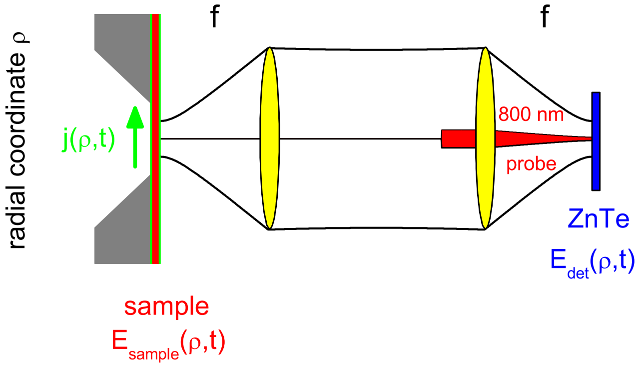

Figure 2.17: (a) In our setup we collimate the emitted radiation and guide it to a second lens, where it is focused onto the electrooptic crystal. In the actual experiment parabolic mirrors are used instead of lenses. According to the classical theory for electromagnetic beam propagation [89] the field on the sample is, apart from a sign change, directly imaged onto the on-axis ($\rho = 0$) of the detector crystal $\mathbf{E}_{\mathrm{det}}(0,t) = -\mathbf{E}_{\mathrm{sample}}(0,t)$.

the ZnTe crystal. The sample near-field translates, apart from a sign change, directly onto the detected electric field $E_{\mathrm{trans}} = -E_{\mathrm{loc}}$. This result holds for frequencies down to 1 THz [35, 81]. Furthermore, the focal diameter of the near infrared probe beam is much smaller than that of the 1 THz beam and, thus, we measure the on-axis field strength ($\rho = 0$) of the gaussian THz beam.

To learn about the emitted field from the moving electrons, we derive the electromagnetic emission of a thin sheet of moving carriers [90, 91]. The sample is described as a nonmagnetic ($\mathbf{B} = \mu_0\mathbf{H}$) infinite sheet in the $x-y$ plane with a surface at $z = 0$. The paths labeled α and β will be used to derive the radiated fields. Using Maxwell's equations in its integral form, we have

$$\oint_\alpha \mathbf{E}\, d\mathbf{s} = -\int_{A(\alpha)} \frac{\partial \mathbf{B}}{\partial t}\mathbf{n}_\alpha\, dA. \tag{2.11}$$

α is the path shown in Fig. 2.18, $A(\alpha)$ is the area enclosed by this path, and $\mathbf{n}_\alpha$ is an unit vector perpendicular to $A(\alpha)$. Because of symmetry, for an infinite sheet $\mathbf{E}$ and $\mathbf{B}$ can not depend on x and y. Furthermore, $\mathbf{E}$ will only have an x component and $\mathbf{B}$ only a y component. Thus Eq. (2.11) becomes

$$E\,a - E'\,a = -a\int_{-l/2}^{0} \frac{\partial B'}{\partial t} dz - a\int_{0}^{l/2} \frac{\partial B}{\partial t} dz. \tag{2.12}$$

For the limit $l \to 0$ of α, the integrals on the right hand side of Eq. (2.12) vanish, because the area enclosed by α tends to zero. $\frac{\partial \mathbf{B}}{\partial t}$ in contrast has to remain finite. Accordingly $\mathbf{E} = \mathbf{E}'$.

Similarly, it holds

$$\oint_\beta \mathbf{H}\, d\mathbf{s} = \int_{A(\beta)} \left(\mathbf{j} + \frac{\partial \mathbf{D}}{\partial t}\right) \mathbf{n}_\beta\, dA. \tag{2.13}$$

Outside the sample the relation between $\mathbf{D}$ and $\mathbf{E}$ is $\mathbf{D} = \varepsilon_0\mathbf{E}$. The current density $\mathbf{j}$ of a thin layer is assumed as a line current density (current divided by length) of $j_l = \int j(z,t)\, dz$.

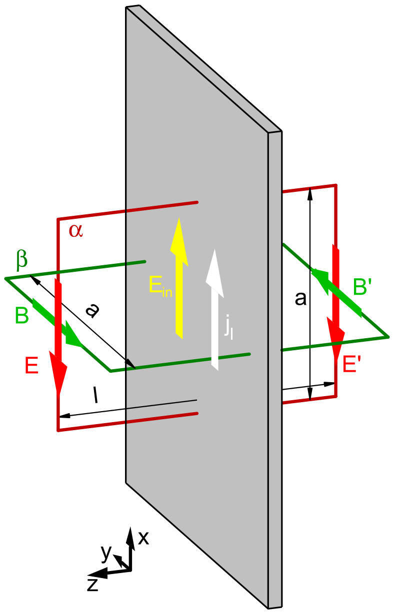

Figure 2.18: Electric field emission of our *n*-type GaAs sample. The incident electric field E_{in} induces an electric current density j_l over the thickness d, which emits in turn a further electromagnetic field. E and B (E' and B') are the emitted fields on the front and on the back side of the sample. α and β are paths used for the derivation of the emitted field of $E_{\text{em}} = \frac{1}{2} Z_0 d j_l$.

One gets

$$B' a - B a = \mu_0 a j_l + \mu_0 a \int_{-l/2}^{0} \frac{\partial D'}{\partial t} dz + \mu_0 a \int_{0}^{l/2} \frac{\partial D}{\partial t} dz. \tag{2.14}$$

Again, in the limit of $l \to 0$ the integrals in Eq. (2.14) will become zero, since $\frac{\partial \mathbf{D}}{\partial t}$ is finite. $B' - B = \mu_0 j_l$ remains. Outside the region of flowing current, the following relation between E and B holds:

$$B_y = \frac{1}{c} E_x, \tag{2.15}$$

$$B'_y = -\frac{1}{c} E'_x = -\frac{1}{c} E_x = -B_y. \tag{2.16}$$

Combining Eq. (2.14) and Eq. (2.16), one obtains with $\mu_0 c = Z_0 = 377\ \Omega$ for the emitted field from the sample:

$$E_{\text{em}} = -\frac{1}{2} Z_0 d j = \frac{1}{2} Z_0 d e n \mathbf{v}. \tag{2.17}$$

Thus a large area emitter with a constant number of carriers emits an electric field proportional to the electron velocity inside the sample. This is primarily a geometrical consequence of the large sheet of emitters. A point emitter instead, emits an electric field proportional to the acceleration of carriers (see Section 3.5). Since we are able to measure E_{em} [Eq. (2.10)], we can directly conclude on the product of free carriers inside our sample and their coherent velocity.

3 Coherent Ballistic High-Field Transport in GaAs

High-field transport experiments in semiconductors, such as GaAs, attracted in the last decades significant research interests [29, 30, 92, 93]. Ballistic transport of electrons according to Newton's Law is prevented after a certain time by scattering processes, which randomize the electron momentum. Phase-resolved THz pulses with field amplitudes of several hundred kV/cm represent new and ideal means to study this high-field transport on a femtosecond timescale (see Section 2.3). Previous nonlinear THz experiments demonstrated the acceleration of carriers using THz pulses for impact ionization in InSb [19, 20]. In the same way we use the electric field of the THz pulses to accelerate electrons in the conduction band of GaAs. The detected electric field emitted from the sample is directly proportional to the induced current [Eq. (2.17)]. The *n*-type GaAs sample was processed into a thin layer, to assure the identical driving field for all carriers. To avoid interfering electron and hole dynamics, the carriers were not photo-excited, but brought into the conduction band by *n*-doping with silicon atoms.

Apart from the addressed fundamental physical question, our experiment is also of high technological relevance. Silicon chips in modern computers for instance, have GHz clock frequencies, which correspond to cycle times in the picoseconds range. Furthermore, modern lithographic methods manufacture devices with conducting pathes, separated only by several tens of nanometers. The physical proximity causes electric field strengths up to several hundred kV/cm. Therefore our experiment explores a new regime of ultrashort times and strong electric fields, which may be of great technological relevance in the near future.

In this chapter first the basic concepts of ballistic transport and Bloch oscillations are introduced. A short overview of previous experiments is given, before the experimental results are presented and discussed.

3.1 Basic Concepts

Eighty years ago, Felix Bloch showed that electron wave functions in the Coulomb potential of the nuclei in a crystal are periodically modulated plane waves [94]. The spatially periodic modulation of these Bloch functions restricts the allowed energies of the electrons, leading to a dispersive band structure $\mathscr{E}(\hbar\mathbf{k})$ containing both allowed (bands) and forbidden energy regions (gaps) [95].

An external electric field accelerates conduction band electrons (charge $-e$) according to Newton's law with:

$$\mathbf{F} = m\mathbf{a}, \tag{3.1}$$

$$\Leftrightarrow -e\mathbf{E} = \hbar d\mathbf{k}/dt. \tag{3.2}$$

Starting at the Γ point with $\mathbf{k} = 0$, Fig. 3.1 (a) illustrates the increasing quasi-momentum $\mathbf{k}$ during acceleration by an external electric field. Various incoherent scattering processes change

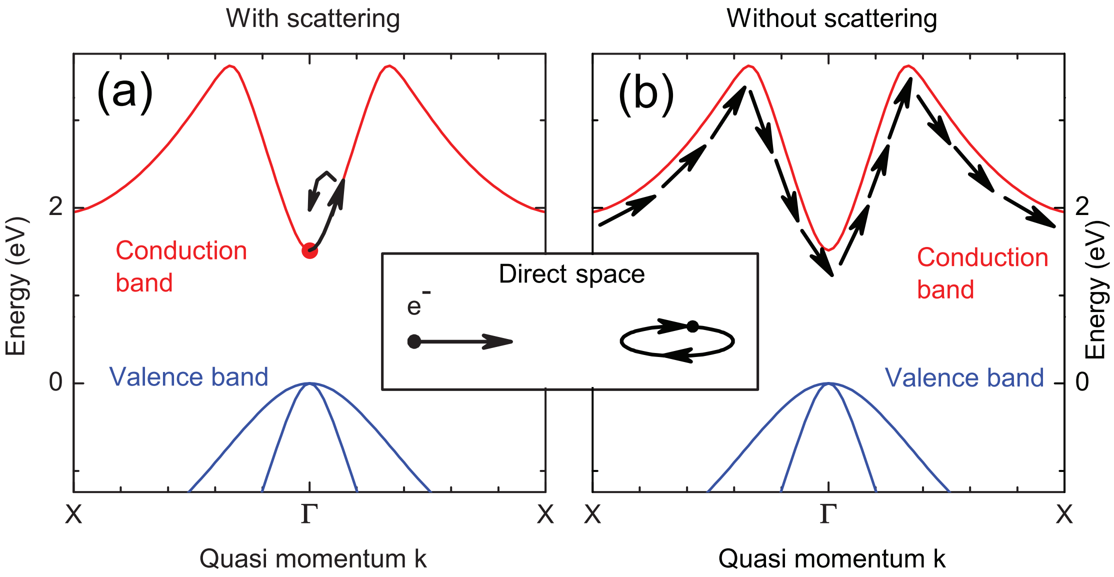

Figure 3.1: Free conduction band electrons are driven by an externally applied electric field. (a) Scattering randomizes the momentum distribution. Only a small average momentum **k** of the entire electron ensemble remains, causing a drift current. (b) Without scattering the electron traverses again and again the Brillouin zone, resulting in Bloch oscillations in direct space (inset).

the momentum of individual electrons and randomize the momentum distribution. Only a small average momentum of the entire electron ensemble remains. This drift-like electron transport is well-known as the ohmic current [l.h.s. of inset in Fig. 3.1 (a)]. Without any scattering processes, ballistic transport occurs as shown in Fig. 3.1 (b). The electrons are expected to follow the dispersion of their band at a constant rate in momentum space [96]. The Brillouin zone in (100) direction of a zincblende crystal with a lattice constant of a extends from $-\frac{2\pi}{a} < k < \frac{2\pi}{a}$. For each electron leaving the Brillouin zone at $k = \frac{2\pi}{a}$, one indistinguishable electron will enter at $k = -\frac{2\pi}{a}$. Accordingly, the electron in Fig. 3.1 (b) traverses again and again the Brillouin zone. The effective mass of a band electron is given by the curvature of its band, $m_{\text{eff}} = \hbar^2[d^2\mathscr{E}(\hbar k)/dk^2]^{-1}$. In the conduction band of GaAs, the effective mass is positive around the Γ and the X points and negative around the band maxima. In this regions the acceleration changes its sign, if the electric field points constantly into one direction. The electron velocity $\mathbf{v}$ in real space is given by the derivative of Eq. (3.2) with respect to the space coordinates:

$$\mathbf{v} = \hbar^{-1}\nabla_{\mathbf{k}}\varepsilon(\hbar\mathbf{k}). \tag{3.3}$$

The integration of Eq. (3.3) along t yields the actual electron motion in real space. It is depicted in the inset of Fig. 3.1, that the electron undergoes coherent periodic Bloch oscillations.

The observation of Bloch oscillations [94] in bulk crystals was prevented so far by effective ultrafast scattering processes. However, several experimental tricks allowed to observe Bloch oscillations in artificial structures. In the first experiments the Brillouin zone was minimized to such an extent, that it could be traversed by electrons even within the momentum relaxation. Since the extension of the Brillouin zone is inversely proportional to the lattice constant a, a periodic structure with a large lattice constant was required. Since the 80's of the last century semiconductor superlattices with a lattice constant of few nanometers were grown by molecular beam epitaxy (MBE). These heterostructures facilitated the first observation of Bloch oscillations in 1992 by Feldmann *et al.* using the four-wave mixing method [97]. Several years later Waschke *et al.* detected the THz radiation, which was emitted by Bloch oscillations, under an applied voltage [98]. The inverse effect, i.e., the manipulation of the an electrical current by incident THz photons was demonstrated by Unterrainer *et al.* [99]. Next people investigated systems with low scattering rates to induce Bloch oscillations. Bloch *et al.* observed Bloch oscillations of cold atoms in optical lattices [100], Delahaye *et al.* found them in Josephson junctions [101] and Christodoulides *et al.* induced Bloch oscillations in optical waveguide arrays [102]. In our experiment we concentrated on the last remaining parameter, i.e., we reduced the oscillation time of Bloch oscillations. The Brillouin zone is traversed before scattering processes suppress the coherent electron motion. To achieve the required electron velocity, strong electric fields of several hundred kV/cm have to be applied on a short timescale. This is accomplished using nonlinear THz spectroscopy as described in Section 2.3.

The prerequisite of Bloch oscillations in bulk GaAs, ballistic transport, was investigated using different approaches. The first experiments in the 80's of the last century used Raman spectra or cross correlations of two transmitted near-infrared pulses to estimate a scattering time of electrons in the femtosecond time range [29, 103]. Pump-probe experiments [104] and in particular luminescence experiments performed by Kash *et al.* [30, 92, 105] found scattering times from the Γ into the X valley of 180 fs and into the L valley of 540 fs. The intensity of the luminescence as a function of frequency exhibits characteristic kinks at energies, where scattering into other valleys sets in. While different values in the range of several hundred femtoseconds have been obtained for the scattering rates out of the Γ valley [104, 106], it was generally accepted, that scattering back into the Γ valley lasts about 100 ps. The intraband motion of electrons was probed by Leitenstorfer *et al.* in Refs. [31, 107]. Electric fields of 130 kV/cm were employed inside a *p-i-n* diode made of GaAs. The carriers were photo-injected using a broadband 10 fs pulse and accelerated by the static built-in electric field. The emitted electric field was focused on a ZnTe crystal and detected with electrooptic sampling. The applied optical setup causes a detected signal, that is proportional to the *acceleration* of the carriers. The authors of Ref. [31] find that electrons are scattered from the Γ valley into the L valley only 20 fs after the electrons achieved sufficient kinetic energy. The effective electron mass in the L valley is substantially larger, which decelerates the electron and emits a field of opposite sign. Surprised by such a short scattering time, the authors state: "This regime is especially interesting since the acceleration period in the Γ valley becomes shorter than the oscillation cycle of the phonons. [...] To our pleasant surprise, we find that the experimental data are in quantitative agreement with theoretical predictions of nonequilibrium spatial transport based on Monte Carlo simulations (of Ref. [108])."

All previous experiments excited simultaneously electrons and holes in GaAs. The influence of concomitantly excited holes in these experiments were investigated by Abe *et al.* [109]. After comparison of the experimental results with a Monte Carlo simulation, the authors conclude a significant influence from the hole population for electric fields above 20 kV/cm. Su *et al.* generated electron-hole pairs in GaAs and investigated the carrier transport in subsequent THz pump-probe experiments [22]. The analysis of the experimental data is complicated because of the thickness of the sample. However, after comparison with two simulations, they deduct for electric fields up to 170 kV/cm intervalley scattering within the pulse duration. Quasi-ballistic transport and side valley transfer after several hundred femtoseconds was found by Schwanhäußer *et al.* [107].

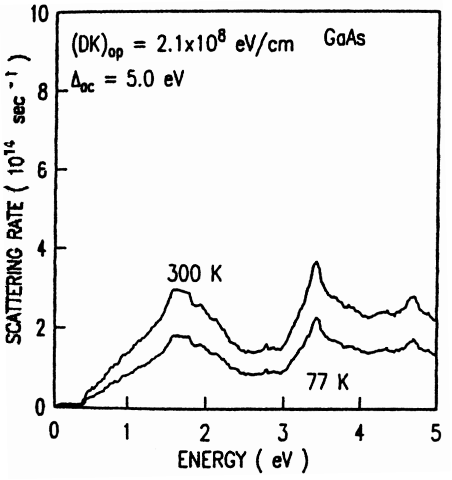

Figure 3.2: Scattering rates obtained with Boltzmann's transport equation and Fermi's golden rule according to Ref. [108]. Scattering rates of (3 fs)$^{-1}$ are predicted for electrons near the negative mass region.

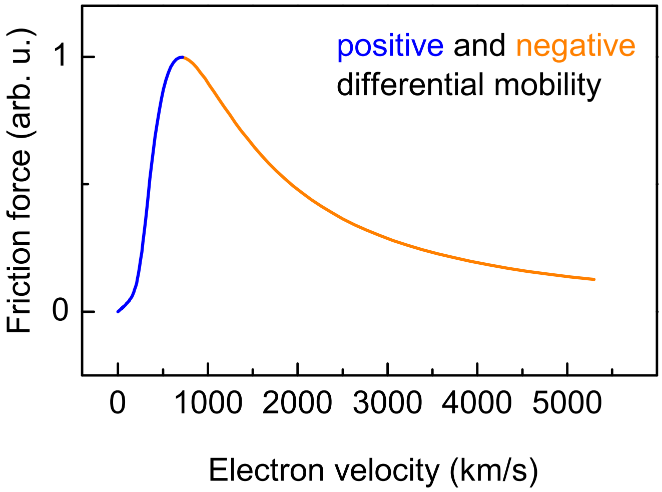

Figure 3.3: Quantum-kinetic decoupling occurs between electrons and surrounding LO phonon for electron velocities above 435 km/s (taken from Ref. [4]). The negative differential mobility (blue solid line) changes sign and the electron experiences a reduced friction force (solid orange line).

Ref. [108] presents theoretical predictions from a Monte Carlo simulation performed by M.V. Fischetti. The author considered the electron behavior in zincblende semiconductors, like GaAs, at high electric fields. Based on Boltzmann's transport equation (BTE) and Fermi's golden rule (FGR), the work predicts extraordinarily high phonon scattering rates depicted in Fig. 3.2. In the negative mass region at electron energies around 1.8 eV scattering times down to 3 fs were predicted. This would preclude ballistic transport at room temperature. Leitenstorfer *et al.* find the agreement between experiment and theory surprisingly, because the applied Fermi's golden rule is not expected to be valid on the short time scales of the experiment. Although this simulation is well-confirmed at low electric fields and on long timescales, the validity on short time scales have remained experimentally unexplored. It is well-known, however, that quantum-kinetic effects need to be incorporated for a realistic description on short time scales [110]. The validity range of the approach in Ref. [108] is discussed in detail in Appendix 7.

Our idea to look for ballistic transport at short time scales was also motivated by a previous experiment of our group published 2007 [4]. Free electrons in polar lattices attract positively charged ions and repel negatively charged ions, creating a self-induced potential trap. The electron and the surrounding LO phonon cloud are considered a quasi-particle, the polaron. The interaction with the crystal lattice is essentially mediated by longitudinal optical (LO) phonons. As a consequence the crystal atoms can react to changes of the spatial position of the electron at most with the LO phonon oscillation time of 110 fs. If the electron moves faster, the potential trap is not able to follow the electron. In turn the electron experiences a strong increase of mobility. This was measured even at THz amplitudes of only 15 kV/cm in Ref. [4]. In Fig. 3.3 the friction force acting on an electron is plotted as a function of its constant velocity v_e. After the electron has decoupled from its potential trap around v_0, the friction force decreases and the mobility rises.

This finding encouraged us to further explore this so-called quantum-kinetic regime of electron transport in response to strong THz pulses. Increasing the mobility at high velocities might allow for Bloch oscillations in bulk GaAs. To obtain the highest THz field strength available, we omitted the probe branch used in Ref. [4], and the entire pulse energy provided by our laser system was used for the generation of the THz pulse. We measured directly the THz field emitted from the sample as explained in Section 2.3.

3.2 Experimental Results

A few-cycle THz pulse with a center frequency of 2 THz was generated by optical rectification of 30 fs pulses from a Ti:sapphire oscillator-amplifier laser system. The THz pulses are focused with a pair of parabolic mirrors onto the free standing sample. The polarization of the electric field is along the [100] direction of the sample. A further pair of parabolic mirrors images the electric field of the transmitted THz pulse onto a thin ZnTe crystal for electrooptic sampling. The experimental setup is shown in Fig. 3.4. The entire optical path of the THz beam is placed in a vacuum of 10^{-6} mbar.

In Figs. 3.6 (a) and (b) transients of the incident $E_{\mathrm{in}}(t)$ and of the transmitted pulses $E_{\mathrm{trans}}(t)$ are shown for an amplitude of 300 kV/cm. The difference between these transients yields the field $E_{\mathrm{em}}(t)$ emitted from the sample [Fig. 3.6 (c)]. The emitted field transients are shown in Fig. 3.5 for amplitudes of (a) 20 kV/cm, (b) 50 kV/cm, (c) 140 kV/cm, (d) 200 kV/cm, and (e) 300 kV/cm at room temperature. The noise level of the experimental data for $E_{\mathrm{em}}(t)$ is 0.5 kV/cm. Increasing the field amplitude [Figs. 3.5 (c) – (e)] generates higher-frequency com-

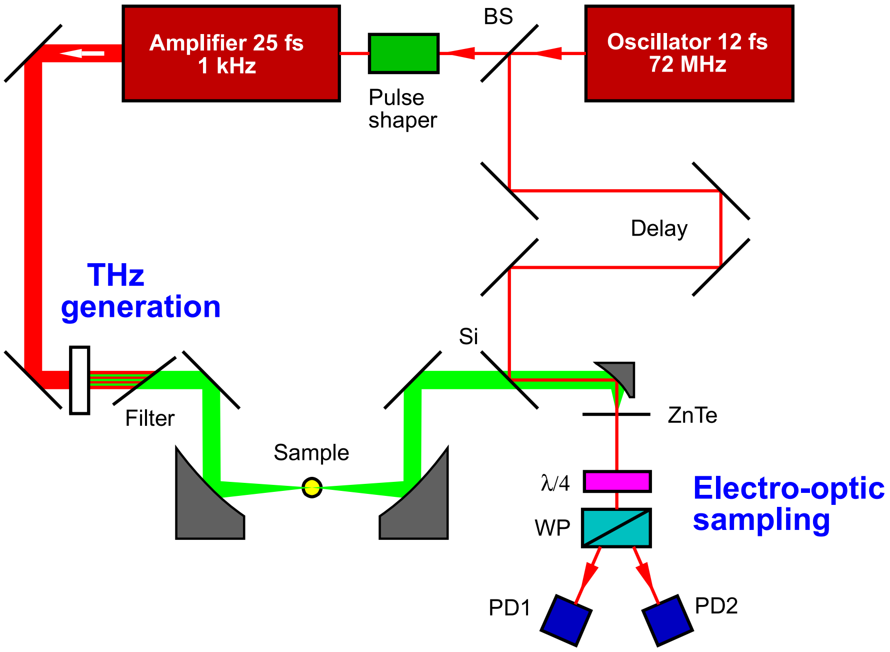

Figure 3.4: The experimental setup consists of a THz source, a sample between two parabolic mirrors and the electrooptic sampling setup. The entire optical path of the THz beam is placed in vacuum.

ponents and a clipping of the emitted field amplitude around $|E_{\mathrm{em}}(t)| < 7$ kV/cm is observed. It was derived in Eq. (2.17) that the emitted field is proportional to the product of number and velocity of free electrons inside the sample. This means for a constant number of carriers, that the emitted field strength at a time t corresponds to one distinct electron velocity. The first derivative of the GaAs bandstructure $\mathscr{E}(\hbar\mathbf{k})$ determines theoretically the electron velocity according to Eq. (3.3). The expected electron velocity as a function of k is shown as a red solid line in Fig. 3.6 (f), (g). For comparison with the experimental curve, the emitted electric field needs to be plotted as a function of k. Integrating Newton's law in Eq. (3.2) along t yields the vector potential, which is for ballistic transport proportional to $k(t)$.

$$\hbar\, d\mathbf{k}/dt = -e\mathbf{E}(\mathbf{t}), \tag{3.4}$$

$$\Leftrightarrow k(t) = -\frac{e}{\hbar}\int_{-\infty}^{t} \mathbf{E}(\mathbf{t}')dt'f'. \tag{3.5}$$

The momentum k of the electron ensemble as a function of time is shown for 300 kV/cm in Fig. 3.6 (d). The black dots in Fig. 3.6 (f) relate the experimentally detected field, and thus the electron velocity, to the electron momentum k. The expected electron velocity derived from the GaAs bandstructure is plotted as a red solid line. We find a very convincing agreement pointing to ballistic transport through more than half of the Brillouin zone. To elucidate the temporal behavior of electrons in detail, five moments from t_1 to t_5 are marked in Fig. 3.6 (f). The effect of the band structure on the electron velocity is seen clearly in the time between t_2 and t_3. During this period, the electric field acting on the electron is negative [Fig. 3.6 (b)]. The electron

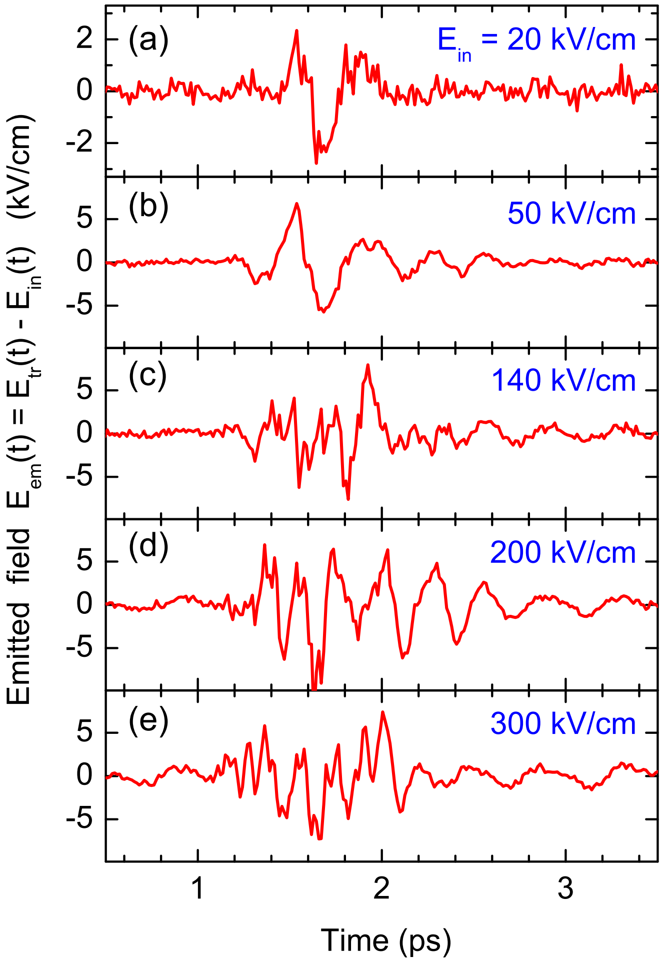

Figure 3.5: Emitted field transients $E_{\text{em}}(t)$ as the difference of E_{trans} and E_{in}, for different amplitudes of the incident electric field. The measurements were taken at room temperature with electrooptic sampling.

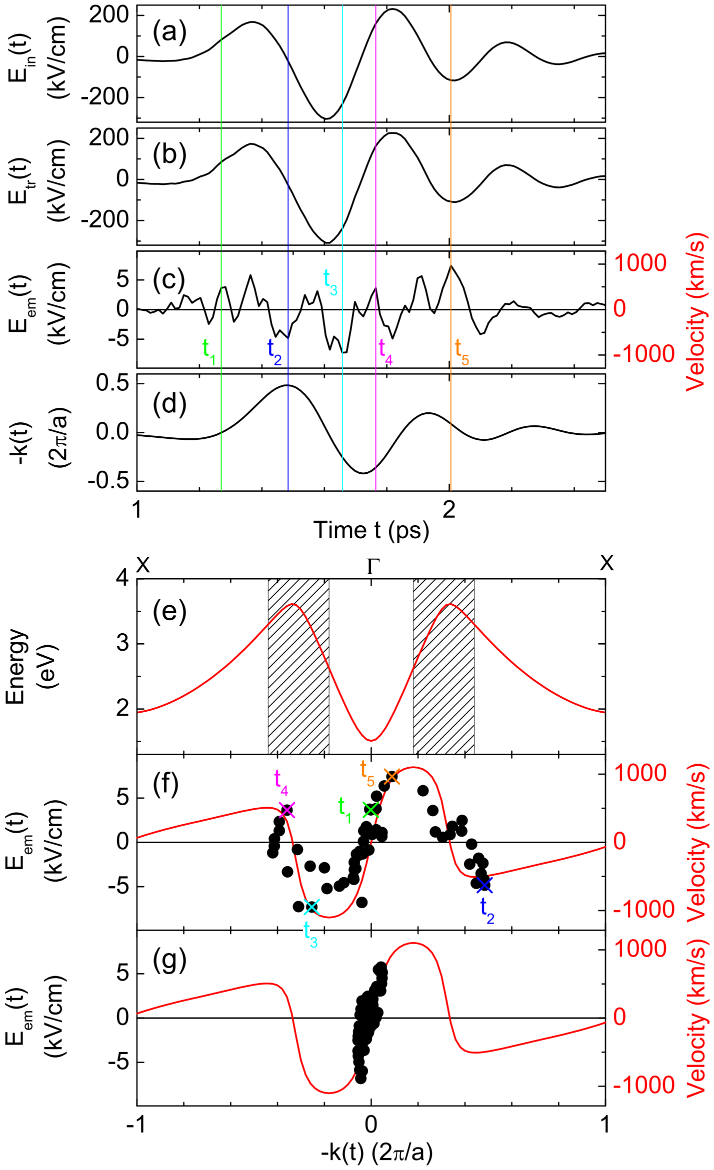

Figure 3.6: (a) Measured incident electric field $E_{\mathrm{in}}(t)$ as a function of time. (b) Electric field transmitted through the sample, $E_{\mathrm{trans}}(t)$. (c) Emitted electric field $E_{\mathrm{em}}(t)$. (d) $-k(t)$ in units of $2\pi/a$ obtained from Eq. (3.2). (e) Lowest conduction band of GaAs in [100] direction. The negative mass regions are hatched [95]. (f) Black dots represent $E_{\mathrm{em}}(t)$ as a function of $-k(t)$. Crosses show the values at the times t_1 to t_5, marked by vertical lines in (a) to (d). Solid line, velocity v calculated using Eq. (3.3). (g) Same plot as in (f), but for an electric field amplitude of 50 kV/cm [see Fig. 3.5 (b)].

velocity is negative at t_2, then gets positive, and then gets negative again [Fig. 3.6 (c)]. Thus, although the electric field has the same direction between t_2 and t_3, there are times with positive and times with negative acceleration, proving that the effective mass of the electron changes sign between t_2 and t_3. Even as late as t_5, the data still agree with the velocity-momentum relationship expected for ballistic transport. Fig. 3.6 (g) shows the momenta k of free electrons at a field amplitude of 50 kV/cm. Again, we find an excellent agreement between experiment and theory. At this lower field strength, the electrons do not gain sufficient energy to escape from the Γ valley and a much smaller part of the Brillouin zone is explored.

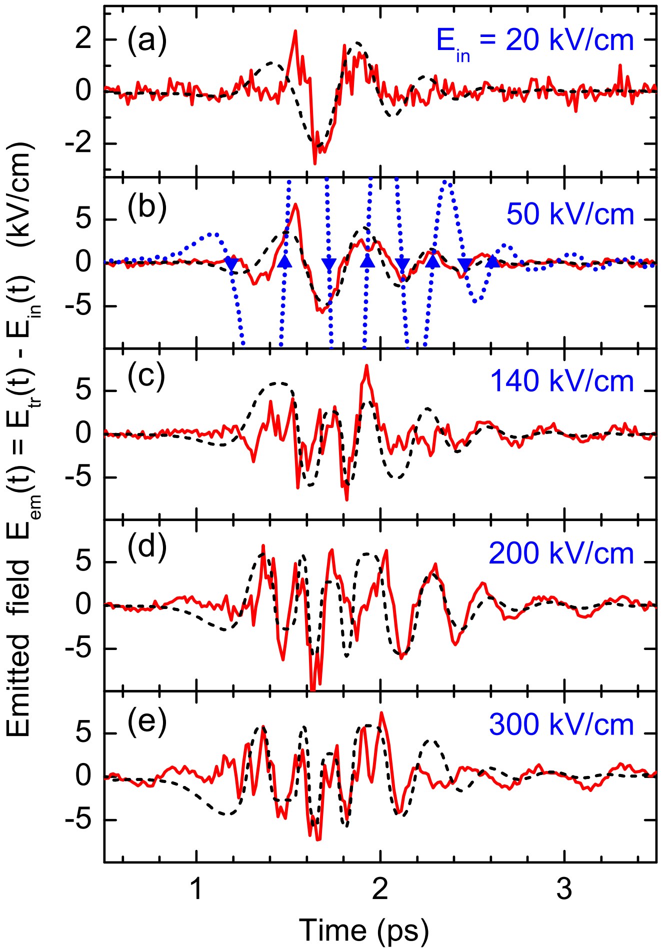

Figure 3.7: Solid lines: emitted field transients $E_{\mathrm{em}}(t)$ for different amplitudes of the incident electric field $E_{\mathrm{in}}(t)$. Dashed lines in (a) to (e): results of the model calculation based on the band structure of GaAs. The dotted line and triangles in (b) show the driving field and its zero-crossings.

In Fig. 3.7 we compare the experimentally recorded emitted fields as a function of time with the theoretical predicted emitted fields for different incident field amplitudes. The dashed curves are calculated assuming ballistic transport according to Eq. (3.2). Our interpretation of the results is in agreement with the experimental data for all THz electric field amplitudes measured. For drift transport, the electron velocity $v(t) \sim E_{\mathrm{em}}(t)$ would be in phase with the driving field $E_{\mathrm{trans}}(t)$ [dotted line in Fig. 3.5 (b)]. We find, however, that the zero-crossings of $E_{\mathrm{trans}}(t)$ (triangles) coincide with the maxima (minima) of $E_{\mathrm{em}}(t)$ demonstrating a 90° phase-delayed velocity, a direct evidence for ballistic transport. The emitted field strength clips at $|E_{\mathrm{em}}(t)| <$ 7 kV/cm [Fig. 3.6 (f)], because it corresponds to the maximum velocity of all electrons present in the conduction band.

To summarize so far, we presented a high-field experiment, in which we measured the electron velocity as a function of its momentum in k space. The experimental results match excellently with the picture of ballistic transport within several hundreds of femtoseconds. These results are in distinct contradiction to the theoretical prediction of a scattering rate of $(3\text{ fs})^{-1}$ reported in Ref. [108].

3.3 The Influence of Scattering Processes on High-Field Transport in GaAs

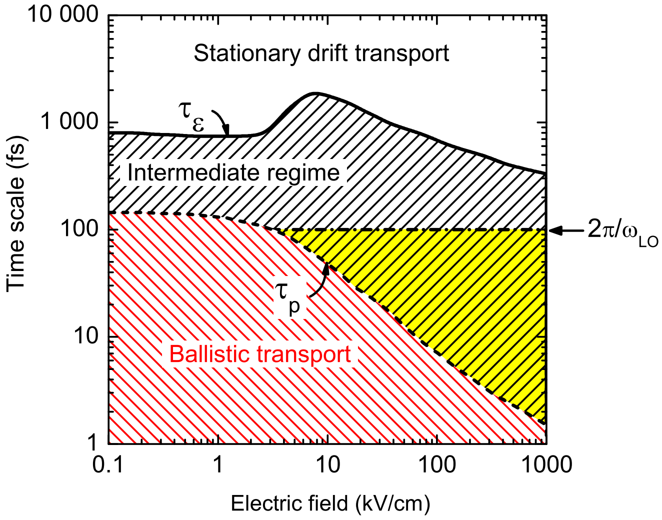

Figure 3.8: Regimes of high-field transport in GaAs as a function of the applied electric field. The energy (τ_ε) and momentum (τ_p) relaxation times from Ref. [108] are valid for times scales longer than $2\pi/\omega_{\text{LO}}$. Quantum-kinetic regime (yellow triangle) allows for quasi-ballistic transport between τ_p and the inverse LO phonon frequency $2\pi/\omega_{\text{LO}}$.

In the following we develop a general approach to describe different transport regimes in GaAs. The theoretical description using the semiclassical Boltzmann's transport equation based on Fermi's golden rule is valid on time scales long compared to the inverse LO phonon frequency $2\pi/\omega_{\text{LO}}$. On shorter time scales and for high fields, this semiclassical approach fails and predicts wrong scenarios. Therefore, we developed a quantum-kinetic theory marked as a yellow triangle in Fig. 3.8. This new regime, presented in detail in Section 3.4, allows for quasi-ballistic transport even beyond τ_p. From the BTE point of view coherent ballistic transport in semiconductors was expected to be limited to extremely small timescales. This is marked in Fig. 3.8 by different regimes of electron transport according to the calculation of Ref. [108]. The two important time constants are the energy relaxation time τ_ε, the average time in which an electron looses its kinetic energy, and the momentum relaxation time τ_p, after which the momentum of the electron randomizes. While inelastic scattering processes change the electron's kinetic energy as well as its momentum, elastic scattering contributes only to τ_p, so that $\tau_p < \tau_\varepsilon$. Coherent ballistic transport obeying Newton's law [Eq. (3.2)] is expected only on short time scales below τ_p in the red hatched area of Fig. 3.8. On long time scales, for $\tau_\varepsilon < t$, stationary drift transport with a hot carrier distribution is predicted. This regime is marked as a white area in Fig. 3.8. On time scales between both relaxation times $\tau_p < t < \tau_\varepsilon$ an intermediate regime (black hatched area) with phenomena like incoherent velocity overshoot is expected [111].

Electrons scatter in semiconductors primarily within the electron ensemble, with impurities, or with phonons. Elastic electron-electron scattering modifies the momentum of individual electrons, but not the overall momentum of the ensemble. Thus, it is fully compatible with bal-

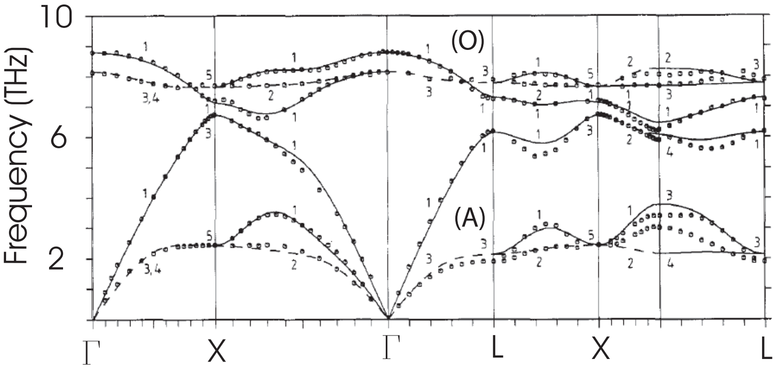

Figure 3.9: The Phonon dispersion in GaAs is taken from Ref. [112]. Three optical modes (O) of almost constant energy for all phonon momenta **q** are distinguished from three acoustic modes (A). The LO phonon energy at the Γ point amounts to 36 meV at room temperature.

listic motion of the entire ensemble. Since our measurement method integrates over the whole electron ensemble, electron-electron scattering is not needed to be considered. Scattering on impurities can be neglected as well, as it will be shown below. Electron-phonon scattering instead, allows for significant momentum transfer rates between electrons and the lattice. Although being in principle inelastic, electron-phonon scattering determines, because of the relatively small phonon energy, primarily τ_p.

Phonons are vibrations of crystal atoms around their positions in an ideally periodic lattice. Such quanta have a distinct momentum $\mathbf{q}$ and a distinct energy $E(\mathbf{q})$. The dispersion relation has been measured by means of inelastic neutron scattering [112]. The results for GaAs are shown in Fig. 3.9. Three acoustic branches (A) starting at the Γ point are distinguished from three optical phonon branches (O) of nearly constant energy around 36 meV or 8.8 THz. Acoustic modes describe a spatially periodic deformation of the unit cell whereas optical modes describe relative motions between atoms with the unit cell. For higher $\mathbf{q}$ values near the zone boundaries, this difference trails off and optical and acoustic oscillations resemble each other. Moreover, one distinguishes between longitudinal and transversal phonons with respect to the propagation direction. Longitudinal optical (LO) phonons in GaAs have the highest energy of 36 meV, which corresponds to an oscillation period of approximatively 110 fs.

The semiclassical model of Ref. [108] based on BTE and FGR predicts scattering times down to $(3\ \mathrm{fs})^{-1}$ (see Fig. 3.2). It is described in many textbooks [113, 114], that Fermi's golden rule applies only to weakly perturbed quantum systems. Furthermore, FGR is exclusively valid, if the time interval between two scattering events t is long compared to the duration of a scattering event Δt (see Appendix 7).

$$\Delta t \ll t \tag{3.6}$$

The inverse interaction time Δt amounts to the time an electron needs to generate or absorb one phonon. Since the crystal lattice reacts at most with the inverse LO phonon frequency, no energy can be transferred to the lattice on shorter time scales. As a consequence, at least the interaction time of one oscillation period is required, until a phonon is irreversibly absorbed or emitted. t, on the other hand, represents the observation time of one scattering process.

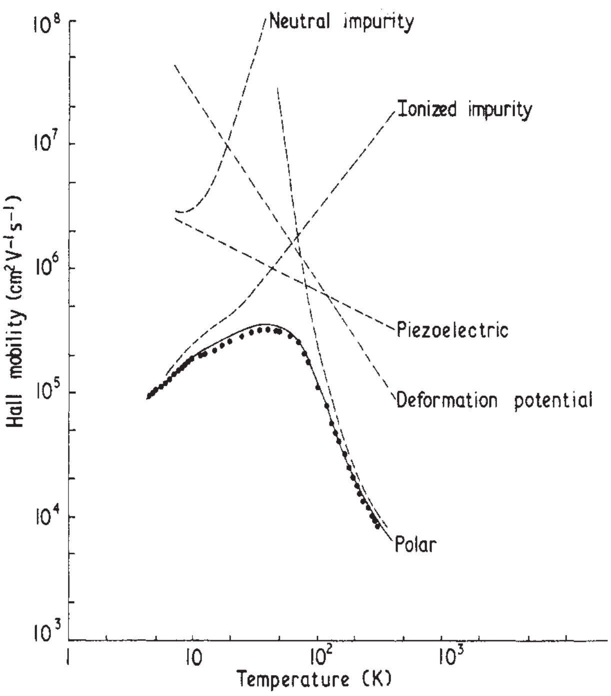

Figure 3.10: Calculated mobility of n-type GaAs as a function of temperature (solid line) [115]. It is in good agreement with the experimental data (dotted curve) of Ref. [116]. The dashed curve represent contributions of the individual scattering processes. Above 100 K the electron mobility is limited mainly by polar optical scattering.

Therefore, t can not be larger than the time between two scattering events, i.e., the scattering rate. Since the shortest phonon oscillation time in GaAs is 110 fs, Fermi's golden rule does not apply anymore to scattering rates of $(3\ \mathrm{fs})^{-1}$.

Therefore, we searched for alternative theoretical concepts to describe electron-phonon scattering on timescales below the inverse phonon frequency. In a first step we considered different interaction mechanism in GaAs to determine the relevant contributions, which need to be incorporated into our theoretical description.

Optical and acoustic phonons interact with electrons in different ways. The change of the electronic bandstructure due to deformation of the lattice is described by a deformation potential. Coupling to acoustic phonons occurs if all atoms of a unit cell are displaced into the same direction. If the atoms in the unit cell are contrarily displaced, the deformation potential couples to optical phonons. Polar materials like GaAs additionally give rise to polar scattering of electrons. In-phase oscillations of oppositely charged atoms cause the piezoelectric effect, which couples to acoustic phonons as well. Out-of-phase oscillations in contrast, induce polar optical scattering of electrons. Further scattering with neutral or ionized impurities may occur in doped materials.

All scattering processes acting on electrons in the drift limit of a direct field determine the electron mobility within a material. This mobility in the Γ valley can be experimentally measured via the Hall effect. In such a measurement a DC-current flows in x-direction and a magnetic field is applied in z-direction. The resulting Lorentz's force shifts electrons into the y-

direction. A Hall voltage across the sample is generated which depends on the carrier density. An additional measurement of the electric conductivity in x-direction reveals the electron mobility. G. Stillman *et al.* performed such an experiment on n-type GaAs 1970 [116]. The obtained mobility as a function of temperature is shown with black dots in Fig. 3.10. Taken as a reference, Fletcher *et al.* reproduced the experimental results with simulations [115] of the overall mobility of free electrons near the Γ point in n-type GaAs (black solid line in Fig. 3.10). Each contributing scattering process on neutral and ionized impurities as well as piezoelectric, deformation potential, and polar optical scattering is plotted individually in Fig. 3.10 with a black dashed line.

Ionized impurities determine dominantly the electron mobility at low temperatures with vanishing phonon populations. Carriers have less kinetic energy and spend more time near the impurities to interact with. Deformation potential scattering with optical [117] and piezoelectric scattering with acoustic phonons [117, 118] increases with temperature. Above 100 K polar optical scattering becomes the dominant process. Moving electrons interact in particular with longitudinal optical (LO) phonons, because of the stronger dipole moment compared with transversal optical phonons. Fig. 3.10 demonstrates that under our experimental conditions of 300 K polar optical and deformation potential scattering is almost two orders of magnitude stronger than piezoelectric scattering. This information is important for the theoretical model, which is derived in the following.

Electrons with sufficient kinetic energy may scatter additionally into the minimum of the X ($\Delta E_{\Gamma L} = 0.29$ eV) or the L side valley ($\Delta E_{\Gamma X} = 0.48$ eV) of GaAs [119]. This intervalley transfer is caused primarily by deformation potential scattering on acoustic phonons with a high momentum. As a consequence, our theoretical model presented in the next section will consider the two dominant scattering mechanisms: polar optical scattering and deformation potential scattering with acoustic phonons.

3.4 Dynamic Quantum-Kinetic Polaron Model

We developed a new approach to get a more specific insight into the microscopic nonlinear dynamics of polarons on ultrafast time scales [120]. Calculations were performed within a nonlinear and a time-dependent extension of the linear model presented in Ref. [121]. We consider a single electron interacting with the local electric field in x-direction and with the phonon modes of the crystal via different types of electron-phonon interactions. The quantum mechanical Hamiltonian [122] reads:

$$\begin{aligned} H(t) = \mathscr{E}(\mathbf{p}) + exE_{\mathrm{loc}}(t) + \sum_{b,\mathbf{q}} \frac{P_{b,\mathbf{q}}^2 + \omega_b^2(\mathbf{q}) Q_{b,\mathbf{q}}^2}{2} \\ + \sum_{b,\mathbf{q}} M_b(\mathbf{q}) \times \left[P_{b,\mathbf{q}} \cos \mathbf{qr} + \omega_b(\mathbf{q}) Q_{b,\mathbf{q}} \sin \mathbf{qr} \right] . \end{aligned} \tag{3.7}$$

$\mathbf{r} = (x, y, z)$ and $\mathbf{p} = (p_x, p_y, p_z)$ denote the position and momentum operators of the electron, respectively. The dispersive band structure of the lowest conduction band is described by $\mathscr{E}(\mathbf{p})$ which can be obtained from, e.g., pseudo-potential calculations [95, 123, 124]. For small excursions of the electron within the lowest minimum of the conduction band the effective mass approximation $\mathscr{E}(\mathbf{p}) = \mathbf{p}^2/2m_{\mathrm{eff}}$ is sufficient to describe the polaron correctly. The local electric field $E_{\mathrm{loc}}(t)$ is the sum of the externally applied electric field and the field reemitted by the coherent motion of all electrons. The latter contains the linear and nonlinear response of the system and accounts for the radiative damping of the electron motion [88]. $Q_{b,\mathbf{q}}$ and $P_{b,\mathbf{q}}$ are the coordinate and the conjugate momentum of the phonon of branch b with the wave vector $\mathbf{q} = (q_x, q_y, q_z)$ and angular frequency $\omega_b(\mathbf{q})$. For simplicity, we limit our calculations to the polar coupling to longitudinal optical phonons ($b =$LO) with a constant frequency $\omega_{\mathrm{LO}}(\mathbf{q}) = \omega_{\mathrm{LO}} =$ const.

$$M_{\mathrm{LO}}(\mathbf{q}) = \sqrt{\frac{e^2}{\varepsilon_0 V}\left(\frac{1}{\varepsilon_\infty} - \frac{1}{\varepsilon_S}\right)} \times \frac{1}{|\mathbf{q}|} \tag{3.8}$$

and coupling to acoustic phonons ($b =$AC) via the deformation potential Ξ with an averaged sound velocity c_{S}

$$M_{\mathrm{AC}}(\mathbf{q}) = \sqrt{\frac{\Xi^2}{\rho V c_{\mathrm{S}}^2}} \tag{3.9}$$

$$\omega_{\mathrm{AC}}(\mathbf{q}) = \frac{2c_{\mathrm{S}} q_{\mathrm{zb}}}{\pi} \sin\left(\frac{\pi|\mathbf{q}|}{2q_{\mathrm{zb}}}\right). \tag{3.10}$$

ε_S is the static relative dielectric constant and ε_∞ is the dielectric constant for frequencies well above the optical phonon frequency, but below electronic excitations. The difference $\varepsilon_\infty^{-1} - \varepsilon_S^{-1}$ is proportional to the polar electron-LO phonon coupling constant α [125]. V is the quantization volume which determines the discretization of the k- and q-space with the zone boundary q_{zb}. ρ stands for the mass density of the crystal.

From Eq. (3.7) we derive the Heisenberg equations of motion for the expectation values of quantum mechanical operators like $\langle x\rangle$, $\langle p_x\rangle$, etc. In this process new quantum mechanical operators containing combinations of canonical variables, e.g., $\langle P_{b,\mathbf{q}} \sin(\mathbf{qr})\rangle$, appear on the right-hand side of the equations of motion. Since we are only interested in the expectation values of the relevant observables and since we would like to close the infinite hierarchy of equations at some level, we expand and subsequently approximate those expectation values. In lowest order one obtains exactly the equations of motion of the classical polaron [126,127]. The classical polaron model predicts, however, an unrealistically high binding energy in the self-induced potential as classical particles correspond to infinitely small wave packets. To overcome this problem one has to go one step further in the expansion of the expectation values of quantum mechanical operators and consider the finite size of the electron wave packet $\Delta x^2 = \langle x^2\rangle - \langle x\rangle^2$. As shown in detail in Refs. [128,129], the dynamics of Δx^2 is inherently connected with the dynamics of both the variance of its conjugate momentum $\Delta p_x^2 = \langle p_x^2\rangle - \langle p_x\rangle^2$ and $\Delta xp = \langle xp_x + p_x x\rangle/2 - \langle x\rangle\langle p_x\rangle$ which is the covariance of x and p. The main result of Refs. [128,129] is that under certain circumstances (which are fulfilled in our case) continuous position measurements of the electron caused by various fluctuating forces of the environment lead to decoherence phenomena in such a way that an initially Gaussian electron wave packet (in Wigner space) stays Gaussian in its further evolution and adjusts its size Δx^2 continuously to the respective momentum uncertainty according to $\Delta x^2 = \hbar^2/4\Delta p_x^2$ (cf. minimum of Heisenberg's uncertainty relation). Such continuous position measurements of the electron lead also to a small random walk in phase space, i.e., diffusion of both the position and momentum of the particle. According to the arguments of the authors of Refs. [128,129] this diffusion is ineffectual in comparison to the wave packet

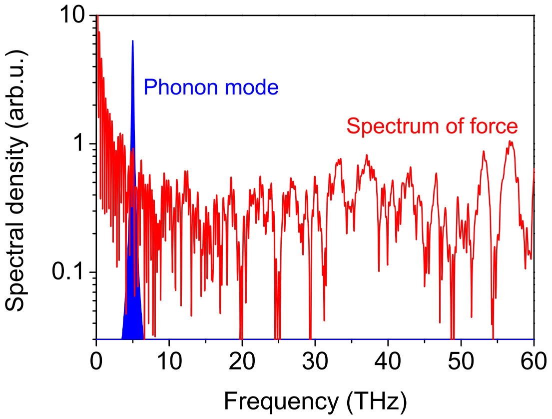

Figure 3.11: Quantum-kinetic decoupling: High electron velocities at 300 kV/cm cause a broad spectrum of the force (red line). The small overlap with narrow phonon modes (e.g., $3.5\frac{\pi}{a}$, blue area) explain the decreased friction force at high electron velocities.

localization and, thus, we completely neglect it in the following. The application of the approximations and arguments discussed above lead to the following system of equations of motion for the expectation values of the operators:

$$\frac{d\langle x\rangle}{dt} = \langle v_x\rangle \quad \text{with the velocity operator:} \quad v_x = \frac{\partial \mathscr{E}(\mathbf{p})}{\partial p_x} \tag{3.11}$$

$$\begin{aligned}\frac{d\langle p_x\rangle}{dt} &= eE_{\text{loc}}(t) + \sum_{b,\mathbf{q}} \exp\left[-\frac{1}{2}\mathbf{q}^2\Delta x^2\right] M_b(\mathbf{q}) \\ &\quad \times \left[\langle P_{b,\mathbf{q}}\rangle\, q_x \sin q_x\langle x\rangle - \omega_b(\mathbf{q})\langle Q_{b,\mathbf{q}}\rangle\, q_x \cos q_x\langle x\rangle\right]\end{aligned} \tag{3.12}$$

$$\frac{d\langle Q_{b,\mathbf{q}}\rangle}{dt} = \langle P_{b,\mathbf{q}}\rangle + M_b(\mathbf{q}) \cos q_x\langle x\rangle \exp\left[-\frac{1}{2}\mathbf{q}^2\Delta x^2\right] \tag{3.13}$$

$$\frac{d\langle P_{b,\mathbf{q}}\rangle}{dt} = -\omega_b^2(\mathbf{q})\langle Q_{b,\mathbf{q}}\rangle - M_b(\mathbf{q})\omega_b(\mathbf{q}) \sin q_x\langle x\rangle \exp\left[-\frac{1}{2}\mathbf{q}^2\Delta x^2\right]. \tag{3.14}$$

The energy transfer of electrons to phonons is described in Eqs. (3.13) and (3.14). The driving term, e.g., in Eq. (3.13), consists of one oscillatory component $M_{b,\mathbf{q}} \cos q_x\langle x\rangle$ and one amplitude factor $\exp\left(-\frac{1}{2}\mathbf{q_x}\Delta x^2\right)$. The oscillatory component demonstrates, that an electron moving at a constant velocity $v_{\text{el}} = \langle x\rangle t$ exerts a force on the phonon oscillator with the frequency $q_x \cdot v_e$. A phonon mode is efficiently excited, only if this frequency matches the resonance condition $\omega_{\text{ph}} = q_x \cdot v_e$. The force created by electrons with the velocity of our experiment has a very broad spectrum with frequency components up to 60 THz (red line in Fig. 3.11). The very small spectral overlap with the phonon mode of $3.5\frac{\pi}{a}$ (blue area) explains the inefficient generation of phonons and thus the weak friction force. This effect is called quantum-kinetic decoupling. The friction force caused by LO phonons was already shown for different velocities in Fig. 3.3. Beyond a critical velocity of 435 km/s, the friction force of the LO phonon mode decreases. The characteristic velocity is achieved for acoustic phonons already at several tens of km/s. This is due to the lower frequency and to the higher q vectors of the relevant acoustic phonon modes. Furthermore, the amplitude factor demonstrates the importance of the polaron wave packet size

($\sim \Delta x^2$) for electron-phonon coupling. A large wave packet couples only to phonon modes with a small momentum $\mid \mathbf{q} \mid$. The smaller the wave packet the higher the friction force, because more phonon modes with higher momenta contribute.

For simplicity we use in our model spherical Gaussian wave packets with the momentum $\langle p_x \rangle$ in x-direction and isotropic momentum fluctuations $\Delta p_x^2 = \Delta p_y^2 = \Delta p_z^2$. Consequently, the expectation values of the kinetic energy $\langle \mathscr{E}(\mathbf{p}) \rangle = \mathscr{E}_{\mathrm{kin}}(\langle p_x \rangle, \Delta p_x^2)$ and the velocity operator $\langle v_x \rangle = \mathscr{V}_x(\langle p_x \rangle, \Delta p_x^2)$ are functions of both $\langle p_x \rangle$ and Δp_x^2. Both two-dimensional functions have been derived from pseudo-potential calculations [95, 123, 124]. The so far missing dynamical variable Δp_x^2 (in turn determining $\Delta x^2 = \Delta y^2 = \Delta z^2 = \hbar^2/4\Delta p_x^2$) can be inferred from an equation of motion of the kinetic energy

$$\frac{d\langle \mathscr{E}(\mathbf{p}) \rangle}{dt} = \frac{\partial \mathscr{E}_{\mathrm{kin}}(\langle p_x \rangle, \Delta p_x^2)}{\partial \langle p_x \rangle} \frac{d\langle p_x \rangle}{dt} + \frac{\partial \mathscr{E}_{\mathrm{kin}}(\langle p_x \rangle, \Delta p_x^2)}{\partial \Delta p_x^2} \frac{d\Delta p_x^2}{dt} \tag{3.15}$$

using the following arguments: The temporal change of the total electron energy $d\langle \mathscr{E}(\mathbf{p}) \rangle/dt$ splits naturally into a ballistic coherent (first term) and an incoherent contribution (second term) the latter of which is connected to the velocity fluctuations of the electron (see also discussion of equations (16) and (A4) of Ref. [130]). Since the acceleration of the electron in the external field does not change its momentum fluctuations, it exclusively contributes to the first term on the r.h.s. of Eq. (3.15). In general, the friction force due to phonon scattering (second term r.h.s. of Eq. (3.12)) will contribute to both terms in Eq. (3.15). In the typical situation, however, the energy relaxation time is distinctly longer than the momentum relaxation time (cf. Fig. 13 of Ref. [108]). Thus, in good approximation we assume that the friction force exclusively contributes to the incoherent contribution of the electron's energy change leading to the following implicit equation of motion for the expectation value of the momentum fluctuations Δp_x^2

$$\begin{aligned} \frac{\partial \mathscr{E}_{\mathrm{kin}}(\langle p_x \rangle, \Delta p_x^2)}{\partial \Delta p_x^2} \frac{d\Delta p_x^2}{dt} &= \\ \mathscr{V}_x(\langle p_x \rangle, \Delta p_x^2) \sum_{b,\mathbf{q}} \exp\left[-\frac{1}{2}\mathbf{q}^2 \Delta x^2\right] M_b(\mathbf{q}) & \\ \times \left[\langle P_{b,\mathbf{q}} \rangle\, q_x \sin q_x \langle x \rangle - \omega_b(\mathbf{q}) \langle Q_{b,\mathbf{q}} \rangle\, q_x \cos q_x \langle x \rangle\right] & \\ + \Gamma_{\mathrm{loss}}(p_x, \Delta p_x^2, T_{\mathrm{L}}) & \\ \times \left[\mathscr{E}_{\mathrm{kin}}(\langle p_x \rangle, m_{\mathrm{eff}} k_{\mathrm{B}} T_{\mathrm{L}}) - \mathscr{E}_{\mathrm{kin}}(\langle p_x \rangle, \Delta p_x^2)\right] . & \end{aligned} \tag{3.16}$$

Emission and absorption of incoherent phonons is described by the energy relaxation rate $\Gamma_{\mathrm{loss}}(p_x, \Delta p_x^2, T_{\mathrm{L}})$, which is generally a "slow" process occurring on a timescale of several hundreds of femtoseconds (cf. Fig. 13 of Ref. [108]). Thus, it can be well described by the Fermi's golden rule approach like in the semi-classical Boltzmann transport equation. In absence of external electric fields this term relaxes the wave-packet size to its value at thermal equilibrium, i.e., $\Delta p_x^2 = m_{\mathrm{eff}} k_{\mathrm{B}} T_{\mathrm{L}}$.

The incoherent energy relaxation heats up the polaron and minimizes the wave packet size. This size determines the friction forces acting on the electron, since only phonons with $\mathbf{q}^2 < 1/\Delta x^2$ can couple efficiently [Eq. (3.12)]. Thus, for large wave packets the friction is weak, leading to ballistic transport, for small ones the friction is strong, leading to drift transport. In

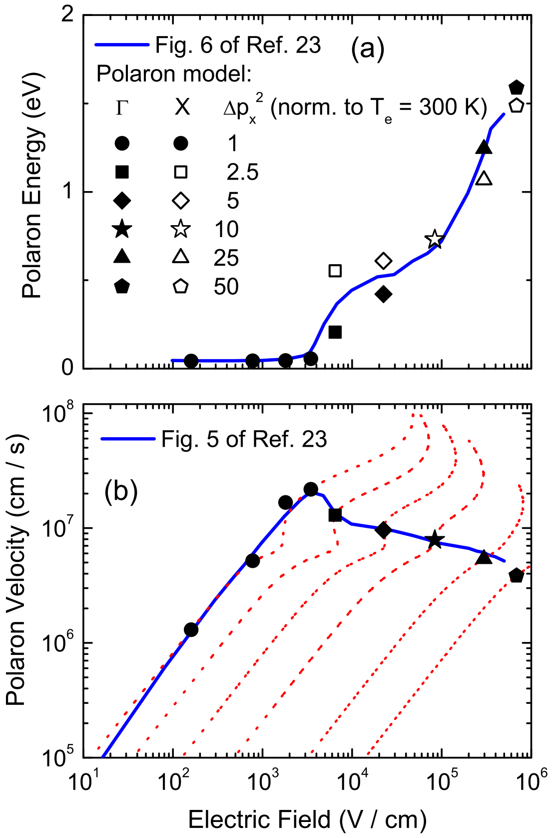

Figure 3.12: (a) Calculated quasi-stationary high field transport of polarons (symbols) in GaAs. For comparison, the blue solid lines show the result of the semi-classical Boltzmann transport equation, i.e., Ensemble Monte Carlo simulations of M. V. Fischetti [108]. Stationary drift velocity of polarons (symbols) as a function of the applied electric field. The dashed lines show drift transport of polarons with various fixed values of the wave packet size $\Delta x^2 = \hbar^2/4\Delta p_x^2$. (b) Corresponding energy of the polarons in both the Γ valley and the X-valley of the crystal.

our experiment, we start with a large wave packet corresponding to a small Δp_x^2. To increase Δp_x^2, incoherent energy has to be supplied by the friction force [Eq. (3.16)], which takes several hundreds of femtoseconds, leading on ultrafast time scales to negligible changes of Δp_x^2 and, thus, to ballistic transport.

Outside the quantum-kinetic regime our dynamic polaron theory and the semiclassical BTE [108] give identical results, e.g., for the stationary drift velocity in high fields [Fig. 1 (b)]. Therefore, we apply an electric field to Eqs. (3.11) – (3.14) and (3.16), which varies distinctly slower in time than the inverse of the incoherent energy loss rate $\Gamma_{\text{loss}}(p_x, \Delta p_x^2, T_L)$. The result of such a calculation is shown in Fig. 3.12.

The symbols in Fig. 3.12 (a) represent the drift velocity of polarons as a function of the applied electric field strength. If the electron-phonon matrix elements depend on the phonon wave vector $|\mathbf{q}|$, one gets a common drift velocity-friction force characteristics for all electrons independent of the conduction band valley they drift in. A good agreement is found with the data calculated with the semiclassical BTE of Ref. [108] (blue solid line). The dashed lines mark drift

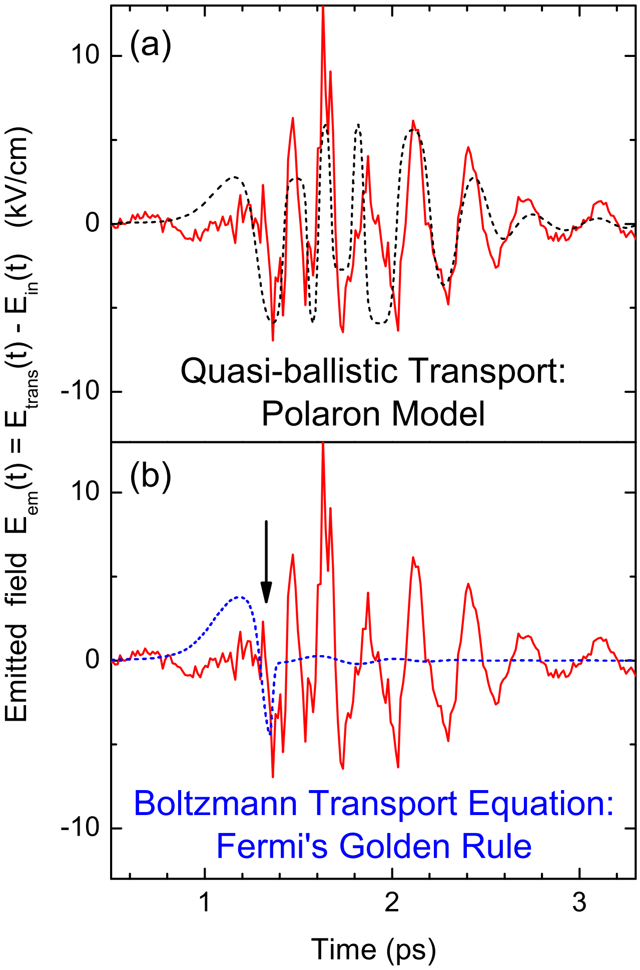

Figure 3.13: (a,b) Red solid lines: emitted field transient $E_{\text{em}}(t)$ for an incident electric field $E_{\text{in}}(t)$ with an amplitude of 300 kV/cm. (a) Black dashed line: result of the model calculation based on the polaron model. (b) Same experimental data as in (a), now compared to the results (blue dashed line) of a calculation assuming the intervalley scattering rates of Ref. [108]. At the time marked by the arrow the electron energies are high enough for scattering into the side valleys.

transport of polarons with various *fixed* values of the wave packet size $\Delta x^2 = \hbar^2/4\Delta p_x^2$. Such a transport behavior is expected on a timescale shorter than the respective energy relaxation time, but long enough to assure transport in the drift limit, i.e., outside the quantum kinetic regime. Fig. 3.12 (b) depicts the polaron energy as a function of the applied field strength. In contrast to the polaron velocity, it depends obviously on the electron's valley. Here the energy of the polarons is shown in both the Γ valley (solid symbols) and the X valley (open symbols).

Next, we compare our experimental results at short timescales below 200 fs with the calculated results of both models. The Monte-Carlo simulation of Ref. [108] predicts efficient scattering into the side valleys before reaching the negative mass regions. Since electrons in the side valleys have rather low velocities ($<$ 200 km/s) [108, 109, 131], it would result in a drastic reduction of the electron velocity and thus of the emitted field. Since the return of electrons into the Γ valley requires more than a picosecond [132], they would remain in the side valleys for the rest of the pulse. Accordingly, one expects a strong signal $E_{\mathrm{em}}(t)$ at the beginning of the pulse, but only very weak signals at later times, as shown by the dashed line in Fig. 3.13 (b). This is in obvious disagreement with the experimental results.

The dynamic polaron theory instead is valid beyond Fermi's golden rule and predicts correctly a quasi-ballistic high-field transport in the quantum kinetic regime. According to our model the size of the electron wave packet $\Delta x^2 = \hbar^2/4\Delta p_x^2$ remains almost constant in our experiments on ultrafast time scales. In particular, a wave packet with large Δx^2 couples only weakly to phonons with large wavevectors, responsible for scattering into the side valleys. One advantage of applying THz pulses instead of a static electric field to drive electrons, is that new phonon correlations are build up after each half-cycle. Therefore our THz pulse performs six times partial Bloch oscillations consecutively. Since intervalley scattering is effectively suppressed the first several hundreds of femtoseconds, we can observe ballistic transport even at the time t_5 in Fig. 3.6. Outside the quantum kinetic regime our dynamic polaron theory and the semiclassical BTE [108] give identical results, e.g., for the stationary drift velocity in high fields [Fig. 3.12 (b)]. For the long times inherent in stationary transport, enough energy can be supplied to the polaron to decrease its wave-packet size to very low values [130], leading to strong friction forces and thus to drift transport [131].

3.5 A Quantum-Kinetic View on Previous High-Field Transport Experiments

After presenting our experimental results and discussing the quantum-kinetic effects on ultrashort time scales, we will get back to Ref. [31]. A quantum-kinetic view may reconcile both experimental results. The detected electric field at 130 kV/cm exhibits a zero crossing after 55 fs, which points according to the authors to intervalley scattering. The achieved drift velocities, however, contradict this interpretation of the experimental data. The Monte Carlo simulation of Ref. [108] predicts in agreement with measurements carried out by Windhorst *et al.* [shown in Fig. 3.14 (b)] drift velocities of around 70 km/s. Integrating the detected electric field in Fig. 4 of Ref. [31] for each sample thickness yields the electron velocity of Ref. [31], which is shown as a black solid line in Fig. 3.14 (a). Surprisingly, the recorded electron velocity peaks at 600 km/s more than eight times above the expected velocity in the drift regime which is indicated as a dashed blue line. The velocity over the entire time range is significantly higher than 70 km/s. On the other hand the obtained velocity agrees reasonably with the red dashed line representing ballistic transport. If we consider the broadband photo excitation causing "hot" polarons

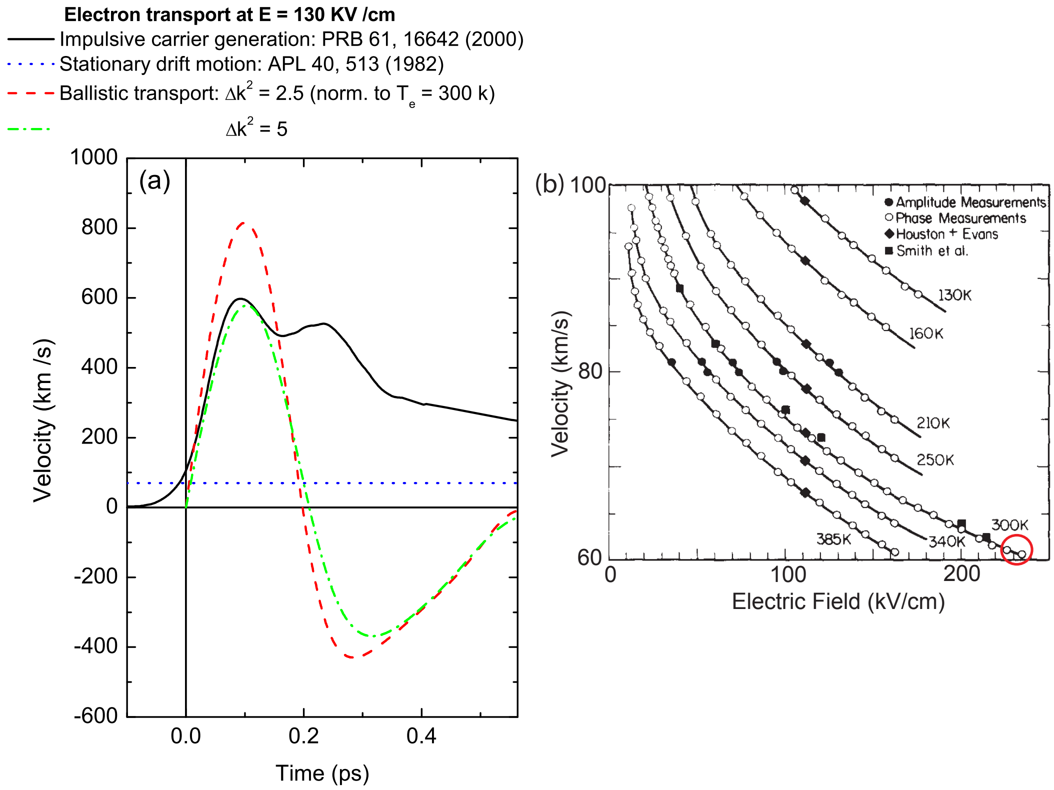

Figure 3.14: (a) The electron velocity (black solid line) in Ref. [31] was obtained by integrating the carrier acceleration along the time. The dashed lines denote the expected electron velocities for ballistic transport with a large (red) and with a small polaron radius (green). (b) Measured electron drift velocities in GaAs at room temperature. A drift velocity of 70 km/s is found at electric field strengths of 130 kV/cm [indicated as a dashed blue line in (a)]. Taken from Ref. [131].

with a five times larger momentum distribution than at room temperature, a better agreement is achieved. The large momentum distribution of the electron ensemble averages over parts of the bandstructure, which lowers the averaged peak velocity. Negative velocities may therefore not be caused by intervalley scattering, but by negative mass regions of the conduction band. This alternative interpretation suggests that the quantum-kinetic regime in GaAs was observed in previous experiments.

4 Terahertz-Induced Interband Tunneling of Electrons in GaAs

4.1 Tunneling and the Role of Decoherence

In the last section we demonstrated coherent ballistic transport in bulk *n*-type GaAs under the electric field of several 100 kV/cm of short THz pulses. Since even at room temperature the interaction with phonons played a minor role within the initial acceleration process, we did not expect major changes for measurements at lower temperatures. Nevertheless, we extended our work presented in the previous Chapter 3.2 down to lower lattice temperatures of 80 K. Coherent carrier transport is observed, but to our surprise the emitted electric field increased significantly. This points to an increased electric current within the sample. It will be shown that the transient THz field promotes electrons from the valence into the conduction band. This can happen either by impact ionization or by interband tunneling.

The process of impact ionization is depicted in Fig. 4.1 (a). Free electrons in the conduction band are accelerated by an external electric field. If the kinetic energy is larger than the bandgap, new electron-hole pairs are generated in scattering processes. Impact ionization in GaAs has been measured and calculated in Refs. [133–135]. The obtained ionization rates shown in Fig. 4.1 (b) will be compared with the observed electron-hole generation of our experiment. Im-

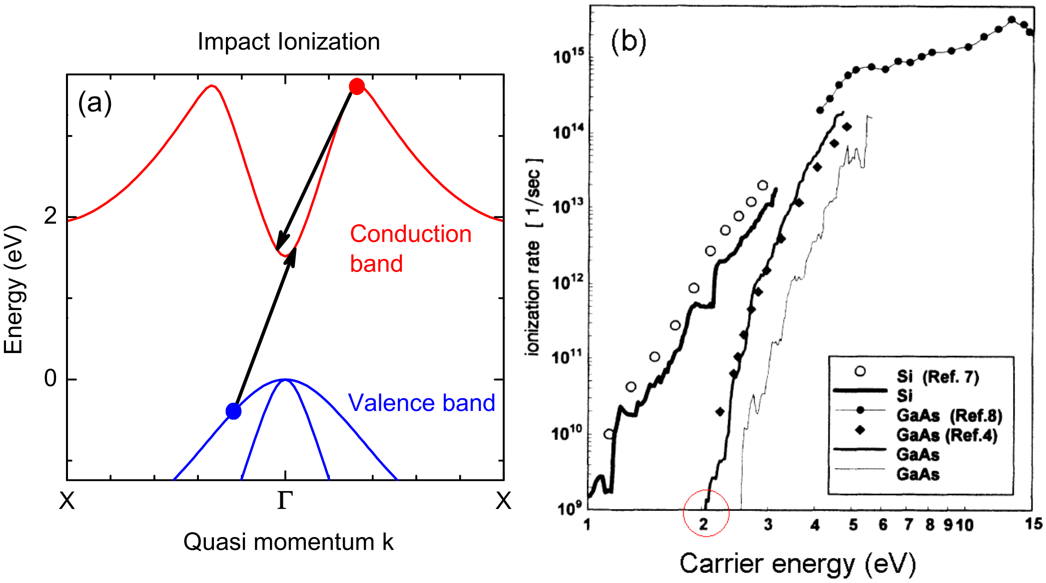

Figure 4.1: (a) Electrons in the conduction band with sufficient kinetic energy may scatter back into the Γ valley and excite an valence band electron. (b) Expected impact ionization rates in GaAs and silicon as obtained in Ref. [133].

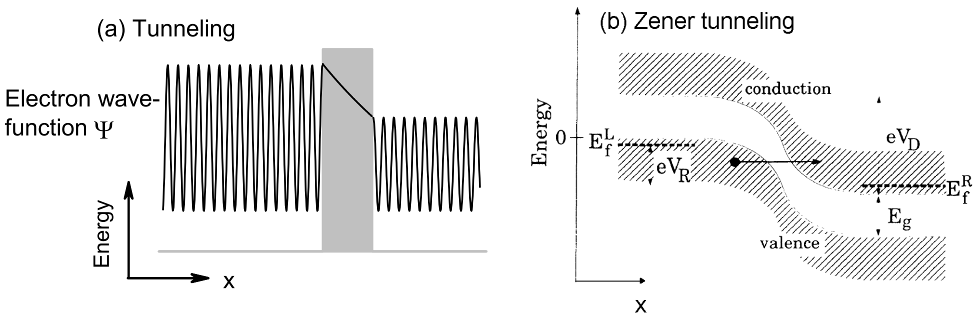

Figure 4.2: (a) The magnitude of a wave function decays exponentially within a potential barrier. (b) A strong electric field distorts the energy levels of the valence band and the conduction band, so that the valence band electron may tunnel into the conduction band. Taken from Ref. [142].

pact ionization was often observed in low-bandgap semiconductors [19,20,133,133,136–141]. The electric field of THz pulses is used in Refs. [19,20] to accelerate free carriers in InSb. An increased absorption in the focal point at low temperatures is observed in Ref. [20] and attributed to impact ionization.

Tunneling between the valence and the conduction band of semiconductors was considered the first time in 1934 by C. Zener [143]. The underlying formalism was originally developed two years earlier by C. Zener and L. Landau to describe the non-adiabatic energy transfer within a quantum-mechanical system under the influence of an electric field [143, 144]. The principle of tunneling is illustrated in Fig. 4.2 (a). An electron wave function ψ, whether stationary or not, decays exponentially within a potential barrier (grey area) and transmits it. The square of the wave function behind the barrier is considered proportional to the tunneling rate.

Zener tunneling is illustrated in Fig. 4.2 (b). An electric field applied to a semiconductor distorts the energy levels of both bands, so that the electron may tunnel through the bandgap into the conduction band. The resulting tunneling rate was estimated by E. O. Kane in 1959, who applied the theoretical model of Zener tunneling to an accurate bandstructure of a semiconductor [145]. Several experiments examined the obtained tunneling rates by recording the reverse current of a *p*-*n*-diode under different conditions [146–148]. However, due to uncontrollable parameters like the tunneling distance of the carriers, the reverse currents agreed only poorly with the theoretical predictions. This problem was solved, when molecular beam epitaxy allowed to grow *p*-*i*-*n*-diodes with an accuracy in the nm range. New static experiments and simulations on Zener tunneling and impact ionization were performed in the 90's [142, 149, 150]. The comparison of experimental results with Monte Carlo simulations demonstrated significant impact ionization in GaAs diodes only for field strengths of several MV/cm [150].

However, time resolved experiments and the consideration of decoherence effects are necessary for a realistic model of the tunneling rate. The tunneling processes in Ref. [142, 145] are considered entirely coherent until, suddenly, the electron has irreversibly tunneled through the barrier and is adapted as entirely incoherent. The relevance of decoherence was highlighted the first time by Kazarinov and Suris in Refs. [151, 152]. Decoherence describes the loss of a defined phase relation between two eigenfunctions of a quantum system [cf. Eq. 6.16]. This loss of information prevents a reversion of a process and thus causes the irreversibility of tunneling processes. Without decoherence, e.g., in a quantum beat experiment [153], the electron wave packet oscillates reversibly back and forth through a barrier until the coherent superposition is destroyed by the probe pulse and the electron is found on one side of the barrier. This transition between reversible quantum mechanics and irreversible classical physics is described in detail by Zurek *et al.* in Refs. [154–156].

4.2 Experimental Results

We performed measurements at temperatures of 200 and 80 K for different field amplitudes between 10 and 300 kV/cm. To cool down the freestanding sample we evacuated the vacuum chamber containing the entire THz beam path. We achieved reliably pressures of 10^{-6} mbar after several hours with a combination of scroll and turbomolecular vacuum pump. The vacuum was further improved using a large area cooling trap filled with liquid nitrogen, which was integrated in the acrylic glass cover of our vacuum chamber. These low pressures were required at low temperatures to prevent any condensation on the sample surface. The sample was mounted on the cooling finger of a liquid helium flow cryostat. A silicon diode as a temperature sensor was mounted on the cooling finger next to the sample. Although the temperature of liquid helium and parts of the cooling finger were well below 10 K, it was difficult to achieve a similar temperature on the sample. The surrounding components, e.g., the parabolic mirrors at room temperature, thermally radiated and heated up the sample. Moreover, the sample was extremely thin ($\approx$ 500 nm), which impeded the heat conductivity from the sample holder to the sample. As a consequence, the lowest sample temperatures achieved amount to roughly 80 K.

As discussed in Section 2.3, the emitted electric field of the sample were measured as the difference between incident and transmitted field $E_{\text{em}} = E_{\text{in}} - E_{\text{trans}}$. The following procedure gave reproducible results with and without sample and thus a reliable measurement of E_{in} and E_{trans}. The cooling finger including the sample was mounted on three linear translation stages. The sample could be moved in three directions with a reproducibility of 10 μm. The THz focal spot was marked with a pinhole, on which a Helium-Neon laser was adjusted as an optical pointer. A camera with a high magnification optics monitored clearly which part of the sample was transmitted by the THz pulse. The arrival time of the THz pulse with a femtosecond accuracy provided an additional characterization of the transmitted material. We measured consecutively E_{in} and E_{trans} by switching between both positions.

Figs. 4.3 (a) – (j) present the emitted electric field transients measured for different incident amplitudes at a sample temperature of 80 and 200 K. The transmitted electric fields are shown as black dashed lines. In the beginning of the pulse, $E_{\text{em}}(t)$ clearly oscillates out-of-phase with $E_{\text{trans}}(t)$, signifying absorption of the THz pulse in the sample. At later times $E_{\text{em}}(t)$ and $E_{\text{trans}}(t)$ are in phase, signifying THz emission. In particular the strength of the emitted field is remarkable. While the emitted fields at room temperature clamp at field strengths of about $\mid E_{\text{em}} \mid = 7$ kV/cm, it reaches up to 25 kV/cm at 200 K [Fig. 4.3 (j)] and even 50 kV/cm at 80 K [Fig. 4.3 (e)]. In Fig. 4.4 (a) the comparison between the emitted electric field for 300 K (red dots) and for 80 K (blue solid line) is shown.

4.3 Discussion

The difference between the incident and the transmitted field yields the field emitted from the sample. According to Eq. (2.17), E_{em} is proportional to the product of carrier density and carrier velocity. The latter is determined exclusively by the applied field strength and the bandstructure

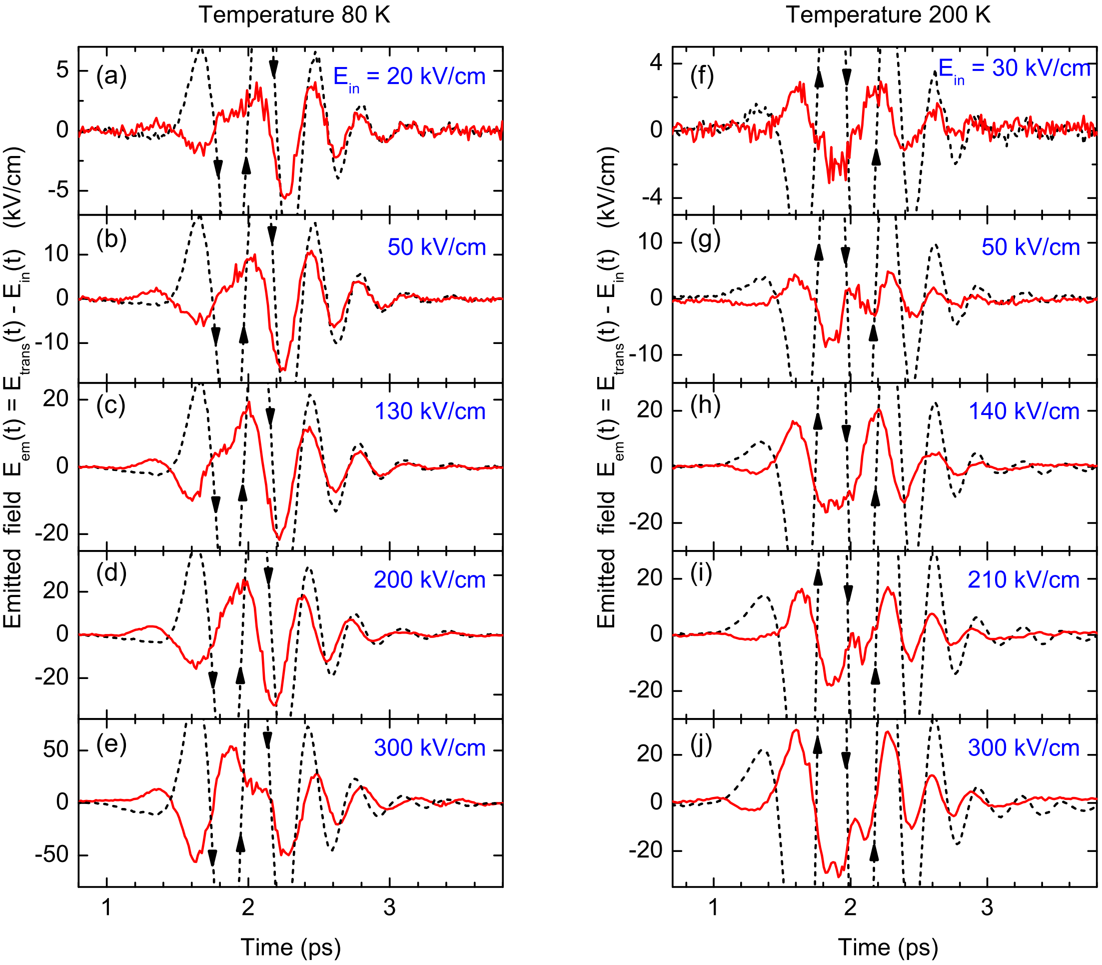

Figure 4.3: Transients of the emitted fields at 80 K (a) – (e) and 200 K (f) – (j) for different amplitudes of the incident field E_{in}. The transmitted fields are shown as black dashed lines.

of GaAs [Eq. (3.3)]. An emitted field amplitude of $| E_{\mathrm{em}} | = 7$ kV/cm at room temperature corresponds to the maximum velocity for ballistic transport of all electrons introduced by doping. Since the k-dispersion of the conduction band changes only marginally at low temperatures, we conclude that the enhanced emitted field is generated by additional free carriers. If we consider the same electron velocity as at room temperature, Eq. (2.17) allows to estimate the required number of carriers to emit an electric field amplitude of 50 kV/cm. We obtain a value of 2×10^{17} cm^{-3}, ten times as many carriers as introduced by doping. The only way to increase the number of carriers to that extent is to promote electrons from the valence into the conduction band. Thus, the THz pulse has to provide at least the band gap energy of $E_g = 1.5$ eV per electron. The transiently absorbed energy [82] normalized to the density N_D of electrons present by doping is

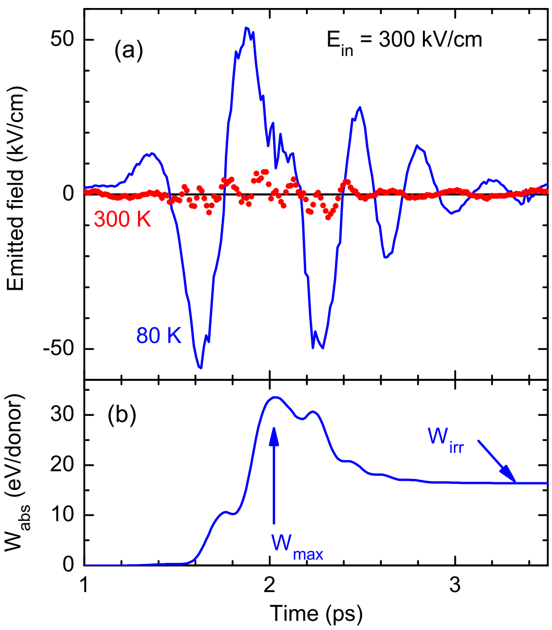

Figure 4.4: (a) Comparison of the recorded emitted field transients $E_{\mathrm{em}}(t)$ for lattice temperatures of $T = 80$ K (blue solid line) and of 300 K (red dots). The incident field amplitude $E_{\mathrm{in}}(t)$ is 300 kV/cm in both cases. (b) Normalized transiently absorbed energy [Eq. (4.1)] for $T = 80$ K. The irreversibly absorbed energy W_{irr} of 16 eV corresponds to $\approx 2 \times 10^{17}$ cm^{-3} field-generated electron-hole pairs.

$$
\begin{aligned}
W_{\mathrm{abs}}(t) &= \frac{1}{N_D}\int_{-\infty}^{t} j(t')\,E_{\mathrm{trans}}(t')dt' \\
&= \frac{-2}{d\,N_D\,\mu_o\,c}\int_{-\infty}^{t} E_{\mathrm{em}}(t')\,E_{\mathrm{trans}}(t')dt'.
\end{aligned}
\tag{4.1}
$$

The blue solid line in Fig. 4.4 (b) represents W_{abs} as a function of time, as it was derived from the measured electric fields. The energy transfer dynamics is described with two characteristic values. The highest absorbed energy W_{max}, stored only temporarily inside the sample, and the irreversibly absorbed energy W_{irr}. The latter determines the number of electron-hole pairs remaining inside the sample even after the THz pulse. For temperatures of 80 K and electric field amplitudes of 300 kV/cm, a large amount of energy $W_{\mathrm{max}} = 33$ eV per donor is temporarily stored inside the sample. Under this condition W_{irr} amounts to an energy density of 16 eV per donor, which is roughly ten times the bandgap energy of GaAs. It suggests that ten electron-hole pairs are generated per initial donor electron resulting in an total number of free carriers of $n = 10N_{\mathrm{D}} = 2 \times 10^{17}\mathrm{cm}^{-3}$. This number agrees well with the number of carriers estimated from the emitted electric field amplitude.

Fig. 4.5 shows W_{max} and W_{irr} as a function of the incident field amplitude for temperatures of 80 (blue), 200 (green) and 300 K (red). The open symbols indicate the maximum energy W_{max} and the closed symbols indicate the irreversibly absorbed energy W_{irr}. W_{max} increases for 80 and 200 K with the pulse intensity ${E_{\mathrm{in}}}^2$, as it is indicated by the blue and the green dashed lines. The hatched area marks the possible range for W_{max} if no tunneling occurs, i.e., if the electron

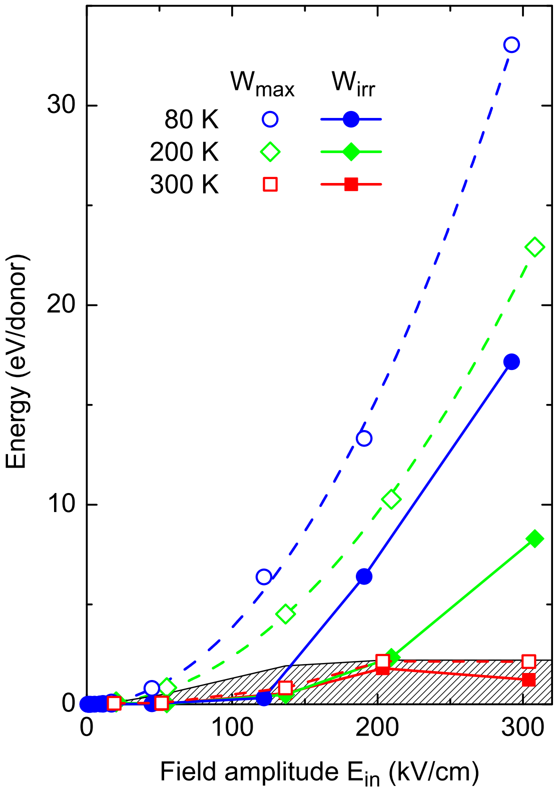

Figure 4.5: Maximum energy $W_{\max}$ (open symbols) and irreversibly absorbed energy W_{irr} (closed symbols) as a function of the incident electric field amplitude, calculated according to Eq. (4.1), for temperatures of 80, 200, and 300 K. For $T = 80$ K and for $T = 200$ K the dashed lines are fits to $W_{\max} = \mathrm{const}\,E_{\mathrm{in}}^2$. The hatched area shows the possible values for $W_{\max}$ if only the electrons present by doping participate, i.e., if no tunneling occurs.

density stays equal to the doping density. In this case the highest value for $W_{\max}$, 2.1 eV, is given by the highest energy an electron can reach in the conduction band relative to the conduction band minimum. Since the data for 300 K stay within this range, the electron density has not increased beyond the doping density. At lower temperatures W_{irr} reaches values of 8 eV/donor for 200 K and even 17 eV/donor at 80 K.

Since the energy of THz photons is not sufficient for interband excitation, the strong electric field of the THz pulse must be responsible for the observed interband transition. The mechanism, either impact ionization or interband tunneling, must explain the experimentally observed temperature dependence, i.e., a negligible increase of free electron density at room temperature and a strong increase at low temperatures.

For impact ionization the kinetic energy needs to be larger than the band gap of 1.5 eV. Theoretical descriptions of impact ionization [133, 136] find ionization rates that depend only on the electron kinetic energy and on the bandstructure. Low temperatures decrease the average lattice constant and increase the bandgap in GaAs from 1.42 eV at room temperature to 1.46 eV at 80 K [157]. But this would rather lower the impact ionization at low temperatures. Also the influence of phonons can not account for a temperature-dependent impact ionization rate.

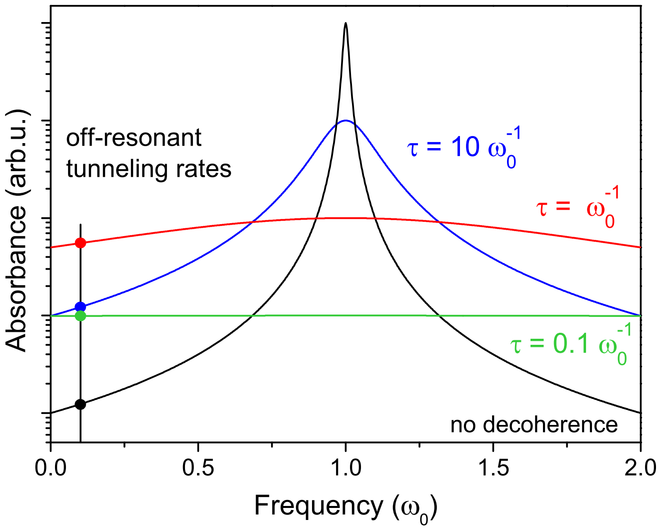

Figure 4.6: Lorentzian line shapes without decoherence (black line) and for decoherence times of $\tau = 10\omega_0{}^{-1}$ (blue line), $\tau = \omega_0{}^{-1}$ (red line), and $\tau = 0.1\omega_0{}^{-1}$ (green line). A significant off-resonant transition rate (dots) at nearly zero frequency is achieved for a decoherence time of $\tau = \omega_0{}^{-1}$.

Our experimental results at room temperature demonstrated only a minor influence of scattering processes on the electron dynamics on ultrashort time scales. As a consequence, also the kinetic energy of the electrons is essentially temperature-independent. But impact ionization could also occur at room temperature. An electron reaches energies of up to 2.1 eV during ballistic transport, which is more than the bandgap energy. According to Fig. 4.1 (b), this kinetic energy results in an impact ionization rate of only 10^9 s^{-1}. Assuming the electron has such high kinetic energies for 100 fs, impact ionization can account at most for the generation of 10^{-4} electron-hole pairs per initially present electron. The experimentally observed generation of 10 electron-hole pairs rules out impact ionization as an explanation of our experimental results.

4.4 Dependence of the Tunneling Rate upon the Decoherence Rate

Static interband tunneling, as it was theoretical described in Refs. [145,147,158] can not explain our experimental findings. According to Eq. (39) of Ref. [145], we find for a static electric field of 300 kV/cm a temperature-independent tunneling rate close to zero. A correct description of interband tunneling needs to incorporate decoherence effects. Kazarinov and Suris derived in Refs. [151,152] the following expression for the influence of decoherence on the tunneling rate R,

$$R \sim \frac{\tau}{1+(\delta\omega\,\tau)^2}. \tag{4.2}$$

The tunneling rate is identical to a transition rate from an initial into a final state. $\delta\omega$ is the detuning from this transition and τ is the decoherence time after which the constant phase relation between the two eigenstates is lost. That means the tunneling process becomes irreversible

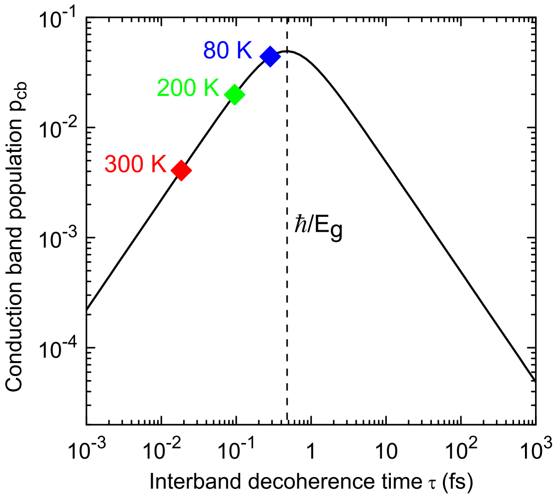

Figure 4.7: Population of the upper level (conduction band) after the end of the exciting THz pulse calculated as a function of the decoherence time τ (dots). The diamonds are estimates for the decoherence times at the three temperatures of our experiment.

after the decoherence time.

The relevance of the decoherence time for the transition rate can be recognized also under a different perspective. A short decoherence time $\tau = T_2^*$ broadens furthermore the spectral width $\Delta\nu$ of an absorption line according to:

$$\Delta\nu = T_2{}^{-1} = 2T_1{}^{-1} + T_2^{*-1}. \tag{4.3}$$

T_1 is the life time of the excited state, which is longer than T_2^*. The black solid line in Fig. 4.6 represents the Lorentzian line shape of a transition at an arbitrary frequency ω_0. Apparently, the highest absorbance at resonant frequencies ω_0 is found without any decoherence (black line). An off-resonant frequency can excite the transition as well, if the line width is sufficiently broad. Different line shapes according to Eq. (4.3) are depicted for the decoherence times $\tau = 10\omega_0{}^{-1}$ (blue line), $\tau = \omega_0{}^{-1}$ (red line), and $\tau = 0.1\omega_0{}^{-1}$ (green line). Fig. 4.6 shows that for the decoherence time $\tau = \Delta\omega^{-1}$ a significant oscillator strength is spread over the entire spectral range between 0 and $2\omega_0$. Even a nearly static electric field with $\omega \approx 0$ efficiently excites the transition, if the decoherence time amounts to $\tau = \Delta\omega^{-1} = \omega_0{}^{-1}$.

Since the THz frequency is much smaller than the bandgap in our experiment, the detuning is approximately $E_g/\hbar$. According to Eq. (4.2) this yields a conduction band population as a function of the decoherence time as shown in Fig. 4.7. The expected tunneling rate increases with the decoherence time until $\tau = \Delta\omega^{-1}$ and subsequently decreases again. Under the reasonable assumption that τ decreases with increasing temperature, the decoherence times at the three temperatures of 80, 200, and 300 K have to be near the values marked in Fig. 4.7 to explain our results. The highest tunneling rate is obtained for the very fast decoherence of $\tau = 0.5$ fs.

Such short decoherence times seem at first very surprising. The spectral width of an interband absorbtion line suggests decoherence times in the order of 100 fs at room temperature and even larger at lower temperatures. However, the decoherence time is not a specific property of the material. It depends on the coherent superposition and on the mechanism of decoherence. Therefore the decoherence times for interband absorption and high-field THz transport are not

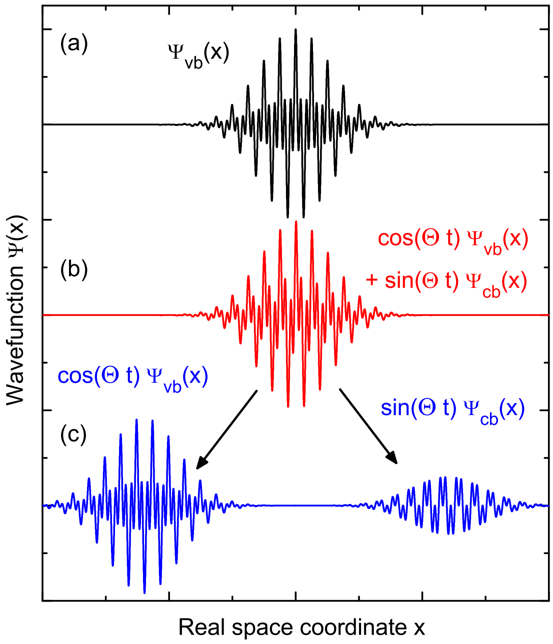

Figure 4.8: Dynamics of the electron wave function during interband tunneling: (a) Valence band electron wavepacket (schematic) before THz excitation. (b) The THz field induces a coherent superposition of valence and conduction band wave packets. The amount of conduction-band character is determined by the parameter Θ. (c) Simultaneously the electric field of the THz pulse spatially separates the conduction-band-like part from the valence-band-like part of the same wavefunction with a pronounced "non-classical" character.

identical.

The decoherence mechanism is explained in Fig. 4.8. The electric field of the THz pulse displaces reversibly the valence band electrons from the lattice atoms. Those virtual electron-hole pairs are responsible for the large amount of reversible stored energy W_{max} in Fig. 4.4. The displacement modifies the fast oscillating cell-periodic part of the wave function in Fig. 4.8 (b), which results in a coherent superposition of a valence band wave packet and a conduction band wave packet [Fig. 4.8 (b)]. At the same time the electric field drives an intraband motion of this coherent superposition. During this motion, the conduction-band-like part moves in the opposite direction as the valence-band-like part. In result the wave function forms an extremely "non-classical" wave packet having two spatially separated density maxima [Fig. 4.8 (c)]. In our experiment the spatial separation of the two components can be as large as $\Delta x = 300$ nm. As shown by Zurek [154–156] (see also Refs. [159–161]), such non-classical wavepackets experience high decoherence rates at finite temperatures T,

$$\tau^{-1} = \tau_{\mathrm{m}}^{-1} \frac{m k_{\mathrm{B}} T (\Delta x)^2}{\hbar^2}. \tag{4.4}$$

In this equation the momentum relaxation time τ_{m} is responsible, e.g., for drift transport. At a temperature of 80 K one finds from the mobility $\tau_{\mathrm{m}} = 1000$ fs. At the maximum of Δx, this results in the very short decoherence time of 0.1 fs. Therefore Eq. (4.4) explains the observed high tunneling rate as well as the temperature dependence. Without the separation of the virtual electron and hole in a THz field, a much lower decoherence rate exists. This explains the narrow spectral width of interband absorption lines, as it is measured in a spectrometer.

4.5 Model Calculations

We performed calculations modeling step-by-step the physical processes taking place. A pseudopotential calculation [95, 162] neglecting spin-orbit interaction with a finite set of local pseudopotentials yields the electronic bandstructure shown in Fig. 4.9 (a). The electric field of the THz pulse induces a coherent superposition of a valence band and a conduction band state. Each of these electron states with wave vector $\mathbf{k}$ in band b is described with the general Bloch wave function

$$\psi_{b,\mathbf{k}}(\mathbf{r},t) = e^{i\mathbf{k}\mathbf{r}} \sum_{\mathbf{G}} c_{b,\mathbf{k},\mathbf{G}}(t)\, e^{i\mathbf{G}\mathbf{r}}, \tag{4.5}$$

as a coherent superposition of plane waves displaced by the reciprocal lattice vectors $\mathbf{G}$. The four highest valence bands and the ten lowest conduction bands were included in our calculation. The coefficients $c_{b,\mathbf{k},\mathbf{G}}$ basically describe the electron wave functions within the crystal lattice driven by the external electric field. The interaction between THz pulse and crystal is given by the Hamiltonian [163]:

$$[H^g(\mathbf{k},\mathbf{A})]_{\mathbf{G},\mathbf{G}'} = \frac{\delta_{\mathbf{G},\mathbf{G}'}}{2m_0}\left[\hbar(\mathbf{k}+\mathbf{G}) - e\mathbf{A}\right]^2 + V(\mathbf{G}-\mathbf{G}'). \tag{4.6}$$

The interaction takes place via the vector potential $\mathbf{A}(t) = \int_0^t \mathbf{E}(t')dt'$. $V(\mathbf{G})$ are the coefficients of the Fourier expansion of the periodic potential and m_0 is the free-electron mass. The evolution of the density matrix ρ, representing the electron wave function under the influence of an external THz pulse, can be calculated with the Liouville equation $\frac{d\rho}{dt} = \frac{1}{i\hbar}[H(t),\rho]$. Without electric field ($\mathbf{A} = 0$) the Hamiltonian yields the single-electron bandstructure, i.e., one gets the band energies $\mathscr{E}_b(\mathbf{k})$ and the corresponding coefficients $c_{b,\mathbf{k},\mathbf{G}}(t)$ for the band b. Our calculations work in the single-particle picture, i.e., all many-body interactions are neglected. Among them electron-electron scattering, which could mix Bloch waves with different $\mathbf{k}$ vectors. Without this mixing, each electron can be labeled by its initial $\mathbf{k}_0$ and band index b_0 before THz excitation. This approximation is justified, because electron-electron scattering conserves the total energy and the total momentum of the electron system. Moreover, even at the highest electron density the typical electric field an electron generates at the position of another electron is only 5 kV/cm, much less than the applied electric fields.

To model the observed interband tunneling correctly, we have to consider additionally decoherence processes of the electron wave function. Therefore the off-diagonal elements of ρ may decay exponentially. Eq. (4.4) yields the decoherence rate as a function of the electron-hole distance. The distance is calculated with

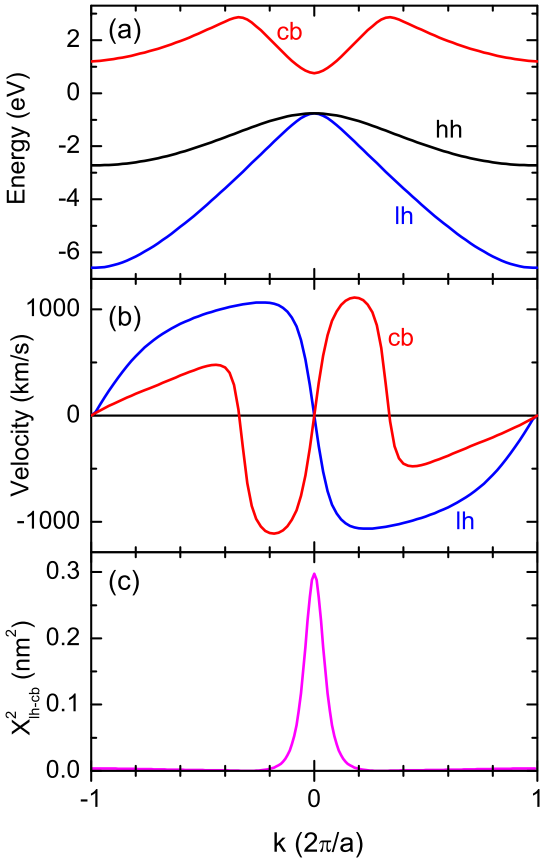

Figure 4.9: (a) Electronic band structure of GaAs along the [100] direction calculated by the local pseudo-potential method without spin-orbit interaction [95, 123, 162]. (b) Corresponding velocity of electrons in the lowest conduction band (cb) and in the light-hole band (lh), Eq. (3.3). (c) Interband matrix element squared $X^2_{\text{lh-cb}}$ for the transition between the light-hole band and the lowest conduction band.

$$k(t) = \int_0^t \mathbf{E}(t')dt' \tag{4.7}$$

$$\Rightarrow v[k(t)] = v(t) \tag{4.8}$$

$$x(t) = \int_0^t v(t')dt' \tag{4.9}$$

In general also the decay of the diagonal elements, caused by spontaneous electron-hole recombination needs to be considered. However, nanosecond electron lifetimes in the conduction band lead to a negligible decay rate. Including decoherence we obtain the following Liouville equation to describe the time evolution of our system:

$$\frac{d\rho}{dt} = \frac{1}{i\hbar}[H(t),\rho] - \Gamma(t,\rho). \tag{4.10}$$

While the electron wave functions are described in the basis g of the crystal lattice, the decoherence process is calculated in the $\mathbf{k}$ and $\mathbf{A}$ dependent eigenbases e of the THz pulse. By diagonalizing the Hamiltonian H, one can switch using the transformation matrices S and S^{-1} between both eigenbasis, $H^e(\mathbf{k},\mathbf{A}) = S(\mathbf{k},\mathbf{A})H^g(\mathbf{k},\mathbf{A})S^{-1}(\mathbf{k},\mathbf{A})$. The electrons present by doping are neglected, because the number is small compared to the total number of conduction band states. Therefore we assume that all valence band states are initially filled and the conduction band states are empty. In a first step, one calculates in the eigenbasis g the coherent superposition of the valence band and the conduction band states caused by the THz pulse. Transforming the wave functions into the basis e allows for considering the decoherence rate of the electron wave function. After back transforming into g, the next time step in the evolution of the electron wave functions is calculated. For the numerical calculation, the size of the time steps has to be below the shortest τ [Eq. (4.4)], i.e., at room temperature at most 0.01 fs. This makes the calculations very time-consuming. From the calculation one obtains the time dependence of the density matrix for the initial $\mathbf{k}$. The resulting current density is obtained from Eq. (3.3) and the emitted electric field from Eq. (2.17).

Results from Model Calculation

A high interband matrix element $X_{b-b'}(\mathbf{k}) = \int \psi^*_{b,\mathbf{k}} x \psi_{b',\mathbf{k}} dV$ is required for tunneling. It can be directly obtained from the band structure calculation. We find that the transition from the heavy-hole band to the conduction band is small, so that basically tunneling from the light-hole band to conduction band contributes. The square of this matrix element $X_{\text{lh-cb}}(\mathbf{k})^2$ lies at the Γ point and is shown in Fig. 4.9 (c). The matrix element decreases rapidly for larger wave vectors, so that only electrons with wave vectors smaller than 1/10 of the Brillouin zone effectively tunnel into the conduction band. From the corresponding k-space volume and the population probability we obtain a total electron density of 3×10^{17} cm^{-3} in the conduction band, which agrees well with the observed value of 2×10^{17} cm^{-3}.

For ballistic transport, the electron wave vector is proportional to the vector potential. Thus, one expects interband tunneling near the zeros of the vector potential. An additional requirement for interband tunneling is a high electric field. For bandwidth limited pulses, the extrema of the electric field and the zero points of the vector potential always coincide. Fig. 4.10 (a) shows that for the chirped pulses of our experiments this is not always fulfilled. The highest tunneling rate is achieved for $t = 1.9$ ps. Since the Γ point is crossed with a high velocity, the carriers tunnel only during several ten femtoseconds through the bandgap. In contrast, for impact ionization the highest tunneling rate is expected for the highest velocities near the extrema of the vector potential.

Decoherence plays the crucial role in ultrafast tunneling processes. The curve for $\gamma_m = 0$ in Fig. 4.10 (b) shows that tunneling remains completely reversible without decoherence. No electrons remain in the conduction band after the THz pulse. For higher decoherence rates of $\gamma_m = (1\ \text{ps})^{-1}$ at 80 K, we find an increased conduction band population of 4×10^{-3} after the end of the pulse. The corresponding population probability at room temperature is 5×10^{-4}, nearly a factor of ten less.

Each tunneling process generates an electron in the conduction band and a hole in the valence band. Since both carrier velocities are of comparable magnitude [see Fig. 4.9 (b)], half of the additional current is carried by electrons and half by light holes. The theoretical curves in Fig. 4.11 (dashed lines) have been calculated with the model described above. While the time dependence of the absorbed energy $W_{\text{abs}}(t)$ agrees quite well with the theoretical curve [Fig. 4.11 (b)], the calculated emitted electric field shows deviations, in particular in the be-

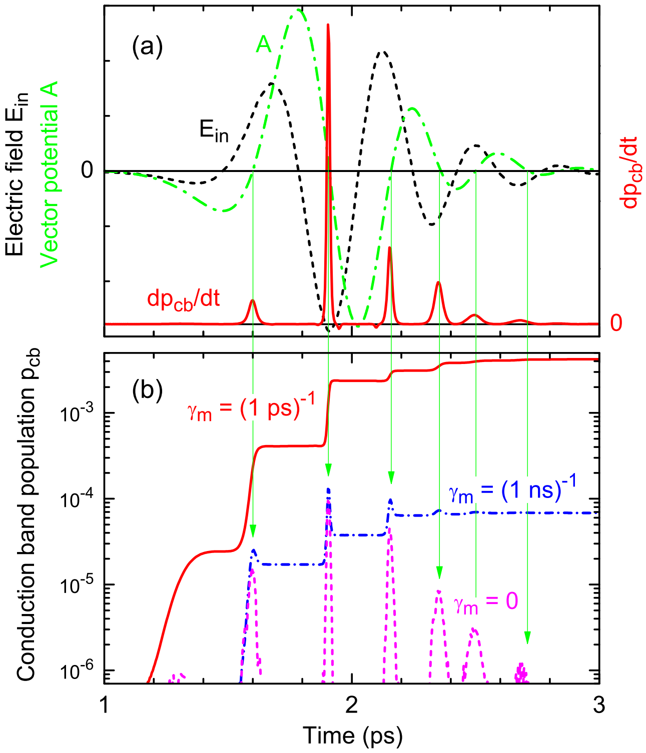

Figure 4.10: (a) Incident electric field $E_{\text{in}}(t)$ (field amplitude 300 kV/cm, dashed line), corresponding vector potential $A(t)$ (dash-dotted line), and time derivative of the conduction band population dp_{cb}/dt calculated for $\gamma_m = (1 \text{ ps})^{-1}$ and $T = 80$ K. The arrows mark the zeros of the vector potential. (b) Time dependence of the conduction band population calculated for different momentum relaxation rates γ_m.

ginning of the pulse [Fig. 4.11 (a)]. Nevertheless, for such a simple model, which neglects all many-body effects like electron-electron scattering and the formation of excitons, the agreement is satisfactory.

In conclusion, the results discussed in this chapter illustrate the important role of decoherence for tunneling processes on ultrafast time scales. High electric fields induce ballistic transport in bulk GaAs on short time scales. At low temperatures THz field-induced interband tunneling from the valence into the conduction band is observed. At 80 K we find up to ten times more THz-induced carriers than present by doping. The THz field induces a coherent superposition of the electron wave function in the valence and in the conduction band. This virtual electron-hole pair is driven by the electric field into opposite directions, which causes very short decoherence time down to 0.1 fs. The predictions of our theoretical model are in good agreement with our experimental results.

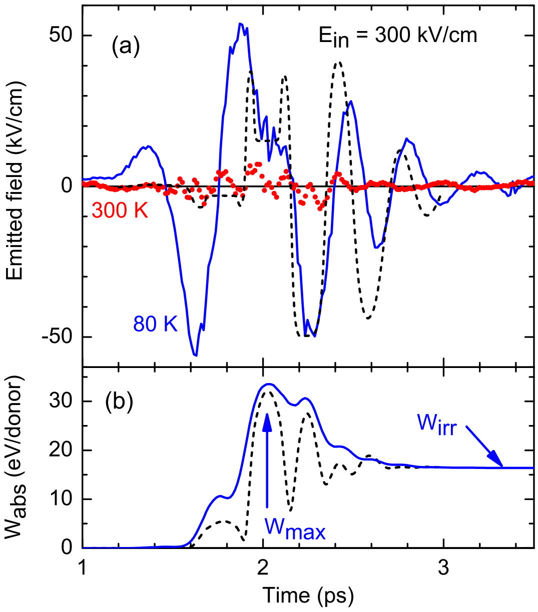

Figure 4.11: Comparison of calculated transients from our model (black dashed lines) with the emitted field transients $E_{\mathrm{em}}(t)$ for lattice temperatures of $T = 80$ K (blue solid line). (a) For the emitted electric field and (b) for the normalized transiently absorbed energy [Eq. (4.1)] at $T = 80$ K.

5 Phase-Resolved Pump-Probe Experiments on a Quantum Cascade Laser

The experiments presented in the previous chapter dealt with field-induced effects in n-type GaAs. Electronic transport was investigated by means of the coherently emitted field from the sample. This experimental concept can be applied, if the sample layer is much thinner than the THz wavelength. To investigate samples with longer propagation lengths, e.g., a cavity, we developed a collinear THz pump-probe scheme based on electrooptic sampling. Chopping the pump beam with half the repetition rate allows for measuring the transmitted probe pulse with and without a preceding pump pulse. Thus we are able to monitor exclusively the pump-induced effect on the sample. This phase-resolved pump-probe experiment is an important intermediate step in the development of two-dimensional THz spectroscopy. Compared to previous experiments, we changed the pulse frequency from 2 THz to 25 THz. The field of the THz pulse is not used to accelerate carriers, but to resonantly excite intersubband transitions in quantum wells. The essential difference to conventional optical pump-probe experiments lies in the phase-resolved detection of the electric field transmitted through the sample.

In the following we investigate and discuss ultrafast gain dynamics of a 500 μm long InGaAs/AlInAs quantum cascade laser (QCL). Electron transport and coherent tunneling processes, now in the rather complex environment of a heterostructure, determine the gain dynamics of the QCL. The first section gives a short introduction and puts our experiment into a wider perspective before the experimental results are presented and discussed.

5.1 Quantum Cascade Lasers

Modern quantum cascade lasers are efficient devices for generating THz radiation. They have a size in the order of several mm^{-3} and convert an electric current directly into THz radiation. QCLs find broad applications in remote sensing of spurious gases [164], control of industrial processes, or in high-speed data transfer [165]. QCLs employ an intersubband transition within a semiconductor heterostructure for lasing. Basic quantum mechanics predicts a split up of the electron wave function in a spatially confined quantum well [51]. These quantum wells are made of very thin semiconductor layers (several nanometers), embedded in a different semiconductor material with a higher bandgap. The resulting energy levels form subbands within a sequence of quantum wells. An external electron supply keeps this intersubband transition inverted and allows for lasing at THz frequencies. R. Kazarinov and R. Suris proposed already in 1971 [151] to use these semiconductor superlattices as lasing devices. Only in the 90's of the last century quantum wells with spatial extensions in the nanometer range and with nearly one monolayer accuracy were grown with molecular beam epitaxy [166, 167]. In 1994 A. Cho in cooperation with the group of F. Capasso succeeded to grow the first $Ga_{1-x}In_xAs/Al_{1-y}In_yAs$ QCL, which emitted laser radiation under bias [168]. Since then quantum cascade lasers developed rapidly.

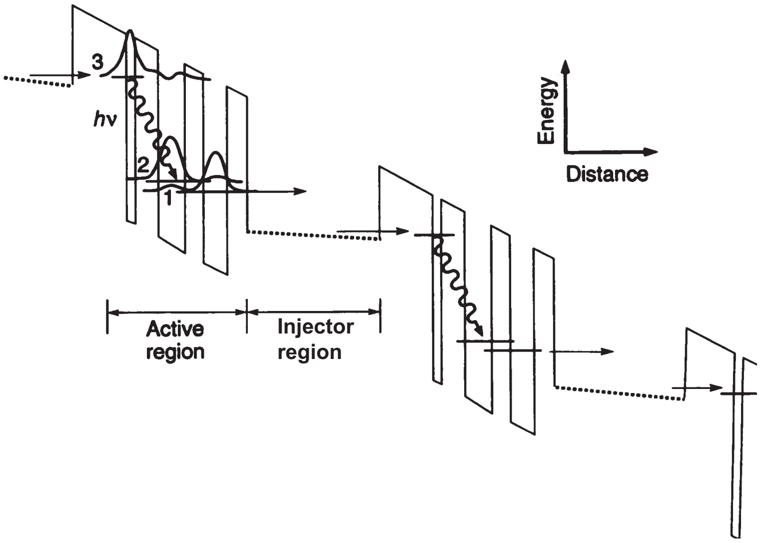

Figure 5.1: Conduction band energy diagram of the first quantum cascade laser (taken from Ref. [168]). Lasing occurs from subband $n = 3$ to subband $n = 2$ in the active region. 25 periods of active and injection regions "recycle" electrons for light emission and ensure high wall-plug efficiencies of up to $\approx 20\%$ [172].

Meanwhile they cover a broad spectral range from 3 μm (100 THz) in the infrared down to 210 μm (1 THz) at THz frequencies [169–171].

It is of great advantage, that crucial properties of QCLs, such as inter quantum well coupling or transition frequencies, are only determined by the electron wave functions. They in turn, can almost be arbitrarily designed by choosing the appropriate material and thickness of each layer. The basic concept is explained in Fig. 5.1. Lasing occurs between the subbands $n = 3$ and $n = 2$. Inversion is favored, if the upper subband has a long life time τ_3 and the lower subband has a short life time τ_2. This is achieved by spatially diagonal laser transitions (see wave functions $n = 3$ and $n = 2$ in Fig. 5.1). The reduced wavefunction overlap causes a small transition matrix element and a long life time τ_3. A quick phonon-assisted depopulation of subband $n = 2$ ensures a short life time τ_2. Therefore the next lower subband $n = 1$ is separated by one LO-phonon energy for efficient depopulation. For optimal electron transport and efficient light emission, the quantum cascade structure is divided into active regions, promoting the actual lasing process, and injector regions, ensuring a fast depopulation of the lower subband and an efficient transport into the upper laser subband of the next period. In contrast to semiconductor lasers, carriers in unipolar QCLs do not recombine after light emission. Thus they can be "recycled" in a long sequence of alternating active and injector regions. The wave guide of a QCL consists in the simplest case of the semiconductor heterostructure itself with cleaved facets at both ends. This Fabry-Perot cavity leads usually to multimode operation. Stable single mode lasing is achieved in distributed feedback lasers (DFB), where the desired wavelength is "Bragg-reflected" by an appropriate modulation of layer thicknesses and thus of the refractive index. The electric current and the operation temperature modify slightly the Bragg condition and allow for a fine tuning of the emitted frequency.

However, QCLs have still not technically matured and extensive research efforts are being undertaken to improve their key properties such as output power and operating temperature.

This requires detailed microscopic insight into the processes occurring during operation. The simplest approach to investigate QCLs analyzes the emitted laser radiation in a spectrometer. This yields basic optical properties like the center frequency or the spectral width of the laser. Deeper insight into the operation mode of a QCL are gained from more sophisticated pump-probe techniques. The first pulse disturbs the active medium and the delayed second pulse probes its temporal behavior [173–175]. The probe pulse experiences a transmission increase, if the preceding pump pulse inverted or bleached the laser transition. A transmission decrease is observed, for pump-induced depletion of the upper laser state. Hence population differences between upper $n = 3$ and lower laser state $n = 2$ are monitored with femtosecond time resolution. Time-independent waveguide losses are neglected in this way and solely the time-dependent active medium is measured.

The separation of pump and probe pulses represents a major difficulty in experiments with QCL devices. Both pulses are resonant to the lasing transition and the the waveguide demands a collinear propagation direction. This prevents a spectral or a spatial separation of both pulses. Eickemeyer *et al.* circumvented this problem by investigating a quantum cascade structure without a resonator [173, 174]. The time dynamics of the active medium remain identical, but a noncollinear pump-probe geometry can be applied. The investigated QC structure was biased only during every second incident pulse. The subtraction of two succeeding pulses yielded exclusively the current-induced transmission change. Eickemeyer *et al.* find prominent oscillations in the pump-probe signal with a period of several hundred femtoseconds. Since the depopulation of the lower laser level occurs within 50 fs, the observed behavior is attributed to electron supply mechanisms from the injector region into the upper laser state. Coherent electron tunneling causes, like in a quantum beat, an alternating transmission change of the probe pulse [161, 174]. Consequently the oscillation frequency is given by the energetic difference between the quantum mechanical energy levels. In agreement with this model, a modified oscillation time is found for other QC samples of different injection barrier thickness.

A separation of pump and probe pulse can also be achieved via different linear polarizations of both incident pulses [175–177]. This method has the disadvantage of a lower signal strength, and it neglects any influence due to birefringence inside the QCL. Choi *et al.* measured in this way the gain depletion of an operating InGaAs/InAlAs QCL [175]. The transmission change as a function of the delay time was reproduced by a three-level rate-equation model for one set of parameters. This set was used for further simulations, which revealed a drastic drop of the upper lasing state life time τ_3. It was not observed as a transmission change, since this is entirely determined by the time constants of emptying the lower subband of the superlattice transport. In this particular experiment no coherent electron transport was found. The investigated QCL emitted at a substantially shorter wavelength of around 5 μm compared to 10 μm in Ref. [173, 174]. Therefore the upper laser state in Refs. [175–177] lies substantially closer to the continuum states, which enhances scattering processes and dephasing. This may have prevented coherent electron oscillations around the injection barrier. A second mechanism suppressing quantum coherences may be inhomogeneous broadening due to, e.g., a distribution of barrier thicknesses in the device.

However, theoretical calculations of the electron transport carried out by other groups identified different regimes of coherent [178] and incoherent [179] electron transport. The pump-probe signals in Ref. [175] display solely the pump-induced transmission change. It remains unclear whether the signal originates from changes in gain or absorption or from changes of the refractive index. This information is obtained only via phase-resolved electrooptic sampling of a broadband pulse transmitted through the laser cavity. In this case, the phase displays the change in the refractive index and the amplitude represents changes in gain or absorption. This relatively new method was first applied by Kroell *et al.* on a 3-THz QCL [24]. Later Parz *et al.* applied the same method to an InGaAs/AlInAs QCL emitting at 25 THz [26]. One short broadband pulse was coupled into the operating device and the transmitted light were phase-resolved detected with electrooptic sampling. The transmitted amplitude increased with applied voltage until the threshold current was reached and optical gain clamping was observed. Furthermore, a slight change in the emitted frequency due to the Stark shift and to elevated temperatures was found. Parts of the light pulse were internally reflected and conducted round trips between both end mirrors. These pulses were stretched in time, because the laser transition amplified only the resonant frequencies.

To learn about the gain recovery of a QCL after strong perturbation, we investigated the device from Ref. [26] in collaboration with W. Parz *et al.* in our experimental setup. The amplified laser-system provided two resonant THz pulses with field amplitudes of several ten kV/cm to disturb the operating QCL. We applied a novel experimental approach combining the phase-resolved detection from Refs. [24, 26] with a femtosecond time resolution of a pump-probe experiment [173, 175]. The pump and the probe pulses of identical direction, wavelength, and polarization are separated by means of their different time of arrival. Changes in gain or absorption and changes in the refractive index are clearly distinguished by the amplitude and phase of the recorded transient. The investigated GaInAs/AlInAs QCL device was held at 100 K and operated both below and above the lasing threshold.

Although it is highly relevant for future applications of QCLs, the exact gain recovery rates remained unclear so far. In principle unipolar QCLs should have much shorter gain recovery times as bipolar semiconductor lasers. The gain dynamics of the latter is predominantly influenced by the recombination of electrons and holes, which happens on a nanosecond time range. A lasing device without this time limitation could, e.g., emit femtosecond pulses. This is of great technological relevance, because sequences of light pulses could contain much more information per time. As a consequence, a drastically higher data transfer rate per lasing device could be realized using the short pulses emitted by QCLs.

5.2 Experimental Results

The investigated QCL consists of 35 periods of $Ga_{0.47}In_{0.53}As$ wells and $Al_{0.48}In_{0.52}As$ barriers grown by MOVPE lattice-matched on an InP substrate. For the measurements the QCL is mounted on the cooling finger of a closed-cycle refrigerator and held at a lattice temperature of 100 K. The QCL has a nominal threshold current for lasing of $I = 300$ mA.

Bandstructure calculations were performed for the present structure using 8-band $k \cdot p$ theory [180–182], including the conduction band nonparabolicity. The spatial density of the corresponding wavefunctions $\mid \psi(x) \mid^2$ is shown in Fig. 5.2. The laser transition, marked by an arrow, occurs between the upper state 2 (red line) and the lower state 1 (blue line). Yellow lines indicate the spatial density of the wave functions in the injector region for electron supply of the upper and electron extraction from the lower state. Electrons tunnel mainly from the injector ground state g, marked in blue, into the upper laser level.

The $I-V$ characteristic of the QCL is presented in Fig. 5.3. Above the operating threshold of 300 mA, the voltage remains nearly constant. This is shown for the dotted blue lines for a current of 400 mA and 650 mA.

The experimental setup is presented in Fig. 5.4. The output of a femtosecond multipass

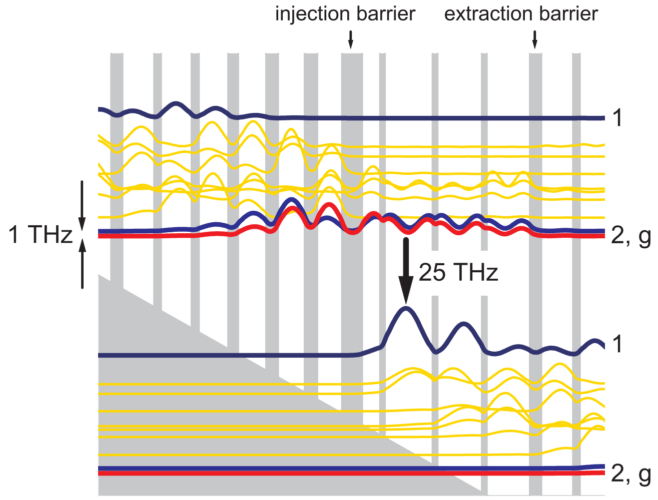

Figure 5.2: Moduli squared of the relevant wavefunctions in the QCL calculated for an applied electric field of 31 kV/cm. The laser transition occurs between states 1 (blue) and 2 (red), g (blue) is the ground state of the injector. The tunnel coupling through the injection barrier causes the splitting of 1 THz. Starting from the extraction barrier, the layer sequence of one period of the QCL is as follows: **1.8**/5/**1.1**/4.8/**1.2**/4.6/**1.6**/4.4/**1.9**/ 4.2/**2**/3.9/**3.2**/2.8/**0.8**/7.5/**0.8**/7/**0.8**/6.8. Thicknesses are in nm, barrier layers are in bold, and doped layers (10^{17} cm^{-3}) are underlined.

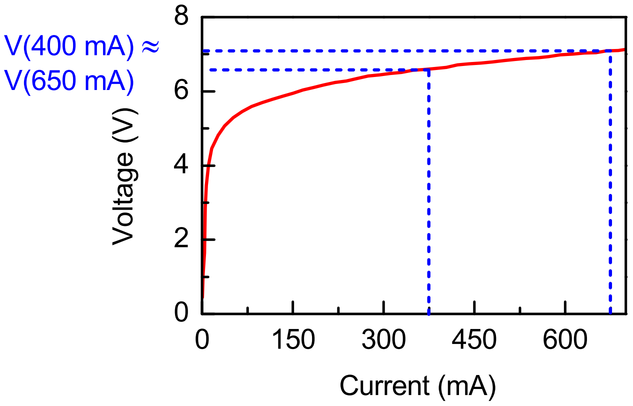

Figure 5.3: $I-V$ characteristic (red line) of the investigated QCL. The blue line represents the optical output power as a function of current. This chart is taken from Ref. [26].

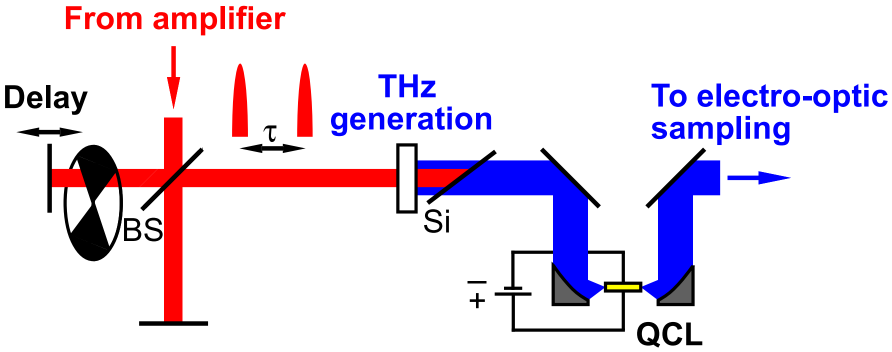

Figure 5.4: Experimental setup for phase-resolved pump-probe measurements on QCLs. A Michelson interferometer generates two pulses with an adjustable delay τ. The pulses at 25 THz pulses are coupled into the QCL at duty cycle operation. The transmitted transients are recorded by electrooptic sampling.

amplifier is split into two pulses with an adjustable delay τ. These pulses are sent onto a GaSe crystal for difference frequency generation [12, 15] of two phase-locked pulses at 25 THz. Both pulses are resonant to the lasing transition of the QCL. They are coupled into the QCL and the transmitted light is detected with electrooptic sampling. To prevent long-term heating effects, the QCL is operated at a 50% duty cycle. This means that current flows through the device several microseconds before and after the incident light pulse. It ensures on the one hand steady state conditions when the pulse arrives, and it limits on the other hand the dissipated energy from the electrical current.

It was a severe experimental challenge to send the incident THz pulses, with a diameter of roughly 20 μm at the focal point, into the QCL laser ridges, which have a cross-sectional area of 5 μm$\times$5 μm. The focal position of the invisible THz pulses was carefully determined with pinholes and marked with a visible helium-neon laser beam. The whole procedure inside the vacuum chamber was monitored with a high resolution camera standing on the transparent cover plate. In this way, we succeeded in coupling a significant fraction of the THz pulses into the laser ridges. Nevertheless, substantial parts of the THz pulses which did not propagate through the QCL reached the electro-optical detector as well (black transients in Fig. 5.5). The large refractive index of $n \approx 3$ of the QCL device delayed the transmitted light by roughly 3.5 ps. Therefore both transients could be distinguished due to their different arrival times. We measured the transmitted pulses both with and without electrical current flowing through the device. Subtracting both transients yields the current-induced effect on the transients. This method ensured on the one hand the functionality of the QCL and on the other hand, that the transmitted light indeed propagated through the biased part of the QCL structure. To record the pump-induced changes as well, the pump pulse was optically chopped at a quarter of the laser repetition rate, i.e., at 250 Hz.

Accordingly four different situations shown in Fig. 5.5 were recorded at each delay time. The transmitted transients are depicted red for a biased device with $I = 650$ mA and blue for an unbiased QCL device. Fig. 5.5 (a) shows the recorded transient without the preceding pump pulse and an unbiased QCL, (b) shows the transient without the pump pulse and a biased QCL, (c) shows the transient with the preceding pump pulse and an unbiased QCL, and (d) shows the transients with the pump pulse and a biased QCL. The black lines are parts of the incident

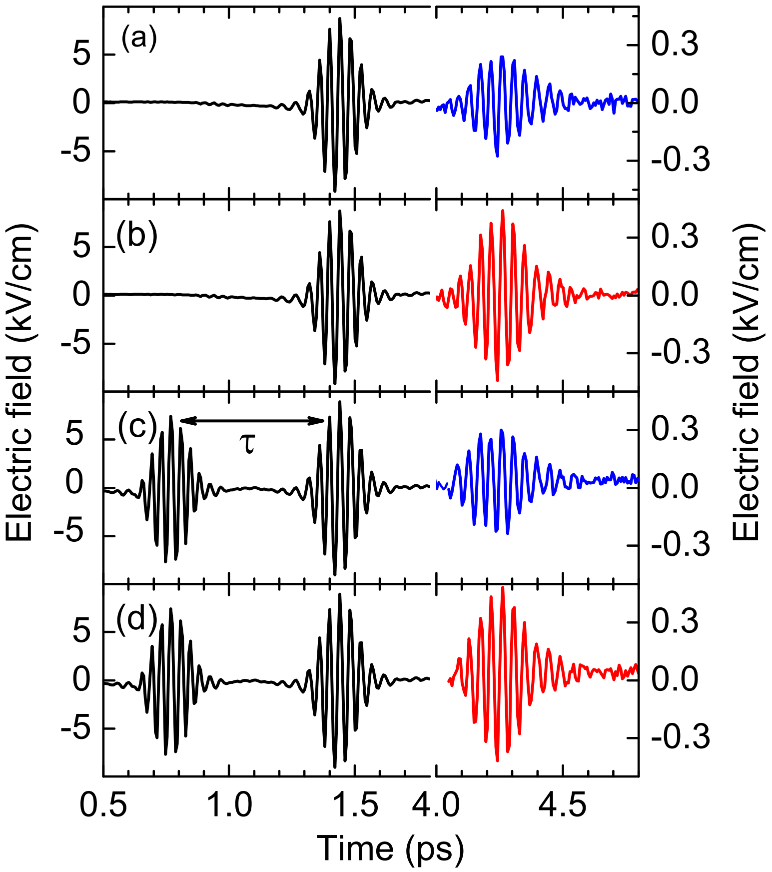

Figure 5.5: Electric field transients detected in the pump-probe experiments. The signals detected at $t < 1.8$ ps did not interact with the QCL and resemble the incident pulses. Transmitted light through the cavity (right part, $t > 4$ ps) is shown as a red line if the QCL was biased ($I = 650$ mA), and as a blue line for an unbiased device. (a) and (b) are the transients without and (c) and (d) with a preceding pump pulse.

pulses, which are not coupled into, but passed by the QCL. They arrive at the detector crystal at times $t < 1.8$ ps, while the pulses transmitted through the QCL are detected at times $t > 4$ ps.

The amplitude and phase, but not the shape, of the transmitted probe pulse depends on the current I and on the pump-probe delay τ. Optical gain within the biased QCL enhances the electric field [Figs. 5.5 (b) and (d)] compared to the transmitted field through the unbiased device [Figs. 5.5 (a) and (c)]. To reveal the gain dynamics inside the laser cavity, the transmitted electric fields with and without a preceding pump pulse are compared. An example for a current of $I = 30$ mA and a delay time of 0.7 ps is shown in Fig. 5.6 (a). The red transient with a preceding pump pulse has a significantly larger amplitude than the black transient without a preceding pump pulse. The indicated phase shift is better recognized in the 2D plot in Fig. 5.6 (b). The electric field versus the real time is shown vertically and the delay time horizontally. At time delay zero the probe transient experiences a pump-induced delay of several femtoseconds.

In Fig. 5.7 (a) the pump-induced transmission changes are shown for different injection currents as a function of delay time τ. The energy of the probe pulse ($\int E_{\mathrm{pr}}(t)^2\,dt$) is normalized to the energy of the pump pulse ($\int E_{\mathrm{pu}}(t)^2\,dt$). For electric currents up to 150 mA the transmission

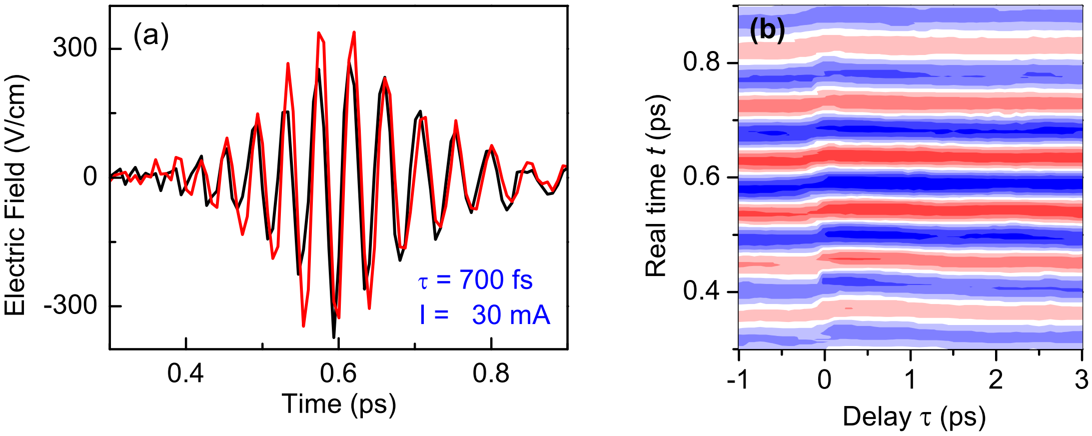

Figure 5.6: (a) Transients through a weakly biased QCL with $I = 30$ mA. The pulse preceded by a pump pulse (red line) exhibits a significantly larger amplitude than the pulse without the preceding pump pulse (black line). (b) A pump-induced phase shift is found at a delay time $\tau = 0$.

exhibits a strong increase of 0.5%, which decays with time constants of 3.5 ps at $I = 0$ and 3 ps at $I = 150$ mA. For I above threshold a decrease of transmission with a nonexponential decay is found [see Fig. 5.7 (c)]. For all currents, the measured kinetics displays an oscillatory component along the delay time axis. The Fourier transform of the data for non-zero injection currents [see Fig. 5.7 (b)] shows a prominent peak at a frequency of 0.8 THz. The pump-induced phase shift of the probe pulse as a function of delay time is shown in Fig. 5.7 (d). For all currents a sharp rise at $\tau = 0$ and a subsequent decay with a time constant of 3 ps is observed. Positive values of the phase shift indicate an increase of the refractive index of the QCL. The phase data do not show the oscillatory component.

5.3 Discussion

The laser transition of the QCL strongly absorbs the pump pulse below threshold [183]. The pump pulse populates the empty upper laser state and saturates the laser transition. The succeeding probe pulse experiences less absorption, which results in the positive transmission change in Fig. 5.7 (a). This bleaching of the lasing transition is observed only below threshold for $I = 0$ (black symbols) and $I = 150$ mA (red symbols). The recovery from this perturbation requires the depopulation of the upper subband and the repopulation of the lower subband. Since LO-phonon-scattering from the injector level into the lower laser state is significantly reduced at 100 K, the absorption recovery is primarily determined by the electron lifetime in the upper subband. Electron heating and cooling processes within the manifold of states in the injector regions may influence the population statistics of both subbands to the same degree. Within 10 ps the transmission change decays nearly to zero and the initial degree of inversion is restored. We therefore conclude an electron lifetime of 3 ps in the upper subband.

Above threshold [Fig. 5.7 (a), (c) for 400 and 650 mA] an external electron supply injects carriers into the upper laser state of the active region and keeps the lasing transition inverted.

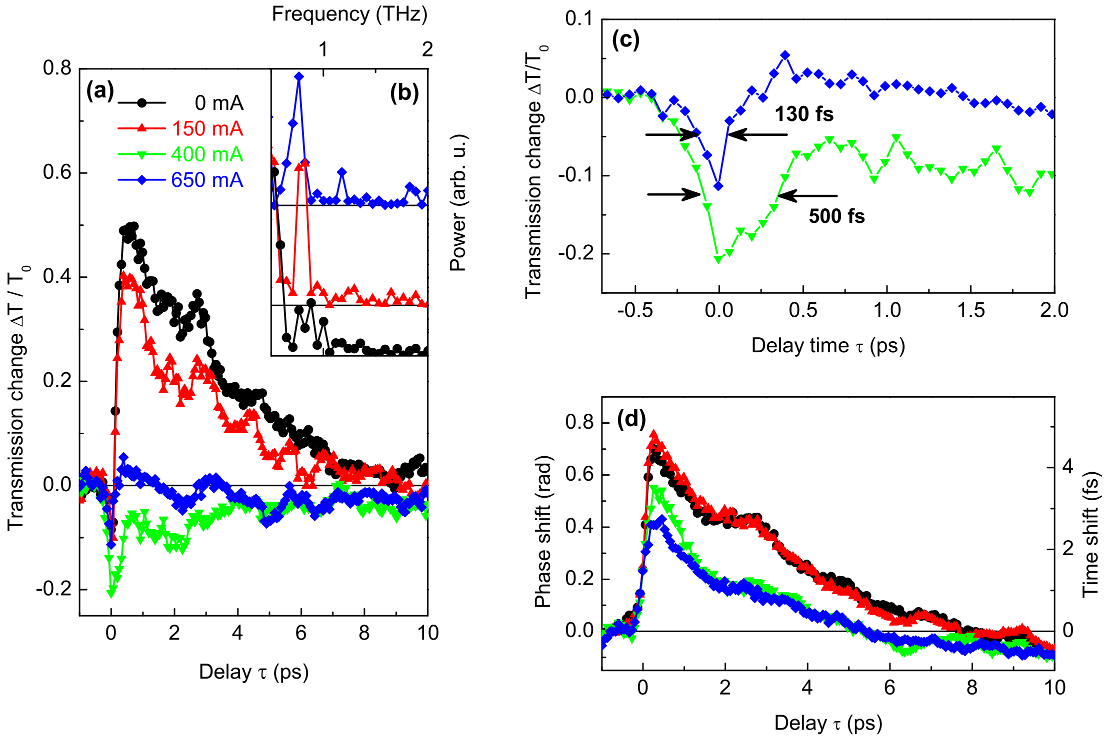

Figure 5.7: (a) Pump-induced change of the transmission as a function of pump-probe delay τ for different currents below and above threshold. (b) Fourier transform of the transmission changes shown in (a). (c) The enlarged curves for the gain recovery. (d) Pump-induced phase shift of the transmitted pulse as a function of pump-probe delay τ, due to electron heating.

The incident pump pulse saturates the gain and depletes the quasi-stationary population inversion. Accordingly, the subsequent probe pulse excites the lasing transition, which results in the negative transmission change. Both transients display a very fast recovery of the transmitted pulse energy within the first picosecond. This time is required to restore the initial inversion of the laser transition, i.e., for gain recovery. Since depopulation of the lower subband is essentially current independent, it resembles the timescale of electron proliferation from the injector through the injection barrier into the active part of the QCL structure. While the gain recovers with a time constant of 500 fs for $I = 400$ [green symbols in Fig. 5.7 (c)], an even faster recovery time of 130 fs is found for $I = 650$ mA (blue symbols). The recovery is followed in both cases by pronounced oscillations at later delay times. The incomplete gain recovery after 10 ps is attributed to additional pump-induced electron heating in the lower laser subband.

In contrast to the transmission change, the phase shift shown in Fig. 5.7 (d) has the same sign for all currents. That points to an off-resonant pump-induced change of the refractive index of the QCL. The elevated electron temperature increases the refractive index and delays the probe pulse. This explains the similar time constants at all currents above and below threshold as well as the missing oscillatory component in the phase data.

The frequency of the oscillations occurring during gain recovery is depicted in Fig. 5.7 (b). A prominent peak is found at a frequency of 0.8 THz. The corresponding period of 1.25 ps is much shorter than the cavity round trip time of 11 ps. The oscillations point to a coherent super-

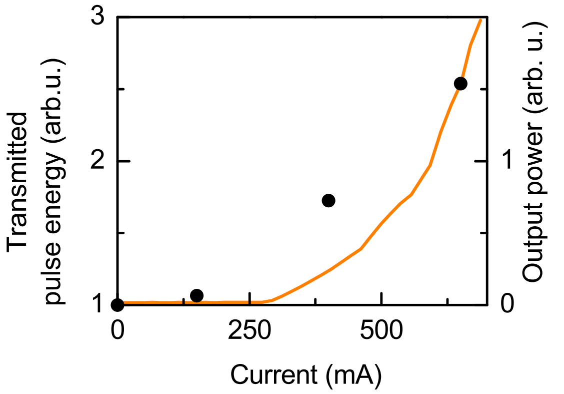

Figure 5.8: Optical gain as a function of current for strong incident electric fields (black symbols). Solid line, QCL output as a function of current (right scale).

position of states on both sides of the injection barrier. After femtosecond gain depletion, this superposition leads to the propagation of a nonstationary electron wavepacket back and forth between injector and active region. Like a quantum beat, this causes gain oscillations, which are read out by the probe pulse. The oscillations were observed already in previous experiments on QCLs [161, 174] and explained theoretically in Ref. [178]. It was shown for GaAs/AlGaAs QC structures, that the coupling between states on both sides of the barrier determines their energy splitting and thus the oscillation frequency [161, 174].

The $k \cdot p$ calculation, depicted in Fig. 5.2, predicts a difference of 1 THz between both energy levels very close to the observed 0.8 THz. In contrast to the tunneling processes discussed in the previous chapter, this tunneling process experiences nearly no decoherence. The electron wave packet tunnels reversibly back and forth until the probe pulse destroys the coherence and measures the probability density of the wave function. The oscillation frequency is given by the energy difference between injector and upper laser state. Since the applied voltage is nearly identical for 400 and 650 mA (see Fig. 5.3), the oscillations are expected to be essentially current-independent. This is confirmed by the observed peak at 0.8 THz at different injection currents. The occurrence of weak oscillations for zero bias points to a certain degree of subband alignment between injector and active region even under such conditions.

The difference between the linear measurement of the gain medium in Ref. [26] and our nonlinear measurement is shown in Fig. 5.8. The orange line demonstrates the optical output power from the QCL as a function of the injected electrical current. While negligible output power is found below threshold current (300 mA), it increases steeply above threshold. The enhanced stimulated emission at high currents is not necessarily accompanied by a higher inversion ratio of the laser transition. Fig. 2 of Ref. [26] demonstrates this phenomenon called gain clamping. The transmission increase of one single THz pulse, monitoring the inversion ratio, remains constant above the current threshold. Nonlinear measurements with much stronger THz pulses demonstrate a qualitatively different behavior. The transmitted pump pulse energy, proportional to $\int E(t)^2 dt$ and normalized to the value without current, is shown as black dots in Fig. 5.8. Below threshold the same behavior as in Ref. [26] is observed. The inversion of the lasing transition increases only slightly with the transmitted pulse energy. Above threshold, no gain clamping, but an increase of the transmitted pulse energy is observed.

The weak pulses of Ref. [26] probed the gain of the lasing transition without changing the inversion ratio substantially. But in our experiment the pulse energies are several orders of magnitudes higher. Even the slope of the THz pulses depletes the upper laser state. Fig. 5.7 (a) showed on the other hand that a current of 650 mA repopulates the upper laser state within 130 fs. Therefore, the 200 fs long THz pulses immediately stimulate the electrons entering the active region for emission and the transmitted pulse energy rises with the electrical current.

6 Collinear Two-Dimensional Terahertz Spectroscopy

Two-dimensional (2D) spectroscopy in the femtosecond time domain has developed into an important method to unravel the dynamics of electronic and/or vibrational excitations of matter and, in particular, to determine the couplings between different excitations [184–191]. 2D spectroscopy in the visible and ultraviolet has provided insight into solvation dynamics of individual molecular chromophores [192], excitonic couplings and excitation transfer in molecular aggregates [193], nanotubes [194] and macromolecular light harvesting systems [195–197], and into the nonlinear response of excitons in bulk and low-dimensional semiconductors [198–200]. In molecular systems, vibrational dynamics and interactions, chemical processes, and, to some extent, structure and structural fluctuations have been mapped by 2D spectroscopy in the infrared wavelength range between 2.5 and 7 μm [185, 186, 188, 190, 191]. Recent works extended the multidimensional concept to three dimensions [201] or applied a collinear beam geometry in combination with phase cycling techniques to select one distinguished nonlinear signal [202].

In this chapter the extension of 2D spectroscopy to THz frequencies is presented and applied to investigate different semiconductor multiple quantum well samples. A collinear beam geometry and a direct phase-resolved detection link our method to nuclear magnetic resonance experiments, where the multidimensional concept was originally developed [203].

6.1 2D Spectroscopy at Infrared Frequencies

Two-dimensional spectroscopy refers to two frequency axes of a recorded spectrum. The 2D signal is measured either in the frequency-domain or in the time-domain. In literature one finds two methods of optical 2D spectroscopy: the Double resonance method [185], i.e., 2D pump-

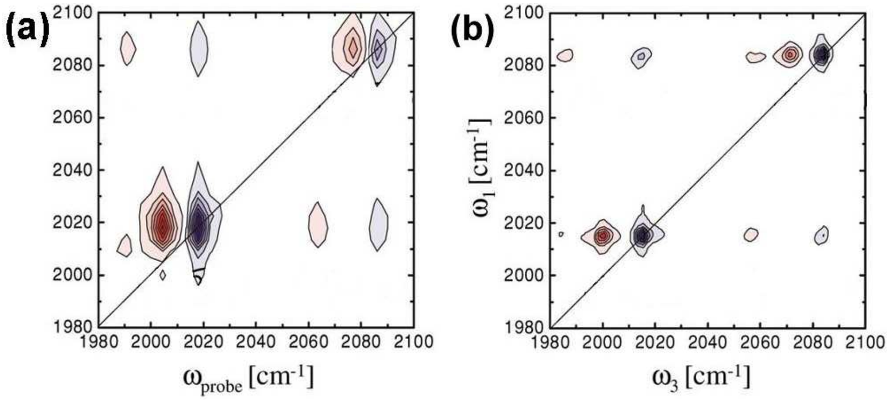

Figure 6.1: Comparison of the 2D correlation spectrum obtained (a) with the 2D pump-probe method and (b) with the 2D photon echo method.

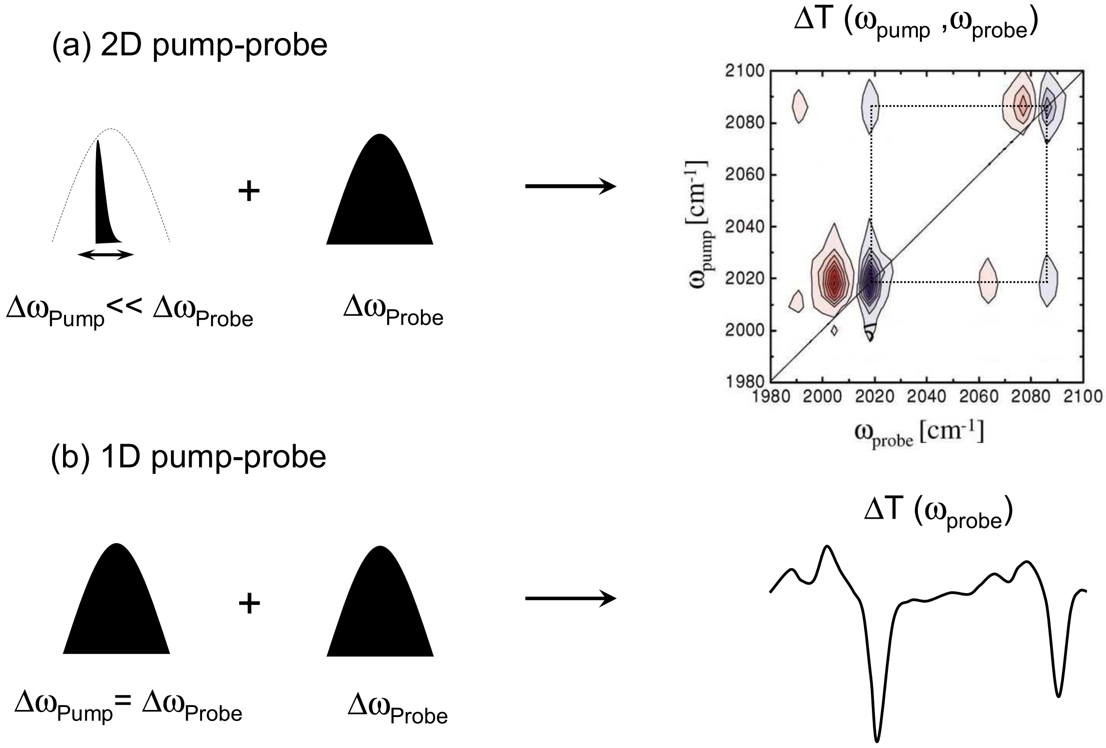

Figure 6.2: (a) The system under investigation is pumped with a narrow-band pulse ($\omega_{\text{pump}} \ll \omega_{\text{probe}}$) and probed with a broad-band pulse ω_{probe}. Varying ω_{pump} yields a 2D spectrum with fundamental transition along the diagonal cross-peak indicating energetic transfer off the diagonal. (b) A broad pump pulse ($\omega_{\text{pump}} = \omega_{\text{probe}}$), used in conventional pump-probe experiments, integrates the spectral intensity along the ω_{pump} axis and yields thus a one-dimensional transmission spectrum $\Delta T(\omega_{\text{probe}})$.

probe method to measure light only in the frequency-domain and the 2D photon echo method, i.e., measuring light in the time and in the frequency-domain. Cervetto *et al.* compared the 2D spectra of the chemical compound $Rh(CO)_2C_5H_7O_2$ (RDC), which were obtained with both methods [204]. Figs. 6.1 (a) and (b) demonstrate that the 2D pump-probe spectrum and the 2D photon echo spectrum yield equivalent results.

The 2D pump-probe method will be explained first, because it demonstrates the advantages of 2D spectroscopy in a direct and illustrative way.

2D Pump-Probe or Double Resonance Spectroscopy

2D spectroscopy reveals primarily couplings between energy levels of a sample. This is accomplished in the 2D pump-probe method in very direct way. A narrow-band pump pulse excites the sample at a certain—excitation—frequency (ω_{pump}) and a subsequent pulse with a broad bandwidth probes the transitions within the sample. Thus for each excitation frequency a transmission spectrum as a function of the detection frequency (ω_{probe}) is obtained, which results in a 2D correlation spectrum. Without energy transfer, excitation and detection frequency remain equal and the corresponding signal occurs on the diagonal of the 2D spectrum. The fundamental transitions appear in Fig. 6.2 (a) at $\omega_{\text{pump}} = \omega_{\text{probe}} = 2020\ \text{cm}^{-1}$ and $\omega_{\text{pump}} = \omega_{\text{probe}} = 2090\ \text{cm}^{-1}$.

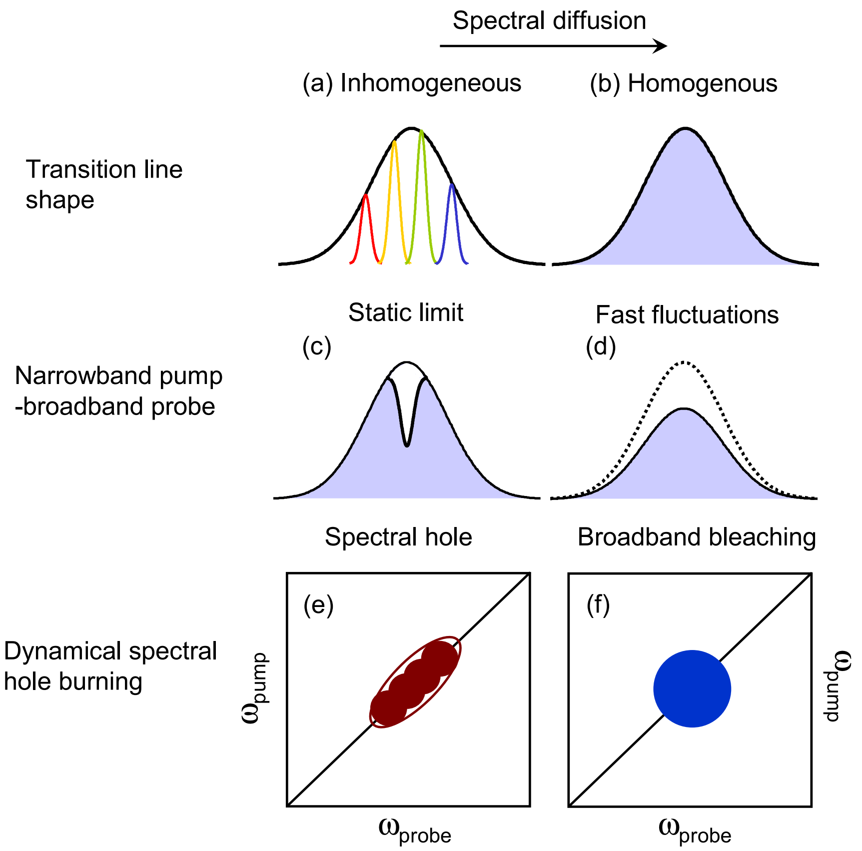

Figure 6.3: (a) Inhomogeneous line shape with various individual transition lines (in color), (b) which are blurred out in homogeneously broadened lines. (c) Spectral hole in inhomogeneous transitions and (d) bleaching of the complete homogeneous line. (e) Inhomogeneous line widths appear elongated in 2D spectra and (f) homogeneous line widths circular on the main diagonal.

If energy is transferred between both transitions, the signal occurs at an excitation frequency of $\omega_{\text{pump}} = 2020\ \text{cm}^{-1}$ and an detection frequency of $\omega_{\text{probe}} = 2090\ \text{cm}^{-1}$, or vice versa. Thus differences between excitation and detection frequency are caused by energetic couplings and appear as off-diagonal cross peaks in the 2D spectrum. They form together with the fundamental peaks the edges of an imaginary square, denoted in Fig. 6.2 (a). Further excited state absorptions (shown red) appear off the diagonal as well, but not on the crossing point of the fundamental frequencies [204]. Since the bandwidth of the pump pulse determines the spectral resolution along ω_{pump}, it is ideally very narrow but widely tunable.

A pump pulse of the identical spectral width as the probe pulse integrates the 2D correlation spectrum along the excitation frequency axis ω_{pump} [see Fig. 6.2 (b)]. Information about energetic couplings is lost and a conventional 1D pump-probe spectrum is obtained.

Apart from monitoring energetic couplings, 2D spectra can distinguish between homogeneous and inhomogeneous line shapes. This gives evidence about line broadening mechanisms within the sample. Usually an absorption line consists of many individual narrow-band transitions [Fig. 6.3 (a)]. One example are periodic quantum wells with irregular layer thicknesses, which affect each transition line individually. Each quantum well exhibits a slightly different transition frequency and the absorption line appears inhomogeneous. Broadening mechanisms affecting each transition, e.g., of radiating or absorbing atoms, ions or molecules, in the same way wash out the individual lines and cause homogeneous broadening [Fig. 6.3 (b)]. One example is the natural line width, due to Heisenberg's uncertainty relation. However, the appearance of a line shape depends also on the observed time scale. We consider Doppler broadening of optical transitions in an atomic gas: on short time scales, i.e., within the collision time, each excited atom moves into one distinct direction with respect to the detector. Depending on this velocity component, each individual atomic transition experiences a different Doppler frequency shift and an inhomogeneously broadened line shape is measured. On long times scales, each atom experiences the identical average of collisions and the line shape appears homogenously broadened.

Pump pulses with a narrow bandwidth bleach only a part of the inhomogeneously broadened ensemble [205, 206]. The resulting spectral hole in the absorption spectrum [see Fig. 6.3 (c)] is subsequently probed by a pulse of a broad brandwidth. Varying the frequency of the narrow-band pump pulse, shifts the spectral hole over the entire inhomogeneously broadened transition. This dynamical hole burning [204] appears as an elongated spectral peak along the diagonal in the 2D correlation spectrum [Fig. 6.3 (e)]. Spectral diffusion will fade away the spectral hole towards a homogeneously broadened transition. As a consequence the pump pulse bleaches the entire line as indicated in Fig. 6.3 (d). Accordingly, the spectral peak of a homogeneously broadened transitions appears as a circular spot on the diagonal of the 2D spectrum [Fig. 6.3 (f)].

Another effect to distinguish an inhomogeneous from a homogeneous transition is the photon echo, which is induced by three pulses. If the transition is inhomogeneously broadened, the photon echo is emitted a certain delay after the third pulse. The exact time of emission is determined by the delay between the first and the second pulse. For homogeneous line shapes the photon echo is emitted immediately after the third pulse.

Noncollinear 2D Photon Echo Experiments

The photon echo, as well as the pump-probe and the third harmonic signals, is part of a $\chi^{(3)}$ four-wave mixing process. The induced polarization $P^{(3)}$ by the three incident pulses $E_1(t-\tau)$, $E_2(t-T)$, and $E_3(t)$ emits the photon echo [207].

$$P^{(3)}(\mathbf{r},t) = \iiint_0^{\infty} \chi^{(3)} E_1(\mathbf{r},t-\tau) E_2(\mathbf{r},t-T) E_3(\mathbf{r},t)\, d\tau dT dt \tag{6.1}$$

A 2D Fourier transformation of this photon echo represents another way to correlate excitation ω_τ and detection frequency ω_t:

$$S_{2D}(\omega_\tau,\omega_t,T) \equiv \iint_{-\infty}^{\infty} P^{(3)}(\omega_\tau,\omega_t,T) e^{i\omega_\tau \tau} e^{i\omega_t t}\, d\tau dt \tag{6.2}$$

The specific reason is discussed in Section 6.5. In a first step, we concentrate on the applied noncollinear beam geometry and the general meaning of the second time axis in 2D experiments.

A commonly used experimental setup for 2D photon echo experiments is shown schematically in Fig. 6.4. Three incident femtosecond pulses of the same center frequency with the wave vectors $\mathbf{k_1}$, $\mathbf{k_2}$, and $\mathbf{k_3}$ overlap on the sample and induce a nonlinear polarization. Various four-wave mixing signals including the photon echoes of interest are emitted. The characteristic direction is given by the sum of the three participating $\mathbf{k}$ vectors. A fourth pulse is superposed

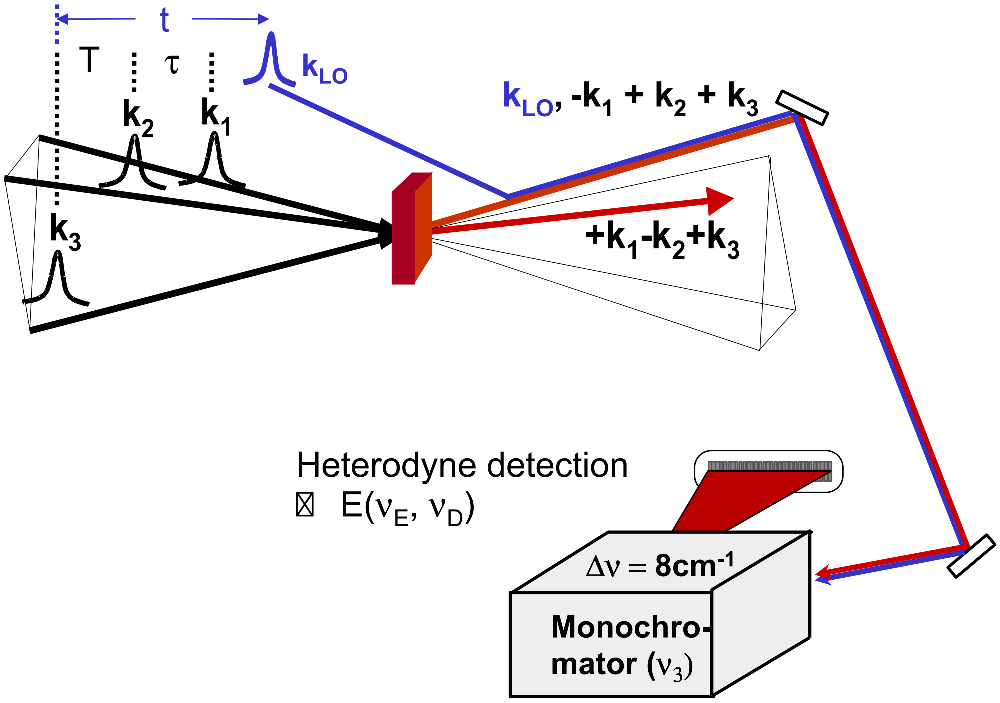

Figure 6.4: 2D photon echo experiments employ mostly three overlapping noncollinear pulses with wavevectors $\mathbf{k_1}$, $\mathbf{k_2}$, and $\mathbf{k_3}$. Photon echoes are emitted into a linear combination and superposed by a local oscillator for heterodyne detection.

on the weak photon echo as a local oscillator. Heterodyne detection using a monochromator and an array of photodiodes measures the combined spectra of both pulses in the frequency domain ω_t. Scanning additionally the excitation time τ and using spectral interferometry yields the electric field $E(\omega_t, \omega_\tau)$ as a function of two frequencies.

The four-wave mixing process is commonly considered to take place in direct space. In the following we will point out the concomitant four-wave mixing process in time. As one consequence, 2D photon echo experiments can be performed using collinearly incident pulses.

6.2 N-Wave Mixing in Space and in Time

An illustrative explanation perceives four-wave mixing as diffraction from a transient grating inside the sample. A snapshot of two noncollinear pulses, approximated as plane waves with the wave vectors $\mathbf{k_1}$ and $\mathbf{k_2}$, shows the spatial interference in Fig. 6.5 (a). The cut along the coordinate $z = 0$ in Fig. 6.5 (b) demonstrates regions of high and of low intensity along the orthogonal coordinate x. A sample in place with a transition resonant to the optical frequency forms a population grating with alternating excited and unexcited regions. A third pulse is diffracted from this spatial grating into various directions. Since each pulse may interact arbitrarily often with the sample, all N-wave mixing signals can be generated with only two pulses. The N-wave mixing process in space is shown schematically for two pulses in Fig. 6.6 (a). The spatial position of the detector determines, which nonlinear signal is measured, e.g., the photon echo marked as a red arrow. The intensity and the phase of the signal are measured as a function

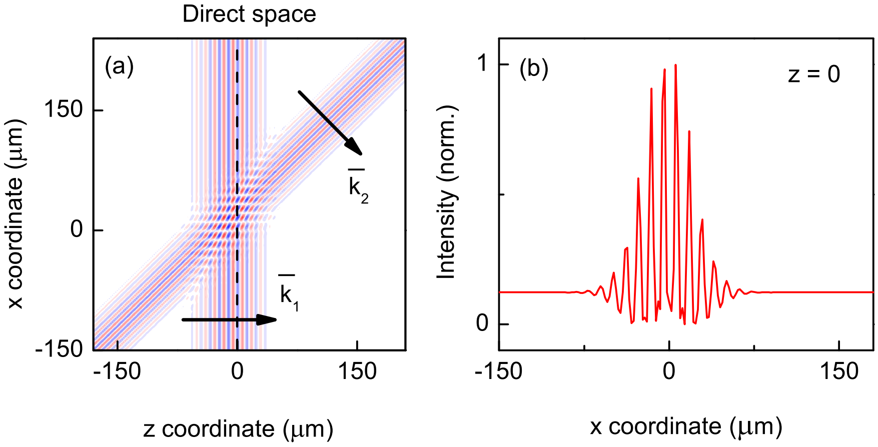

Figure 6.5: (a) Snapshot of two noncollinear pulses with $\mathbf{k_1}$ and $\mathbf{k_2}$ in two space dimensions. (b) Cut through (a) for $z = 0$. Alternating high and low excitation densities create a spatial transient grating within the sample.

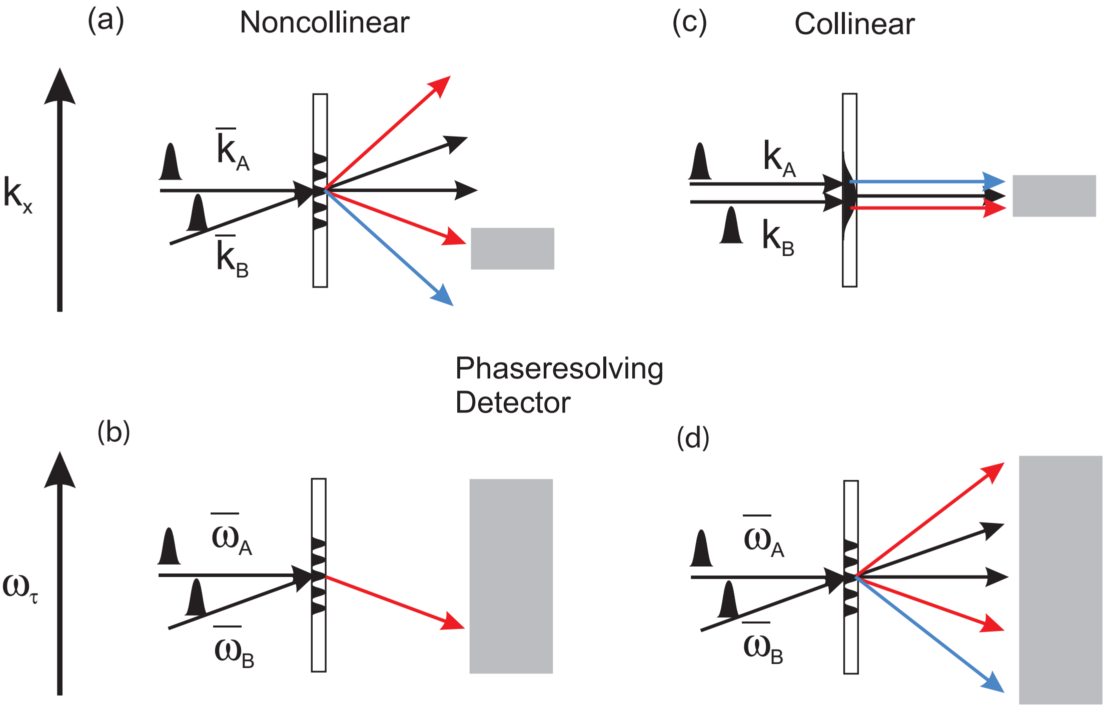

Figure 6.6: N-wave mixing in space for (a) noncollinear and (c) collinear incident pulses. (b) Additional N-wave mixing in time diffracts only one detected signal for noncollinear pulses, and (d) all detected signals for collinear incident pulses.

of the delay between both incident pulses.

Though previously not considered, two time delayed pulses generate a transient population grating in time as well. The situation is completely analogous to that shown in Fig. 6.5. Fig. 6.7 (a) displays the electric field of two pulses separated by the delay τ as measured with

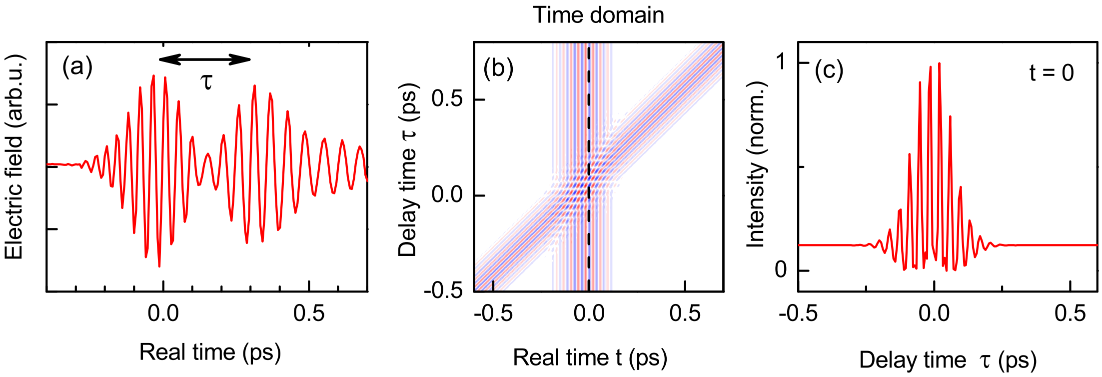

Figure 6.7: (a) Electric field of two collinear pulses as a function of the real time t. (b) Two-dimensional plot of the electric field as a function of the real time t and the delay time τ. (b) A variable delay between the two pulses forms a transient population grating along the τ dimension.

electrooptic sampling. The delay is changed after each electrooptic scan and the transient is recorded again. This yields the electric field as a function of the real time t and the delay time τ [Fig. 6.7 (b)]. The real time t resembles the detection time, and the delay time τ resembles the excitation time in terms of the previous section. The exact relations between the different time definitions are explained in Section 6.9. The cut for $t = 0$ in Fig. 6.7 (c) demonstrates the identical transient grating in time as in space.

As a consequence, the photon echo on the detector experiences a spectral diffraction into a certain excitation frequency ω_τ [Fig. 6.6 (b)]. This is the reason for the appearance of the photon echo at an excitation frequency approximatively equal to the detection frequency in conventional 2D photon echo experiments [see Fig. 6.1 (c)]. Fig. 6.6 (c) shows that two incident collinear pulses do not generate any spatial grating. All nonlinear-orders of the N-wave mixing signal are emitted into one direction onto the detector. However, the pulse delay still generates a temporal grating, from which the nonlinear signal is diffracted into characteristic ω_τ components.

One positive side effect of this geometry is the increased interaction length between sample and incident pulses. Higher order signals are caused by several pulse interactions of the same pulse. Accordingly, they are more sensitive to the pulse delay and have a higher ω_τ component. Hence a collinear beam geometry measures the complete nonlinear signal and still distinguishes between signals of different order. In general N-wave mixing takes place in space and in time. However, for collinear incident pulses, N-wave mixing in space is reduced onto one dimension and the diffraction occurs entirely in the time domain. In analogy to $\mathbf{k}$ vectors in space, frequency vectors in time are introduced in the following. Therefore, a simplified experimental situation without any sample is considered.

Frequency Vectors

Fig. 6.8 (a) displays the electric field of two pulses separated by the delay τ. One pulse, A, is kept constant in t, and the other pulse B, is delayed after each scan. The 2D Fourier transform shown in Fig. 6.8 (b) exhibits two spectral peaks, one corresponding to each pulse. The frequency components ω_t and ω_τ of each pulse can be described with the frequency vectors ω_A and ω_B. The electric field of pulse A does not oscillate along the delay time τ and

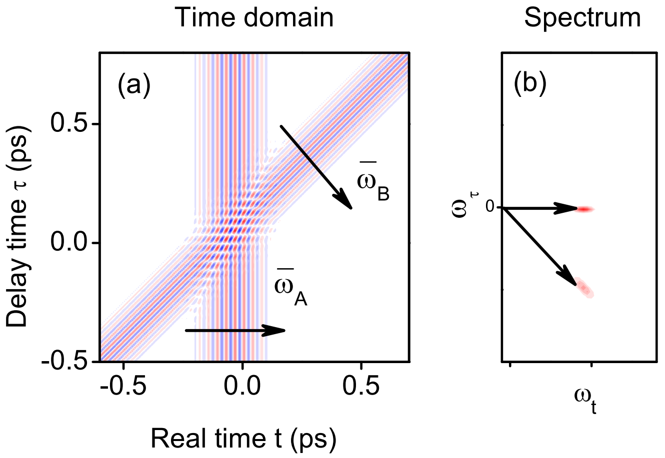

Figure 6.8: (a) Electric field as a function of t and τ and corresponding frequency vectors in the time and (c) in the frequency domain.

consequently, $\omega_\tau = 0$. The real time frequency ω_t on the other hand, amounts constantly to the center frequency ω_0. Thus the spectral peak of pulse A is found in the 2D spectrum at $\omega_A = (\omega_\tau = 0, \omega_t = \omega_0)$. The electric field of pulse B obviously oscillates along τ, so that pulse B appears at $\omega_B = (-\omega_0, \omega_0)$.

The meaning of the delay time frequency axis is illustrated in Fig. 6.9. It shows (a) two simulated pulses separated by a delay time of 300 fs. The corresponding spectrum along the real time frequency axis ω_t is shown in Fig. 6.9 (b). The phase difference between both pulses cause spectral interference resulting in spectral fringes depending on the delay τ. These fringes are shifted for a different τ steadily through the absolute value spectrum. This behavior is demonstrated for delay times between 300 fs and 360 fs in Figs. 6.9 (c) – (f). The black spot represents exemplarily the spectral density of the double pulse spectrum at the frequency $\omega_t =$ 25 THz. The spectral density oscillates between 0 for (a) 300 fs and (f) 340 fs and 1 for (d) 320 fs and (h) 360 fs. The delay time frequency axis represents this oscillation of the spectral density with respect to the delay time.

Frequency vectors ω_A and ω_B are completely analogous to the **k** vectors $\mathbf{k_A}$ and $\mathbf{k_B}$. This can be shown also mathematically. The incident electric field as a function of the real time t and the delay time τ writes [208]:

$$\mathbf{E_A}(t,\tau) = \mathbf{E_{A,0}} \exp\{i[\mathbf{k_A}\mathbf{r} - \omega_0(t-\tau)]\} + c.c. \tag{6.3}$$

Using the frequency vector $\omega_A = (\omega_\tau, \omega_t)$ and the time vector $\mathbf{t'} = (\tau, t)$ we obtain for the electric field

$$\mathbf{E_A}(\mathbf{r},\mathbf{t'}) = \mathbf{E_{A,0}} e^{i(\mathbf{k_A}\mathbf{r} - \omega_A \mathbf{t'})} + c.c. \tag{6.4}$$

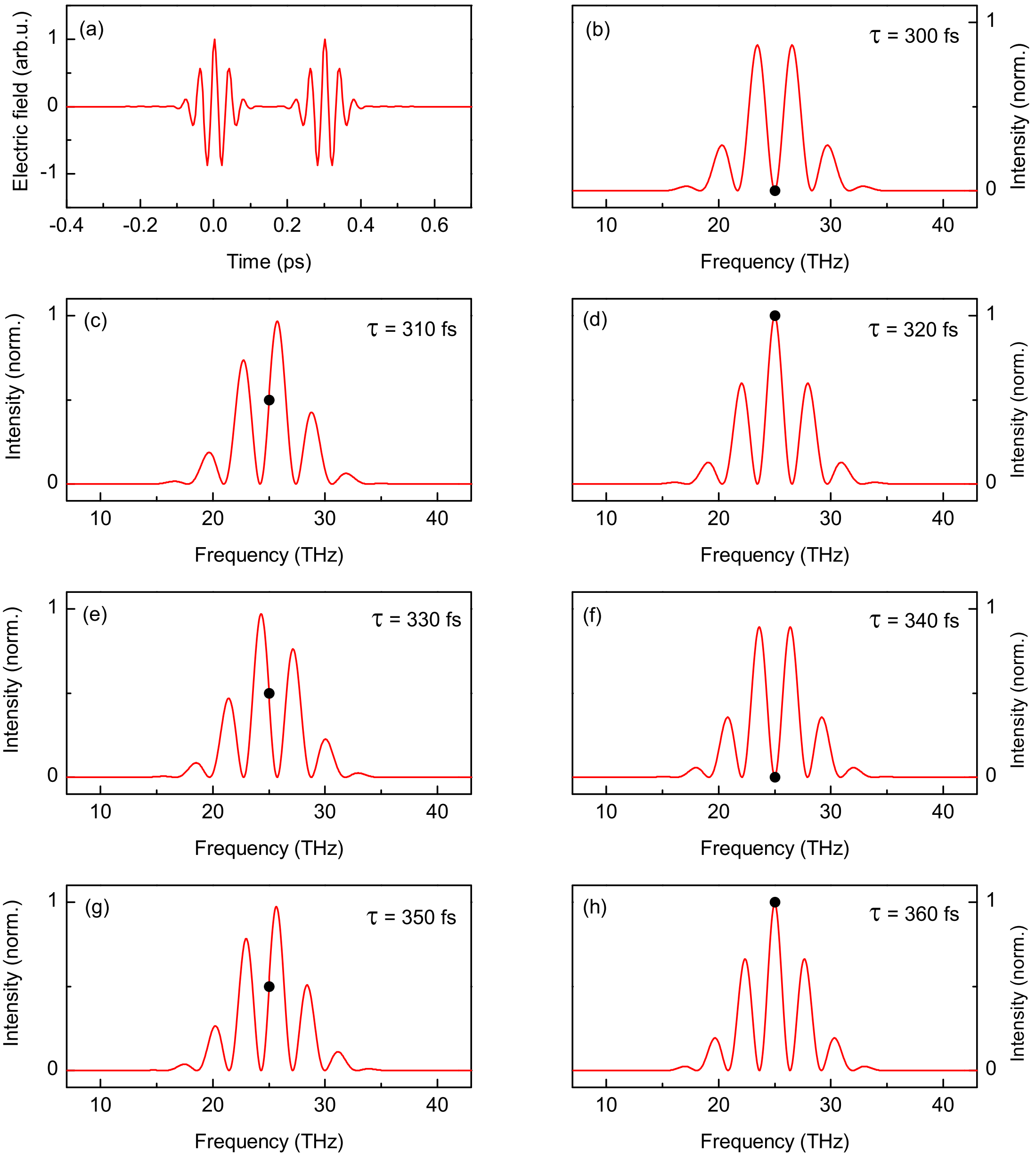

Figure 6.9: (a) Two pulses separated by the delay time $\tau = 300$ fs in the time domain and (b) the frequency domain. The shifting of the spectral fringes can be recognized in the double pulse spectra for (b) 300 fs, (c) 310 fs, (d) 320 fs, (e) 330 fs, (f) 340 fs, (g) 350 fs, and (h) 360 fs. The spectral density at 25 THz (black symbol) oscillates with the delay time frequency ω_τ.

Accordingly, the degenerate four-wave mixing signal induced by the pulses $\mathbf{E_A}(\mathbf{r},\mathbf{t'})$ and $\mathbf{E_B}(\mathbf{r},\mathbf{t'})$ is given by:

$$\sum_{j=0}^{3}\mathbf{E_A}^{j}\mathbf{E_B}^{3-j} \sim \exp\left[i(3\mathbf{k_A}\mathbf{r}-3\omega_A\mathbf{t'})\right] \tag{6.5}$$

$$+ \exp\left[i(3\mathbf{k_B}\mathbf{r}-3\omega_B\mathbf{t})\right] \tag{6.6}$$

$$+ \exp\left\{i\left[(2\mathbf{k_A}+\mathbf{k_B})\mathbf{r}-(2\omega_A+\omega_B)\mathbf{t'}\right]\right\} \tag{6.7}$$

$$+ \exp\left\{i\left[(\mathbf{k_A}+2\mathbf{k_B})\mathbf{r}-(\omega_A+2\omega_B)\mathbf{t'}\right]\right\} \tag{6.8}$$

$$+ \exp\left\{i\left[(\mathbf{k_A}-\mathbf{k_A}+\mathbf{k_B})\mathbf{r}-(\omega_A-\omega_A+\omega_B)\mathbf{t'}\right]\right\} \tag{6.9}$$

$$+ \exp\left\{i\left[(\mathbf{k_B}-\mathbf{k_B}+\mathbf{k_A})\mathbf{r}-(\omega_B-\omega_B+\omega_A)\mathbf{t'}\right]\right\} \tag{6.10}$$

$$+ \exp\left\{i\left[(2\mathbf{k_A}-\mathbf{k_B})\mathbf{r}-(2\omega_A-\omega_B)\mathbf{t'}\right]\right\} \tag{6.11}$$

$$+ \exp\left\{i\left[(-\mathbf{k_A}+2\mathbf{k_B})\mathbf{r}-(-\omega_A+2\omega_B)\mathbf{t'}\right]\right\} \tag{6.12}$$

$$+ c.c. \tag{6.13}$$

The terms (6.5) – (6.8) describe the third harmonic generation, the terms (6.9) – (6.10) the describe the pump-probe signal, and the last two terms (6.11) – (6.12) represent the photon echoes. Each signal can be unambiguously identified, because it appears at one characteristic frequency in the 2D spectrum.

6.3 Collinear Two-Dimensional THz Spectroscopy

A collinear beam geometry reduces the incident wave vector $\mathbf{k}$ onto a scalar k with only one component. As a consequence, the nonlinear signal is measured together with the transmitted pulses. To separate the different electric fields, we placed two choppers, synchronized to the laser repetition rate of 1 kHz, into the experimental setup. Fig. 6.10 displays the recorded signal configurations. Chopper 1, operating at 500 Hz, blocks every second pulse A. Chopper 2, operating at 250 Hz, blocks every second pair of pulses B. In this way, the combined electric field of both transmitted pulses AB, the individual transient of pulse A, and the individual transient of pulse B, are measured. The different electric field transients are shown in Fig. 6.11. The black line in Fig. 6.11 (a) represents the combined electric field of both pulses including the nonlinear signal $\mathbf{E}_{\mathrm{AB}}$. The red and the blue line in Fig. 6.11 (b) are the electric fields of pulse A, $\mathbf{E}_{\mathrm{A}}$, and of pulse B, $\mathbf{E}_{\mathrm{B}}$, respectively. Subtracting the individual transients $\mathbf{E}_{\mathrm{A}}+\mathbf{E}_{\mathrm{B}}$ from the combined electric field $\mathbf{E}_{\mathrm{AB}}$ yields the part of the nonlinear signal, which is induced by both pulses A and B. This is shown as a green solid line in Fig. 6.11 (c). For clarity, the amplitude is enlarged by a factor of three. The transmitted pulses are denoted by a black dashed line.

To test our 2D concept, we performed simulations of the induced nonlinear signal in independent two-level systems with an energy spacing of 25 THz. The evolution of the density matrix is calculated under the influence of two resonant pulses. The transmitted pulses as well as the derivation of the induced nonlinear polarization is depicted in Fig. 6.12 (a). Both incident pulses are subtracted and the nonlinear polarization of the density matrix is obtained. This corresponds directly to the nonlinear signal emitted from the sample [Fig. 6.12 (b)]. Fourier transformation yields the absolute value of the 2D spectrum, which is shown in Fig. 6.12 (c). As predicted qualitatively in Fig. 6.6 (b) and quantitatively from the terms (6.9) – (6.13), spectral diffraction causes various spectral peaks at linear combinations of the incident frequency vectors. The

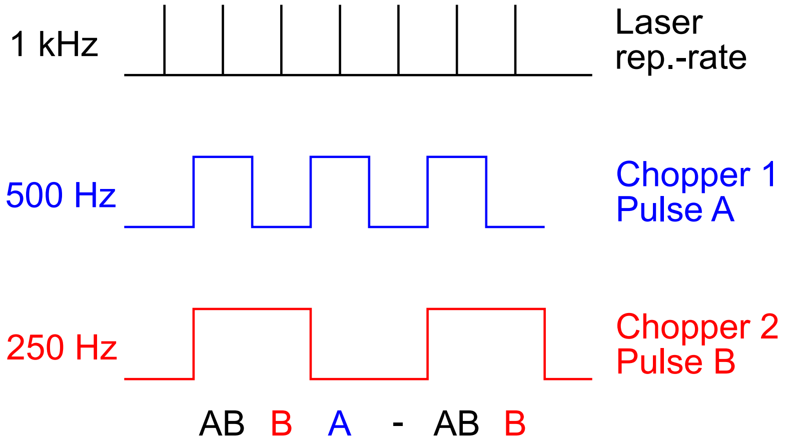

Figure 6.10: The inserted chopper 1 operates at 500 THz and chopper 2 at 250 THz. Synchronized to the laser repetition rate of 1 kHz, the electric field of only pulse A, only pulse B and the combined electric field of both pulses AB is recorded.

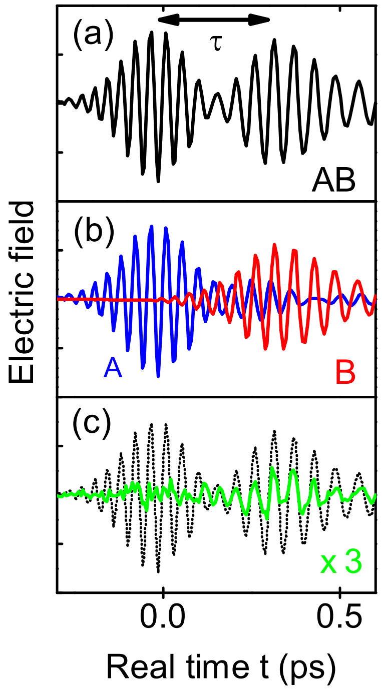

Figure 6.11: Two choppers allow for measuring (a) the combined electric field transients of pulse A and B ($\mathbf{E}_{\mathrm{AB}}$ black line) and (b) of the individual transients of pulse A ($\mathbf{E}_{\mathrm{A}}$ blue line) and pulse B ($\mathbf{E}_{\mathrm{B}}$ red line). (c) Subtracting $\mathbf{E}_{\mathrm{AB}} - \mathbf{E}_{\mathrm{A}} - \mathbf{E}_{\mathrm{B}}$ yields the nonlinear emitted field $\mathbf{E}_{\mathrm{NL}}$ depicted as a green line.

peaks at negative real time frequencies $\omega_t < 0$ stem from complex conjugate terms (6.13). Since no additional information is contained, these signals will be neglected in the following.

The meaning of each spectral spot is explained in Fig. 6.13. Both incident frequency vectors ω_A and ω_B overlap on the sample and generate nonlinear signals at linear combinations

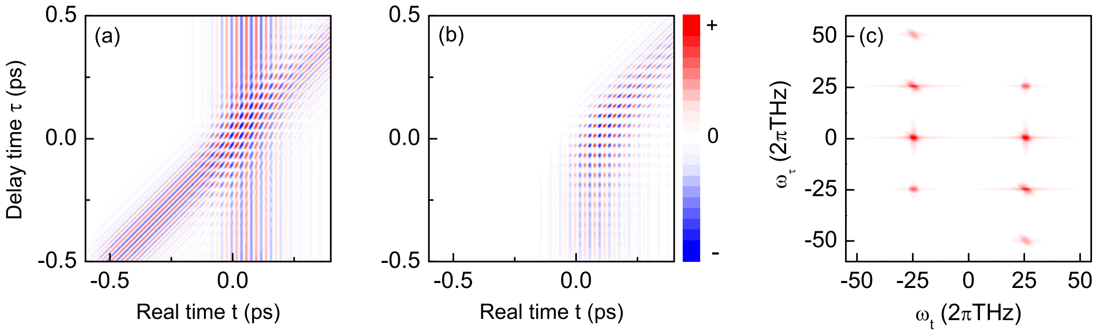

Figure 6.12: (a) Simulated transmitted pulses through a two-level system. (b) Subtracting the transients of the individual pulses yields the nonlinear signal along two time axes *t* and τ. (c) Corresponding 2D spectrum obtained by Fourier transformation of the nonlinear signal in (b).

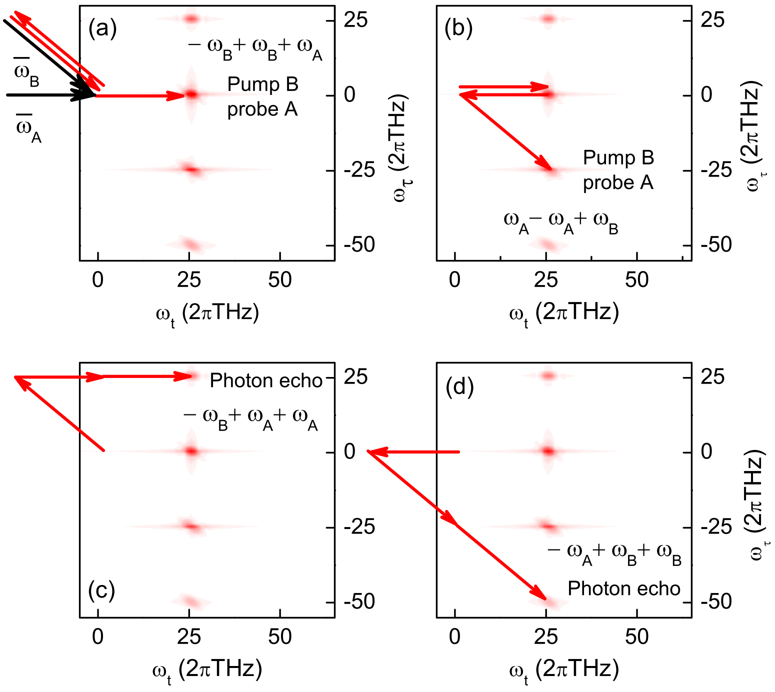

Figure 6.13: Spectral diffraction generates various peaks at frequencies given by linear combinations of the incident frequency vectors ω_A and ω_B. (a) and (b) display linear combinations of frequency vectors for pump-probe signals. (a) Pulse B may pump and pulse A probe the system, or (b) vice versa. Two-pulse photon echoes appear at (c) $\omega_\mathrm{PE1} = -\omega_B + 2\omega_A$, and at $\omega_\mathrm{PE2} = -\omega_A + 2\omega_B$.

of their frequency vectors. The spectral peak at $(25\,\mathrm{THz}, 0)$ is caused by the linear combinations of $\pm\omega_B \mp \omega_B + \omega_A$ [terms (6.9) and (6.10)]. Both linear combinations describe the identical Liouville pathway, which will be depicted in Fig. 6.26. Two interactions of the

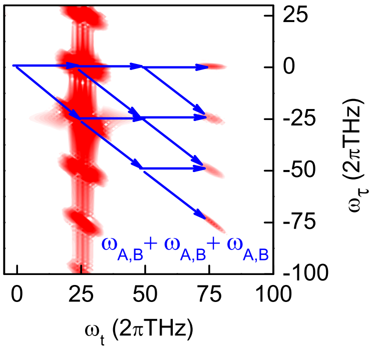

Figure 6.14: Simulated third harmonic peaks at $\omega_t = 75$ THz. These high real time frequencies are not detected anymore in our electrooptic sampling setup.

bra and the ket part of pulse B change the population, which is subsequently read out by pulse A [Fig. 6.13 (a)]. If pulse A pumps and pulse B probes the sample, the signal appears at $\omega_A - \omega_A + \omega_B = (-25\text{ THz}, 25\text{ THz})$ in Fig. 6.13 (b). A photon echo with two incident pulses is only generated, if the second pulse interacts twice with the system. Photon echo 1 in Fig. 6.13 (c) appears at $\omega_{\text{PE1}} = -\omega_B + 2\omega_A = (25\text{ THz}, 25\text{ THz})$ and photon echo 2 [Fig. 6.13 (d)] is found at $\omega_{\text{PE2}} = -\omega_A + 2\omega_B = (-50\text{ THz}, 25\text{ THz})$.

The simulation produces also third harmonic signals stemming from the terms (6.5) – (6.8). They are shown in Fig. 6.14. Linear combinations of frequency vectors cause four different spots at a real time frequency of $\omega_t = 75$ 2πTHz and at different ω_τ frequencies ($0 \leq \omega_\tau \leq 75$ 2πTHz). In a first application of collinear 2D THz spectroscopy, we use a multiple quantum well sample to test the concept and evaluate the validity range.

6.4 Decomposition of Rabi Flops into Nonlinear Signals of Different Orders

Multiple quantum well sample

The first collinear 2D THz experiment confirms our 2D concept based on N-wave mixing in time. We investigated a multiple quantum well (MQW) sample of alternating layers of GaAs and $\text{Al}_{0.35}\text{Ga}_{0.65}\text{As}$. Different bandgaps of both materials confine the electron wavefunctions spatially in one dimension. The broad quantum wells of 10-nm width feature a large dipole moment of $\mu \approx e_0 \times 2.3$ nm at THz frequencies. Accordingly, we expected strong nonlinearities even at lower field strengths. Since only p polarized light is absorbed by the intersubband transitions, the sample were processed into a prism. Diffraction on the surface of the prism provides a component of p polarized light [see Fig. 6.15 (d)].

Our sample (M4.1166) consists of 51 GaAs quantum wells separated by 20-nm-thick $\text{Al}_{0.35}\text{Ga}_{0.65}\text{As}$ barriers. The barrier centers are doped with Si, resulting in an electron concentration of $n_s = 5 \times 10^{10}$ cm^2 per quantum well. There are three bound subbands in the quantum wells shown in Fig. 6.15 (a). Only the lowest subband is populated. Since the two lowest subbands are rather parallel around the Γ point (b), a relative narrow absorption line is found at linear transmission measurements. The result shown in Fig. 6.15 (c) demonstrates an

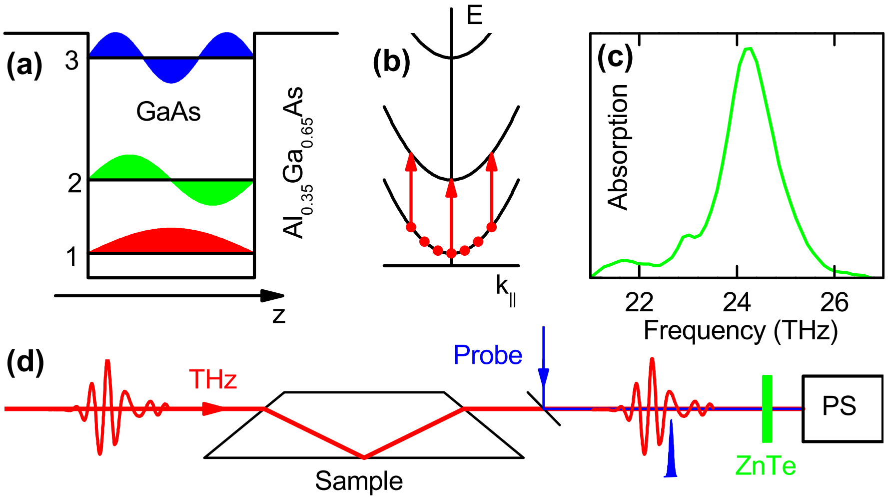

Figure 6.15: (a) Three subbands within the quantum well. (b) Incident pulses excite electrons around the Γ point from the first into the second subband. (c) The resulting narrow absorption line at 25 THz is observed in linear transmission measurements.(d) A prism-shaped sample provides p-polarized light for intersubband excitation.

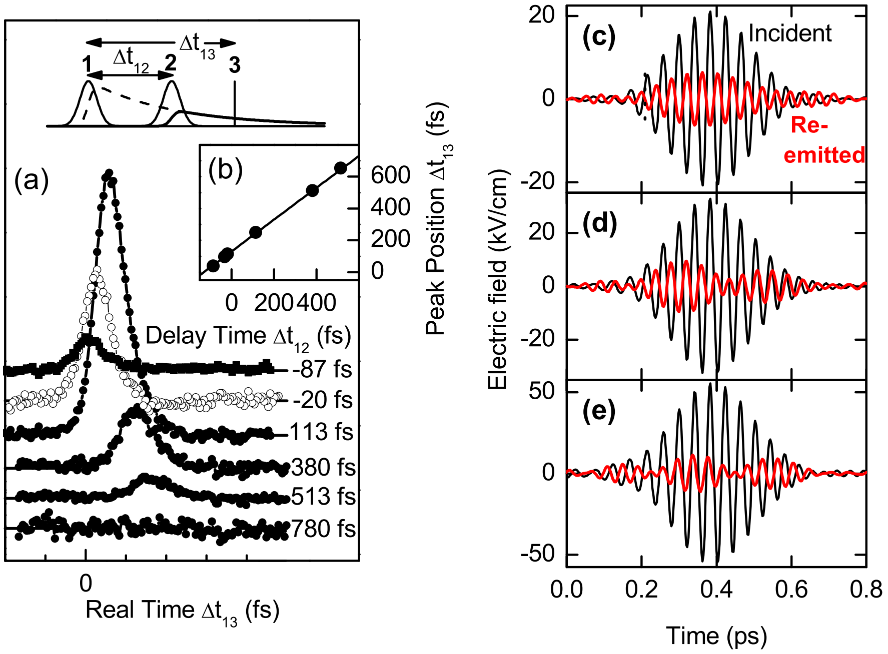

Figure 6.16: (a) Emitted photon echoes for a time-delayed second pulse. (b) The homogeneously broadened transition emits a photon echo constantly several femtosecond after the second pulse [23]. (c) – (e) Rabi flopping at different incident field amplitudes. An emitted field (red line) out-of-phase with the incident field (black line) represents absorption and an in-phase emitted field represents stimulated emission [209].

absorption line at 25 THz with a spectral width (FWHM) of $\Delta\nu = 0.8$ THz using $\omega = 2\pi\nu$.

Several properties of the multiple quantum well sample were known from previous experiments [23,210,211]. One-dimensional photon echo studies [23] addressed the question whether the intersubband transition is homogenously or inhomogenously broadened. Figs. 6.16 (a) and (b) show that the recorded signals occur immediately after the second pulse and no further photon echo τ after the second pulse is found. This indicates a free induction decay on a homogeneously broadened transition and a high structural quality of the quantum wells.

Because the third subband is located at considerably higher energies than the first and the second subband [212], a two-level system is still a good approximation. The experiment in Ref. [211] employed strong THz pulses to drive Rabi oscillations on the intersubband transition of the quantum wells [213]. In this case not the oscillating population is monitored, but the emitted field from the coherent polarization. The transients at different field amplitudes, detected with electrooptic sampling, are shown in Figs. 6.16 (c) – (e). The black line represents the incident and the red line the emitted electric field. If incident and emitted field are out-of-phase, the two-level system absorbs energy; and if both fields are in-phase, energy is emitted. One complete Rabi oscillation is achieved for field amplitudes of 30 kV/cm. It is of particular interest to observe Rabi oscillation with two-dimensional spectroscopy, because the underlying perturbation theory is expected to break down. The $\chi^{(3)}$ approximation describes the induced polarization only in the beginning of the Rabi flop. To describe mathematically the polarization of one entire Rabi oscillation, nonlinear orders up to $\chi^{(15)}$ are required. Since each nonlinear order translates into a distinct spectral peak in our 2D spectrum, we can directly observe up to which order of perturbation the N-wave mixing picture is still valid.

Experiment

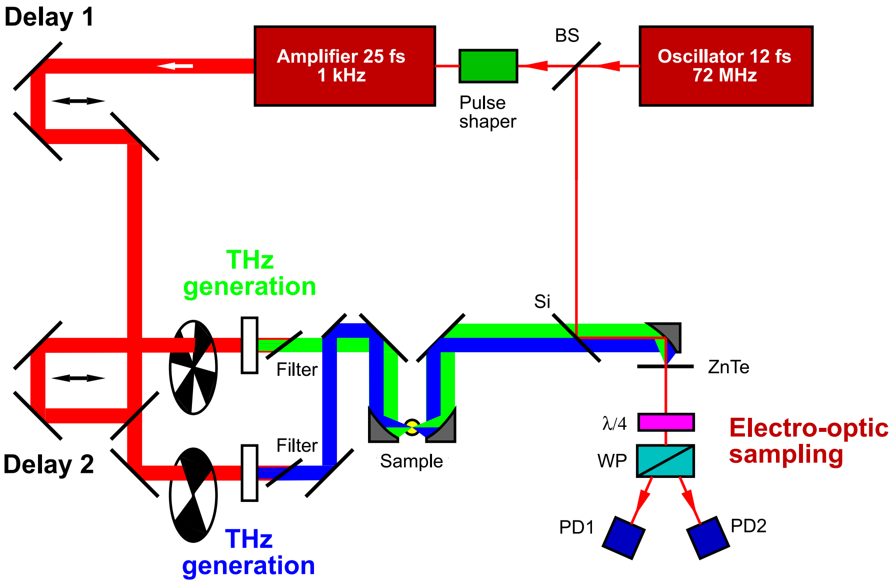

Figure 6.17: Experimental setup of the collinear 2D THz experiments. GaSe crystals allow for an adjustable time delay τ between both pulses and the generation of tunable THz pulses at 2 THz or between 10 and 30 THz.

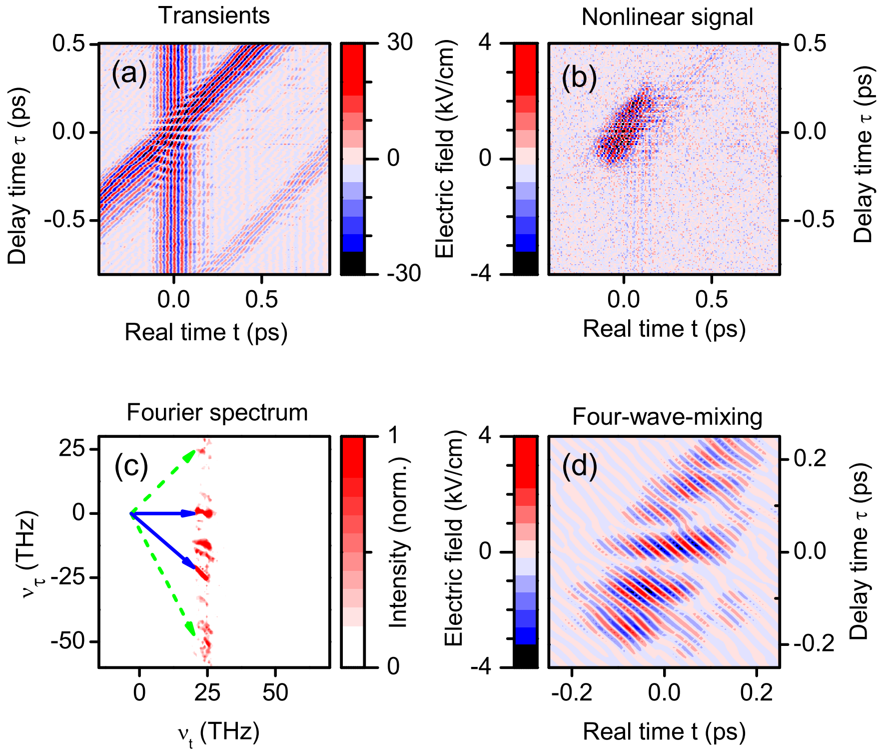

Figure 6.18: Experimental data. (a) Measured transients $E_{AB}(t,\tau)$. (b) Resulting nonlinear signal $E_{\mathrm{NL}}(t,\tau)$. (c) Fourier transform of $E_{\mathrm{NL}}(t,\tau)$. The pump-probe signals are indicated with solid arrows and the four-wave-mixing signals with dashed arrows. (d) Four-wave mixing signal in the time domain, i.e., the back transformation of the signal at $\nu_t = \nu_0$, $\nu_\tau = -\nu_0$.

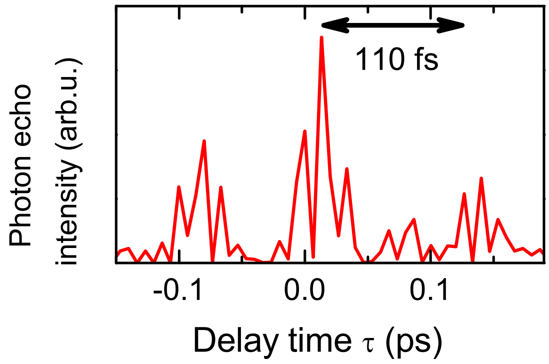

Figure 6.19: Cut along the delay time through the photon echo intensity at $t = 0$. The oscillation time of 110 fs (≈ 9 THz) coincides with the LO phonon frequency in GaAs.

In our experiment, the output from a femtosecond multipass amplifier is split into two pulses with an adjustable delay τ. These pulses are sent onto two different GaSe crystals oriented for the phase-matched difference frequency generation [12, 15] of two phase-locked pulses A and B. The experimental setup is shown schematically in Fig. 6.17. The center of pulse A is kept constant at $t = 0$, and the delay time τ between pulses A and B is varied from $\tau = -0.7$ ps to $\tau = 0.7$ ps. The center frequency of both pulses at $\nu_0 = 25$ THz is resonant to the intersubband transition of the sample. The temporal width (FWHM) of the electric field envelope is 200 fs. The 12 fs detection pulse of our electrooptic sampling setup resolves real time frequencies up to 40 THz. Thus we are not able to measure nonlinear signals of the third harmonic frequency. The maximal delay time frequency ω_τ is determined by the time steps $\Delta\tau$. For a step size of $\Delta\tau = 7$ fs in our experiment, delay time frequencies of ω_τ from -75 THz up to 75 THz are detected. This delay time frequency is completely independent from the detector bandwidth. All experiments were performed at a sample temperature of 50 K.

Experimental results for an amplitude of 30 kV/cm are presented in Fig. 6.18. In panel (a) the transients transmitted through the sample are shown. The second wavefront, about 1 ps after pulse B, stems from a weak internal reflection in the 50 μm thick GaSe crystal and does not cause a nonlinear signal. The nonlinear signal in Fig. 6.18 (b) was obtained by subtracting $E_\mathrm{B}(t,\tau)$ and $E_\mathrm{A}(t)$ from $E_\mathrm{AB}(t,\tau)$. The Fourier transformation of the nonlinear signal, shown in Fig. 6.18 (c), displays the main features of the simulated response in Fig. 6.13. Spectral filtering and inverse Fourier transforming of the photon echo at $\nu_\mathrm{PE} = (25\ \mathrm{THz}, 25\ \mathrm{THz})$ yields the signal in the time domain in Fig. 6.18 (d). Oscillations along the delay time are recognized and emphasized in a cut through the intensity of the photon echo along $t = 0$ in Fig. 6.19. The oscillation time amounts to 110 fs, i.e., 9 THz, which coincides with the LO phonon frequency in GaAs of 8.8 THz [214]. We believe therefore, that highly nonlinear Rabi oscillations generate additional frequency components to induce quantum beats between the excited state and the an LO phonon oscillations. A cooperation with an theory group of Prof. A. Knorr investigates currently the possibilities of such a process.

Since the transition is homogeneously broadened, we expect a circular spectral peak on the photon echo position of $\nu_\mathrm{PE1} = (25\ \mathrm{THz}, 25\ \mathrm{THz})$ and $\nu_\mathrm{PE2} = (-50\ \mathrm{THz}, 25\ \mathrm{THz})$. Noise around the photon echo signals complicates the analysis, but a circular peak at ν_PE1 can be anticipated. The type of line broadening can be analyzed also by the emission time of the emitted photon echo. Therefore both photon echoes are spectrally filtered out and transformed back into the time domain. We define the temporal position of a pulse or the photon echo by its center of gravity, given by

$$t_c = \frac{\int t E(t)^2 dt}{\int E(t)^2 dt}. \tag{6.14}$$

The resulting time of both incident pulses A and B, as well as for both photon echoes is shown in Fig. 6.20. The photon echo signal occurs constantly with the last pulse. For clarity the photon echo is shifted back in real time by 200 fs. A time-delayed photon echo generated within an inhomogeneous transition would be expected to occur along the red dashed lines. Thus Fig. 6.20 confirms the earlier result of a predominantly homogenously broadened transition [23].

Furthermore, 2D spectra as a function of the incident field amplitude were recorded. Each panel shown in Fig. 6.21 is normalized to the respective signal maximum. Due to the large dipole moment, electric field strengths of several tens of kilovolts per centimeter are sufficient to drive Rabi oscillations within the intersubband transition [209].

The 2D spectrum shown in Fig. 6.21 (a) was measured with an electric field amplitude of 10 kV/cm. Two pump-probe signals at $\nu_\tau = 0$ and $\nu_\tau = -25$ THz and a weak photon echo spot at $\nu_\tau = 25$ THz are found. A field amplitude of 18 kV/cm [Fig. 6.21 (b)] corresponds to a Rabi oscillation with a pulse area of $\theta = \frac{\pi}{2} \int |\mu E(t))| dt = 1\pi$ for one of the two pulses. At

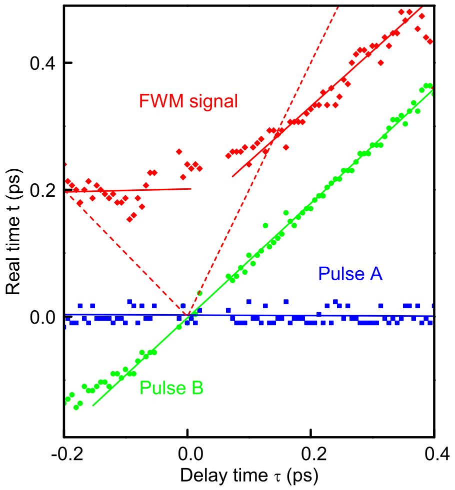

Figure 6.20: Temporal position of the two pulses A and B, and of the photon echoes. Both photon echoes appear at a constant temporal delay after the second of the two pulses. It confirms a predominantly homogenously broadened transition [23]. A time delayed photon echo would occur along the dashed lines.

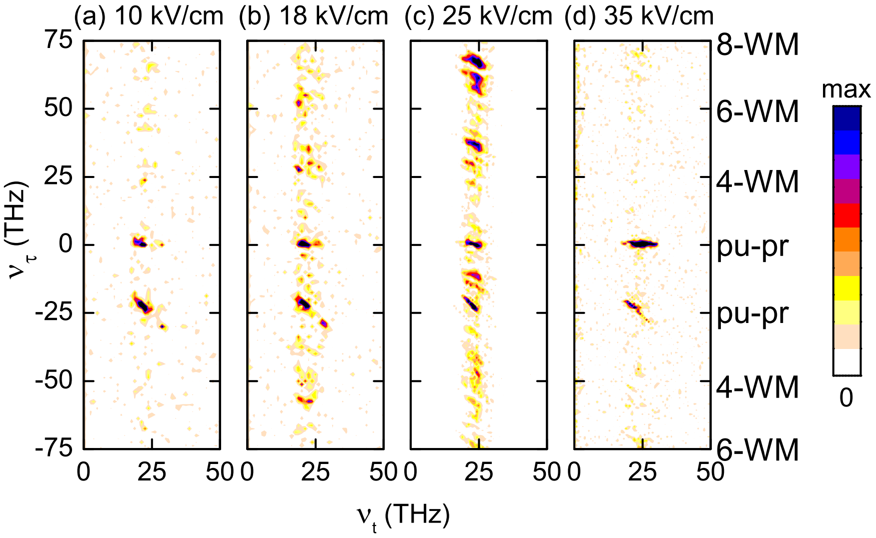

Figure 6.21: Experimental data: Contour plots (normalized to the respective signal maximum) of measured 2D spectra $F(\nu_t, \nu_\tau)$ for various electric field strengths of the phase-locked pulse pair as indicated. The field strength of 18 kV/cm corresponds approximately to a pulse area of $\theta = 1\pi$.

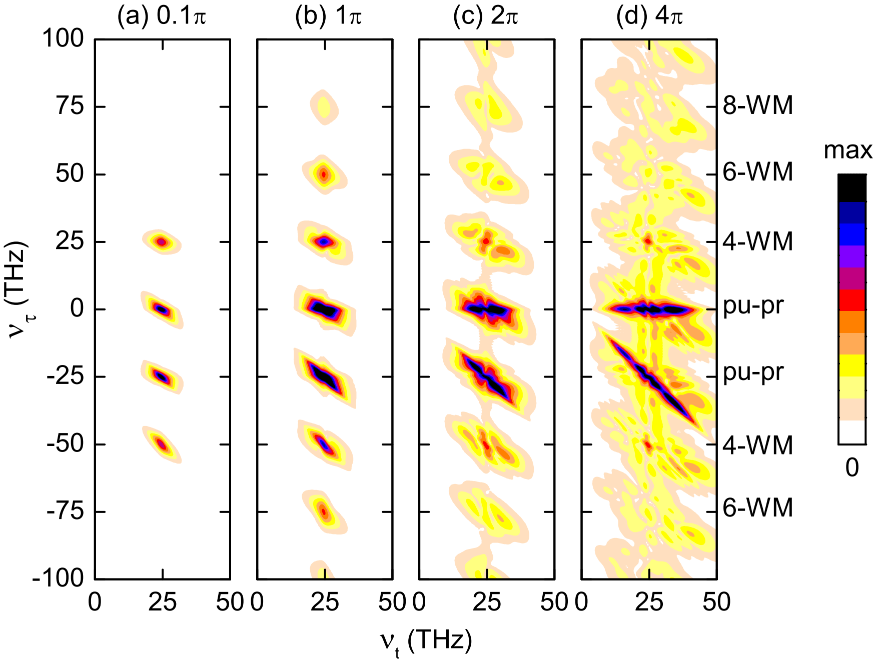

Figure 6.22: Theoretical simulation: Calculated 2D spectra $F(\nu_t, \nu_\tau)$ for various electric field strengths of the phase-locked pulse pair. The indicated pulse areas θ at the top of the panels correspond to a single driving pulse. Obviously, an approximative description with third-order response functions is only valid for very small pulse areas $\theta \ll 1$.

this pulse area, the $\chi^{(3)}$ approximation breaks down. Starting with this field strength we observe the simultaneous occurrence of all higher-order n-wave mixing processes, i.e., six-wave mixing, eight-wave mixing, etc. For even higher field amplitudes of 25 kV/cm shown in Fig. 6.21 (c), we observe in the nonlinear 2D spectra a broad streak along all ν_τ frequencies. This streak is centered around $\nu_t = \nu_0$. It gradually broadens further with increasing field amplitude. This is a characteristic feature of very high field strengths in Fig. 6.21 (d) (35 kV/cm). Two intense, sharp and elongated pump-probe signals at both $\nu_\tau = 0$ and $\nu_\tau = -\nu_0$ dominate the 2D spectrum.

The experimental observations of Fig. 6.21 are fully reproduced by theoretical calculations of the density matrix simulating the pulse-pair driven Rabi oscillations of a homogeneously broadened two-level system [209]. Fig. 6.22 shows the calculated 2D spectra $F(\nu_t, \nu_\tau)$ for various electric field strengths of the phase-locked pulse pair. The indicated pulse areas θ at the top of the panels correspond to a single driving pulse. To better illustrate the changes with θ, Fig. 6.22 spans a larger range of electric field amplitudes than possible in the experiment. Therefore the panels in Fig. 6.21 and in Fig. 6.22 do not directly correspond to each other.

The theoretical simulations give a deeper insight into the characteristic features observed in the experiment. In particular the following points are important:

(i) Obviously, an approximative description with third-order response functions is only valid for very small pulse areas $\theta \ll 1$.

(ii) In the simulations, it is in principle possible to choose an electric-field amplitude so that an n-wave mixing process is above a detection limit, but not an $n+2$-wave-mixing process. However, the electric-field range where such is the case gets progressively smaller for increasing n. In practice, the consequence of this is that once the $\chi^{(3)}$ approximation breaks down, all n-wave mixing processes occur simultaneously.

(iii) The time-dependent Rabi frequency leads to pronounced sidebands of the carrier frequency, which in turn broaden the spots of all n-wave mixing processes leading eventually to a broad, structured streak along the ν_τ axis.

(iv) For large pulse areas the two elongated pump-probe features dominate the nonlinear 2D spectra. In the language of Feynman diagrams this effect has the following reason: Outside the temporal overlap of pulses A and B, $\chi^{(n)}$-processes of arbitrary order contributing to the pump-probe spots at both $\nu_\tau = 0$ and $\nu_\tau = -\nu_0$ contain an increasing number of contributing Feynman diagrams still obeying the rotating-wave-approximation.

(v) Most importantly, the comparison of our experiments with theory in the non-perturbative regime shows that beyond the $\chi^{(3)}$-approximation a perturbative description of nonlinear 2D spectra using double-sided Feynman diagrams becomes untractable from the numerical point of view and is not helpful in analyzing the physical origin of the nonlinear signals.

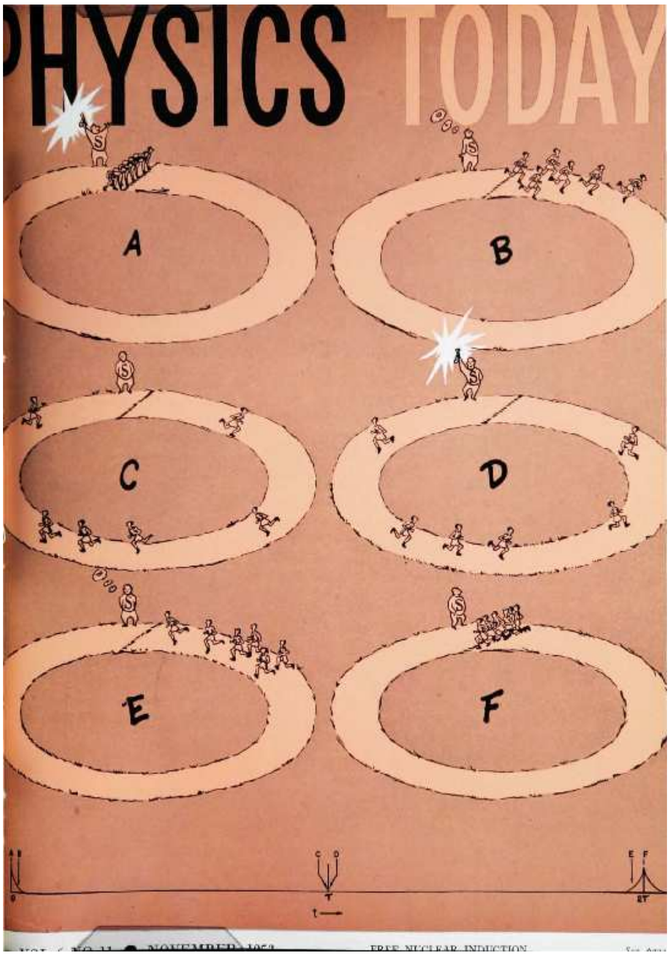

Figure 6.23: Cover page of “Physics Today” in 1953 [215]. The photon echo is explained in analogy to a middle-distant race.

6.5 Why Does a Phase-resolved Photon Echo Contain the 2D Correlation Spectrum ?

While the previous experiment analyzed primarily the magnitude of the entire nonlinear signal, more detailed information is obtained from the 2D correlation spectrum of the photon echo. With the help of a density matrix formalism it will be explained in the following, why in particular the photon echo reveals two-dimensional information about energetic couplings, spectral diffusion or line shapes.

The photon echo is a nonlinear signal, which is generally induced by three pulses. The journal “Physics Today” dedicated a cover page in 1953 to the explanation of the photon echo (see Fig. 6.23). It illustrates the phase behavior of a quantum system in the following way: several runners in a stadium, each on an own track, correspond to the phase evolutions of the microscopical transitions within an inhomogeneously broadened line shape. (A) After the referee starts the race with a shot, i.e., the first pulse, some runners will be faster than the others (B and C). The curvature favors the runners of the inner tracks. This means in physical terms that the phases of the microscopical transitions disperse, because they oscillate at slightly different frequencies. However, after the time τ a second shot (i.e., the second pulse) stops the runners before a third shot (i.e., the third pulse) (D) makes them to turn around and run back. (E) Since each athlete runs once again the same distance with his own velocity, (F) all runners will be in phase again on the starting point. Accordingly, at the time τ after the third pulse, each microscopical transition will have the same phase. Under this condition the free induction decay of each quantum system sums up constructively and a photon echo is emitted. The link between the runners and the phase evolution of a quantum system is explained in the following for the case of a density matrix of a two-level system.

The Phase Evolution of a Two-Level System

We assume a two-level system with the orthogonal eigenfunctions $\mid 0\rangle$ and $\mid 1\rangle$. The energy eigenlevels are separated by $\varepsilon_1 - \varepsilon_0 = \hbar\omega_0$. Both eigenfunctions may coherently superpose, which is described with the density matrix ρ

$$\rho = \sum_{n,m=0}^{1} c_n {c_m}^* \mid n\rangle\langle m \mid . \tag{6.15}$$

The elements of the density matrix can be calculated with $\rho_{n,m} = \langle n \mid \rho \mid m\rangle$

$$\rho = \begin{pmatrix} \rho_{00} & \rho_{01} \\ \rho_{10} & \rho_{11} \end{pmatrix} = \begin{pmatrix} c_0 c_0^* & c_0 c_1^* \\ c_1 c_0^* & c_1 c_1^* \end{pmatrix} . \tag{6.16}$$

The diagonal elements represent populations of the ground (ρ_{00}) and of the excited state (ρ_{11}) and the off diagonal elements indicate the degree of the coherent superposition between both eigenstates. The density matrix is Hermitian [Eq. (6.17)] and may reside without any decoherence in a pure state [Eq. (6.18)]

$$\rho_{01} = {\rho_{01}}^*, \tag{6.17}$$

$$\rho_{00} + \rho_{11} = 1. \tag{6.18}$$

For a density matrix initially in the ground state, we can define a population change $b = 1 - \rho_{11}$ and the initial coherence of the system $a = c_1 c_0^* = c_0 c_1^*$

$$\rho = \begin{pmatrix} 1-b & a^* \\ a & b \end{pmatrix} . \tag{6.19}$$

On the other hand we can define for an unperturbed two-level system a Hamilton operater in the eigenbasis

$$H = \begin{pmatrix} \varepsilon_0 & 0 \\ 0 & \varepsilon_1 \end{pmatrix} . \tag{6.20}$$

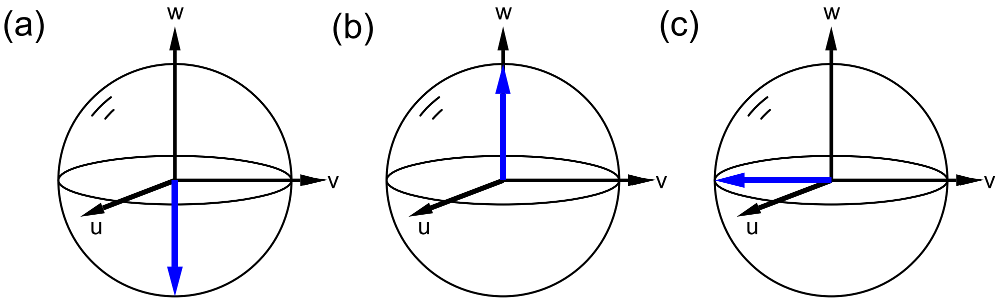

Figure 6.24: The Bloch sphere has one absorptive component (**u**), one dispersive component (**v**), and one component indicating inversion (**z**). The Bloch vector (a) in the ground state $(0,0,-1)$, in (c) the excited state $(0,0,1)$, and in (b) a coherent superposition of the ground and excited states.

Using the Liouville equation one can calculate the individual elements $\rho_{m,n}$ for an unperturbed two-level system

$$\frac{d}{dt}\rho = -\frac{i}{\hbar}[H,\rho] \tag{6.21}$$

$$\Leftrightarrow \frac{d}{dt}\begin{pmatrix}\rho_{00} & \rho_{01}\\ \rho_{10} & \rho_{11}\end{pmatrix} = -\frac{i}{\hbar}\left[\begin{pmatrix}\varepsilon_0 & 0\\ 0 & \varepsilon_1\end{pmatrix}\begin{pmatrix}\rho_{00} & \rho_{01}\\ \rho_{10} & \rho_{11}\end{pmatrix} - \begin{pmatrix}\rho_{00} & \rho_{01}\\ \rho_{10} & \rho_{11}\end{pmatrix}\begin{pmatrix}\varepsilon_0 & 0\\ 0 & \varepsilon_1\end{pmatrix}\right] \tag{6.22}$$

$$\Leftrightarrow \frac{d}{dt}\begin{pmatrix}\rho_{00} & \rho_{01}\\ \rho_{10} & \rho_{11}\end{pmatrix} = -\frac{i}{\hbar}\begin{pmatrix}0 & \rho_{01}(\omega_0)\\ \rho_{10}\rho_{01}(\omega_0) & 0\end{pmatrix}. \tag{6.23}$$

Thus we obtain for the elements of the density matrix

$$\rho_{00}(t) = \rho_{00} \tag{6.24}$$
$$\rho_{11}(t) = \rho_{11} \tag{6.25}$$
$$\rho_{01}(t) = e^{i\omega_0 t}a(0) = a(t) \tag{6.26}$$
$$\rho_{10}(t) = e^{i\omega_0 t}a^*(0) = a^*(t) \tag{6.27}$$
$$\tag{6.28}$$

Obviously there is no change of population (ρ_{nn} =const.) without an external perturbation. The off diagonal elements oscillate with the frequency ω_0. A coherent superposition of ground and excited state exhibits a constant phase relation between both eigenfunctions $\mid 0\rangle$ and $\mid 1\rangle$. Accordingly, also the resulting wave function $\mid \psi\rangle = c_0 \mid 0\rangle + c_1 e^{i\omega_0 t} \mid 1\rangle$ oscillates with the transition frequency ω_0. The photon echo picture presented above referred to this phase evolution of $\mid \psi\rangle$ as an analog to the middle-distant runner. With $\mid \psi\rangle$ also the electron distribution oscillates, which is different for the pure eigenstates $\mid 0\rangle$ and $\mid 1\rangle$. The resulting dipole moment enables efficient coupling of the two-level system onto the external light field during a coherent superposition.

The actual state of the density matrix is illustrated with a Bloch vector in Fig. 6.24. The three axes of the coordinate system **u**, **v**, and **z**, stand for the dispersive (**u**), and the absorptive components (**v**), and for the inversion of the two-level system (**z**). Thus the Bloch vector in the

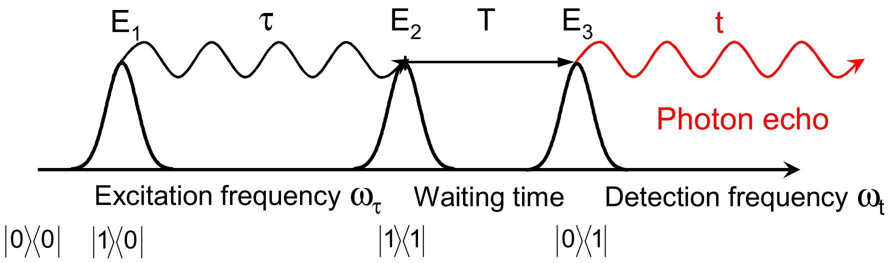

Figure 6.25: Coherent photon echo induced by three incident pulses E_1, E_2, and E_3. E_1 and E_2 are separated by the excitation time τ, E_2 and E_3 are separated by the waiting time T. After E_3 starts the detection time t.

ground state $\mid 0\rangle$ points down to $(0,0,-1)$ [Fig. 6.24 (a)] and in the excited state $\mid 1\rangle$ it points up to $(0,0,1)$ [Fig. 3.1 (b)]. During excitation with a resonant light field, the Bloch vector precesses from the bottom upwards [Fig. 6.24 (c)] and the **u** and the **v** components oscillate.

The Phase Evolution During a Photon Echo

Noncollinear 2D IR experiments use the photon echo signal to correlate the excitation frequency with the detection frequency. Mostly molecular samples of small spatial extension and thus with relatively weak dipole moments are investigated. The induced nonlinearities are small and well-described within the $\chi^{(3)}$ approximation. That means the Bloch vector is deflected only slightly from the ground state and the Bloch sphere can be approximated as a cubic parabola. But coherent superpositions between the ground and the excited state are induced—to a smaller extent—as well. A perturbation theory of nonlinear optics within the $\chi^{(3)}$ approximation was developed [43, 216] to describe the quantum mechanical occurrence during four-wave mixing.

The density matrix $\hat{\rho}$ of a two-level system is approximated in a first step by a sequence of perturbations of increasing order.

$$\hat{\rho} = \rho^{(0)} + \rho^{(1)} + \rho^{(2)} + \cdots \tag{6.29}$$

Each perturbation of the system caused by a δ-like light pulse adds one density matrix $\rho^{(n)}$ onto the unperturbed density matrix of a pure state $\rho^{(0)}$. The first perturbation $\rho^{(1)}$ goes linear with the electric field and stands for a coherent superposition. The second perturbation $\rho^{(2)}$ is proportional to the intensity and represents the change in population.

$$\rho^{(0)} = \begin{pmatrix} 1 & 0 \\ 0 & 0 \end{pmatrix}, \rho^{(1)} = \begin{pmatrix} 0 & a^*(t) \\ a(t) & 0 \end{pmatrix}, \rho^{(2)} = \begin{pmatrix} -b & 0 \\ 0 & b \end{pmatrix}. \tag{6.30}$$

Each perturbation acting on the unperturbed density matrix $\rho \sim\mid 0\rangle\langle 0\mid$ causes an increase or a decrease of one quantum number, depending on whether the bra or the ket part of the electric field interacts with the system. If the induced coherent superposition precesses freely, radiation is emitted as a free induction decay.

Fig. 6.25 illustrates a photon echo induced by the three subsequent pulses E_1, E_2, and E_3. Pulse E_1 excites the system and induces a coherent superposition $\mid 0\rangle\langle 1\mid$. The wave function oscillates during the excitation time τ with the excitation frequency ω_τ. The second pulse E_2

interrupts the oscillation and changes the population of the system to $|\,1\rangle\langle 1\,|$. The phase stands still during this waiting time T. Energetic transfer or spectral diffusion occurs within T. To investigate these effects several 2D spectra at different waiting times T are recorded. The third pulse E_3 initiates a further coherent superposition, for instance, by changing the state of the density matrix to $|\,1\rangle\langle 0\,|$. This emits finally the photon echo. The time after the last pulse is called the detection time t. Photon echoes are also induced only by two pulses. In this case, the second pulse interacts twice with the system and the waiting time T amounts to zero. The two-pulse photon echo is considered degenerate, because of the simultaneous second and third pulse interaction.

Liouville Pathways

The evolution of the quantum system is unambiguously determined by the Liouville path, i.e., by the trajectory in the phase space. The Liouville path is often illustrated using double-sided Feynman diagrams [216]. The two pure quantum states are denoted in the center. Time increases from bottom to top and each interaction between laser pulse and quantum system is indicated by an arrow. An arrow pointing to the right represents an electric field with $\exp[i(\mathbf{kr}-\omega t)]$, and the complex conjugate $\exp[-i(\mathbf{kr}-\omega t)]$ is represented by an arrow pointing to the left. Moreover, an arrow pointing towards the diagram increases the quantum number of the eigenstate, and an arrow pointing away decreases the quantum number. Since the four-wave mixing signal is emitted with the last interaction, the arrow $\mathbf{k}_{\mathrm{FWM}}$ is marked red and points necessarily away. The generated nonlinear signal is emitted into the direction of the sum of the three participating $\mathbf{k}$ vectors. According to these rules the Liouville path causing the photon echo of Fig. 6.25 looks as follows:

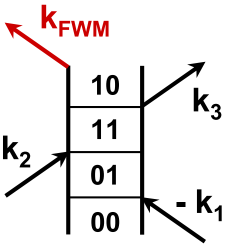

Liouville pathways causing pump-probe and third harmonic signals are shown in Fig. 6.26. To generate a pump-probe signal, the pump pulse interacts twice with the system, once with the bra and once with the ket part. The induced inversion is read out by the second pulse. For third harmonic generation, three pulse interactions excite the three quantum state $|\,3\rangle\langle 0\,|$ or $|\,0\rangle\langle 3\,|$, which emits in turn the frequency $3\omega_0$.

However, pump-probe and third harmonic signals do not provide 2D spectra, because no phase evolution during the excitation time is stored. This information is only contained in the Liouville pathways of photon echo signals, which are presented in Fig. 6.27. Fig. 6.27 (a) shows the rephasing Liouville pathways (PE), where the phase evolution during excitation time is reversed during detection time. Nonrephasing photon echoes are also called “virtual echoes” (VE). The corresponding Liouville pathways in Fig. 6.27 (b) demonstrate that the phase evolves into the same direction for the excitation and the detection time. The conjugate complex diagrams of the Liouville pathways in Fig. 6.27 are not shown.

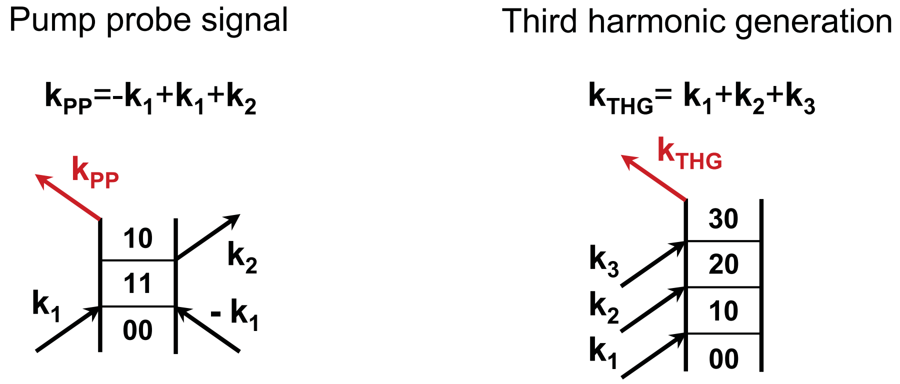

Figure 6.26: Pump-probe and third harmonic signals are FWM signals as well. The pump-probe pathway excites the system simultaneously with the bra and ket part of the pulse. Therefore the population is changed immediately and no phase oscillation takes place. One pulse interacts three times with the system for third harmonic generation. All three $\mathbf{k_1}$ vectors sum up and the threefold frequency is emitted.

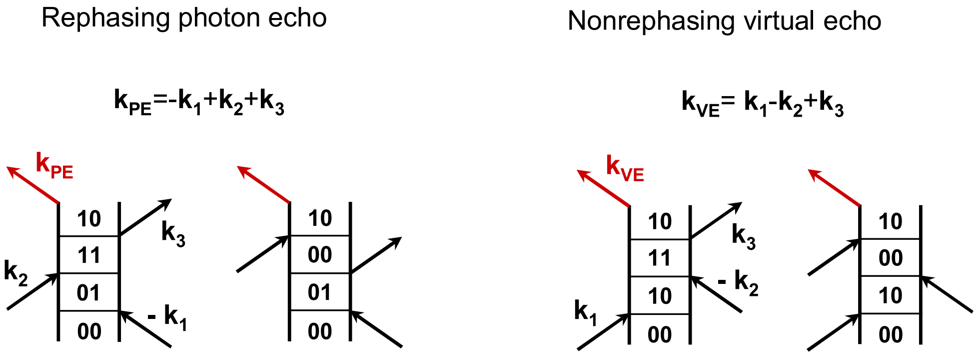

Figure 6.27: (a) Rephasing photon echoes reverse the initial phase evolution after the third pulse. They are emitted into the direction of $\mathbf{k}_{\text{PE}} = -\mathbf{k_1} + \mathbf{k_2} + \mathbf{k_3}$. (b) The phase evolution in nonrephasing Liouville pathways points only into one direction. These virtual echoes are emitted into another direction of $\mathbf{k}_{\text{VE}} = \mathbf{k_1} - \mathbf{k_2} + \mathbf{k_3}$.

Two Frequency Axes Within the Photon Echo

Both frequencies ω_τ and ω_t of a 2D spectrum are contained within the photon echo or the virtual echo. The excitation frequency ω_τ is given by the phase oscillation along the excitation time τ and the detection frequency ω_t by the phase oscillation along the detection time t. While the detection frequency of the photon echo can be simply measured with a spectrometer, the measurement of the excitation frequency requires some further consideration. The phase of the system does not evolve during the waiting time T between the excitation and the detection time. This means the phase after the excitation time τ is equal to the phase in the beginning of the detection time t. As a consequence the evolution of the excitation phase is displayed by the initial phase of the photon echo as a function of τ. Thus Fourier transforming the electric field of the photon echo along τ reveals the acquired excitation frequency.

Energetic couplings may be imagined as follows: The first broadband pulse excites a coherent

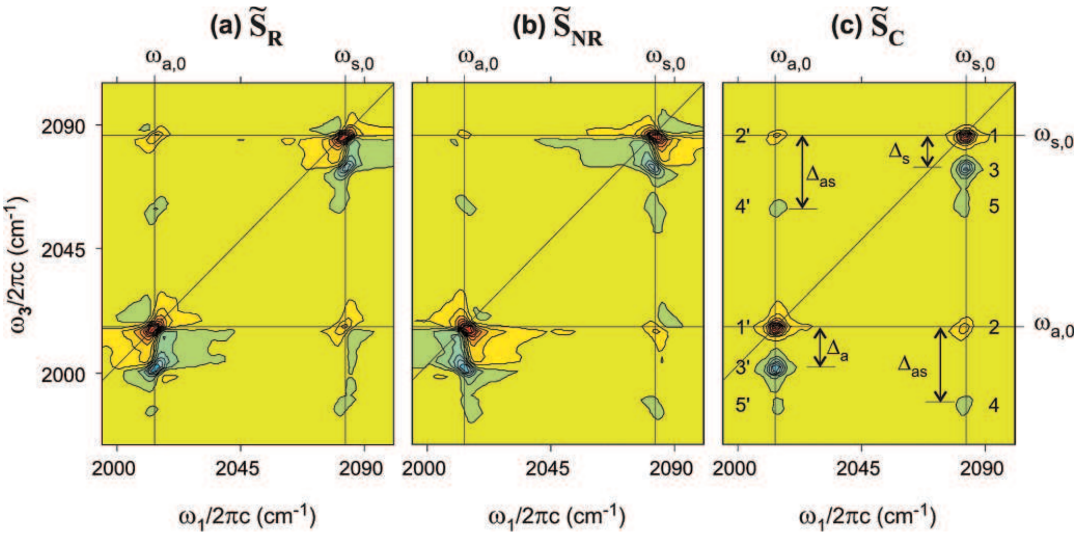

Figure 6.28: (a) Fourier transformed photon echoes exhibit a poor spectral resolution due to phase-twisted peaks containing both absorptive and dispersive components. (b) Complementary "nonrephasing photon echo". (c) The purely absorptive 2D correlation spectrum with better spectral resolution is obtained by adding and phasing (a) and (b). The phasing procedure requires an additional pump-probe experiment. These spectra are taken from Ref. [189].

superposition and the system oscillates with a certain excitation frequency of the transition. If energy is, coherently or incoherently, transferred to another transition, then the coherent superposition induced by the third pulse, and thus the emitted photon echo, oscillates with a modified detection frequency [204]. Accordingly the excitation and detection frequencies are not equal and the energy transfer is indicated as an off-diagonal cross peak in the 2D spectrum.

6.6 Phasing Procedures

The rephasing photon echo and the nonrephasing virtual echo are measured in noncollinear 2D photon echo experiments by two separate scans. Using the "box" beam geometry allows to measure the photon echo in the direction of $-\mathbf{k_1}+\mathbf{k_2}+\mathbf{k_3}$ and the virtual echo in the direction of $\mathbf{k_1}-\mathbf{k_2}+\mathbf{k_3}$ on one detector just by exchanging the time order of the first two pulses. The real parts of both spectra are shown in Figs. 6.28 (a) and (b). One finds phase-twisted peaks of low spectral resolution, because absorptive and dispersive components are superposed. To obtain a purely absorptive spectrum for the real part [Fig. 6.28 (c)] and a purely dispersive spectrum of the imaginary part, the phase of the photon echo signal with respect to the last pulse is required. This phase does not relate to the carrier-offset phase, which is often considered in spectral interferometry. A noncollinear beam geometry implies, that the photon echo and the last pulse can not be measured at once, because both signals are emitted into different direction. Thus the absolute phase has to be determined by an additional phasing procedure.

Fig. 6.29 depicts the different phases of the assumed two-level quantum system. φ_1, φ_2, φ_3, $\Delta\varphi_{\mathrm{PE}}$, and φ_{LO} stand for the phase of the quantum system after the first, the second, the third pulse, the phase shift of the photon echo, and after the local oscillator. If the photon echo is

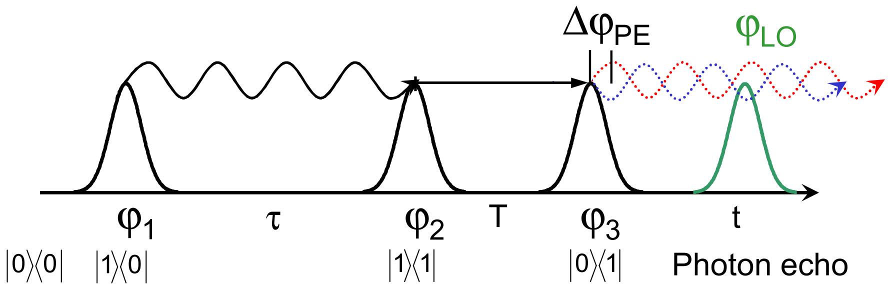

Figure 6.29: Depending on the phase difference $\Delta\varphi_{\mathrm{PE}}$ the emitted photon echo is either in-phase with the last pulse, signifying emission or out-of-phase signifying absorption. Only for the correct $\Delta\varphi_{\mathrm{PE}}$ yields a purely absorptive 2D correlation spectrum.

in phase with the last pulse, i.e., for $\Delta\varphi_{\mathrm{LO}} = n2\pi$ with $n = 0, 1, 2..$, this frequency component is emitted from the system. If the photon echo is out of phase, i.e., for $\Delta\varphi_{\mathrm{LO}} = (n+1)2\pi$, the frequency component is absorbed from the sample. For other phase differences a mixture of absorption and dispersion exists. Since the phase in Figs. 6.29 (a) and (b) is also influenced by the phases $\varphi_1, \varphi_2, \varphi_3$, and φ_{LO}, $\Delta\varphi_{\mathrm{PE}}$ can not be directly aligned to obtain a purely absorptive spectrum.

However, it is known that the phase evolves during the excitation time and reverses during the detection time for a rephasing photon echo. For a virtual echo, the time ordering of the first two pulses is exchanged and the phase evolution during excitation and detection time points into the same direction. Thus the phases of the quantum system for both signals in Figs. 6.29 (a) and (b) are given by:

$$\varphi_{PE} = (\varphi_1 - \varphi_2) - (\varphi_3 - \varphi_{\mathrm{LO}}) + \Delta\varphi_{\mathrm{PE}} \tag{6.31}$$

$$\varphi_{VE} = (\varphi_2 - \varphi_1) + (\varphi_3 - \varphi_{\mathrm{LO}}) + \Delta\varphi_{\mathrm{VE}} \tag{6.32}$$

Adding the rephasing signal in Fig. 6.29 (a) onto the nonrephasing spectra in Fig. 6.29 (b) cancels out the influences of all other phases and exclusively $\Delta\varphi_{\mathrm{PE}}$ can be aligned.

$$\varphi_{\mathrm{PE}} = \Delta\varphi_{\mathrm{PE}}. \tag{6.33}$$

$\Delta\varphi_{\mathrm{PE}}$ is determined by an additional pump-probe experiment. Pump-probe spectra are inherently correctly phased, because transmission changes are detected directly in frequency domain without using a local oscillator. The correctly phased 2D correlation spectrum in Fig. 6.1 exhibits qualitatively the same signals than the 2D pump-probe spectrum.

Having such a 2D pump-probe spectrum, allows for aligning $\Delta\varphi_{\mathrm{PE}}$ of the 2D correlation spectrum until both spectra are identical. To keep the experimental effort of the phasing procedure reasonable, this comparison is performed only in one frequency axis ω_t. According to Fig. 6.2 (b), an integration of the 2D pump-probe spectrum along the ω_τ is achieved with a conventional pump-probe experiment using a broad-band pump pulse. The integration along ω_τ of the 2D correlation spectrum, i.e., the sum of the nonrephasing and rephasing spectrum, is carried out mathematically. Both 1D spectra are compared, and $\Delta\varphi_{\mathrm{PE}}$ is adjusted for the best agreement. $\Delta\varphi_{\mathrm{PE}}$ is delay time independent and yields therefore the purely absorptive 2D correlation spectrum in Fig. 6.28 (c).

This phasing procedure is not necessary for a collinear beam geometry, because the absolute phase, i.e., the phase evolution between the last pulse and the photon echo, is directly measured. The general case for three incident pulses is illustrated in Fig. 6.30. For $\tau < 0$ the excitation time is varied and the waiting time T between second and third pulse remains constant. In this case the photon echo is emitted in the time quadrant of $t > 0$ and $\tau < 0$. The frequency vector is given by the linear combination of $\omega_{\mathrm{PE}} = -\omega_A + \omega_B + \omega_C$ [see Fig. 6.30 (a)]. The nonrephasing virtual echo in Fig. 6.30 (b) is emitted in the same time quadrant but with a frequency vector of $\omega_{\mathrm{VE}} = \omega_A - \omega_B + \omega_C$. Since all pulses are measured simultaneously, we know exactly the phase ($\Delta\varphi_{\mathrm{PE}}$ in Fig. 6.29) between photon echo signal and last pulse. Therefore the data are correctly phased, just by setting the pulse overlap between pulse A and B to zero in the delay time and the third pulse C has to set to zero in the real time.

A simulated emitted photon echo at a spectral position of $\omega_{\mathrm{PE}} = (-\omega_0, \omega_0)$ is shown in Fig. 6.31 (a). Even though correctly phased, the relatively sharp time cuts impose a phase-twisted character on the spectral peak in Fig. 6.31 (b). The nonrephasing virtual echo at (ω_0, ω_0) exhibits the same frequency as the pump-probe signal. Both signals can be separated in the time domain, since they appear in different time quadrants. The phase of the virtual echo oscillates in the excitation time, stays constant during the waiting time, and it continues the oscillation in the detection time. Thus for $T = 0$, the nonrephasing virtual echo is identical to the free induction decay. If this free induction decay is induced by the first pulse and perturbed by two complementary interactions of the second pulse, it will translate in our measurement method into a nonlinear signal after the second pulse. This signal is mirrored on the delay time axis $\tau = 0$ and shown in the time and in the spectral domain in Figs. 6.31 (c) and (d), respectively. Adding up these two signals eliminates the sharp edges in the of the photon echo in the time domain and yields a purely absorptive line shape in the frequency domain shown in Figs. 6.30 (e) and (f).

Furthermore, the absolute phase allows to isolate different signals and back-transform them into the time domain. This is shown for both photon echoes, both pump-probe signals, and both perturbed free induction decays (PFID) in Fig. 6.32. Each nonlinear signal is unambiguously identified by its spectral position and its time quadrant. Both properties are listed for each of the depicted signals in Table 6.1.

Table 6.1: Time ordering and frequency vectors $\nu = (\nu_t, \nu_\tau)$ of the nonlinear signals in Fig. 6.32. Columns 5 to 7 explain the differences in the time definition compared to conventional 2D experiments).

Experiment	Delay	ν_t	ν_τ	τ	T	t
(a) A-B-B photon echo	$\tau < 0$	$2\nu_B - \nu_A$	ν_A	$-\tau$	$T = 0$	t
(b) A pump - B probe	$\tau < 0$	ν_B	0	$T = 0$	$-\tau$	t
(c) PFID A pu. - B pr.	$\tau > 0$	ν_B	0	τ	$T = 0$	$t - \tau$
(d) B pump - A probe	$\tau > 0$	ν_A	$-\nu_A$	$T = 0$	τ	$t - \tau$
(e) PFID B pu. - A pr.	$\tau < 0$	ν_A	$-\nu_A$	$-\tau$	$T = 0$	t
(f) B-A-A photon echo	$\tau > 0$	$2\nu_A - \nu_B$	$-2\nu_A$	τ	$T = 0$	$t - \tau$

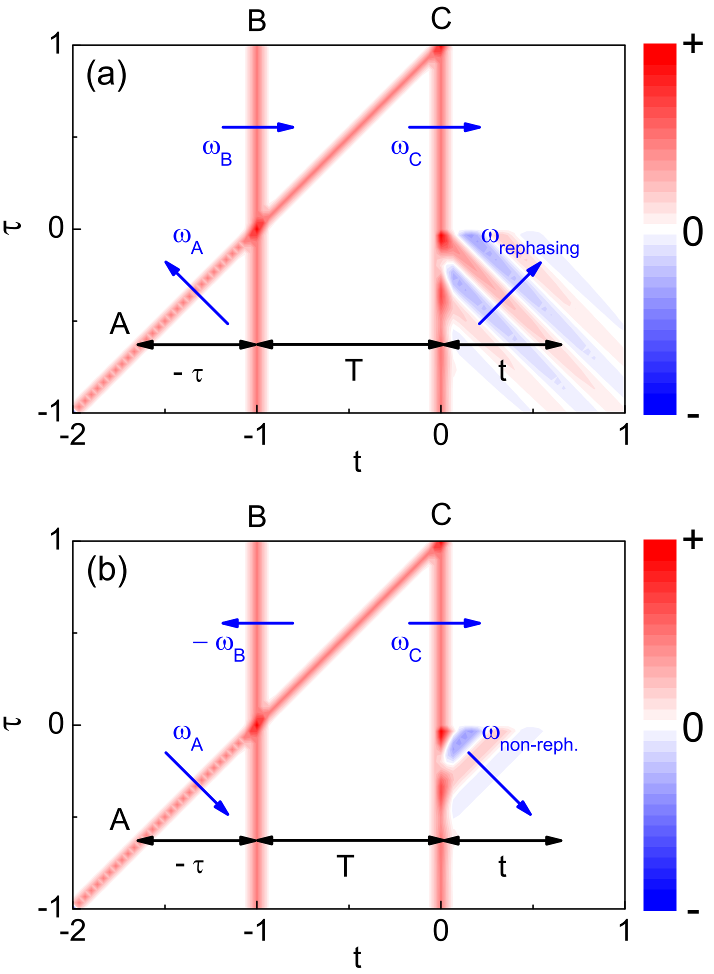

Figure 6.30: Two-dimensional contour plots of three gaussian electric field pulses A, B, and C as a function of both the real time t and the delay τ between pulses A and B. The waiting time T between pulses B and C is a fixed parameter in this plot. (a) The electric field of the photon echo (rephasing contribution to the nonlinear signal) occurs in the quadrant with $t > 0$ and $\tau < 0$ with phase fronts perpendicular to that of pulse A. (b) Corresponding non-rephasing signal identified by phase fronts parallel to that of pulse A. The orientation of the phase fronts in the two-dimensional time domain (t and τ) can be uniquely determined by the orientation of the respective frequency vector ω (blue arrows) in the two-dimensional Fourier domain (ω_t and ω_τ).

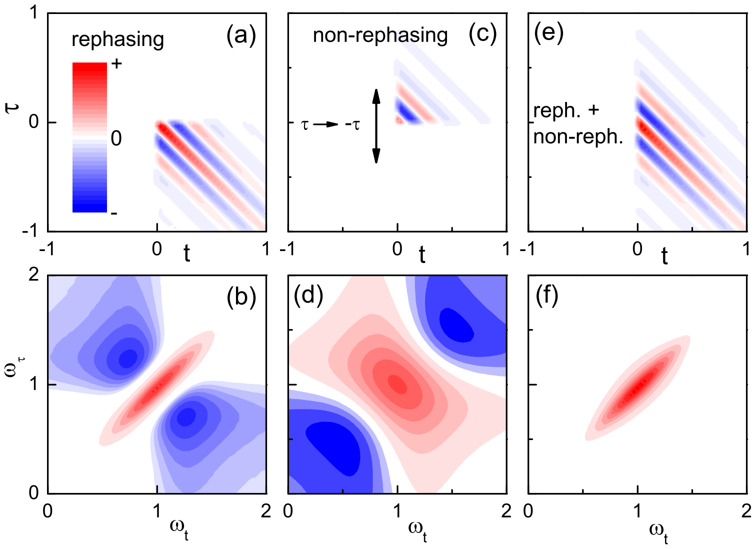

Figure 6.31: (a) The rephasing and (b) nonrephasing four-wave mixing signal in the time domain and (b), (d) in the frequency domain. Sharp time cuts along $\tau = 0$ and $t = 0$ cause phase-twisted line shapes. (e) Adding both signals onto each other avoids the sharp time cut and (f) a purely absorptive line shape is obtained.

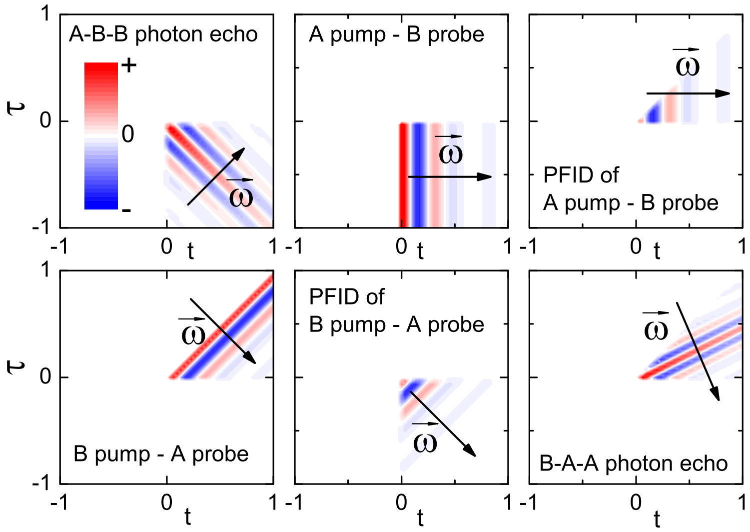

Figure 6.32: The photon echoes, the pump-probe signals, and the perturbed free induction decays in the time domain. The frequency vector ω and corresponding time quadrant identifies each nonlinear signal unambiguously.

6.7 2D THz Correlation Spectroscopy on Multiple Quantum Wells

In this experiment a multiple quantum well structure is studied by linear and 2D spectroscopy. The sample (M4.2112) consists of 20 GaAs quantum wells of 11 nm thickness separated by 20-nm-thick $Al_{0.35}Ga_{0.65}As$ barriers. The barrier centers are doped with Si, resulting in an electron concentration of $n_s = 1.5 \times 10^{10}$ cm^2 per quantum well. Linear absorption measurements were performed using a *Varian 640 – IR* FT-IR spectrometer. The ceramic globar provided light between 500 – 9600 cm^{-1} (i.e., 15 – 290 THz), which was detected using a HgCdTe detector sensitive between 450 – 10000 cm^{-1} (i.e., 1 – 290 THz). The prism shaped samples were placed in the 2 cm wide beam waist of the spectrometer. A screen enclosing the sample assured that all detected light was transmitted through the sample. Using a mesh polarizer we used the spectrum for s polarized light as a reference for the absorption spectrum for p polarized light.

The absorbance of sample M4.2112 is shown in Fig. 6.33 (a). Two intersubband transitions are found at 18 THz and at 25 THz. This agrees well with the predicted $1 \leftrightarrow 2$ and $2 \leftrightarrow 3$ transitions from a $k \cdot p$ calculation. The corresponding bound states are expected at 50 meV (n=1), 120 meV (n=2), and 230 meV (n=3) [see Fig. 6.33 (b)]. While the dipole moments on the $1 \leftrightarrow 2$ and $2 \leftrightarrow 3$ transition are of similar magnitude, the small thermal population of the n=2 subband results in a much weaker $2 \leftrightarrow 3$ absorption.

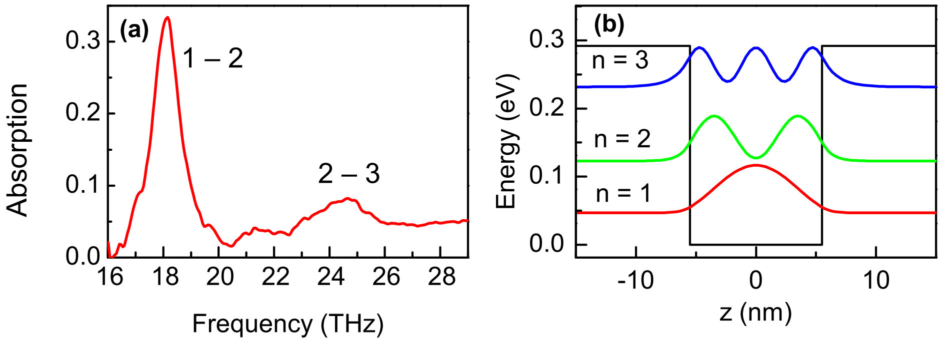

Figure 6.33: (a) Linear intersubband absorption at room temperature. The two absorption lines correspond to the $1 \leftrightarrow 2$ and $2 \leftrightarrow 3$ between bound states in the quantum well. (b) Potential energy and $|\Psi_n(x)|^2$ for the three lowest subbands of AlGaAs/GaAs quantum wells.

The two-dimensional scan using strong THz pulses was performed as described previous. While pulse B is kept constant in the real time, the time of pulse A was varied after each scan. The nonlinear signal emitted from the sample is obtained as the difference $E_{\mathrm{NL}}(t,\tau) = E_{\mathrm{AB}}(t,\tau) - E_{\mathrm{A}}(t,\tau) - E_{\mathrm{B}}(t)$. The electric field as a function of the real time t and the delay time τ is shown in Fig. 6.34 (a). The rephasing A-B-B photon echo contribution to the nonlinear signal in the time domain is depicted in Fig. 6.34 (b). Its nonrephasing counterpart, i.e., the perturbed free induction decay contribution of the B pump-A probe experiment, is depicted in Fig. 6.34 (c).

Applying to the nonlinear signal the procedure discussed in the previous section yields the 2D correlation spectrum in Fig. 6.35 (a). Adjacent to the $1 \leftrightarrow 2$ intersubband transition, two pronounced positive peaks are observed along the diagonal at 17.3 and 19.7 THz. The 2D

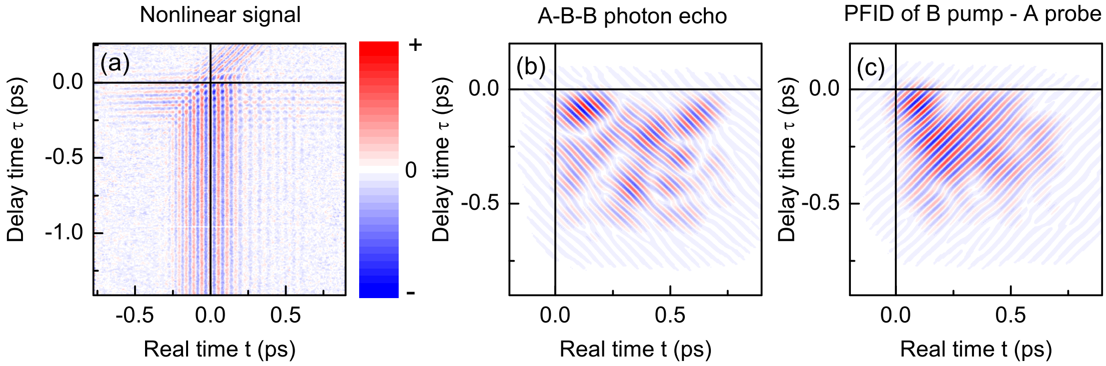

Figure 6.34: (a) Emitted nonlinear signal as function of real time t and delay time τ. (b) Perturbed free induction decay contribution of the B pump–A probe experiment. (c) A-B-B photon echo contribution to the nonlinear signal.

correlation spectrum shows signals along the excitation axis ν_τ exclusively at those positions where the sample absorbs light. Therefore, we plot on the r.h.s. of Fig. 6.35 (a) the linear absorption spectrum for comparison. It should be noted that there is no pronounced diagonal contribution to the 2D spectrum at the spectral position of the $2 \leftrightarrow 3$ intersubband transition at 25 THz, even though pulses A and B have significant spectral density at that spectral position. In addition to the 2D spectrum, we extracted the A pump–B probe signal from Fig. 6.34 (a) and calculated the spectrally resolved transmission change according to

$$\frac{\Delta T(\nu_t,\tau)}{T_0(\nu_t,-\infty)} = \frac{E^*_{\mathrm{NL}}(\nu_t,\tau)E_{\mathrm{B}}(\nu_t)+E_{\mathrm{NL}}(\nu_t,\tau)E_{\mathrm{B}}(\nu_t)^*}{E_{\mathrm{B}}(\nu_t)^*E_{\mathrm{B}}(\nu_t)}. \tag{6.34}$$

The result presented in Fig. 6.35 (d) does not display any signal on the $2 \leftrightarrow 3$ intersubband transition ($\nu_t = 25$ THz) either. Evidently, the nonlinear response of our sample is dominated by the much stronger $1 \leftrightarrow 2$ intersubband transition at $\nu_t = 18$ THz. The A pump–B probe signal in Fig. 6.35 (d) shows an unexpectedly broad spectral width on the $1 \leftrightarrow 2$ transition [red dashed line on the r.h.s. of Fig. 6.35 (d)] which is observed even at late times until the complete decay of the pump-probe signal (not shown).

A most interesting and surprising feature in the measured 2D correlation spectrum [Fig. 6.35 (a)] is the intense negative signal (blue spot) on the diagonal located exactly at the absorption maximum of the $1 \leftrightarrow 2$ intersubband transition at 18 THz. Negative signals on the diagonal are absent in most published 2D spectra. In order to find out which mechanism can cause negative signals on the diagonal for $T = 0$ we performed model calculations.

The usual formalism to derive 2D spectra is based on a perturbative density matrix approach in a rotating wave approximation (e.g., in Ref. [189]), i.e., it neglected non-resonant contributions. Moreover, contributions from multiple interactions of a single pulse during temporal pulse overlap are neglected. To assess such assumptions, we performed density matrix calculations without rotating wave approximation [211]. One important result is the fact that non-resonant terms and multiple interactions can be neglected only when the relation $\omega_{\text{system}} \gg \Delta\omega_{\text{pulse}} \gg \Delta\omega_{\text{system}}$ holds (ω_{system}: transition frequency, $\Delta\omega_{\text{pulse}}$: spectral bandwidth of the pulses, $\Delta\omega_{\text{system}}$: spectral width of the transition). For the experiments discussed in Ref. [189], one estimates a ratio of $\omega_{\text{system}} : \Delta\omega_{\text{pulse}} : \Delta\omega_{\text{system}} = 30 : 3 : 1$ whereas a typical experiment in the THz range has a ratio of only $\omega_{\text{system}} : \Delta\omega_{\text{pulse}} : \Delta\omega_{\text{system}} = 4 : 2 : 1$. For shorter THz pulses (larger $\Delta\omega_{\text{pulse}}$), non-resonant interaction terms come into play. For longer pulses of high intensity, one has to consider multiple interactions of one pulse with the system during the pulse overlap. A general advantage of the density matrix approach is that it is not restricted to the $\chi^{(3)}$ limit and, thus, can describe phenomena like Rabi oscillations [33, 211].

In Figs. 6.35 (b,c) and (e,f) we show 2D correlation spectra and A pump–B probe signals, respectively, calculated for a homogeneously broadened two-level system with parameters close to the $1 \leftrightarrow 2$ intersubband transition of our sample. Panels (b) and (e) display results for the $\chi^{(3)}$ limit, i.e., an interaction of the sample with weak pulses. We get the expected result for the 2D correlation spectrum, a strong positive peak on the diagonal centered at 18 THz. Its shape is round and complemented by small negative signals in its vicinity.

The latter features are a consequence of the small ratio $\omega_{\text{system}} : \Delta\omega_{\text{pulse}} : \Delta\omega_{\text{system}} = 4:2:1$ for our experimental situation. The pump-probe signal calculated in the $\chi^{(3)}$ limit [Fig. 6.35 (e)] displays a perturbed free induction decay at negative delay times and matches at late delay times τ the spectral shape of the linear absorption spectrum almost perfectly. Both the sign of the calculated 2D correlation signal on the diagonal and the spectrum of the pump-probe signal at late delay times are in disagreement with the data in Figs. 6.35 (a,d). We conclude that the measured nonlinear response is beyond the $\chi^{(3)}$ limit.

A prominent mechanism generating a strong negative signal on the diagonal is the interaction of a sequence of strong pulses with the two-level system. Calculations for this limit are shown in Figs. 6.35 (c) and (f). We characterize the strength of the pulses by their pulse area given by

$$\Theta_{\text{A,B}} = \frac{d_{12}}{\hbar} \int_{-\infty}^{+\infty} \Re\left[\mathscr{E}_{A,B}(t)\right] dt. \tag{6.35}$$

d_{12} is the transition dipole moment, $\hbar$ is Planck's constant divided by 2π, and $\Re\left[\mathscr{E}_{A,B}(t)\right]$ is the real part of the slowly varying envelope of the pulses [1]. According to the reduced spectral overlap with the intersubband absorption line an off-resonant pulse has a smaller area than a resonant one, i.e., $\Theta_{\text{A}} \approx 0.5\Theta_{\text{B}}$.

In the particular case shown in Figs. 6.35 (c) and (f), the application of the off-resonant pulse A plus the resonant pulse B with a total pulse area $\Theta_{\text{A}} + \Theta_{\text{B}} = 2\pi$ results in a complete Rabi flop of the two-level system. The complete inversion of the system by the first pulse leads to stimulated emission triggered by the second pulse and a π phase change of the nonlinearly emitted electric field (negative signal on the diagonal in Fig. 6.35 (c). An analysis of the pump-probe part of our calculation [Fig. 6.35 (f)] shows that the Rabi flopping during the pulse overlap causes –at late delay times τ– a pronounced minimum of the A pump–B probe signal at the peak position of the linear absorption spectrum. We see a precursor of this theoretically predicted dip in our experimental data [red dashed line r.h.s. of Fig. 6.35 (d)]. Based on the strong resemblance of Fig. 6.35 (a) with panel (c) and of Fig. 6.35 (d) with panel (f), we assign the negative peak on the diagonal of the 2D spectrum and the spectral envelope of the pump-probe signal at late delays to a 2π Rabi flop. The extremely large dipole moment of the intersubband transition $d \approx e_0 \times 2.5$ nm (e_0: elementary charge) allows for a very strong coupling to the THz field with the result that a 100 fs long resonant THz pulse with an amplitude of 50 kV/cm is already a π-pulse. Thus, even non-resonantly driving THz pulses with amplitudes of several tens of kilovolts per centimeter can be used for quantum control in collinear 2D terahertz spectroscopy similar to the well developed concepts in NMR [217].

---

[1] Please note that the relation $\Theta = \int \Omega_{Rabi} dt$ is not strictly fulfilled for nonresonant interactions beyond the rotating wave approximation.

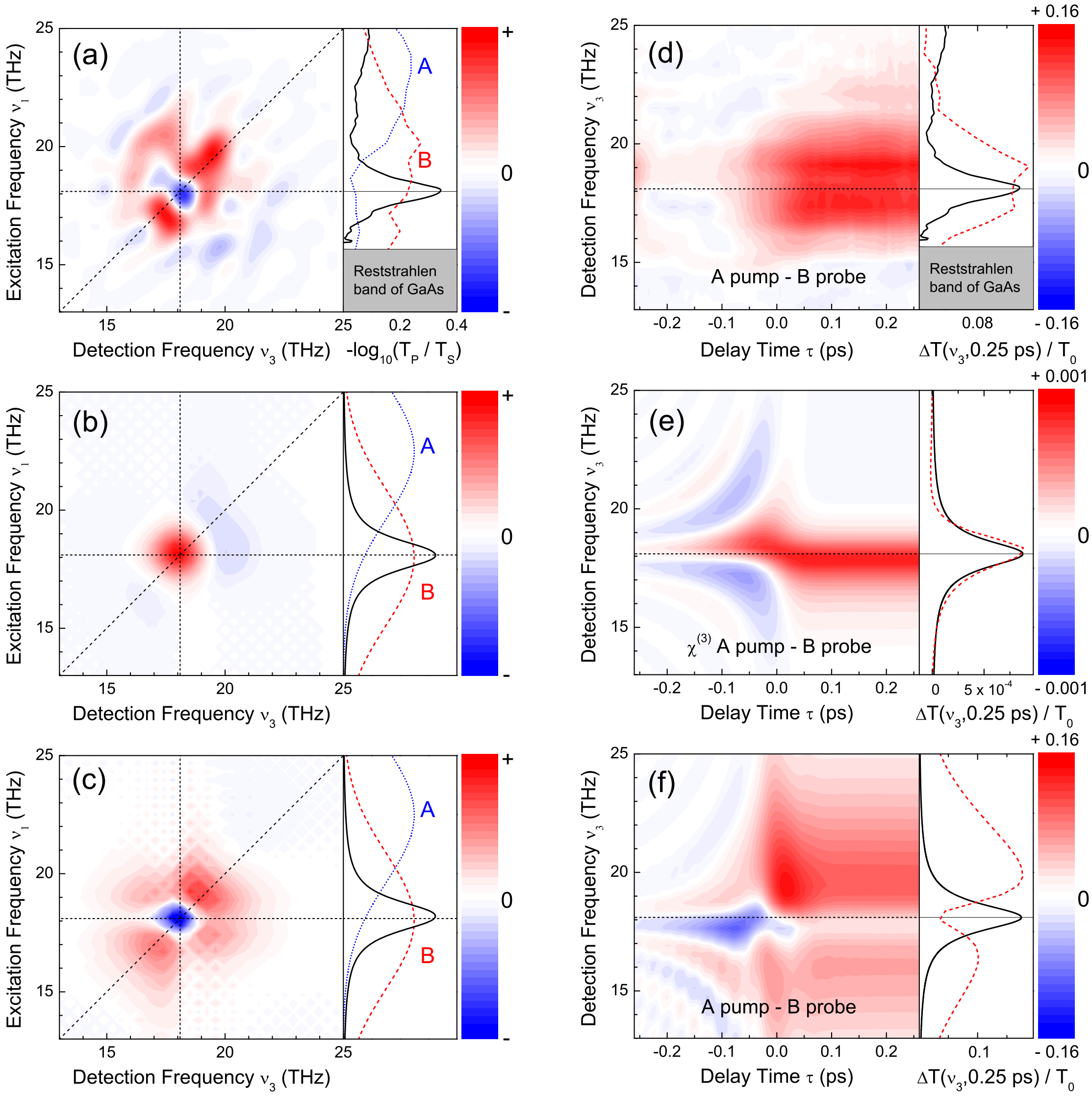

Figure 6.35: (a) 2D correlation spectrum as a function of the excitation frequency ν_τ and detection frequency ν_t obtained from the measured 2D scan shown in Fig. 6.34. The linear absorption spectrum and pulse spectra are shown for comparison on the right hand side. (b) Calculated 2D correlation spectrum for a homogeneously broadened two-level system driven by weak pulses, i.e., the $\chi^{(3)}$ limit. (c) Same two level system driven by strong pulses. Applying the off-resonant pulse A plus the resonant pulse B results in a complete Rabi flop of the two-level system, i.e., they have together a pulse area of $\Theta_\mathrm{A} + \Theta_\mathrm{B} = 2\pi$. (d,e,f) Experimental and calculated signals of the corresponding A pump–B probe experiment. Here, the spectrally resolved transmission change $\Delta T(\nu_t, \tau)/T_0(\nu_t, -\infty)$ is plotted as a function of delay τ (contour plots). Panels on the right hand side: Linear absorption spectrum (black lines) and cross section of the pump-probe signal for $\tau = 0.25$ ps (red dashed lines).

6.8 Energetic Couplings between Asymmetric Double Quantum Wells

In the last experiment presented in this thesis the asymmetric double quantum well structure (a-DQWS) M4.2118 is investigated. The sample consists of 10 GaAs double quantum wells of 9 and 12 nm thickness separated by 2-nm-thick $\mathrm{Al_{0.35}Ga_{0.65}As}$ barrier. Each double quantum well is separated by a barrier of 15 nm. The barrier centers are doped with Si, resulting in an electron concentration of $n_s = 1 \times 10^{12}$ cm^2 per double quantum well. The properties of all investigated quantum well sample are summarized in Appendix 7.

Linear measurements were performed in a wide spectral range between 2 and 40 THz at different temperatures at the Helmholtz Zentrum Berlin (Bessy). The transmitted synchrotron radiation between 2 THz and 17 THz was detected with a helium-cooled bolometer within a FT-IR spectrometer (*Bruker* 66/*v*). Higher frequencies up to 60 THz were provided by a globar and detected with a nitrogen-cooled HgCdTe detector. The black dashed line in Fig. 6.36 (a) depicts the absorbance at 7 K and the red line depicts the absorbance at room temperature. We find two distinct absorption peaks at 17 THz and 24 THz, indicating the fundamental transitions in the broad and in the narrow well. At 7 K we observe a slight blue shift of around 0.7 THz for both transition frequencies.

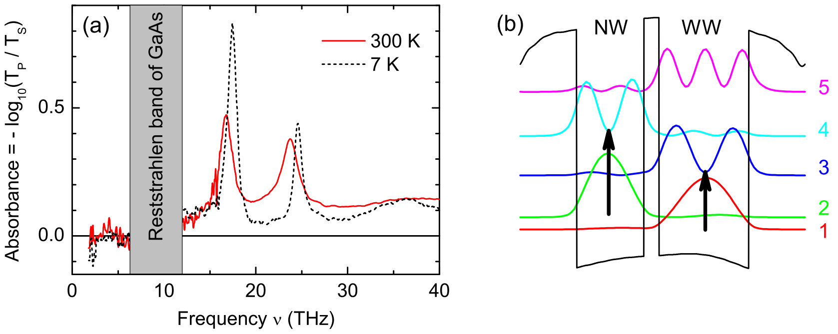

Figure 6.36: (a) Linear transmission measurements between 2 and 40 THz for 7 K (black dashed line) and at room temperature (red solid line). (b) Calculated electronic wavefunctions in the a-DQWS. The fundamental transitions in the broad and in the narrow quantum well agree well with the observed absorption lines.

A single particle $k \cdot p$ calculation [218, 219] yields the spatial density of the electronic wave functions within the quantum wells, Fig. 6.36 (b). The transitions $1 \leftrightarrow 3$ in the broad well (17 THz) and $2 \leftrightarrow 4$ in the narrow well (24 THz) match perfectly with the observed linear absorption lines. The narrow spectral widths of 1 THz for both lines at 7 K point to homogenously broadened lines. While the spectral width of the $1 \leftrightarrow 3$ transition increases moderately by 0.4 THz at room temperature, a drastic broadening is observed for the $2 \leftrightarrow 4$ transition. The spectral width nearly doubles to 2 THz (red solid line). The distinct shoulder to lower frequencies points to an additional transition between both peaks. The population of the ground state and the excited state is deducted from the enclosed area under both absorption peaks. As expected from a Boltzmann distribution we find a significant increase of the $1 \leftrightarrow 3$ absorption at 7 K and a concomitant decrease of the $2 \leftrightarrow 4$ absorption line. The reason for the additional oscillator strength at room temperature is investigated in detail with collinear 2D THz spectroscopy.

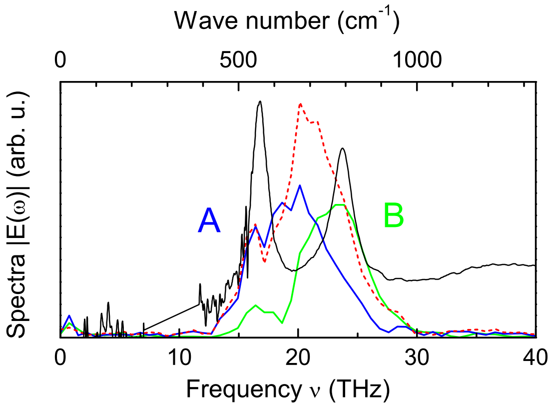

Figure 6.37: Pulse A (blue dashed dotted line) excites primarily the transition at 18 THz in the broad quantum well and pulse B (green dashed line) the transition in the narrow quantum at 24 THz. Two different colors of the pulse cover a wide range from $15 < \nu_t < 25$ THz in the 2D spectrum.

The frequencies of the two incident pulses were tuned to the absorption frequencies of the sample (see Fig. 6.37). While pulse A (blue dashed dotted line) excites primarily the $1 \leftrightarrow 3$ transition at 18 THz, pulse B (green dashed line) excites the $2 \leftrightarrow 4$ transition at 24 THz. Both pulses are spectrally broad (> 5 THz) and moderate intensities of each pulse overlap the entire spectral region of interest. The incident field amplitude is 60 kV/cm. The experiments were performed at room temperature. Pulse B is kept constant in the real time t, while pulse A is shifted in the delay time τ after each scan. Fig. 6.38 (a) shows the nonlinearly emitted field from the sample as a function of both time axes. One recognizes the pump-probe signals with the second of both pulses. The magnitude of the Fourier transform of this nonlinear signal is presented in Fig. 6.38 (b). The 2D spectrum is dominated by the pump-probe spots at $\nu_{\mathrm{AB}} = (0, 20\ \mathrm{THz})$ and $\nu_{\mathrm{BA}} = (-20, 20\ \mathrm{THz})$. The photon echo spots at $\nu_{\mathrm{PE1}} = (20, 20\ \mathrm{THz})$ and $\nu_{\mathrm{PE2}} = (-40, 20\ \mathrm{THz})$ are significantly weaker but can clearly be identified. Additionally, one finds a difference frequency mixing signal at $\nu_{\mathrm{DF}} = (20\ \mathrm{THz}, 0)$ [the spot at $(20\ \mathrm{THz}, 0)$ is the complex conjugate of ν_{DF}]. In the time domain this $\chi^{(2)}$ signal shows up as horizontal lines near the pulse overlap. A 2D scan without the sample in place identifies the ZnTe crystal as the source for the observed $\chi^{(2)}$ signal.

We start our data analysis with the pump-probe signal at $\nu_{\mathrm{AB}} = (0, 20\ \mathrm{THz})$. The transmission changes for different delay times τ are shown in Fig. 6.39 (a). One finds a prominent transmission decrease at a real time frequency of $\nu_t \approx 21$ THz and a transmission increase at $\nu_t \approx 24$ THz. Fig. 6.39 (b) highlights the main observations using three cuts through the contour plot at $\nu_t = 21$ THz (blue line), $\nu_t = 24$ THz (red line), and $\nu_t = 22$ THz (black line). For better comparison the curve at $\nu_t = 21$ THz is plotted with an opposite sign. While the transmission decreases immediately at $\tau = 0$, the transmission increase is delayed by 180 fs. This points to relaxation processes within the sample. Furthermore, a prominent oscillation with a period of 110 fs is found at $\nu_t = 22$ THz.

The 2D correlation spectrum is shown in Fig. 6.40. The linear absorption spectrum is shown in the right panel. In agreement to the linear absorption spectrum, we find two peaks on the diagonal at (18 THz, 18 THz) and at (24 THz, 24 THz). Interestingly, one observes additional signals in the spectral region between both fundamental transitions.

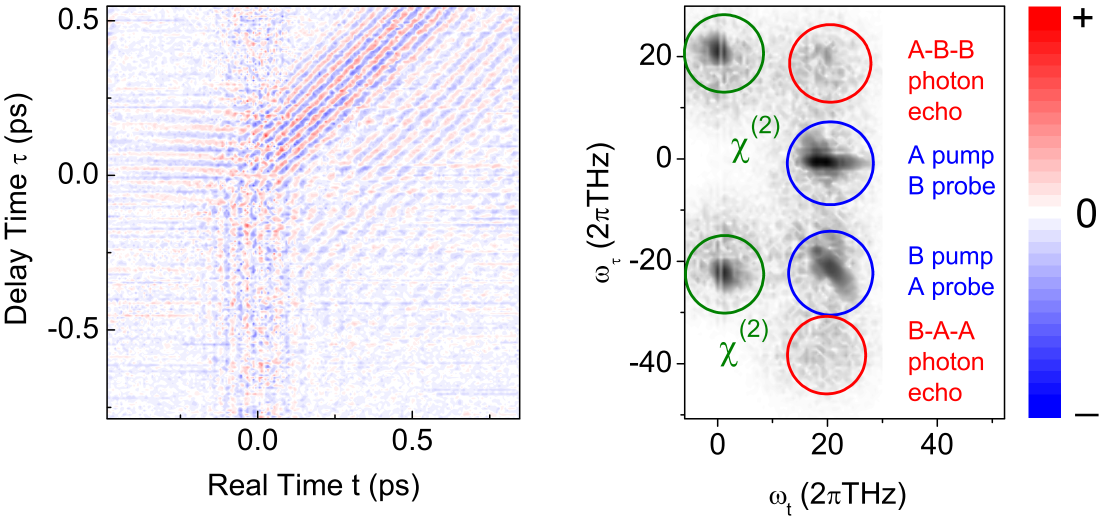

Figure 6.38: (a) The nonlinear signal emitted from the sample as a function of τ and t. (b) The magnitude of the Fourier transform exhibits pump-probe spots, photon echo spots, and a difference frequency signal.

Discussion

Each of the three recorded signals, the linear transmission (Fig. 6.36), the spectrally resolved pump-probe signal (Fig. 6.39), and the 2D correlation spectrum (Fig. 6.40), displays an absorption between both fundamental transitions at 18 and 24 THz. The linear absorption spectrum exhibits a shoulder at 22 THz only at room temperature. The fact, that this spectral region becomes transparent at 7 K points to a phonon effect. This explanation is confirmed by the spectrally resolved pump-probe spectrum. At 22 THz, a strong oscillation with a period of the inverse LO phonon frequency is found. This suggests that the signals around 22 THz in the 2D correlation spectrum are also caused by phonons. Since the measurements on multiple quantum wells demonstrated phonon oscillations (Fig. 6.19), we conclude that coupling to LO phonons modifies the energy levels of a a-DQWS as well. Indications for strong coupling of intersubband transitions to LO phonons were already found in spectral hole burning experiments performed on strongly polar materials like GaN/AlGaN heterostructures [206, 220].

LO phonons have an equidistant ladder of lattice excitations shown on the r.h.s. in Fig. 6.41. The mixing of electronic states of a quantum well and phonon states forms the quasi-particle called intersubband polaron. Depending on the coupling strength a completely new polaronic energy level system is constituted. We model the polaronic system of the a-DQWS, i.e., the coupling of the electronic with the LO phonon system with a direct product. The resulting Hamiltonian of the complete a-DQWS is given by:

$$\begin{aligned} H &= H^0_{\mathrm{IS}} \otimes I_{\mathrm{LO}} + I_{\mathrm{IS}} \otimes H^0_{\mathrm{LO}} \\ &\quad - (D_{\mathrm{IS}} \otimes I_{\mathrm{LO}} + I_{\mathrm{IS}} \otimes D_{\mathrm{LO}}) E(t) \\ &\quad + \alpha (D_{\mathrm{IS}} \otimes I_{\mathrm{LO}})(I_{\mathrm{IS}} \otimes D_{\mathrm{LO}}) \end{aligned} \tag{6.36}$$

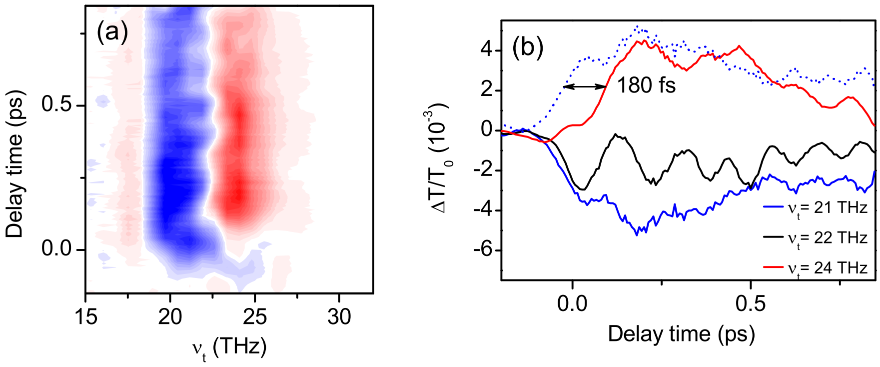

Figure 6.39: (a) Spectrally resolved transmission changes induced by pulse B at different delay times τ. Over the entire range of delay times a transmission decrease is observed at $\nu_t = 21$ THz and a delayed increase in transmission is observed for $\nu_t = 24$ THz. (b) Cuts along the delay time for $\nu_t = 20$ THz (blue line, multiplied by -1 for clarity) and $\nu_t = 24$ THz (red line). An oscillatory behavior with a period of 110 fs is found at 22 THz.

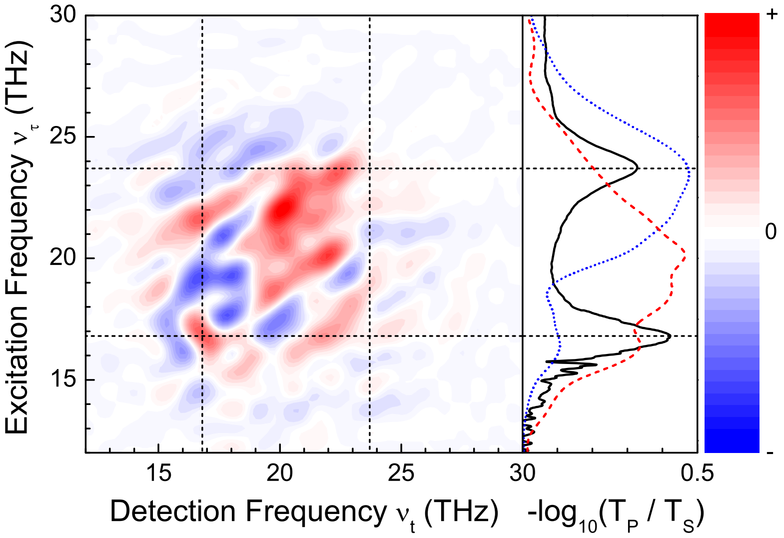

Figure 6.40: The 2D correlation spectrum of the a-DQWS exhibits fundamental transitions on the diagonal and additional signals in the spectral region in between. The linear absorption spectrum and the incident pulses are shown for comparison on the right hand side.

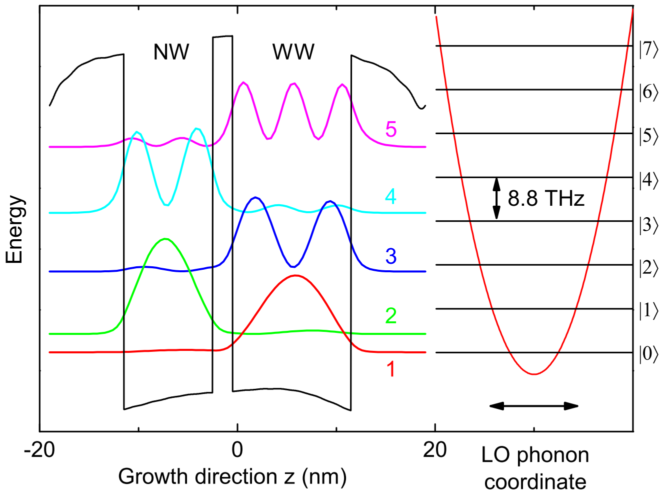

Figure 6.41: (a) The anharmonic electronic system couples to (b) the harmonic lattice system of equidistant LO phonon excitations. To model the resulting excitations of the entire system, we assume the electronic system to be equidistant.

H^0_{IS} and H^0_{LO} are the unperturbed Hamiltonians, I^0_{IS} and I^0_{LO} the identity operators of the respective Hilbert space, and D^0_{IS} and D^0_{LO} are the electric dipole operators of the intersubband transition and the phonon oscillator, respectively. The second term describes the coupling to the electromagnetic field and the last term proportional to α stands for an electric dipole-dipole interaction between the two transition dipoles.

The results of the calculations are summarized in Figs. 6.42. The contour plot in Fig. 6.42 (c) demonstrates the expected transitions of the polaronic system as a function of the dimensionless coupling parameter α. Without coupling (for $\alpha = 0$) the electronic transitions and the LO phonon excitation exist independently from each other. This situation is depicted as a dash-dotted blue line in Fig. 6.42 (a). Essentially, it consists of two intra-well transitions ($1 \longrightarrow 3$ and $2 \longrightarrow 4$) and two photon assisted tunneling processes, i.e., $2 \longrightarrow 3$ and $1 \longrightarrow 4$ transitions.

In contrast, with increasing dipole-dipole coupling, i.e., for $0 < \alpha \leq 1$ the calculated linear absorption spectrum [contour plot Fig. 6.42 (c)] gradually develops distinct polaronic signatures. For $\alpha \approx 1$, i.e., a very strong coupling of electrons and phonons, we observe pronounced changes of the intersubband polaron absorption spectrum which explain our experimental findings. The solid line in Fig. 6.42 (a) is the expected linear absorption spectrum for $\alpha \approx 1$. It resembles the main features of the linear absorption spectrum at room temperature [Fig. 6.42 (b)]: (i) the tunneling-assisted $2 \longrightarrow 3$ transition is almost completely suppressed and (ii) a new transition occurs at $\nu_t = 22$ THz between the two major lines. Exactly at this excitation frequency $\nu_t = 22$ THz we observe in the experimental 2D correlation spectrum (Fig. 6.40) the highest signal on the diagonal and pronounced cross peaks with the fundamental $1 \longrightarrow 3$ transition. The polaron model predicts that the excitation at $\nu_t = 23$ THz is the Stokes phonon sideband of the photon assisted tunneling $2 \longrightarrow 3$ transition. This is fully confirmed by the LO phonon quantum beat with 8.8 THz observed at a detection frequency of $\nu_t = 22$ THz in the spectrally resolved pump-probe measurement (Fig. 6.39).

Finally, a more quantitative picture of the intersubband polaron coupling is derived, i.e., in particular the dimensionless coupling constant α is estimated. A good overview on electron-

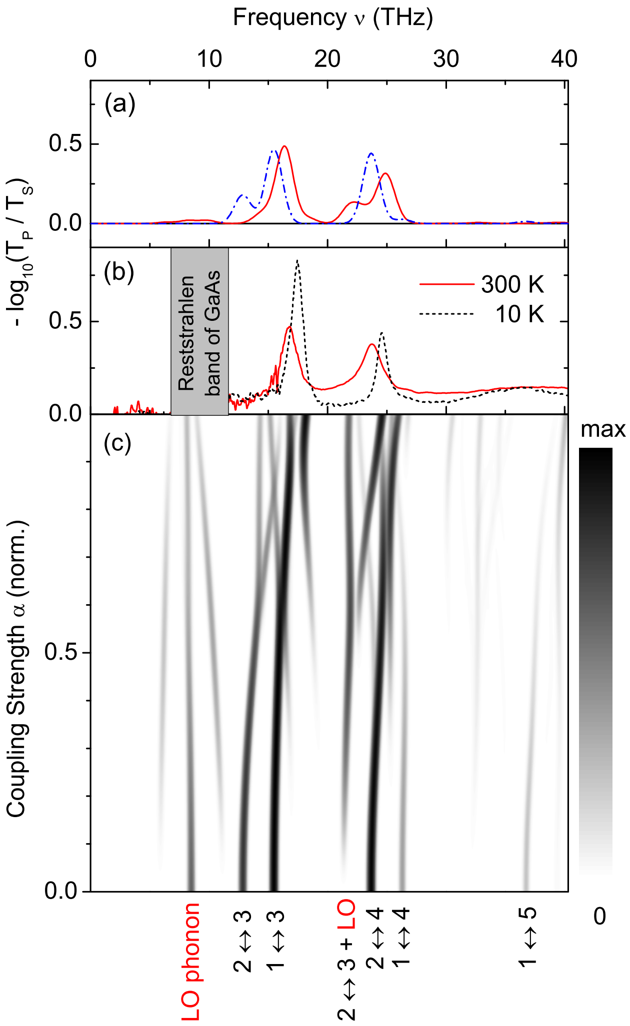

Figure 6.42: (c) Predicted transitions of the coupled electron-phonon system as a function of the coupling parameter α. (a) The expected linear absorption spectra without coupling (dashed blue line) and with strong coupling ($\alpha = 1$, red solid line). (b) The experimentally obtained linear absorption spectra for comparison.

phonon couplings in nanostructures of various dimensions can be found in Ref. [221]. In particular Section 6.4 of this review article contains the relevant information. Interestingly, one gets the strongest coupling for the lowest dimension of the system, i.e., the smaller the volume covered by the wave function of the electron the more pronounced the polaronic signatures in intersubband(-level) absorption.

In the a-DQWS the value of α depends on the electron-LO phonon coupling strength α_{ep} and on the spatial extent of the electron in-plane wavefunction. The high value of $\alpha \approx 1$ derived from our data points to a substantial in-plane localization. There are two possible reasons for such a strong localization: On the one hand the interface has monolayer fluctuations. This static disorder, however, is much too weak to explain the strong polaronic character of the IS absorption. On the other hand, scattering processes can lead to dynamic localization. Interestingly, one gets the right value for $\alpha \approx 1$ for an in-plane electron wave packet having the size of the thermal De Broglie wavelength: $\Delta x^2 = \hbar^2/4m_{\mathrm{eff}}k_{\mathrm{B}}T$. This means that spatially inhomogeneous electronic wave functions play a crucial role in the physics of intersubband polarons. This important fact was learned already in various experiments on polarons in 3-dimensional bulk material in Section 3.4 [4, 222].

In conclusion, we have demonstrated the measurement of two-dimensional correlation spectra in the THz domain. In a collinear interaction geometry of phase-locked pulse sequences with a semiconductor quantum well sample, different contributions to the nonlinear intersubband response of electrons were separated and analyzed by calculations beyond the rotating-wave approximation. The shape of the 2D correlation spectrum and the spectrum of the pump-probe signal display features due to a Rabi flop induced by THz pulses of moderate electric field strength. The 2D correlation spectrum of an asymmetric double quantum well structure demonstrated a strong coupling on LO phonons and energetic couplings between resulting polaronic states are observed. A simple model describes the coupling of electronic and LO phonon excitations with a direct product. The results reproduce the observed experimental features. The strong coupling of the large intersubband dipoles to the THz field will allow for implementing coherent control schemes to steer the response of the system, very similar to the concepts applied in nuclear magnetic resonance. Moreover, collinear 2D THz spectroscopy has the potential to unravel complex coupling schemes of elementary excitations in bulk and nanostructured solids.

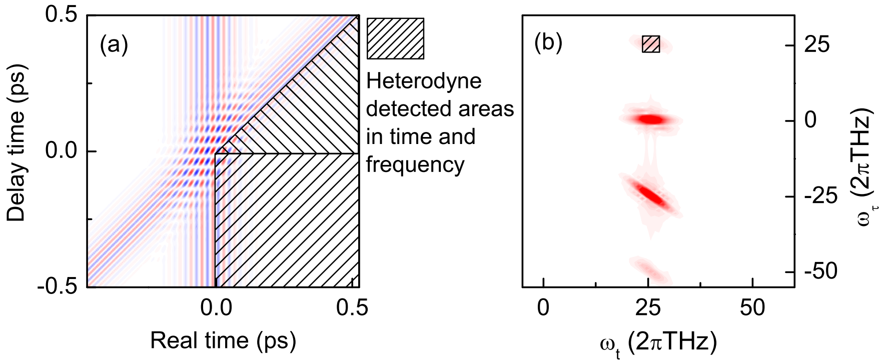

Figure 6.43: (a) Differences between 2D spectroscopy with collinear and noncollinear beam geometry (a) in the time domain (b) and in the frequency domain. While is fixed real time window is measured in a collinear beam geometry, the detection time starts with last pulse for a noncollinear setup. (b) 2D correlation spectra monitor exclusively a section around the photon echo [189], while a much larger spectrum is displayed in collinear 2D THz experiments.

6.9 Remarks on Collinear 2D Spectroscopy

To put our collinear 2D THz method into a wider context, in this section the novelties of collinear 2D spectroscopy are discussed from the perspective of conventional 2D photon echo methods. It makes no difference, whether the phase-resolved detection is accomplished with heterodyne detection or with electrooptic sampling. The main difference to 2D THz spectroscopy is the collinear beam geometry. It is due to the diffuse propagation direction of the THz radiation and to the detection with electrooptic sampling, that a noncollinear beam geometry is hardly to realize at THz frequencies.

The difference in the time definition is illustrated in Fig. 6.43. The local oscillator in a noncollinear experiment defines the detection time, which is set into relation with the excitation time via the phasing procedure. Thus the detection time starts always with the last pulse [see black hatched areas in Fig. 6.43 (a)]. Collinear electrooptic sampling instead measures a fixed detection time window. This means both detection times are equivalent for $\tau < 0$ if pulse A, which is constant in time, acts last with the sample. For $\tau > 0$ our detection time includes a further τ dependence and, e.g., the photon echo appears at $\omega_\tau = 2\omega_t$.

Noncollinear experiments record exclusively the photon echo, which is displayed in a 2D correlation spectra of about 150 $\text{cm}^{-1} \times 150\ \text{cm}^{-1}$ or 3 THz × 3 THz [see hatched area in Fig. 6.43 (b) and Ref. [189]]. Collinear 2D THz spectroscopy instead monitors all present nonlinear signals in the 2D spectrum. The detected spectral range is limited in the real time frequency ω_t by the detector bandwidth and in the delay time frequency only by the step size $\Delta\tau$.

One advantage of the 2D Fourier transformation is the improved signal-to-noise ratio for each detected nonlinear signal. This is shown exemplarily for the pump-probe signal in Fig. 6.44. The three lines depict the pump-probe spectra extracted from the identical data set. The black line represents a conventional one-dimensional pump-probe spectrum for one particular delay time. Averaging the one-dimensional pump-probe spectra for all delay times yields a better signal-

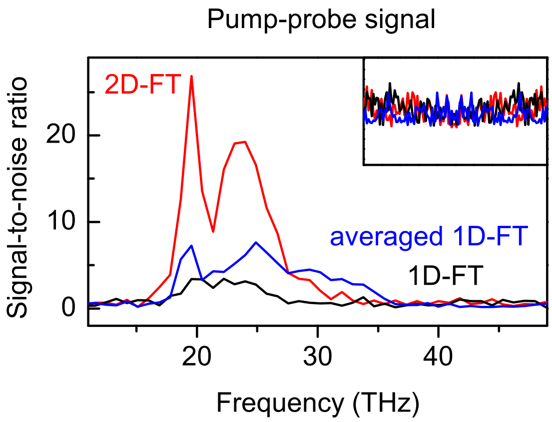

Figure 6.44: Conventional pump-probe spectra for one particular delay time (black), averaged one-dimensional pump-probe spectra (blue), and two-dimensional pump-probe spectra (red).

to-noise ratio as demonstrated by the blue line. A further drastic improvement by the factor of four is achieved, if the pump-probe signal is Fourier transformed in two time dimension (red line). The inset demonstrates that the noise level of all three spectra in Fig. 6.44 is equal. A 1D Fourier transform decouples the signal from all noise, which fluctuates with another frequency. A 2D Fourier transform decouples the signal additionally from all noise, which has another time dependence on the second pulse than the pump-probe signal. This causes the substantially better separation of signal and noise along two time dimensions.

In general a time axis is defined solely by two incidents, i.e., two pulses in our case. In order to lift up the degeneracy of nonlinear signals, the observed process has to be linked to the two defining incidents. This is assured by the observation of a N-wave mixing signal along the delay time axis. Since we arbitrarily control the delay between both pulses, the delay time axis and the real time axis are linear independent and orthogonal to each other. The delay time τ is given by the envelopes of both pulses. On a coarse timescale ω_τ separates different physical occurrences like pump-probe spots, photon echoes, six-wave mixing processes and so on. But on the fine time scale of the carrier-wave frequency of the photon echo, ω_τ represents the excitation frequency and monitors energetic couplings.

One could argue that the real time t is a delay time between the sampling pulse for electrooptic sampling and the THz pulse to measure as well. The fundamental difference to the delay time τ, however, is the strict link to the reality. Since the oscillation of the THz field, as well as the extended optical path of the sampling pulse are strictly determined, t represents indeed a real time, which measures frequencies like a spectrometer.

The employment of three or only two pulses in principle makes no difference. However, for 2D relaxation spectra with a waiting $T \neq 0$ three incident pulses are necessary. One additional Michelson interferometer could split the second pulse and introduce an additional waiting time $T \neq 0$ in our setup. Two choppers would be still sufficient to extract the nonlinear 2D signal. Since we claimed the complete equivalence of ω and $\mathbf{k}$, we conclude this chapter with some general considerations about space ($\mathbf{k}$) and time (ω).

6.10 General Relation between k and ω

Applying a second pulse in an experiment introduces necessarily a second delay time axis τ. This translates into a second frequency component ω_τ, if a nonlinear process induced by both pulses is investigated. We pointed out, that the resulting frequency vector ω is completely equivalent to the **k** vector in space. In the following we will contemplate shortly about the relation between frequency, defining the time, and the wavenumber **k**, defining the space. We will point out some consequences, which lead us to an intuitive illustration of relativistic effects within the unit circle.

Definition of Time and Space

To get an idea of time, we consider first how it is measured. Each clock consists of an oscillator and a mechanism to count the periods. In Fig. 6.45 (a) a pendulum oscillating with ω_0 is shown. A modern atomic clock employs an atomic transition in Cs at a frequency of ω_0. $9,192,631,778 \approx 9 \times 10^9$ periods of this transition frequency ω_0 define nowadays one second. Counting the electric field oscillations and summarizing a certain number to seconds or minutes yields the time T [see Fig. 6.45 (b)].

$$t = 1\text{s} = 9 \times 10^9 \text{ periods of } \omega_0 \tag{6.37}$$

$$\Rightarrow T = \omega_0 t \tag{6.38}$$

Like the unit of time, also the unit of space, the meter, is defined by a certain number of periods of the frequency ω_0. The only difference is a multiplication with the light velocity (c) resulting in a wavevector $\mathbf{k} = \omega/c$. The official definition says: "One meter is the distance traveled by light in vacuum in $1/299,792,458$ of a second." The definition of a second and the wavenumber $k = l^{-1}$ allows to express the definition of one meter of length (l) as follows:

$$l = 1\text{m} = c \cdot \frac{1s}{299,792,458} \approx c \cdot \frac{9 \times 10^9}{3 \times 10^8} \text{ periods of } \omega_0 \tag{6.39}$$

$$\Rightarrow (kc)^{-1} = 30 \text{ periods of } \omega_0 \tag{6.40}$$

Illustration of the Relativistic Effects on the Unit Circle

It was mentioned above, that the delay time frequency vector ω_τ and the real time frequency vector ω_t stand orthogonal on each other, because both frequencies are completely independent from each other. The real time t is strictly determined by the reality and the delay time τ is arbitrarily controlled by the experimenter. What if we consider two noncollinear or even orthogonal real time frequencies? One could imagine a constellation depicted in Fig. 6.46. With the velocity between two inertial systems, the enclosed angle between both frequency vectors increases until it reaches 90° at light velocity. Measuring the time of the moving inertial system regards only the projected frequency component $\omega_0' < \omega_0$. Thus moving clocks proceed slower, $T > T' = \omega' t$. Photons moving with the light velocity c exhibit no projected frequency component at all, $\omega' = 0$, and accordingly no time passes by.

To approach this issue in a more general way, we consider an inertial system consisting of just of one particle with the mass at rest m_0. We describe our inertial system with two orthogonal

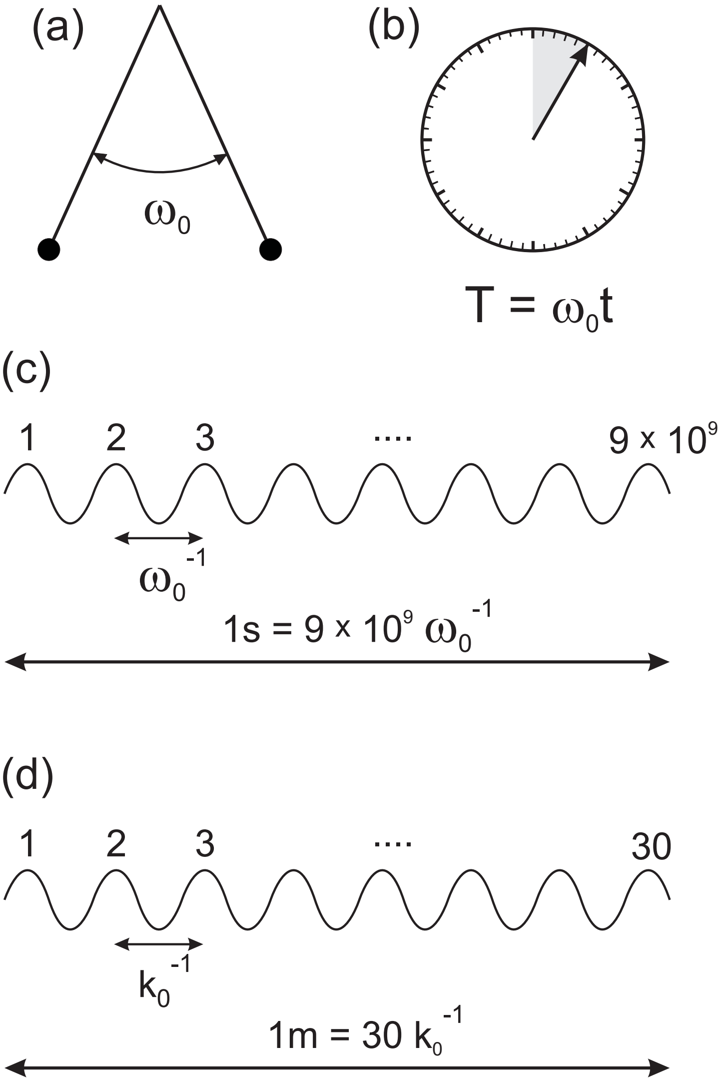

Figure 6.45: (a) A clock consists of an oscillator at ω_0 and a counter. (b) The counter translates the number of periods into seconds and minutes, $T = \omega_0 t$. (c) 9×10^9 periods (ω_0^{-1}) at the transition frequency ω_0 define a second. (d) A fraction of a second multiplied with the light velocity c defines a meter, i.e., 30 periods in space (k_0^{-1}) at ω_0.

axes, one for the real time frequency ω, defining the time of the system, and one for one room coordinate k^{-1}. Also Lorentz vectors describe a time axis standing orthogonal on the spatial axes [223].

A second inertial system moving with the relative velocity v is shown red in Fig. 6.47 (b). Both coordinate systems enclose an growing angle with v. From the own inertial system (black) one measures only the projections of the other inertial system (red). We obtain for the projected space coordinate k', $\frac{k'}{k_0} = \frac{mv\hbar}{m_0 v\hbar} = \frac{m}{m_0}$, with m for the relativistic mass. According to de-Broglie each moving mass exhibits a frequency component of $\omega_{\mathrm{DB}} = \frac{m_0 vc}{\hbar}$. The projection onto the frequency axis yields $\frac{\omega_{\mathrm{DB}}}{\omega_0} = \frac{m_0 vc\hbar}{m_0 c^2\hbar} = \frac{v}{c}$. Also the eigenfrequency of the system changes from ω_0

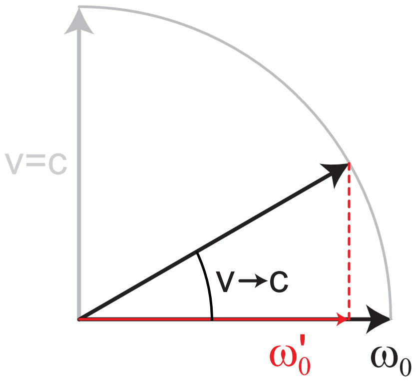

Figure 6.46: Two noncollinear real time frequency vectors ω_0 enclose an angle proportional to the relative velocity of both inertial systems. Since the moving clock seems to operates only with the projected frequency ω'_0, time proceeds slower in the moving inertial system. No time passes by ($\omega'_0 = 0$) for photons moving with c.

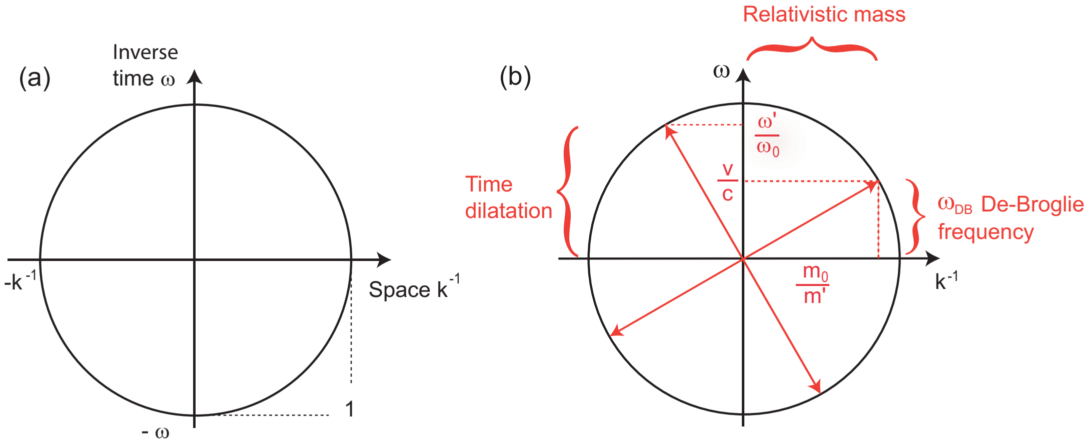

Figure 6.47: (a) Coordinate system illustrating time (ω) and space [k^{-1}], matter and antimatter. Two inertial systems moving with respect to each other introduce a rotation, which results in a relativistic mass m', time dilatation T', Length contraction L', and the Doppler effect.

to ω'. Using the theorem of intercepting lines, we obtain $\frac{\omega'}{\omega_0} = \frac{m}{m_0}$. Since the projected values are equal to the original values at rest, the radii of the circles in Fig. 6.47 are 1. This explains in an intuitive way the relativistic phenomena of an relativistic mass m, the time dilatation T', and the length contraction $L' = T'c$. Using the sentence of Pythagoras we obtain

$$m' = \frac{m_0}{\sqrt{1-\left(\frac{v}{c}\right)^2}} \tag{6.41}$$

$$T' = T_0\sqrt{1-\left(\frac{v}{c}\right)^2} \tag{6.42}$$

$$L' = L_0\sqrt{1-\left(\frac{v}{c}\right)^2}. \tag{6.43}$$

An external photon provided a reference frequency and thus the clock rate to measure the time. It is interesting to note that also a mass particle itself seems to feature an eigenfrequency, which determines, e.g., the time to decay. Even the classical eigenfrequency of a harmonic oscillator $\omega_0 = \sqrt{\frac{F}{lm_0}}$, with $\sqrt{\frac{F}{l}}$ for the spring constant, yields the identical time dilatation as in Eq. (6.42).

Also the Doppler effect is easily derived using this picture. Two contributions shift the emitted frequency from a moving source. Firstly, the time dilatation $\omega' = \omega_0\sqrt{1-\left(\frac{v}{c}\right)^2}$ and secondly, the de-Broglie frequency $\omega_{\mathrm{DB}} = \omega'\left(\frac{v}{c}\right)$ of the emitting system. It corresponds in Fig. 6.47 (b) to the sum of the projected frequency ω' and the projected de-Broglie frequency $\omega' \cdot \frac{v}{c}$. Depending on whether both systems approach or move away from each each the k^{-1} or the $-k^{-1}$ component, i.e., a positive or negative velocity, has to be considered. This yields in agreement with the literature [223]:

$$\omega_{\mathrm{D}}\left(1 \pm \frac{v}{c}\right) = \omega_0\sqrt{1-\left(\frac{v}{c}\right)^2} \tag{6.44}$$

The identical results are obtained by considering the energy of the system. It can be measured by stopping the photon ($E_{\mathrm{ext}} = \hbar\omega_0$ for $m_0 = 0$) or by annihilating the mass ($E_{\mathrm{int}} = mc^2$ for $m_0 \neq 0$). The internal energy (E_{ext}), contained in the mass, and the external energy (E_{ext}) contained in the velocity, are always equal and represent two different perspectives on the same entity. Therefore, the frequency and the space component can be converted into each other. Bringing matter and antimatter onto one position reduces the mass at rest to zero and generates photons of the frequencies ω and $-\omega$.

$$E^2 = (\hbar\omega_0)^2 = (m_0c^2)^2 + (\mathbf{p}c)^2 \tag{6.45}$$

$$\Leftrightarrow \left(\frac{E_{\mathrm{ext}}}{E_{\mathrm{int}}}\right)^2 = \left(\frac{\hbar\omega}{mc^2}\right)^2 = 1 = \left(\frac{m_0}{m}\right)^2 + \left(\frac{v}{c}\right)^2 \tag{6.46}$$

In conclusion, the extension of 2D spectroscopy to THz frequencies was presented in this chapter. Our method is applicable in the complete frequency range where electrooptic sampling is feasible, i.e., from 1 THz to approximatively 100 THz [224], corresponding to a wavelength of 3 μm or to 3333 cm^{-1}.

The collinear beam geometry cancels N-wave mixing in space, but maintains it in time. Therefore, e.g., the pump-probe signal and the photon echo is measured at once, but still can be individually analyzed. The first experiment decomposed Rabi oscillations on an intersubband transition into nonlinear signals of different order. A gradual transition from the $\chi^{(3)}$ approximation to the non-perturbative regime, dissecting the different nonlinear orders is observed.

We have demonstrated for the first time 2D correlation spectra in the THz domain. We find a Rabi flop on the intersubband transition of multiple quantum wells induced by THz pulses of moderate electric field strength. Polaronic features within an asymmetric double quantum well sample are found in linear measurements, in the pump probe signal and in the 2D correlation spectrum. Cross peaks indicate energetic couplings between different polaronic states. The general consideration about the relation of $\mathbf{k}$ and ω yields a simplified illustration of the relativistic effects on a unit circle.

7 Conclusions

Nonlinear THz spectroscopy is a novel versatile tool to investigate and manipulate material properties with femtosecond time resolution. Located between the electronic and the optic part of the electromagnetic spectrum, THz radiation can be used to study both field-induced effects and low energy excitations. In combination with a phase-resolved detection scheme, this offers various opportunities for nonlinear experiments. The generation process of strong THz pulses was investigated within a laser-induced plasma. Different experimental techniques making use in particular of the phase-resolved detection of THz radiation have been developed. The 2D method, yielding comprehensive information about a sample, was extended to THz frequencies. Various experiments provided insight into the fields of high-field electron transport, gain recovery of QCLs, and THz excitations of quantum well structures.

THz Generation and Propagation Effects within a Laser-induced Plasma

The generation and the propagation of strong THz pulses within a laser-induced plasma was studied experimentally and reproduced theoretically. A field correlation technique using a HgCdTe detector measured all generated frequencies between 20 and 170 THz. Varying the argon pressure within the generation chamber changed the plasma volume and allowed for investigating nonlinear propagation effects.

- The ionization current is unambiguously identified as the source of the THz radiation with frequency components of above 50 THz. The generated spectra in a two color plasma are reproduced by a $3+1$-dimensional simulation based on the ionization current model.

- Slight plasma-induced blue shifts of the driving pulse broaden the emitted spectrum and shift the spectral maximum to higher frequencies. This behavior is observed for larger plasma volumes at higher gas pressures.

Ballistic Transport in Bulk GaAs on Ultrashort Timescales

Using the electric field of THz pulses, we studied unipolar electron transport in n-type GaAs on a femtosecond timescale. The moving electrons emit an electric field, which is measured in a phase-resolved way using electrooptic sampling. Analyzing this field gives insight into coherent electronic motions within the sample.

- The emitted electric field per electron momentum at room temperature agrees excellently with the field expected for ballistic transport. Amplitudes of 7 kV/cm are generated by all electrons present by doping. Ballistic velocities of up to 1000 km/s are deduced.

- Electric field strengths of 300 kV/cm accelerate conduction band electrons through more than half of the Brillouin zone, i.e., the electrons perform partial Bloch oscillations.

- Semiclassical descriptions based on Fermi's golden rule apply only to time scales longer than 120 fs. To describe electron transport on shorter time scales, a dynamic polaron model was developed. The predictions agree well with our experimental results on short time scales and yield the observed drift velocity on long time scales.

Field-induced Interband Tunneling in GaAs

The high-field experiments on *n*-type GaAs were extended to lower temperatures. For incident field amplitudes of 300 kV/cm and lattice temperatures of 80 K, substantially stronger emitted fields with amplitudes up to 50 kV/cm were observed.

- The off-resonant THz field generates electron-hole pairs in GaAs via interband tunneling. For the highest field strengths the density of free electrons and holes was enhanced by a factor of 10.
- The interband tunneling rate depends on the interband decoherence. The electric field induces a coherent superposition of electron states in the conduction band and in the valence band. Simultaneously the electric field drives these electrons and holes into opposite directions, which results in a highly nonclassical wave function with a very fast and temperature-dependent decoherence rate.
- The process of interband tunneling in dependence of the decoherence was theoretically modeled. The results agree well with our experimental data.

Gain Dynamics of a Quantum Cascade Laser

A QCL under operation was investigated in a phase-resolved pump-probe experiment. Pump and probe pulses of identical wavelength, polarization, and propagation direction through the laser waveguide are separated by the time of arrival. The pump pulse (25 THz) perturbed the lasing transition of an InGaAs/AlInAs QCL in operation. The gain recovery, measured by the transmitted amplitude of the probe pulse, is clearly separated from the change of the refractive index, monitored via a nonlinear phase shift.

- Depending on the electric current the gain recovers within several hundred (at 450 mA) or even within 130 fs at 650 mA.
- The observed recovery kinetics is superimposed by oscillations with a frequency of 0.8 THz, due to coherent electron tunneling through the injection barrier. The oscillation frequency is given by the energy splitting of bonding and antibonding states through the injection barrier.
- The phase shift is caused by an elevated electron temperature due to nonresonant transitions within the QCL.

Collinear 2D THz Spectroscopy

The novel method of collinear 2D spectroscopy extends the 2D approach to the entire frequency range where electrooptic sampling is feasible, i.e., from below 1 THz to at least 100 THz, corresponding to wavenumbers between 3 cm^{-1} and 3300 cm^{-1}. The novelties resulting from the collinear beam geometry and the main result of the first experiment is summarized as follows:

- Two-dimensional frequency vectors replace the **k** vectors used in non-collinear phase matching geometries. N-wave mixing occurs generally in space as well as in time. All nonlinear signals are measured simultaneously and can be separated by their spectral positions in the 2D frequency space.
- The collinear beam geometry allow for determining the absolute phase of the signals and makes an additional experiment for the phasing procedure obsolete.
- The signal-to-noise ratio of all nonlinear signals is enhanced roughly by the factor of 4. The 2D Fourier transformation decouples signal and noise along one further dimension.
- Rabi oscillations on an intersubband transition of quantum wells were decomposed into N-wave mixing peaks of different order. The underlying perturbation theory breaks down for pulse areas above 4π. In this case the 2D spectrum is dominated by two elongated pump-probe spots and only a streak of spectral intensity is found along ν_τ.
- The generalized relation between **k** and ω allows for an intuitive visualization of relativistic effects on an unit circle.

2D THz spectroscopy on Multiple Quantum Wells

We studied a multiple quantum well structure (MQWS) and an asymmetric double quantum well structure (a-DQWS) using linear and nonlinear 2D THz spectroscopy.

- The first 2D correlation spectra in the THz range are demonstrated. The collinear beam geometry makes an additional experiment for a phasing procedure redundant.
- MQWS: A 2π Rabi flop causes the negative dip on the diagonal of the 2D correlation spectrum. This feature as well as the spectrally resolved pump probe signal is reproduced by a calculation of the density matrix beyond the rotating wave approximation.
- a-DQWS: The electronic eigenlevels couple strongly to LO phonons, which results in a polaronic energy level system at room temperature. Cross peaks within the 2D correlation spectrum demonstrate the energetic coupling between different polaronic states.

Future Prospects

Several experiments demonstrated already the versatile potential of nonlinear THz spectroscopy. The possibility to apply strong electric fields within femtoseconds on nearly every material of interest is remarkable. The electron transfer of more complex systems such as macromolecules or organic semiconductors could be investigated in the presented way, if a thin film of molecules is available. One could even think about breaking chemical bonds by rearranging electron distributions between atoms. This field-induced chemistry could pave new ways to control chemical reactions.

Collinear 2D THz spectroscopy is a promising new approach in the field of THz physics. Keeping in mind the maturing times of NMR or optical 2D techniques, there may be still a huge potential for optimization and space for new ideas. A better phase-alignment can be achieved by recording an additional picosecond pulse as an optical ruler. Novel THz sources [59] could provide sufficiently high field strengths to induce photon echoes in the fingerprint region of complex molecules. Similar to NMR experiments, the coupling of two rotational modes could reveal the spatial proximity of characteristic groups and thus the structure of the molecule. Furthermore, the low ratio of $\omega_{\text{system}} \gg \Delta\omega_{\text{pulse}} \gg \Delta\omega_{\text{system}}$ allows to coherently manipulate the sample system using the incident pulse shapes. This technique is applied with great success in NMR experiments to evoke certain spin behaviors and response functions with sequences of several hundred pulses.

Semiclassical Boltzmann Transport Equation

In this appendix the semiclassical approach to simulate the scattering rate of Ref. [108] in Fig. 3.2 is described. The simulation employed Boltzmann's transport equation (BTE) and Fermi's golden rule (FGR). Both expressions will be derived and explained in the following. It will be shown that the results of Fermi's golden rule are only valid on time scales long compared to the time between two scattering processes.

The understanding of electric conductivity is closely linked to L. Boltzmann and his kinetic theory from 1872. The Boltzmann Equation sets the framework to describe many particle processes, e.g., in atomic gases or, that is interesting in our context, for electric currents. Under a single-particle approximation, Boltzmann described an ensemble of carriers in phase space unambiguously with the non-equilibrium distribution function $g(\mathbf{r},\mathbf{k},t)$. If all scattering processes are neglected, an externally applied electric field would modify the coordinates in phase space according to the classical equations of motion [225]:

$$\dot{\mathbf{r}} = \mathbf{v}(\mathbf{k}) \tag{1}$$

$$\hbar\dot{\mathbf{k}} = -e\left(\mathbf{E} + \frac{1}{c}\mathbf{v}\times\mathbf{H}\right) = \mathbf{F}(\mathbf{r},\mathbf{k}). \tag{2}$$

Thus electrons at $(\mathbf{v},\mathbf{k},t)$ had at earlier times $(t-dt)$ the coordinates $(\mathbf{r}-\mathbf{v}(\mathbf{k})dt, \mathbf{k}-\mathbf{F}dt/\hbar)$. Furthermore, electrons may have scattered out or into the phase segment of $(\mathbf{r},\mathbf{k},t)$, which is regarded in the expression $\left(\frac{\partial g}{\partial t}\right)_{col}$. The combination of both terms determine the temporal evolution of the non-equilibrium distribution function

$$g(\mathbf{r},\mathbf{k},t) = g\left(\mathbf{r}-\mathbf{v}(\mathbf{k})dt, \mathbf{k}-\mathbf{F}dt/\hbar, t-dt\right) + \left(\frac{\partial g(\mathbf{r},\mathbf{k},t)}{\partial t}\right)_{col}. \tag{3}$$

Evolving the left hand side to the linear order in dt, reduces Eq. (3) for $dt \to 0$ to the Boltzmann equation:

$$\frac{\partial g}{\partial t} + \mathbf{v}\cdot\frac{\partial}{\partial \mathbf{r}}g + \mathbf{F}\cdot\frac{1}{\hbar}\frac{\partial}{\partial \mathbf{k}}g = \left(\frac{\partial g}{\partial t}\right)_{col}. \tag{4}$$

The drift terms on the left hand side express Newton's law and the collision term on the right hand side stands for all scattering processes of the ensemble. The validity of Boltzmann's transport equation depends only on the description of scattering processes within the collision term. The first and most basic assumption for the scattering term stems from Paul Drude and it was surprisingly successful.

$$\left(\frac{dg(\mathbf{k})}{dt}\right)_{col} = \frac{g(\mathbf{k})-g^0(\mathbf{k})}{\tau(\mathbf{k})}. \tag{5}$$

He assumed that scattering occurs. Free carriers inside a conductor are adapted as an ideal electron gas with an average time of flight between two scattering processes. For most semiconductors this empirical relaxation time τ amounts to approximatively $\tau_{\mathrm{SC}} = 200$ fs. The relaxation time approximation does not distinguish between electrons and holes as carriers or between scattering with phonons, electrons or impurities. Just the simple change of the distribution function $g(\mathbf{k})$ in scattering events is stated [Eq. (5)]. However, the results are relative accurate and, e.g., ohmic currents, are well-explained by this model.

$$\left(\frac{dg(\mathbf{k})}{dt}\right)_{col} = -\int \frac{d\mathbf{k}'}{(2\pi)^3} \left\{P_{\mathbf{k},\mathbf{k}'} g(\mathbf{k}) \left[1-g(\mathbf{k}')\right] - P_{\mathbf{k}',\mathbf{k}} g(\mathbf{k}') \left[1-g(\mathbf{k})\right]\right\}. \tag{6}$$

The next refinement [Eq. (6)] considers already the fermionic character of electrons. Pauli blocking prevents scattering from $\mathbf{k}'$ into an occupied $\mathbf{k}$ position and vice versa. The transition probabilities $P_{\mathbf{k},\mathbf{k}'}$ and $P_{\mathbf{k}',\mathbf{k}}$ for such a scattering event are calculated with Fermi's golden rule derived in the next section. Deduced from quantum mechanical perturbation theory, it regards the actual microscopical situation including wave function overlap and density of states.

The Validity of Fermi's Golden Rule

The expression was derived originally 1927 by G. Wentzel from the quantum mechanical perturbation theory [226]. It describes the transition probability between eigenstates caused by an external perturbation potential $V(t)$. V is assumed to be small compared to the unperturbed Hamilton operator H_0. It is switched on at a time t_0 and remains constant afterwards. Using the Heaviside function $\Theta(t)$, the perturbation potential is written as $V(t) = V\Theta(t)$. This situation is described for $t \geq t_0$ in the Schrödinger equation

$$i\hbar \frac{\partial}{\partial t} \mid \psi, t\rangle = [H_0 + V(t)] \mid \psi, t\rangle. \tag{7}$$

The Dirac formalism separates out the known part of H_0 and the remaining perturbation term is evolved into a Neumann sequence. Its first order term P_{mn} expresses the transition probability from one energy eigenstate $\mid m\rangle$ into another orthogonal eigenstate $\mid n\rangle$:

$$\begin{aligned} P_{\mathrm{mn}} &= \left| \frac{1}{\hbar} \int_{t_0}^{t} dt' e^{i(E_n - E_m)t'/\hbar} \langle n \mid V \mid m\rangle \right|^2 && (8) \\ &= \frac{1}{\hbar^2} \left| \frac{e^{i\omega_{\mathrm{nm}} t} - 1}{\omega_{\mathrm{nm}}} \langle n \mid V \mid m\rangle \right|^2 && (9) \\ &= \frac{1}{\hbar^2} \left[\frac{sin^2 \omega_{\mathrm{nm}} t/2}{\omega_{\mathrm{nm}}/2} \right]^2 |\langle n \mid V \mid m\rangle|^2 . && (10) \end{aligned}$$

It will be shown that $\frac{sin^2 \omega_{\mathrm{nm}} t/2}{\omega_{\mathrm{nm}}/2}$ from Eq. (10) is equivalent to the Dirac function δ on long time scales. We substitute the expression with

$$\delta_t(\alpha) = \frac{sin^2 \alpha t}{\pi \alpha^2 t}. \tag{11}$$

Its functional characteristics can be classified as follows

$$\delta_t(\alpha) \begin{cases} t/\pi & \text{for } \alpha = 0 \\ \leq 1/\pi\alpha^2 t & \text{for } \alpha \neq 0 \end{cases} \tag{12}$$

Integration over t of Eq. (11) yields for any function $F(\alpha)$ for $t \to \infty$

$$\lim_{t\to\infty} \int_{-\infty}^{\infty} d\alpha \delta_t(\alpha) F(\alpha) = F(0). \tag{13}$$

This is exactly the behavior of a δ function. That means only on long time scales $t \to \infty$ the equation holds

$$\lim_{t\to\infty} \delta_t(\alpha) = \delta(\alpha). \tag{14}$$

This substitution limits the validity of Fermi's Golden Rule only to long times scales. Inserting Eq. (14) into Eq. (10), yields for the transition probability P_{mn}

$$P_{\mathrm{mn}}(t) = t\frac{2\pi}{\hbar}\delta(E_n - E_m) \left| \langle n \mid V \mid m \rangle \right|^2. \tag{15}$$

It results in a transition rate, i.e., the transition probability per time, of

$$\Gamma_{\mathrm{mn}} = \frac{2\pi}{\hbar}\delta(E_n - E_m) \left| \langle n \mid V \mid m \rangle \right|^2. \tag{16}$$

Electronic states within a periodic semiconductor form continuous valence and conduction bands. The electron lifetime of the conduction band eigenstate $\mid m\rangle$, for one distinct momentum $\mathbf{k}$ and one distinct energy E, needs to be calculated. Scattering into all other conduction band eigenstates $\mid n\rangle$ is allowed, if energy and momentum is conserved. The number of possible states to scatter into is given by the density of states $\rho(E)$. In this case the dependence of ρ on the momenta can be ignored, because LO phonons have nearly the same energy for all $\mathbf{q}$ momenta (see Fig. 3.9). Since the energy is conserved one LO phonon will be addressed, which fulfils the momentum conservation as well. Thus we obtain for the transition rate out of the eigenstate $\mid m\rangle$

$$\sum_n \Gamma_{\mathrm{mn}} = \rho(E_n)\frac{2\pi}{\hbar} \left| \langle n \mid V \mid m \rangle \right|^2. \tag{17}$$

Most important in our context is the validity range of Fermi's Golden Rule. It is illustrated in Fig. 1. The expression for the transition probability in Eq. (15) is based on the approximation of $\frac{sin^2\omega_{\mathrm{nm}}t/2}{\omega_{\mathrm{nm}}/2}^2$ in Eq. (10) as a δ function. This approximation is only valid for energetic widths $2\pi\hbar/t$ much smaller than the width of the energy distribution of the final states ΔE [113]. The second condition requires a sufficient number of final states within the δ-like function. Translated into the time domain, the following condition must hold:

$$\frac{2\pi\hbar}{\Delta E} \ll t \ll \frac{2\pi\hbar}{\delta\varepsilon} \tag{18}$$

For continuous energy bands of semiconductors ($\delta\varepsilon \approx 0$) the r.h.s. of the inequation 18 is certainly fulfilled. To clarify the validity of Fermi's Golden Rule on short times, we consider Heisenberg's uncertainty relation $\Delta E \Delta t \geq h$. The minimal energetic width of the transition (ΔE)

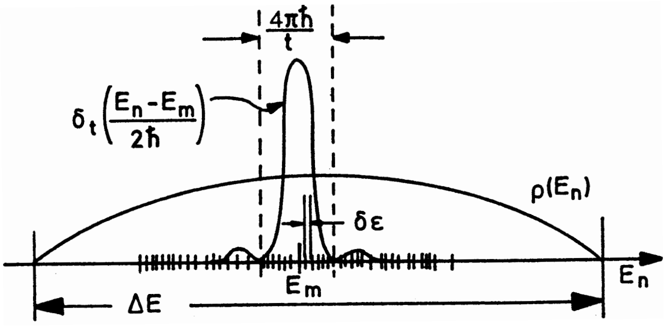

Figure 1: The approximation of $\delta_t \approx \delta$ remains valid if ΔE is much larger and $\delta\varepsilon$ is much smaller than δ_t, i.e., for $\frac{2\pi\hbar}{\Delta E} \ll t \ll \frac{2\pi\hbar}{\delta\varepsilon}$. This chart is taken from Ref. [113].

is proportional to the inverse interaction time (Δt^{-1}, given by phonon energy to scatter with). Inserting Heisenberg's uncertainty relation into Eq. (18) yields

$$\Delta t \ll t. \tag{19}$$

Thus Fermi's golden rule applies only to scattering times t long compared to the interaction time Δt, i.e., inverse oscillation period of the phonon to scatter with.

Multiple Quantum Well Samples

In this appendix the multiple quantum well samples described in Chapter 6 are summarized. All samples were grown in the Paul-Drude-Institute in Berlin and consist of alternating layers of GaAs and $Al_{0.35}Ga_{0.65}As$. Different bandgaps of both materials confine the electron wavefunctions spatially in one dimension. The broad quantum wells in the order of 10 nm feature a large dipole moment of $\mu \approx e_0 \times 2.3$ nm at THz frequencies. Accordingly, we expected strong nonlinearities even at lower field strengths. Since only p polarized light is absorbed by the intersubband transitions, all samples were processed into prisms. Diffraction on the surface of the prism provides a component of p polarized light [see Fig. 6.15 (d)].

The nominal properties of the multiple quantum well sample are listed in Table 1. Linear absorption measurements were performed on all samples. Samples M4.1166 and M4.2112 were studied at room temperature using a *Varian 640 – IR* FT-IR spectrometer. The ceramic globar provided light between 50 – 9600 cm^{-1} (i.e., 13 – 300 THz), which was detected using a HgCdTe detector sensitive between 450 – 10000 cm^{-1} (i.e., 1 – 290 THz). The prism shaped samples were placed in the 2 cm wide beam waist of the spectrometer. A screen enclosing the sample assured that all detected light was transmitted through the sample. Using a mesh polarizer we used the spectrum for s polarized light as a reference for the absorption spectrum for p polarized light.

The absorbances of the different samples as well as the predicted wave functions from a $k \cdot p$ calculation are shown in Figs. 2 (a), 4 (b), and 3 (b).

Table 1: Properties of the investigated quantum well samples

Sample	M4.1166	M4.2112	M4.2118
Well width (nm)	10	11	9 and 12
Barrier width (nm)	20	20	15
Doping density (cm^{-2})	5×10^{10}	1.5×10^{11}	1×10^{12}
Number of q.w.	51	20	10
IS transition (THz)	25	18	17 and 24
Line width (THz)	0.8	1.4	1.4 and 2

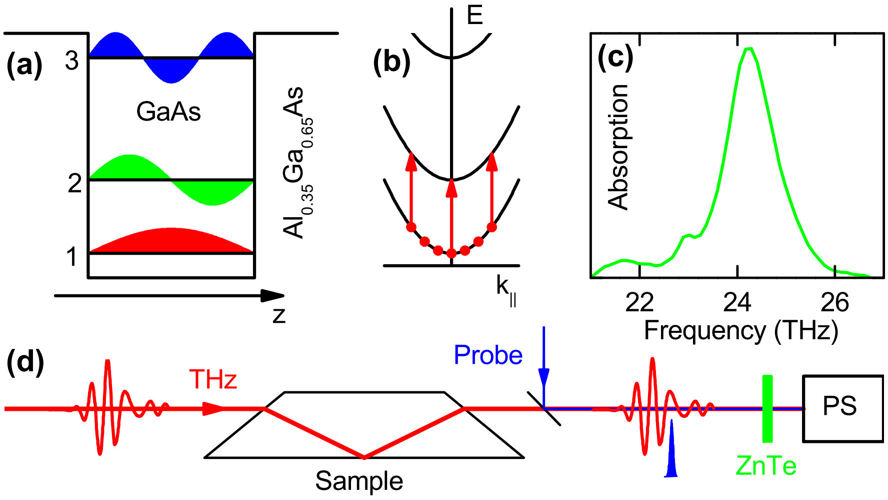

Figure 2: (a) Three subbands within the quantum well. (b) Incident pulses excite electrons around the Γ point from the first into the second subband. (c) The resulting narrow absorption line at 25 THz is observed in linear transmission measurements.(d) A prism-shaped sample provides *p* polarized light for intersubband excitation.

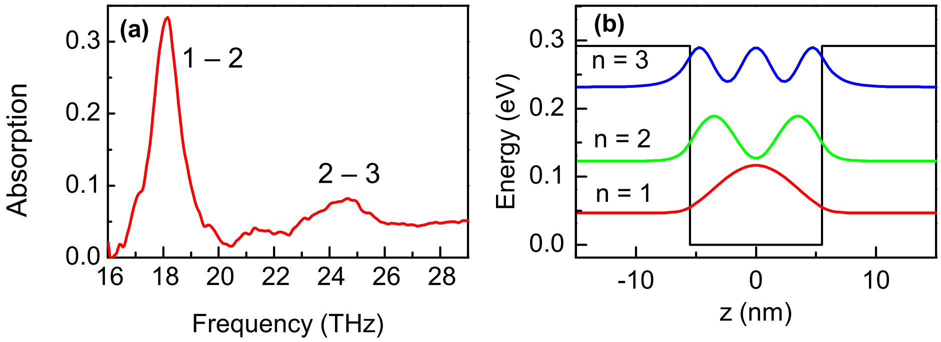

Figure 3: (a) Linear intersubband absorption at room temperature. The two absorption lines correspond to the $1 \leftrightarrow 2$ and $2 \leftrightarrow 3$ between bound states in the quantum well. (b) Potential energy and $|\Psi_n(x)|^2$ for the three lowest subbands of AlGaAs/GaAs quantum wells.

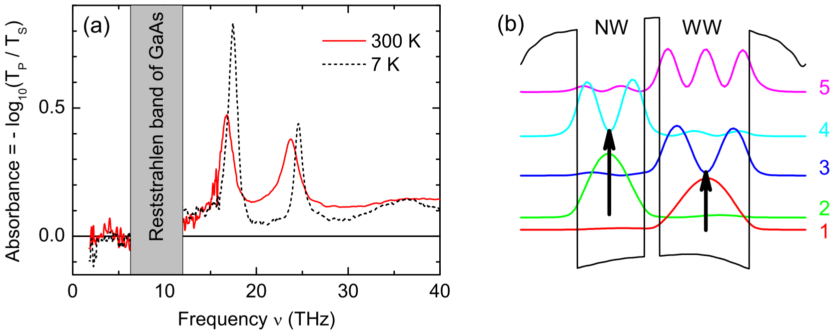

Figure 4: (a) Linear transmission measurements between 2 and 40 THz for 7 K (black dashed line) and at room temperature (red solid line). (b) Calculated electronic wavefunctions in the a-DQWS. The fundamental transitions in the broad and in the narrow quantum well agree well with the observed absorption lines.

Publications

Articles directly relevant to the content of this thesis:

- Two-Dimensional Terahertz Correlation Spectra of Electronic Excitations in Semiconductor Quantum Wells
  W. Kuehn, K. Reimann, M. Woerner, T. Elsaesser und R. Hey
  Journal of Physical Chemistry in press

- Coherent ballistic motion of electrons in a periodic potential
  W. Kuehn, P. Gaal, K. Reimann, M. Woerner, T. Elsaesser und R. Hey
  Physical Review Letters 104, 146602-1–4 (2010)

- THz-induced interband tunneling of electrons in GaAs
  W. Kuehn, P. Gaal, K. Reimann, M. Woerner, T. Elsaesser und R. Hey
  Physical Review B 82, 075204-1–8 (2010)

- Ultrafast spatio-temporal dynamics of terahertz generation by ionizing two-color femtosecond pulses in gases
  I. Babushkin, W. Kuehn, C. Köhler, S. Skupin, L. Bergé, K. Reimann, M. Woerner, J. Herrmann und T. Elsaesser
  Physical Review Letters 105, 053903-1–4 (2010)

- Nonlinear terahertz spectroscopy
  M. Woerner, W. Kuehn, K. Reimann, T. Elsaesser und R. Hey
  Proceedings of SPIE 7600, 76001T (2010)

- Phase-resolved two-dimensional spectroscopy based on collinear n-wave mixing in the ultrafast time domain
  W. Kuehn, K. Reimann, M. Woerner, T. Elsaesser und R. Hey
  Journal of Chemical Physics 130, 164503-1–6 (2009)

- Ultrafast phase-resolved pump-probe measurements on a quantum cascade laser
  W. Kuehn, W. Parz, P. Gaal, K. Reimann, M. Woerner, T. Elsaesser, T. Müller, J. Darmo, K. Unterrainer, M. Austerer, G. Strasser, L. R. Wilson, J. W. Cockburn, A. B. Krysa und J. S. Roberts
  Applied Physics Letters 93, 151106-1–3 (2008)

Other articles:

- Nonlinear THz response of n-type GaAs
  M. Woerner, W. Kuehn, P. Gaal, K. Reimann, T. Elsaesser und R. Hey
  Proceedings of SPIE 7214, 72140W (2009)

- Carrier-wave Rabi flopping on radiatively coupled shallow donor transitions in *n*-type GaAs
  P. Gaal, W. Kuehn, K. Reimann, M. Woerner, T. Elsaesser, R. Hey, J. S. Lee und U. Schade
  Physical Review B 77, 235204-1–6 (2008)

- Nonlinear terahertz and midinfrared response of *n*-type GaAs
  M. Woerner, P. Gaal, W. Kühn, K. Reimann, T. Elsaesser, R. Hey und K. H. Ploog
  Advances in Solid State Physics 47, R. Haug (Ed.), Berlin, Springer 2008, 237–249

- Internal motions of a quasiparticle governing its ultrafast nonlinear response
  P. Gaal, W. Kuehn, K. Reimann, M. Woerner, T. Elsaesser und R. Hey
  Nature 450, 1210–1213 (2007)

Conference proceedings:

- High field transport of photo-injected electrons in GaAs: Transition from ballistic to drift motion
  P. Bowlan, W. Kuehn, K. Reimann, M. Woerner, T. Elsaesser, R. Hey und C. Flytzanis
  Conference on Lasers and Electro-Optics, Baltimore 2011, submitted

- Ultrafast coherent high-field electron transport in GaAs
  W. Kuehn, P. Gaal, K. Reimann, M. Woerner, T. Elsaesser und R. Hey
  17th International Conference on Ultrafast Phenomena, Snowmass Village 2010

- Coherent energy transport between coupled quantum wells studied by two-dimensional terahertz spectroscopy
  W. Kuehn, K. Reimann, M. Woerner, T. Elsaesser und R. Hey
  17th International Conference on Ultrafast Phenomena, Snowmass Village 2010

- Nonlinear terahertz spectroscopy
  M. Woerner, W. Kuehn, K. Reimann, T. Elsaesser und R. Hey
  Photonics West, San Francisco 2010, invited

- Two-color two-dimensional terahertz spectroscopy on intersubband transitions of coupled quantum wells
  W. Kuehn, K. Reimann, M. Woerner, T. Elsaesser und R. Hey
  Quantum Electronics and Laser Science Conference, San Jose 2010

- Propagation effects in THz generation by ionizing two-color laser pulses
  C. Köhler, W. Kuehn, I. Babushkin, S. Skupin, L. Bergé, K. Reimann, M. Woerner, J. Herrmann, T. Elsaesser
  EOS Annual Meeting, Paris 2010

- Nonlinear THz response of *n*-type GaAs
  M. Woerner, W. Kuehn, P. Gaal, K. Reimann, T. Elsaesser und R. Hey
  Photonics West, San Jose 2009, invited

- Femtosecond dynamics of a midinfrared quantum cascade laser
  W. Kuehn, W. Parz, P. Gaal, K. Reimann, M. Woerner, T. Elsaesser, T. Müller, J. Darmo,

K. Unterrainer, M. Austerer, G. Strasser, L. R. Wilson, J. W. Cockburn, A. B. Krysa und J. S. Roberts
Conference on Lasers and Electro-Optics, Baltimore 2009

- High-order optical nonlinearities from collinear time-resolved two-dimensional spectroscopy
  W. Kuehn, P. Gaal, K. Reimann, M. Woerner, T. Elsaesser und R. Hey
  International Quantum Electronics Conference, Baltimore 2009, invited

- Bloch oscillations and Zener tunneling in bulk GaAs
  W. Kuehn, P. Gaal, K. Reimann, M. Woerner, T. Elsaesser und R. Hey
  International Quantum Electronics Conference, Baltimore 2009

- Statical and dynamical properties of intersubband-gain in midinfrared quantum cascade lasers
  W. Parz, O. Pfäffli, T. Müller, J. Darmo, M. Austerer, G. Strasser, Karl Unterrainer, W. Kühn, P. Gaal, K. Reimann, M. Woerner, T. Elsaesser, L. Wilson, J. Cockburn, A. Krysa und J. Roberts
  16th International Conference on Electron Dynamics in Semiconductors, Optoelectronics and Nanostructures, Montpellier 2009

- Teasing a quasiparticle—the ultrafast nonlinear response of the Fröhlich polaron in GaAs
  P. Gaal, W. Kuehn, K. Reimann, M. Woerner, T. Elsaesser und R. Hey
  XVI International Conference on Ultrafast Phenomena, Stresa 2008

- Rabi oscillations in a shallow donor system driven by intense THz radiation
  P. Gaal, W. Kuehn, K. Reimann, M. Woerner, T. Elsaesser und R. Hey
  XVI International Conference on Ultrafast Phenomena, Stresa 2008

- Terahertz-field-induced midinfrared gain and absorption in *n*-type GaAs
  P. Gaal, W. Kuehn, K. Reimann, M. Woerner, T. Elsaesser und R. Hey
  15th International Conference on Nonequilibrium Carrier Dynamics in Semiconductors, Tokyo 2007

- Nonlinear terahertz and midinfrared response of *n*-type GaAs
  M. Woerner, P. Gaal, W. Kuehn, K. Reimann, T. Elsaesser, R. Hey und K. Ploog
  Frühjahrstagung der DPG, Regensburg 2007, invited

Bibliography

[1] D. H. Auston, Picosecond optoelectronic switching and gating in silicon, Appl. Phys. Lett. **2**6, 101–103 (1975).

[2] R. R. Jones, D. You, and P. H. Bucksbaum, Ionization of Rydberg Atoms by Subpicosecond Half-Cycle Electromagnetic Pulses, Phys. Rev. Lett. **7**0, 1236–1239 (1993).

[3] S. D. Ganichev and W. Prettl, *Intense Terahertz Excitation of Semiconductors*, (Oxford University Press, Oxford, 2006).

[4] P. Gaal, W. Kuehn, K. Reimann, M. Woerner, T. Elsaesser, and R. Hey, Internal motions of a quasiparticle governing its ultrafast nonlinear response, Nature **4**50, 1210–1213 (2007).

[5] G. Günter, A. A. Anappara, J. Hees, A. Sell, G. Biasiol, L. Sorba, S. De Liberato, C. Ciuti, A. Tredicucci, A. Leitenstorfer, and R. Huber, Sub-cycle switch-on of ultrastrong light–matter interaction, Nature **4**58, 178–181 (2009).

[6] D. Clery, Terahertz on a chip, Science **2**97, 763–764 (2002).

[7] Masayoshi Tonouchi, Cutting-edge terahertz technology, Nature Photon. **1**, 97–105 (2007).

[8] A. Deninger and T. Renner, Laser zur THz-Erzeugung, Physik Journal **9**, 6–8 (2008).

[9] J. Jonuscheit, M. Herrmann, and R. Beigang, Transparente Analyse, Physik Journal **8**, 31–36 (2009).

[10] D. You, R. R. Jones, P. H. Bucksbaum, and D. R. Dykaar, Generation of high-power sub-single-cycle 500-fs electromagnetic pulses, Opt. Lett. **1**8, 290–292 (1993).

[11] R. A. Kaindl, D. C. Smith, M. Joschko, M. P. Hasselbeck, M. Woerner, and T. Elsaesser, Femtosecond infrared pulses tunable from 9 to 18 μm at an 88-MHz repetition rate, Opt. Lett. **2**3, 861–863 (1998).

[12] R. A. Kaindl, F. Eickemeyer, M. Woerner, and T. Elsaesser, Broadband phase-matched difference frequency mixing of femtosecond pulses in GaSe: Experiment and theory, Appl. Phys. Lett. **7**5, 1060–1062 (1999).

[13] R. A. Kaindl, M. Wurm, K. Reimann, P. Hamm, A. M. Weiner, and M. Woerner, Generation, shaping, and characterization of intense femtosecond pulses tunable between 3 and 20 μm, J. Opt. Soc. Am. B **1**7, 2086–2094 (2000).

[14] F. Eickemeyer, R. A. Kaindl, M. Woerner, T. Elsaesser, and A. M. Weiner, Controlled shaping of ultrafast electric field transients in the mid-infrared spectral range, Opt. Lett. **2**5, 1472–1474 (2000).

[15] K. Reimann, R. P. Smith, A. M. Weiner, T. Elsaesser, and M. Woerner, Direct field-resolved detection of terahertz transients with amplitudes of megavolts per centimeter, Opt. Lett. **2**8, 471–473 (2003).

[16] T. Bartel, P. Gaal, K. Reimann, M. Woerner, and T. Elsaesser, Generation of single-cycle THz transients with high electric-field amplitudes, Opt. Lett. **3**0, 2805–2807 (2005).

[17] Q. Wu and X.-C. Zhang, Free-space electro-optic sampling of terahertz beams, Appl. Phys. Lett. **6**7, 3523–3525 (1995).

[18] Q. Wu and X.-C. Zhang, 7 terahertz broadband GaP electro-optic sensor, Appl. Phys. Lett. **7**0, 1784–1786 (1997).

[19] Matthias C. Hoffmann, János Hebling, Harold Y. Hwang, Ka-Lo Yeh, and Keith A. Nelson, Impact ionization in InSb probed by terahertz pump—terahertz probe spectroscopy, Phys. Rev. B **7**9, 161201(R) (2009).

[20] H. Wen, M. Wiczer, and A. M. Lindenberg, Ultrafast electron cascades in semiconductors driven by intense femtosecond terahertz pulses, Phys. Rev. B **7**8, 125203 (2008).

[21] L. Razzari, F. H. Su, G. Sharma, F. Blanchard, A. Ayesheshim, H.-C. Bandulet, R. Morandotti, J.-C. Kieffer, T. Ozaki, M. Reid, and F. A. Hegmann, Nonlinear ultrafast modulation of the optical absorption of intense few-cycle terahertz pulses in *n*-doped semiconductors, Phys. Rev. B **7**9, 193204 (2009).

[22] F. H. Su, F. Blanchard, G. Sharma, L. Razzari, A. Ayesheshim, T. L. Cocker, L. V. Titova, T. Ozaki, J.-C. Kieffer, R. Morandotti, M. Reid, and F. A. Hegmann, Terahertz pulse induced intervalley scattering in photoexcited GaAs, Opt. Express **1**7, 9620–9629 (2009).

[23] R. A. Kaindl, K. Reimann, M. Woerner, T. Elsaesser, R. Hey, and K. H. Ploog, Homogeneous broadening and excitation-induced dephasing of intersubband transitions in a quasi-two-dimensional electron gas, Phys. Rev. B **6**3, 161308(R)-1–4 (2001).

[24] Josef Kröll, Juraj Darmo, Sukhdeep S. Dhillon, Xavier Marcadet, Michel Calligaro, Carlo Sirtori, and Karl Unterrainer, Phase-resolved measurements of stimulated emission in a laser, Nature **4**49, 698–701 (2007).

[25] W. Kuehn, W. Parz, P. Gaal, K. Reimann, M. Woerner, T. Elsaesser, T. Müller, J. Darmo, K. Unterrainer, M. Austerer, G. Strasser, L. R. Wilson, J. W. Cockburn, A. B. Krysa, and J. S. Roberts, Ultrafast phase-resolved pump-probe measurements on a quantum cascade laser, Appl. Phys. Lett. **9**3, 151106-1–3 (2008).

[26] Wolfgang Parz, Thomas Müller, Juraj Darmo, Karl Unterrainer, Max Austerer, Gottfried Strasser, Luke R. Wilson, John W. Cockburn, Andrey B. Krysa, and John S. Roberts, Ultrafast probing of light-matter interaction in a midinfrared quantum cascade laser, Appl. Phys. Lett. **9**3, 091105 (2008).

[27] P. Gaal, K. Reimann, M. Woerner, T. Elsaesser, R. Hey, and K. H. Ploog, Nonlinear terahertz response of *n*-type GaAs, Phys. Rev. Lett. **9**6, 187402-1–4 (2006).

[28] R. A. Kaindl, M. Woerner, T. Elsaesser, D. C. Smith, J. F. Ryan, G. A. Farnan, M. P. McCurry, and D. G. Walmsley, Ultrafast mid-infrared response of $YBa_2Cu_3O_{7-\delta}$, Science **2**87, 470–473 (2000).

[29] C. L. Tang and D. J. Erskine, Femtosecond Relaxation of Photoexcited Nonequilibrium Carriers in $Al_xGa_{1-x}As$, Phys. Rev. Lett. **5**1, 840–844 (1983).

[30] J. A. Kash, R. G. Ulbrich, and J. C. Tsang, Quantitative Measurements of Intervalley and Carrier-carrier Scattering in GaAs with Hot Luminescence, Solid State Electron. **3**2, 1277–1281 (1989).

[31] A. Leitenstorfer, S. Hunsche, J. Shah, M. C. Nuss, and W. H. Knox, Femtosecond high-field transport in compound semiconductors, Phys. Rev. B **6**1, 16642–16652 (2000).

[32] W. Kuehn, P. Gaal, K. Reimann, M. Woerner, T. Elsaesser, and R. Hey, THz-induced interband tunneling of electrons in GaAs, Phys. Rev. B **8**2, 075204-1–8 (2010).

[33] W. Kuehn, K. Reimann, M. Woerner, and T. Elsaesser, Phase-resolved two-dimensional spectroscopy based on collinear *n*-wave mixing in the ultrafast time domain, J. Chem. Phys. **1**30, 164503-1–6 (2009).

[34] W. Kuehn, K. Reimann, M. Woerner, T. Elsaesser, and R. Hey, Two-dimensional terahertz correlation spectra of electronic excitations in semiconductor quantum wells, J. Phys. Chem. A, in print.

[35] Peter Gaál, Nonlinear THz spectroscopy on n-type GaAs, Ph. D. thesis, Humboldt-Universität Berlin, 2008.

[36] F. Eickemeyer, Ultrafast dynamics of coherent intersubband polarizations in quantum wells and quantum cascade laser structures, Ph. D. thesis, Humboldt-Universität Berlin, 2002.

[37] R. E. M. de Bekker, L. M. Claessen, and P. Wyder, Generation of very short far-infrared pulses by cavity dumping a molecular gas-laser, J. Appl. Phys. **6**8, 3729–3731 (1990).

[38] R. Paiella, F. Capasso, C. Gmachl, D. L. Sivco, J. N. Baillargeon, A. L. Hutchinson, A. Y. Cho, and H. Liu, Self-mode-locking of quantum cascade lasers with giant ultrafast optical nonlinearities, Science **2**90, 1739–1742 (2000).

[39] G. Mourou, C. V. Stancampiano, and D. Blumenthal, Picosecond microwave pulse generation, Appl. Phys. Lett. **3**8, 470–472 (1981).

[40] J. H. Kim, A. Polley, and S. E. Ralph, Efficient photoconductive terahertz source using line excitation, Opt. Lett. **3**0, 2490–2492 (2005).

[41] D. H. Auston, K. P. Cheung, J. A. Valdmanis, and D. A. Kleinman, Cherenkov radiation from femtosecond optical pulses in electro-optic media, Phys. Rev. Lett. **5**3, 1555–1558 (1984).

[42] A. Bonvalet, M. Joffre, J. L. Martin, and A. Migus, Generation of ultrabroadband femtosecond pulses in the mid-infrared by optical rectification of 15 fs light pulses at 100 MHz repetition rate, Appl. Phys. Lett. **6**7, 2907–2909 (1995).

[43] N. Bloembergen, *Nonlinear Optics*, (Benjamin, Reading, Mass., 1965).

[44] Y. R. Shen, Recent advances in nonlinear optics, Rev. Mod. Phys. **4**8, 1–32 (1976).

[45] M. Wegener, *Extreme Nonlinear Optics*, (Springer, Berlin, 2005).

[46] P. N. Butcher and D. Cotter, *The Elements of Nonlinear Optics*, (Cambridge University Press, Cambridge, 1990).

[47] P. A. Franken, A. E. Hill, C. W. Peters, and G. Weinreich, Generation of optical harmonics, Phys. Rev. Lett. **7**, 118–119 (1961).

[48] M. Bass, P. A. Franken, J. F. Ward, and G. Weinreich, Optical rectification, Phys. Rev. Lett. **9**, 446–448 (1962).

[49] W. Shi, Y. J. Ding, N. Fernelius, and K. Vodopyanov, Efficient, tunable, and coherent 0.18–5.27-THz source based on GaSe crystal, Opt. Lett. **2**7, 1454–1456 (2002) **28**, 136(E) (2003).

[50] P. D. Maker, R. W. Terhune, M. Nisenoff, and C. M. Savage, Effects of dispersion and focusing on the production of optical harmonics, Phys. Rev. Lett. **8**, 21–22 (1962).

[51] A. Yariv, *Quantum Electronics*, 3rd ed. (Wiley, New York, 1989).

[52] R. A. Kaindl, Ultrafast mid-infrared studies of low-energy excitations in solids, Ph. D. thesis, Humboldt-Universität Berlin, 2000.

[53] János Hebling, Ka-Lo Yeh, Matthias C. Hoffmann, Balázs Bartal, and Keith A. Nelson, Generation of high-power terahertz pulses by tilted-pulse-front excitation and their application possibilities, J. Opt. Soc. Am. B **2**5, 6–19 (2008).

[54] T. Löffler, T. Hahn, M. Thomson, F. Jacob, and H. G. Roskos, Large-area electro-optic ZnTe terahertz emitters, Opt. Express **1**3, 5353–5362 (2005).

[55] T. Tanabe, K. Suto, J. Nishizawa, K. Saito, and T. Kimura, Frequency-tunable terahertz wave generation via excitation of phonon-polaritons in GaP, J. Phys. D **3**6, 953–957 (2003).

[56] B. Bartal, I. Z. Kozma, A. G. Stepanov, G. Almási, J. Kuhl, E. Riedle, and J. Hebling, Toward generation of μJ range sub-ps THz pulses by optical rectification, Appl. Phys. B **8**6, 419–423 (2007).

[57] J. R. Morris and Y. R. Shen, Far-infrared generation by picosecond pulses in electro-optical materials, Opt. Commun. **3**, 81–84 (1971).

[58] T. Elsaesser and M. C. Nuss, Femtosecond pulses in the mid-infrared generated by down-conversion of a traveling-wave dye laser, Opt. Lett. **1**6, 411–413 (1991).

[59] Alexander Sell, Alfred Leitenstorfer, and Rupert Huber, Phase-locked generation and field-resolved detection of widely tunable terahertz pulses with amplitudes exceeding 100 MV/cm, Opt. Lett. **3**3, 2767–2769 (2008).

[60] H. Hamster and R. W. Falcone, *Proposed Source of Sub-picosecond Far Infrared Radiation*, (Springer, Berlin, 1990).

[61] H. Hamster, A. Sullivan, S. Gordon, W. White, and R. W. Falcone, Subpicosecond, electromagnetic pulses from intense laser-plasma interaction, Phys. Rev. Lett. **7**1, 2725–2728 (1993).

[62] Mark D. Thomson, Markus Kreß, Torsten Löffler, and Hartmut G. Roskos, Broadband THz emission from gas plasmas induced by femtosecond optical pulses: From fundamentals to applications, Laser & Photon. Rev. **1**, 349–368 (2007).

[63] F. Löser, M. M. Dignam, Yu. A. Kosevich, K. Köhler, and K. Leo, Self-induced Shapiro effect in semiconductor superlattices, Phys. Rev. Lett. **8**5, 4763–4766 (2000).

[64] T. Löffler and H. G. Roskos, Gas-pressure dependence of terahertz-pulse generation in a laser-generated nitrogen plasma, J. Appl. Phys. **9**1, 2611–2614 (2002).

[65] D. J. Cook and R. M. Hochstrasser, Intense terahertz pulses by four-wave rectification in air, Opt. Lett. **2**5, 1210–1212 (2000).

[66] M. Kreß, T. Löffler, M. D. Thomson, R. Dörner, H. Gimpel, K. Zrost, T. Ergler, R. Moshammer, U. Morgner, J. Ullrich, and H. G. Roskos, Determination of the carrier-envelope phase of few-cycle laser pulses with terahertz-emission spectroscopy, Nature Phys. **2**, 327–331 (2006).

[67] M. Kress, T. Löffler, S. Eden, M. Thomson, and H. G. Roskos, Terahertz-pulse generation by photoionization of air with laser pulses composed of both fundamental and second-harmonic waves, Opt. Lett. **2**9, 1120–1122 (2004).

[68] U. W. Kim, S. J. Oh, I. Maeng, C. Kang, and J.-H. Son, Terahertz electrical characteristics of heavily doped n-GaAs thin films, J. Korean Phys. Soc. **5**0, 789–792 (2007).

[69] K. Y. Kim, A. J. Taylor, J. H. Glownia, and G. Rodriguez, Coherent control of terahertz supercontinuum generation in ultrafast laser-gas interactions, Nature Photon. **2**, 605–609 (2008).

[70] I. Babushkin, W. Kuehn, C. Köhler, S. Skupin, L. Bergé, K. Reimann, M. Woerner, J. Herrmann, and T. Elsaesser, Ultrafast spatio-temporal dynamics of terahertz generation by ionizing two-color femtosecond pulses in gases, Phys. Rev. Lett. **1**05, 053903-1–4 (2010).

[71] M. Uiberacker, T. Uphues, M. Schultze, A. J. Verhoef, V. Yakovlev, M. F. Kling, J. Rauschenberger, N. M. Kabachnik, H. Schröder, M. Lezius, K. L. Kompa, H.-G. Muller, , M. J. J. Vrakking, S. Hendel, U. Kleineberg, U. Heinzmann, M. Drescher, and F. Krausz, Attosecond real-time observation of electron tunnelling in atoms, Nature **4**46, 627–632 (2007).

[72] T. Sekikawa, A. Kosuge, T. Kanai, and S. Watanabe, Nonlinear optics in the extreme ultraviolet, Nature **4**32, 605–608 (2004).

[73] A. Leitenstorfer, S. Hunsche, J. Shah, M. C. Nuss, and W. H. Knox, Detectors and sources for ultrabroadband electro-optic sampling: Experiment and theory, Appl. Phys. Lett. **7**4, 1516–1518 (1999).

[74] S. C. Rae and K. Burnett, Detailed simulations of plasma-induced spectral blueshifting, Phys. Rev. A **4**6, 1084–1090 (1992).

[75] Q. Wu and X.-C. Zhang, Free-space electro-optics sampling of mid-infrared pulses, Appl. Phys. Lett. **7**1, 1285–1286 (1997).

[76] F. Pockels, Ueber den Einfluss des elektrostatischen Feldes auf das optische Verhalten piëzoelektrischer Krystalle, Abh. Ges. Wissensch. Göttingen **3**9, 1–204 (1894).

[77] J. van Tilborg, C. B. Schroeder, C. V. Filip, C. Tóth, C. G. R. Geddes, G. Fubiani, R. Huber, R. A. Kaindl, E. Esarey, and W. P. Leemans, Temporal characterization of femtosecond laser-plasma-accelerated electron bunches using terahertz radiation, Phys. Rev. Lett. **9**6, 014801 (2006).

[78] Jie Shan, A. S. Weling, E. Knoesel, L. Bartels, M. Bonn, A. Nahata, G. A. Reider, and T. F. Heinz, Single-shot measurement of terahertz electromagnetic pulses by use of electro-optic sampling, Opt. Lett. **2**5, 426–428 (2000).

[79] P. C. M. Planken, H.-K. Nienhuys, H. J. Bakker, and T. Wenckebach, Measurement and calculation of the orientation dependence of terahertz pulse detection in ZnTe, J. Opt. Soc. Am. B **1**8, 313–317 (2001).

[80] W. L. Faust and C. H. Henry, Mixing of visible and near-resonance infrared light in GaP, Phys. Rev. Lett. **1**7, 1265–1268 (1966).

[81] T. Hattori, R. Rundsawang, K. Ohta, and K. Tukamoto, Gaussian beam analysis of temporal waveform of focused terahertz pulses, Jpn. J. Appl. Phys. **4**1, 5198–5204 (2002).

[82] P. Gaal, W. Kuehn, K. Reimann, M. Woerner, T. Elsaesser, R. Hey, J. S. Lee, and U. Schade, Carrier-wave Rabi flopping on radiatively coupled shallow donor transitions in n-type GaAs, Phys. Rev. B **7**7, 235204-1–6 (2008).

[83] Alexander Sell, Rüdiger Scheu, Alfred Leitenstorfer, and Rupert Huber, Field-resolved detection of phase-locked infrared transients from a compact Er:fiber system tunable between 55 and 107 THz, Appl. Phys. Lett. **9**3, 2511071–2511073 (2008).

[84] J. Dai, X. Xie, and X.-C. Zhang, Detection of broadband terahertz waves with a laser-induced plasma in gases, Phys. Rev. Lett. **9**7, 103903 (2006).

[85] C. V. McLaughlin, X. Zheng, and L. M. Hayden, Comparison of parallel-plate and inplane polymer films for terahertz sensing, Appl. Opt. **4**6, 6283- (2007).

[86] F. G. Sun, Z. P. Jiang, and X. C. Zhang, Analysis of terahertz pulse measurement with a chirped probe beam, Appl. Phys. Lett. **7**3, 2233–2235 (1998).

[87] J. J. LePore, An improved technique for selective etching of GaAs and $Ga_{1-x}Al_xAs$, J. Appl. Phys. **5**1, 6441–6442 (1980).

[88] T. Stroucken, A. Knorr, P. Thomas, and S. W. Koch, Coherent dynamics of radiatively coupled quantum-well excitons, Phys. Rev. B **5**3, 2026–2033 (1996).

[89] L. W. Davis, Theory of electromagnetic beams, Phys. Rev. A **1**9, 1177–1179 (1979).

[90] J. T. Darrow, X.-C. Zhang, D. H. Auston, and J. D. Morse, Saturation properties of large-aperture photoconducting antennas, IEEE J. Quantum Electron. **2**8, 1607–1616 (1992).

[91] K. Reimann, Table-top sources of ultrashort THz pulses, Rep. Prog. Phys. **7**0, 1597–1632 (2007).

[92] J. Shah, B. Deveaud, W. T. Tsang, A. C. Gossard, and P. Lugli, Determination of Intervalley Scattering Rates in GaAs by Subpicosecond Luminescence Spectroscopy, Phys. Rev. Lett. **5**9, 2222–2225 (1987).

[93] W. Z. Lin, L. G. Fujimoto, E. P. Ippen, and R. A. Logan, Femtosecond carrier dynamics in GaAs, Appl. Phys. Lett. **5**0, 124–126 (1987).

[94] F. Bloch, Über die Quantenmechanik der Elektronen in Kristallgittern, Z. Phys. **5**2, 555–600 (1929).

[95] James R. Chelikowsky and Marvin L. Cohen, Nonlocal pseudopotential calculations for the electronic structure of eleven diamond and zinc-blende semiconductors, Phys. Rev. B **1**4, 556–582 (1976) **30**, 4828(E) (1984).

[96] B. K. Ridley, *Quantum Processes in Semiconductors*, 3rd ed. (Oxford University Press, Oxford, 1993).

[97] J. Feldmann, K. Leo, J. Shah, D. A. B. Miller, J. E. Cunningham, T. Meier, G. von Plessen, A. Schulze, P. Thomas, and S. Schmitt-Rink, Optical investigation of Bloch oscillations in a semiconductor superlattice, Phys. Rev. B **4**6, 7252–7255 (1992).

[98] C. Waschke, H. G. Roskos, R. Schwedler, K. Leo, H. Kurz, and K. Köhler, Coherent submillimeter-wave emission from Bloch oscillations in a semiconductor superlattice, Phys. Rev. Lett. **7**0, 3319–3322 (1993).

[99] K. Unterrainer, B. J. Keay, M. C. Wanke, S. J. Allen, D. Leonard, G. Medeiros-Ribeiro, U. Bhattacharya, and M. J. W. Rodwell, Inverse Bloch oscillator: Strong terahertz-photocurrent resonances at the Bloch frequency, Phys. Rev. Lett. **7**6, 2973–2976 (1996).

[100] Immanuel Bloch, Quantum coherence and entanglement with ultracold atoms in optical lattices, Nature **4**53, 1016–1022 (2008).

[101] J. Delahaye, J. Hassel, R. Lindell, M. Sillanpää, M. Paalanen, H. Seppä, and P. Hakonen, Low-noise current amplifier based on mesoscopic Josephson junction, Science **2**99, 1045–1048 (2003).

[102] Demetrios N. Christodoulides, Falk Lederer, and Yaron Silberberg, Discretizing light behaviour in linear and nonlinear waveguide lattices, Nature **4**24, 817–823 (2003).

[103] C. L. Collins and P. Y. Yu, Generation of nonequilibrium optical phonons in GaAs and their application in studying intervalley electron-phonon scattering, Phys. Rev. B **3**0, 4501–4515 (1984).

[104] P. C. Becker, H. L. Fragnito, C. H. Brito Cruz, J. Shah, R. L. Fork, J. E. Cunningham, J. E. Henry, and C. V. Shank, Femtosecond intervalley scattering in GaAs, Appl. Phys. Lett. **5**3, 2089–2090 (1988).

[105] R. G. Ulbrich, J. A. Kash, and J. C. Tsang, Hot-electron recombination at neutral acceptors in GaAs: A cw probe of femtosecond intervalley scattering, Phys. Rev. Lett. **6**2, 949–952 (1989).

[106] A. J. Taylor, D. J. Erskine, and C. L. Tang, Ultrafast relaxation dynamics of photoexcited carriers in GaAs and related compounds, J. Opt. Soc. Am. B **2**, 663–673 (1985).

[107] A. Schwanhäußer, M. Betz, M. Eckardt, S. Trumm, L. Robledo, S. Malzer, A. Leitenstorfer, and G. H. Döhler, Ultrafast transport of electrons in GaAs: Direct observation of quasiballistic motion and side valley transfer, Phys. Rev. B **7**0, 085211 (2004).

[108] M. V. Fischetti, Monte Carlo simulation of transport in technologically significant semiconductors of the diamond and zinc-blende structures. I. Homogeneous transport, IEEE Trans. Electron Dev. **3**8, 634–649 (1991).

[109] M. Abe, S. Madhavi, Y. Shimada, Y. Otsuka, K. Hirakawa, and K. Tomizawa, Transient carrier velocities in bulk GaAs: Quantitative comparison between terahertz data and ensemble Monte Carlo calculations, Appl. Phys. Lett. **8**1, 679–681 (2002).

[110] H. Haug and A. P. Jauho, *Quantum Kinetics in Transport and Optics of Semiconductors*, (Springer, Berlin, 1996).

[111] A. Schenk, Halbleiterbauelemente - Physikalische Grundlagen und Simulation, http://e-collection.ethbib.ethz.ch/eserv/eth:24954/eth-24954-01.pdf.

[112] D. Strauch and B. Dorner, Phonon dispersion in GaAs, J. Phys. Condens. Matter **2**, 1457–1474 (1990).

[113] F. Schwabl, *Quantenmechanik*, (Springer, Berlin, 1992).

[114] W. Nolting, *Theoretische Physik*, (Zimmermann-Neufang, Ulmen, 1994).

[115] K. Fletcher and P. N. Butcher, An exact solution of the linearized Boltzmann equation with applications to the Hall mobility and Hall factor of n-GaAs, J. Phys. C **5**, 212–224 (1972).

[116] G. E. Stillman, C. M. Wolfe, and J. O. Dimmock, Hall coefficient factor for polar mode scattering in n-type GaAs, J. Phys. Chem. Solids **3**1, 1199–1204 (1970).

[117] J. Bardeen and W. Shockley, Deformation potentials and mobilities in non-polar crystals, Phys. Rev. **8**0, 72–80 (1950).

[118] K. Hübner, Piezoelectricity in zincblende- and wurtzite-type crystals, Phys. Stat. Sol. B **5**7, 241 (1973).

[119] P. Y. Yu and M. Cardona, *Fundamentals of Semiconductors*, (Springer, Berlin, 1996).

[120] Michael Woerner and Thomas Elsaesser, Nonlinear terahertz studies of ultrafast quasiparticle dynamics in semiconductors, in *Dynamics at Solid State Surfaces and Interfaces*, edited by Uwe Bovensiepen, Hrvoje Petek, and Martin Wolf (Wiley-VCH, Weinheim, 2010), Vol. 1, p. 3–32.

[121] W. Magnus and W. Schoenmaker, Dissipative motion of an electron-phonon system in a uniform electric field: An exact solution, Phys. Rev. B **4**7, 1276–1281 (1993).

[122] T. D. Lee, F. E. Low, and D. Pines, The motion of slow electrons in a polar crystal, Phys. Rev. **9**0, 297–302 (1953).

[123] Marvin L. Cohen and T. K. Bergstresser, Band structures and pseudopotential form factors for fourteen semiconductors of the diamond and zinc-blende structures, Phys. Rev. **1**41, 789–796 (1966).

[124] John P. Walter and Marvin L. Cohen, Calculation of the reflectivity, modulated reflectivity, and band structure of GaAs, GaP, ZnSe, and ZnS, Phys. Rev. **1**83, 763–772 (1969) **B 1**, 942(E) (1970).

[125] F. M. Peeters and J. T. Devreese, Radius, self-induced potential, and number of virtual optical phonons of a polaron, Phys. Rev. B **3**1, 4890–4899 (1985).

[126] L. Bányai, Motion of a classical polaron in a dc electric field, Phys. Rev. Lett. **7**0, 1674–1677 (1993).

[127] G. Meinert, L. Bányai, and P. Gartner, Classical polarons in a constant electric field, Phys. Rev. B **6**3, 245203 (2001).

[128] Tanmoy Bhattacharya, Salman Habib, and Kurt Jacobs, The emergence of classical dynamics in a quantum world, Los Alamos Science **2**7, 110–125 (2002).

[129] Tanmoy Bhattacharya, Salman Habib, and Kurt Jacobs, Continuous quantum measurement and the quantum to classical transition, Phys. Rev. A **6**7, 042103 (2003).

[130] J. H. Jensen and J. A. Sauls, Polarons near the Cerenkov velocity, Phys. Rev. B **3**8, 13387–13394 (1988).

[131] T. H. Windhorn, T. J. Roth, L. M. Zinkiewicz, O. L. Gaddy, and G. E. Stillman, High field temperature dependent electron drift velocities in GaAs, Appl. Phys. Lett. **4**0, 513–515 (1982).

[132] T. Tsuruoka, H. Hashimoto, and S. Ushioda, Real-space observation of electron transport in AlGaAs/GaAs quantum wells using a scanning tunneling microscope, Thin Solid Films **4**64-465, 469–472 (2004).

[133] Michael Stobbe, Ronald Redmer, and Wolfgang Schattke, Impact ionization rate in GaAs, Phys. Rev. B **4**9, 4494–4500 (1994).

[134] J. Bude and K. Hess, Thresholds of impact ionization in semiconductors, J. Appl. Phys. **7**2, 3554–3561 (1992).

[135] M. Stobbe, A. Könies, R. Redmer, J. Henk, and W. Schattke, Interband transitions rate in GaAs, Phys. Rev. B **4**4, 11105–11110 (1991).

[136] P. A. Wolff, Theory of electron multiplication in silicon and germanium, Phys. Rev. **9**5, 1415–1420 (1954).

[137] I. Melngailis, G. E. Stillman, J. O. Dimmock, and C. M. Wolfe, Far-infrared recombination radiation from impact-ionized shallow donors in GaAs, Phys. Rev. Lett. **2**3, 1111–1114 (1969).

[138] J. T. Devreese, R. G. van Welzenis, and R. P. Evrard, Impact ionisation probability in InSb, Appl. Phys. A **2**9, 125–132 (1982).

[139] Sabine Kolodinski, Jürgen H. Werner, Thomas Wittchen, and Hans J. Queisser, Quantum efficiencies exceeding unity due to impact ionization in silicon solar cells, Appl. Phys. Lett. **6**3, 2405–2407 (1993).

[140] S. D. Ganichev, J. Diener, and W. Prettl, Nonlinear far-infrared absorption in InSb due to light impact ionization, Appl. Phys. Lett. **6**4, 1977–1979 (1994).

[141] A. G. Markelz, N. G. Asmar, B. Brar, and E. G. Gwinn, Interband impact ionization by terahertz illumination of InAs heterostructures, Appl. Phys. Lett. **6**9, 3975–3977 (1996).

[142] Aldo Di Carlo, P. Vogl, and W. Pötz, Theory of Zener tunneling and Wannier-Stark states in semiconductors, Phys. Rev. B **5**0, 8358–8377 (1994).

[143] C. Zener, Non-adiabatic Crossing of Energy Levels, Proc. Roy. Soc. A **1**37, 696–702 (1932).

[144] L. Landau, Zur Theorie der Energieubertragung. II, Phys. Sov. Union **2**, 46–51 (1932).

[145] E. O. Kane, Zener tunneling in semiconductors, J. Phys. Chem. Solids **1**2, 181–188 (1959).

[146] A. G. Chynoweth and K. G. McKay, Internal Field Emission in Silicon *p*-*n* Junctions, Phys. Rev. **1**06, 418–427 (1957).

[147] John V. Morgan and Evan O. Kane, Observation of direct tunneling in germanium, Phys. Rev. Lett. **3**, 466–468 (1959).

[148] D. J. Dumin and G. L. Pearson, Properties of gallium arsenide diodes between 4.2 and 300 K, J. Appl. Phys. **3**6, 3418–3426 (1965).

[149] L. Gaul, S. Huber, J. Freyer, and M. Claassen, Determination of tunnel-generation rate from GaAs PIN-structures, Solid State Electron. **3**4, 723–726 (1991).

[150] D. Liebig, P. Lugli, P. Vogl, M. Claassen, and W. Harth, Tunneling and ionization phenomena in GaAs PIN diodes, Microelectron. Engin. **1**9, 127–130 (1992).

[151] R. F. Kazarinov and R. A. Suris, Possibility of the amplification of electromagnetic waves in a semiconductor with a superlattice, Fiz. Tekh. Poluprovodn. **5**, 797–800 (1971) [Sov. Phys. Semicond. **5**, 707–709 (1971)].

[152] R. F. Kazarinov and R. A. Suris, Electric and electromagnetic properties of semiconductors with a superlattice, Fiz. Tekh. Poluprovodn. **6**, 148–162 (1972) [Sov. Phys. Semicond. **6**, 120–131 (1972)].

[153] H. G. Roskos, M. C. Nuss, J. Shah, K. Leo, D. A. B. Miller, A. M. Fox, S. Schmitt-Rink, and K. Köhler, Coherent submillimeter-wave emissions from charge oscillations in a double-well potential, Phys. Rev. Lett. **6**8, 2216–2219 (1992).

[154] Wojciech H. Zurek, Decoherence and the transition from quantum to classical, Phys. Today **4**4(10), 36–44 (1991).

[155] Wojciech H. Zurek, Decoherence and the transition from quantum to classical—revisited, Los Alamos Science **2**7, 86–109 (2002).

[156] Wojciech Hubert Zurek, Decoherence, einselection, and the quantum origins of the classical, Rev. Mod. Phys. **7**5, 715–775 (2003).

[157] Y. P. Varshni, Temperature dependence of the energy gap in semiconductors, Physica **3**4, 149–154 (1967).

[158] E. O. Kane, Theory of tunneling, J. Appl. Phys. **3**2, 83–91 (1961).

[159] A. O. Caldeira and A. J. Leggett, Path integral approach to quantum Brownian motion, Physica **1**21A, 587–616 (1983).

[160] A. J. Leggett, S. Chakravarty, A. T. Dorsey, Matthew P. A. Fisher, Anupam Garg, and W. Zwerger, Dynamics of the dissipative two-state system, Rev. Mod. Phys. **5**9, 1–85 (1987).

[161] M. Woerner, K. Reimann, and T. Elsaesser, Coherent charge transport in semiconductor quantum cascade structures, J. Phys.: Condens. Matter **1**6, R25–48 (2004).

[162] James R. Chelikowsky and Marvin L. Cohen, Electronic structure of GaAs, Phys. Rev. Lett. **3**2, 674–677 (1974).

[163] Mackillo Kira, Walter Hoyer, and Stephan W. Koch, Microscopic theory of the semiconductor terahertz response, Phys. Status Solidi B **2**38, 443–450 (2003).

[164] E. Normand, I. Howieson, and M. T. McCulloch, Quantum-cascade lasers enable gas-sensing technology, Laser Focus World **4**3, 90–92 (2007).

[165] M. Razeghi, S. Slivken, Y. Bai, and S. R. Darvish, The Quantum Cascade LASER: A Versatile and Powerful Tool, Opt. Phot. N. **1**9, 42–47 (2008).

[166] A. Y. Cho, Advances in molecular beam epitaxy (MBE), J. Crys. Gr. **1**11, 1–13 (1991).

[167] S. Mantl and H. L. Bay, New method for epitaxial heterostructure layer growth, Appl. Phys. Lett. **6**1, 267–269 (1992).

[168] J. Faist, F. Capasso, D. L. Sivco, A. L. Hutchinson, C. Sirtori, and A. Y. Cho, Quantum cascade laser, Science **2**64, 553–556 (1994).

[169] M. P. Semtsiv, M. Wienold, S. Dressler, and W. T. Masselink, Short-wavelength ($\lambda \approx$ 3.05 μm InP-based strain-compensated quantum-cascade laser., Appl. Phys. Lett. **9**0, 0511111–0511113 (2007).

[170] G. Scalari, C. Walther, J. Faist, H. Beere, and D. Ritchie, Electrically switchable, two-color quantum cascade laser emitting at 1.39 and 2.3 THz, Appl. Phys. Lett. **8**8, 1411021–1411023 (2006).

[171] M. Wienold, M. P. Semtsiv, I. Bayrakli W. T. Masselink, M. Ziegler, K. Kennedy, and R. Hogg, Optical and thermal characteristics of narrow-ridge quantum-cascade lasers, J. Appl. Phys. **1**03, 0831131–0831131 (2008).

[172] A. Evans, S. R. Darvish, S. Slivken, J. Nguyen, Y. Bai, and M. Razeghi, Buried heterostructure quantum cascade lasers with high continuous-wave wall plug efficiency, Appl. Phys. Lett. **9**1, 0711011–0711013 (2007).

[173] F. Eickemeyer, R. A. Kaindl, M. Woerner, T. Elsaesser, S. Barbieri, P. Kruck, C. Sirtori, and J. Nagle, Large electrically induced transmission changes of GaAs/AlGaAs quantum cascade structures, Appl. Phys. Lett. **7**6, 3254–3256 (2000).

[174] F. Eickemeyer, K. Reimann, M. Woerner, T. Elsaesser, S. Barbieri, C. Sirtori, G. Strasser, T. Müller, R. Bratschitsch, and K. Unterrainer, Ultrafast coherent electron transport in semiconductor quantum cascade structures, Phys. Rev. Lett. **8**9, 047402-1–4 (2002).

[175] Hyunyong Choi, Laurent Diehl, Zong-Kwei Wu, Marcella Giovannini, Jérôme Faist, Federico Capasso, and Theodore B. Norris, Gain recovery dynamics and photon-driven transport in quantum cascade lasers, Phys. Rev. Lett. **1**00, 167401 (2008).

[176] Hyunyong Choi, Laurent Diehl, Marcella Giovannini, Jérôme Faist, Federico Capasso, and Theodore B. Norris, Femtosecond pump-probe studies of carrier transport and gain dynamics in quantum cascade lasers, Phys. Status Solidi C **5**, 225–228 (2008).

[177] Hyunyong Choi, Theodore B. Norris, Tobias Gresch, Marcella Giovannini, Jérôme Faist, Laurent Diehl, and Federico Capasso, Femtosecond dynamics of resonant tunneling and superlattice relaxation in quantum cascade lasers, Appl. Phys. Lett. **9**2, 122114 (2008).

[178] S.-C. Lee, F. Banit, M. Woerner, and A. Wacker, Quantum mechanical wavepacket transport in quantum cascade laser structures, Phys. Rev. B **7**3, 245320 (2006).

[179] R. C. Iotti and F. Rossi, On the nature of charge transport in quantum-cascade lasers, Phys. Rev. Lett. **8**7, 146603 (2001).

[180] P. Enders, A. Bärwolff, M. Woerner, and D. Suisky, $\mathbf{k}\cdot\mathbf{p}$ theory of energy bands, wave functions, and optical selection rules in strained tetrahedral semiconductors, Phys. Rev. B **5**1, 16695–16704 (1995).

[181] I. Vurgaftman, J. R. Meyer, and L. R. Ram-Mohan, Band parameters for III–V compound semiconductors and their alloys, J. Appl. Phys. **8**9, 5815–5875 (2001).

[182] K. Reimann, R. A. Kaindl, and M. Woerner, Optical deformation-potential scattering of holes in multiple quantum well structures, Phys. Rev. B **6**5, 045302 (2002).

[183] M. F. Pereira, Jr., R. Nelander, A. Wacker, D. G. Revin, M. R. Soulby, L. R. Wilson, J. W. Cockburn, A. B. Krysa, J. S. Roberts, and R. J. Airey, Characterization of intersubband devices combining a nonequilibrium many body theory with transmission spectroscopy experiments, J. Mater. Sci. Mater. Electron. **1**8, 689–694 (2007).

[184] Shaul Mukamel, Multidimensional femtosecond correlation spectroscopies of electronic and vibrational excitations, Annu. Rev. Phys. Chem. **5**1, 691–729 (2000).

[185] Peter Hamm, Manho Lim, and Robin M. Hochstrasser, Structure of the amide I band of peptides measured by femtosecond nonlinear-infrared spectroscopy, J. Phys. Chem. B **1**02, 6123–6138 (1998).

[186] M. C. Asplund, M. T. Zanni, and R. M. Hochstrasser, Two-dimensional infrared spectroscopy of peptides by phase-controlled femtosecond vibrational photon echoes, Proc. Natl. Acad. Sci. USA **9**7, 8219–8224 (2000).

[187] K. Okumura, A. Tokmakoff, and Y. Tanimura, Two-dimensional line-shape analysis of photon-echo signal, Chem. Phys. Lett. **3**14, 488–495 (1999).

[188] Sander Woutersen and Peter Hamm, Nonlinear two-dimensional vibrational spectroscopy of peptides, J. Phys.: Condens. Matter **1**4, R1035–1062 (2002).

[189] M. Khalil, N. Demirdöven, and A. Tokmakoff, Coherent 2D IR spectroscopy: Molecular structure and dynamics in solution, J. Phys. Chem. A **1**07, 5258–5279 (2003).

[190] M. L. Cowan, B. D. Bruner, N. Huse, J. R. Dwyer, B. Chugh, E. T. J. Nibbering, T. Elsaesser, and R. J. D. Miller, Ultrafast memory loss and energy redistribution in the hydrogen bond network of liquid H_2O, Nature **4**34, 199–202 (2005).

[191] N. Huse, B. D. Bruner, M. L. Cowan, J. Dreyer, E. T. J. Nibbering, R. J. D. Miller, and T. Elsaesser, Anharmonic Couplings Underlying the Ultrafast Vibrational Dynamics of Hydrogen Bonds in Liquids, Phys. Rev. Lett. **9**5, 147402–147402 (2005).

[192] J. D. Hybl, A. Yu, D. A. Farrow, and D. M. Jonas, Polar Solvation Dynamics in the Femtosecond Evolution of Two-Dimensional Fourier Transform Spectra, J. Phys. Chem. **1**06, 7651–7654 (2002).

[193] F. Milota, J. Sperling, A. Nemeth, T. Manal, and H. F. Kauffmann, Two-Dimensional Electronic Spectroscopy of Molecular Excitons, Acc. Chem. Res. **4**2, 1364–1374 (2009).

[194] J. Sperling, A. Nemeth, J. Hauer, D. Abramavicius, S. Mukamel, H. F. Kauffmann, and F. Milota, Excitons and Disorder in Molecular Nanotubes: A 2D Electronic Spectroscopy Study and First Comparison to a Microscopic Model, J. Phys. Chem. A **1**14, 8179–8189 (2010).

[195] Tobias Brixner, Jens Stenger, Harsha M. Vaswani, Minhaeng Cho, Robert E. Blankenship, and Graham R. Fleming, Two-dimensional spectroscopy of electronic couplings in photosynthesis, Nature **4**34, 625–628 (2005).

[196] Y. C. Cheng and G. R. Fleming, Dynamics of Light Harvesting in Photosynthesis, Annu. Rev. Phys. Chem. **6**0, 241–262 (2009).

[197] G. Panitchayangkoon, D. Hayes, K. A. Fransted, J. R. Caram, E. Harel J. Wen, R. E. Blankenship, and G. S. Engel, Long-lived quantum coherence in photosynthetic complexes at physiological temperature, Proc. Nat. Acad. Sci. Am. **1**07, 12766–12770 (2010).

[198] X. Li, T. Zhang, C. N. Borca, and S. T. Cundiff, Many-Body Interactions in Semiconductors Probed by Optical Two-Dimensional Fourier Transform Spectroscopy, Phys. Rev. Lett. **9**6, 0574061–0574064 (2006).

[199] K. W. Stone, K. Gundogdu, D. B. Turner, X. Li, S. T. Cundiff, and K. A. Nelson, Two-Quantum 2D FT Electronic Spectroscopy of Biexcitons in GaAs Quantum Wells, Science **3**24, 1169–1173 (2009).

[200] D. B. Turner and K. A. Nelson, Coherent measurements of high-order electronic correlations in quantum wells, Nature **4**66, 1089–1092 (2010).

[201] Sean Garrett-Roe and Peter Hamm, Purely absorptive three-dimensional infrared spectroscopy, J. Chem. Phys. **1**30, 164510 (2009).

[202] Peifang Tian, Dorine Keusters, Yoshifumi Suzaki, and Warren S. Warren, Femtosecond phase-coherent two-dimensional spectroscopy, Science **3**00, 1553–1555 (2003).

[203] W. P. Aue, E. Bartholdi, and R. R. Ernst, Two-dimensional spectroscopy. Application to nuclear magnetic resonance, J. Chem. Phys. **6**4, 2229–2246 (1976).

[204] Valentina Cervetto, Jan Helbing, Jens Bredenbeck, and Peter Hamm, Double-resonance versus pulsed Fourier transform two-dimensional infrared spectroscopy: An experimental and theoretical comparison, J. Chem. Phys. **1**21, 5935–5942 (2004).

[205] W. H. Knox, C. Hirlimann, D. A. B. Miller, J. Shah, D. S. Chemla, and C. V. Shank, Femtosecond Excitations of Nonthermal Carrier Populations in GaAs Quantum Wells, Phys. Rev. Lett. **5**6, 1191–1193 (1986).

[206] Z. Wang, K. Reimann, M. Woerner, T. Elsaesser, D. Hofstetter, J. Hwang, W. J. Schaff, and L. F. Eastman, Optical phonon sidebands of electronic intersubband absorption in strongly polar semiconductor heterostructures, Phys. Rev. Lett. **9**4, 037403-1–4 (2005).

[207] D. M. Jonas, Two-dimensional femtosecond spectroscopy, Annu. Rev. Phys. Chem. **5**4, 425–463 (2003).

[208] T. Zhang, C. N. Borca, X. Li, and S. T. Cundiff, Optical two-dimensional Fourier transform spectroscopy with active interferometric stabilization, Opt. Expr. **1**3, 7432–7441 (2005).

[209] C. W. Luo, K. Reimann, M. Woerner, T. Elsaesser, R. Hey, and K. H. Ploog, Rabi oscillations of intersubband transitions in GaAs/AlGaAs MQWs, Semicond. Sci. Technol. **1**9, S285–286 (2004).

[210] F. Eickemeyer, M. Woerner, A. M. Weiner, T. Elsaesser, R. Hey, and K. H. Ploog, Coherent nonlinear propagation of ultrafast electric field transients through intersubband resonances, Appl. Phys. Lett. **7**9, 165–167 (2001).

[211] C. W. Luo, K. Reimann, M. Woerner, T. Elsaesser, R. Hey, and K. H. Ploog, Phase-resolved nonlinear response of a two-dimensional electron gas under femtosecond intersubband excitation, Phys. Rev. Lett. **9**2, 047402-1–4 (2004).

[212] T. Shih, K. Reimann, M. Woerner, T. Elsaesser, I. Waldmüller, A. Knorr, R. Hey, and K. H. Ploog, Nonlinear response of radiatively coupled intersubband transitions of quasi–two-dimensional electrons, Phys. Rev. B **7**2, 195338-1–8 (2005).

[213] I. I. Rabi, Space quantization in a gyrating magnetic field, Phys. Rev. **5**1, 652–654 (1937).

[214] *Landolt-Börnstein – Zahlenwerte und Funktionen aus Naturwissenschaften und Technik*, edited by U. Rössler (Springer, Berlin, 2001), Vol. III/41A1α.

[215] Front page, 1953.

[216] S. Mukamel, *Principles of Nonlinear Optical Spectroscopy*, (Oxford University Press, New York, 1995).

[217] R. R. Ernst, G. Bodenhausen, and A. Wokaun, *Principles of Nuclear Magnetic Resonance in One and Two Dimensions*, (Oxford University Press, Oxford, 1987).

[218] E. O. Kane, Band structure of indium antimonide, J. Phys. Chem. Solids **1**, 249–261 (1957).

[219] K. Reimann, R. A. Kaindl, and M. Woerner, Optical deformation-potential scattering of holes in multiple quantum well structures, Phys. Rev. B **6**5, 045302-1–10 (2002).

[220] Z. Wang, K. Reimann, M. Woerner, T. Elsaesser, D. Hofstetter, E. Baumann, F. R. Giorgetta, H. Wu, W. J. Schaff, and L. F. Eastman, Ultrafast hole-burning in intersubband absorption lines of GaN/AlN superlattices, Appl. Phys. Lett. **8**9, 151103-1–3 (2006).

[221] T. Kuhn, Density matrix theory of coherent ultrafast dynamics, in *Theory of Transport Properties of Semiconductor Nanostructures*, edited by E. Schöll (Chapman & Hall, London, 1998), p. 173–214.

[222] W. Kuehn, K. Reimann, M. Woerner, T. Elsaesser, and R. Hey, Two-color two-dimensional terahertz spectroscopy on intersubband transitions of coupled quantum wells, Quantum Electronics and Laser Science Conference, San Jose 2010.

[223] L. D. Landau and E. M. Lifschitz, *Lehrbuch der Theoretischen Physik II – Feldtheorie*, 5th ed. (Akademie-Verlag, Berlin, 1990).

[224] C. Kübler, R. Huber, and A. Leitenstorfer, Ultrabroadband terahertz pulses: generation and field-resolved detection, Semicond. Sci. Technol. **2**0, S128–133 (2005).

[225] N. W. Ashcroft and N. D. Mermin, *Festkörperphysik*, 3rd ed. (Oldenbourg, München, 2007).

[226] G. Wentzel, Über strahlungslose Quantensprünge, Z. Phys. **4**3, 524–530 (1927).

Danksagung

Ich werde meine Promotion als eine sehr schöne und intensive Zeit in Erinnerung behalten. Deshalb möchte ich allen ganz herzlich danken, mit denen ich in dieser Zeit zusammen arbeiten durfte und die zum Gelingen dieser Doktorarbeit beigetragen haben.

Ich danke besonders Herrn Professor Thomas Elsässer für die fachliche Betreuung dieser Arbeit und für die anregenden Diskussionen und Ratschläge. Auch die hervorragende Ausstattung, sowie die internationale Vernetzung des Max Born Instituts waren für diese Arbeit mit entscheidend.

Herrn Professor Peter Hamm, und Herrn Professor W. Ted Masselink danke ich sehr herzlich für die Bereitschaft und die Zeit, diese Arbeit zu lesen und zu begutachten.

Besonderer Dank gilt außerdem unserem Abteilungsleiter Dr. Michael Wörner. Sein Wissen, seine Kreativität und seine Neugier habe ich in zahlreichen lehrreichen und spannenden Diskussionen sehr zu schätzen gelernt. Mit seinem unermüdlichen Einsatz hat Michael wesentlich zum Gelingen dieser Arbeit beigetragen.

Ich danke Herrn Professor Klaus Reimann für die engelsgleiche Geduld alle meine Fragen zu beantworten. Seine klaren physikalischen Bilder komplexer Sachverhalte haben meine Neugier und meinen Spaß an der Physik stets neu geschürt.

Ich danke der gesamten Arbeitsgruppe Sergej, Benjamin, Flavio, Philipp, Johannes, Gaby und Pamela für die Unterstützung, wann immer sie nötig war und für die sehr angenehme Arbeitsatmosphäre. Insbesondere wünsche ich Pamela viel Spaß und Erfolg bei der Weiterführung des Experiments. Herrn Dr. Rudolf Hey danke ich für die Herstellung der Quantentrogproben, und Herrn Dr. Ulrich Schade danke ich für die Unterstützung bei den linearen Absorptionsmessungen. Auch bei Herrn Dr. Ihar Babushkin, Herrn Dr. Stefan Skupin und Herrn Dr. Joachim Herrmann bedanke ich mich herzlich für die gute Zusammenarbeit.

Nicht zuletzt danke ich meiner Freundin Angela, sowie meinen Eltern Hsueh-Ying und Ludwig für die emotionale Unterstützung und den gewissen Rahmen, der konzentriertes Arbeiten während der Promotion erst möglich gemacht hat.

List of Figures

1.1 Optics meets transport . . . 2

2.1 Oscillator setup . . . 6
2.2 Amplifier and compressor setup . . . 6
2.3 THz pulses generated in GaSe . . . 8
2.4 Difference frequency mixing in GaSe . . . 9
2.5 THz emission from a laser-induced plasma . . . 10
2.6 Experimental setup . . . 11
2.7 Measured interferograms and corresponding spectra . . . 13
2.8 Ionization process within the plasma . . . 14
2.9 Computed plasma channel for 200 mbar . . . 14
2.10 Comparison between experimental and simulated generated spectra . . . 15
2.11 Propagation effects cause substantially different obtained spectra . . . 16
2.12 Electrooptic sampling . . . 17
2.13 Measured parameters at IR/VIS and THz frequencies . . . 20
2.14 Sample design . . . 22
2.15 Photograph of sample . . . 22
2.16 Thin film sample . . . 23
2.17 Imaging geometry with two focussing elements . . . 24
2.18 Emitted field . . . 25

3.1 Conduction band electrons under the force of an external electric field . . . 28
3.2 Scattering rates in GaAs obtained with FGR . . . 30
3.3 Decreasing friction force at high velocities . . . 30
3.4 Experimental setup . . . 32
3.5 Emitted field transients . . . 33
3.6 Analyzes of recorded data . . . 34
3.7 Comparison of experiment theory . . . 36
3.8 Different transport regimes in GaAs . . . 37
3.9 Phonon dispersion relation in GaAs . . . 38
3.10 Different scattering processes in *n*-type GaAs . . . 39
3.11 Quantum-kinetic decoupling . . . 42
3.12 Comparison of polaron and BTE model on long time scales . . . 44
3.13 Comparison of polaron and BTE model on short time scales . . . 45
3.14 Electron velocities in Ref. [31] and Ref. [131] . . . 47

4.1 Process of impact ionization and expected ionization rates in GaAs . . . 49
4.2 Tunneling through a barrier and through a bandgap . . . 50
4.3 Emitted field at 80 K 200 K . . . 52
4.4 Emitted field at 300 K and at 80 K . . . 53

4.5 Absorbed energy at different field amplitudes 54
4.6 Off-resonant excitation 55
4.7 Tunneling rate as a function of decoherence 56
4.8 Decoherence in field-induced interband tunneling 57
4.9 Electronic bandstructure of GaAs 59
4.10 Tunneling rate according to our model 61
4.11 Comparison between theory and experiment 62

5.1 Quantum cascade structure 64
5.2 Calculated wavefunctions within a QCL 67
5.3 $I-V$ characteristic of the QCL 67
5.4 Experimental setup 68
5.5 Four recorded situation per delay time 69
5.6 Pump induced change in amplitude and phase 70
5.7 Pump-induced change in amplitude and phase 71
5.8 Optical gain as a function of current 72

6.1 Comparison between double resonance and 2D photon method 75
6.2 Pump-probe experiments in one and two dimensions 76
6.3 Dynamical spectral hole burning 77
6.4 Setup for 2D photon echo experiments 79
6.5 Transient grating in space 80
6.6 N-wave mixing in space and in time 80
6.7 Transient grating in delay time 81
6.8 Recorded electric field in time and frequency domain 82
6.9 Double pulse spectrum 83
6.10 Recorded constellations of electric fields 85
6.11 Measured nonlinear signal 85
6.12 Simulated nonlinear signal in two dimensions 86
6.13 Two-dimensional spectrum 86
6.14 Third harmonic generation 87
6.15 Investigated multiple quantum well sample 88
6.16 Previous experiments on the MQW sample 88
6.17 Experimental setup 89
6.18 Experimental data for 30 kV/cm 90
6.19 Oscillating photon echo intensity 90
6.20 Time of emitted photon echoes 92
6.21 Experimental: 2D spectra of Rabi oscillation 93
6.22 Theoretical: 2D spectra of Rabi oscillation 93
6.23 Illustration of photon echo 95
6.24 The Bloch vector represents a two-level system in a pure state 97
6.25 Four-wave mixing signal 98
6.26 Feynman diagrams of pump-probe and third harmonic FWM signal 100
6.27 Rephasing photon echoes and nonrephasing virtual echoes 100
6.28 Rehasing, nonrephasing and 2D correlation spectrum 101
6.29 Phase evolution during a photon echo 102
6.30 Emission of the photon echo and the virtual echo 104

6.31 Addition of rephasing and nonrephasing echo 105
6.32 Each nonlinear is unambiguously identified 105
6.33 Linear absorption spectrum and calculated bound states 106
6.34 Nonlinear signal 107
6.35 Experimental and simulated 2D correlation spectra 109
6.36 Linear absorption and calculated wavefunctions of the a-DQWS 110
6.37 Incident pulses to study the a-DQWS 111
6.38 Nonlinear signal and the corresponding 2D spectrum 112
6.39 Spectrally resolved transmission changes 113
6.40 2D correlation spectrum of the a-DQWS 113
6.41 Coupling of electronic and LO phonon excitations 114
6.42 Predicted intersubband polaron states 115
6.43 Differences between a collinear and a noncollinear setup 117
6.44 Improvement of the signal-to-noise ratio in 2D experiments 118
6.45 Definition of second and meter 120
6.46 Time dilatation explained with frequency vectors 121
6.47 Illustration of time and space 121

1 Limitations of FGR 132

2 Investigated multiple quantum well sample 134
3 Linear absorption spectrum and calculated bound states 134
4 Linear absorption and calculated wavefunctions of the a-DQWS 135

List of Tables

2.1 Parameters of the oscillator and the multipass amplifier laser system 7

6.1 Nonlinear signals in the time and in the frequency domain 103

1 Properties of the investigated quantum well samples 133

Selbständigkeitserklärung

Ich erkläre, dass ich die vorliegende Arbeit selbständig und nur unter Verwendung der angegebenen Literatur und Hilfsmittel angefertigt habe.

Berlin, den 9. Dezember 2010 Wilhelm Kühn